DYNAMIC MODELLING, TRANSIENT BEHAVIOUR ANALYSIS AND SCHEDULING OF VOLATILE ORGANIC COMPOUND (VOC) ABATEMENT SYSTEMS FOR THE PHARMA INDUSTRY

THE UNIVERSITY
of EDINBURGH

Vasiliki Tzanakopoulou
Doctor of Philosophy Thesis
University of Edinburgh
2024

Declaration

In accordance with assessment regulation 34, I declare the following:

(a) This thesis has been composed by myself.

(b) This PhD thesis is my own, except where explicitly stated otherwise within the text.

(c) This PhD thesis has not been submitted for any other degree or professional qualification.

(d) Any included publications are my own work, except where explicitly stated otherwise within the text.

Vasiliki Tzanakopoulou

Acknowledgements

Completing a PhD thesis is a journey that often feels like a solitary pursuit, but it in my experience is anything but that. There are numerous individuals and entities who have been instrumental to this endeavour, a short account of which follows:

First and foremost, my principal supervisor, Professor Dimitrios I. Gerogiorgis, whose expertise, mentorship, humour, and unwavering support have been essential in shaping this research and my growth as a researcher.

My PhD Thesis examiners, Professor Joan Cordiner, Professor Xianfeng Fan and Dr Smitha Gopinath, for their thorough and detailed critical review of this thesis and for examining my viva voce.

My industrial supervisors, Dr Michael Pollitt, and Dr Daniel Castro Rodriguez, to whom I extend my sincere appreciation for their collaboration, expertise, mentorship and contribution to this research.

Special thanks are due to Dr Mauro Luberti for his invaluable advice and insights throughout my doctoral journey, as well as, my alma matter Professors, Dr Marc Assael and Dr Michael Georgiadis for their encouragement, support and advice in undertaking this pursuit.

I am deeply indebted to my colleagues and fellow graduate students, whose camaraderie, and support have made the journey of pursuing a PhD more enjoyable and fulfilling.

Special thanks are due to the Scottish Research Partnership in Engineering (SRPe), GlaxoSmithKline, and the University of Edinburgh for their financial support.

I am also grateful to my family, friends and partner for their unwavering love, encouragement, and understanding throughout this journey. Their belief in me, patience, and emotional support have been a constant source of strength and motivation.

Abstract

Active Pharmaceutical Ingredient (API) manufacturing is heavily reliant on solvents for reactions and separations. Among them, Volatile Organic Compounds (VOCs) reign supreme, although their emissions pose a risk both to the environment and human health. With the effects of climate change becoming more prominent, stringent regulations are in place to ensure the enforcement of environment-conscious industrial. Adsorption on activated carbon beds is an established VOC control technology, often preferred on an industrial level due to the low cost of installation and maintenance, as well as its effectiveness in treating large volumetric streams containing trace amounts of pollutants. However, the simultaneous feeding of varying composition and load waste streams from plant-wide process vents under batch operation causes quick and irregular bed saturation, leading to sub-optimal process efficiency, with higher operational costs due to frequent adsorbent material regeneration outsourcing. Despite the multitude of studies on adsorption over the years, there is a profound mismatch towards the proportion of research focused on multicomponent VOC adsorption under realistic industrial conditions. Mathematical modelling and simulations are valuable tools towards understanding the complex interactions of competing solvent emission streams and allow process optimisation without the need for costly and resource-intensive pilot plant experiments.

This PhD thesis aims to elucidate the intrinsic relationships between complex pharmaceutical manufacturing solvent vapour mixtures and propose operational optimisation scenarios to minimise environmental leak risks as well as maximise process efficiency, at an even lower operational cost. In order to address the dire need for reliable thermodynamic parameter values, a Langmuir Isotherm parameter database is established for organic solvents based on published experimental data. Next, a dynamic, multicomponent, nonisothermal adsorption model is constructed and used to highlight the interactions of key VOC binary mixtures under a range of steady-state and transient feed conditions, temperatures, activated carbon bed structures, column lengths and stream velocities. Furthermore, Hodograph Theory breakthrough metrics are compared with validated simulation results to test the extrapolation potential of single component mixture predictions to multicomponent mixtures as a quick, operational plant decision-making tool. The dynamic model simulation results for the different mixtures are then employed to inform Mixed Integer Linear Programming (MILP) scheduling models for process optimisation and comparative economic evaluation. This PhD thesis highlights the immense value of systematic and rigorous model-based simulation and optimisation campaigns for VOC emission abatement systems in the pharmaceutical industry.

Lay Summary

This PhD thesis presents a concentrated effort on dynamic modelling, scheduling and economic evaluation of Volatile Organic Compound (VOC) emissions abatement in the pharmaceutical industry. VOCs are at the heart of primary pharmaceutical manufacturing, comprising 56% of total solvent mass. While their properties are indispensable for reactions and separations, the inevitable emissions from process units can pose serious risks to the atmosphere, ecosystems and human health, with industrial processes contributing to ca 60% of anthropogenic VOC emissions in the UK. Stringent environmental protection laws render end-of-pipe abatement essential. Adsorption with activated carbon is an established VOC control technique on an industrial level, however, its operation is often suboptimal due to the complex mixtures and frequent need for adsorbent regeneration which comes at high cost.

This thesis firstly presents the calculation of Langmuir Isotherm model parameters based on published experimental data of single-component VOC adsorption on activated carbon for acetone, dichloromethane, chloroform and toluene. Chapter four presents the development of the dynamic simulations model, which is multicomponent, non-isothermal and uses the Linear Driving Force model for solid phase mass transport and the Langmuir Isotherm for equilibrium. In the next chapters the model is validated with published experimental data and key binary mixtures of trace concentrations VOCs and their adsorption characteristics are examined. Moreover, the effect of several process parameters such as flowrate, temperature and column length are investigated. Key metrics of Hodograph Theory derived from single component adsorption are compared to our dynamic simulation (gPROMS$^{®}$) results as an assessment of their suitability for extrapolation to multicomponent mixtures ultimately to act as a tool to assist operational decision-making prior to the engagement of further resources. Furthermore, the thesis continues to present VOC adsorption of pharmaceutically-relevant solvent mixtures under transient feed conditions, informed by industrial operation. Finally, a mixed integer linear programming (MILP) model for Active Pharmaceutical Ingredient (API) production scheduling is formulated and solved to optimality with respect to makespan minimisation, while accounting for VOC emissions abatement informed by gPROMS$^{®}$ simulation results. Based on the MILP results and industrial data, a detailed operating expenditure economic evaluation of different VOC emission scenarios is presented and analysed. The insights from this thesis can be extended across industries where VOC emissions abatement via adsorption is employed, paving the way for process optimisation under environmentally friendly scenarios that align with market demands.

Contents

List of Figures

List of Tables

PART I

INTRODUCTION & MOTIVATION

Chapter 1

Introduction

This chapter provides some background on volatile organic compounds. The main properties, emission trends by country and sectors over the past decades, and their effects on human health and the environment are first discussed, followed by a discussion on their use in the context of pharmaceutical manufacturing. Next, the main developments in VOC emissions abatement technologies are introduced with a focus on adsorption processes and their main characteristics.

1.1 Volatile Organic Compounds

Volatile Organic Compounds (VOCs) are organic substances with high vapour pressure and low boiling points. VOCs are emitted from both natural and anthropogenic sources. Natural sources include vegetation, naturally occurring forest fires, as well as anaerobic moors processes (David & Niculescu, 2021). Anthropogenic VOC sources comprise the industrial processes (paints, resins, chemicals and pharmaceuticals manufacturing), transportation, household product solvent use, agriculture, waste as well as fugitive emissions from fuels (EPA, 2024; Koppmann, 2007).

1.1.1 VOC Emissions in the manufacturing sector

Figure 1 summarizes the VOC emissions percentage by contributing sector in the UK between 1990-2021. Over the past 30 years in the UK, great VOC emissions reductions have been achieved in the transportation and fugitive emissions sectors, possibly due to stricter vehicle emission standards, in combination with a decrease in coal mining activity and better mitigation of emissions in the petroleum fuels manufacturing, respectively. The VOC emissions mix in the UK has therefore changed over the last thirty years. The decline in emissions from the transportation sector has allowed industrial processes to dominate the emissions mix. Specifically, the increase is associated with the chemicals and pharmaceuticals manufacturing as well as the food and drinks industry. Agricultural emissions, also an increasingly dominant sector, are primarily attributed to the use of pesticides. This shift in the contributing sector bears significance due to the different VOCs associated with each sector and by extension their presence in the atmosphere.

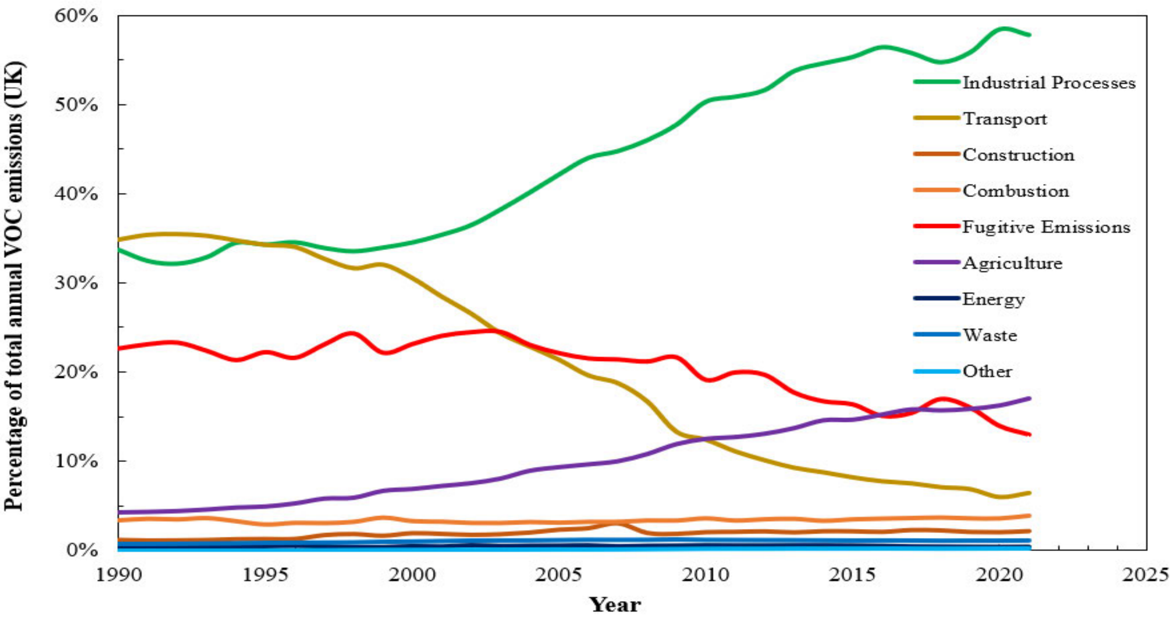

Figure 1. Percentage (%) of VOC emissions by sector in UK between 1990-2021 (data from: UK Department of Environment, 2023).

Figure 2 further elucidates the contribution of the UK industrial sector to VOC emissions between 1990-2021. Specifically, it can be deducted that between 1990-2021, there has been a decrease in the industrial VOC emissions of 51%. This decline is attributed to the enforcement of stricter environmental regulations. However, trends may differ across the globe due to the lack of harmonisation of environmental protection policies.

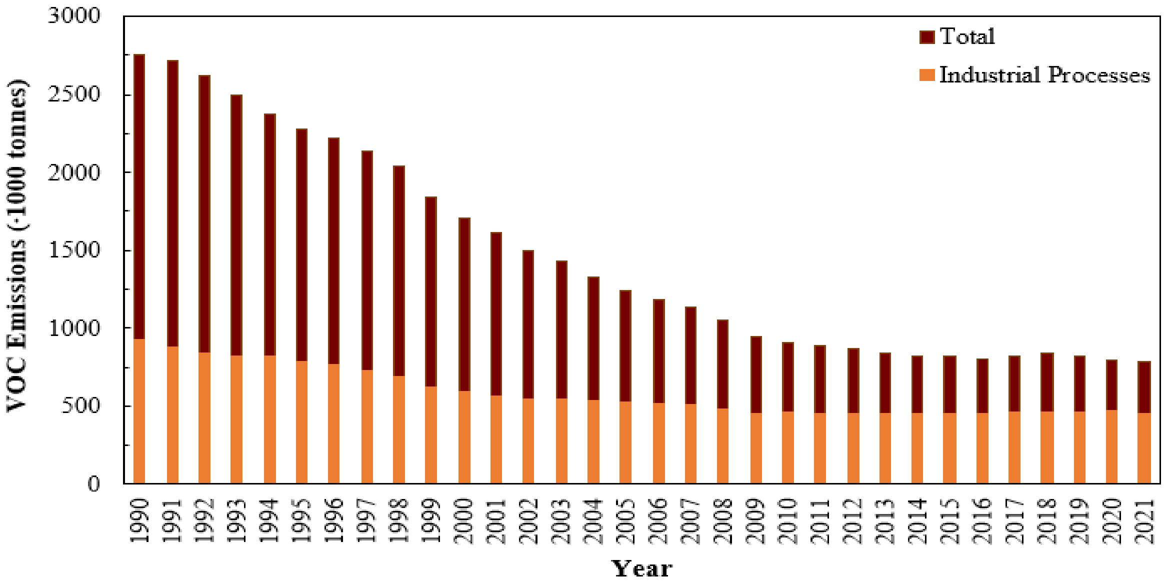

Figure 2. Total vs industrial sector VOC emissions in the UK between 1990-2021 (Department of Environment, 2023).

According to the Department of Environment (2023), out of the 579 ktonnes of overall solvent and industrial process sector non-methane VOC emissions in 2017, subdivided into 9 source categories, it is possible that the pharmaceutical industry falls into the 13% of “other industry processes” and the 3% of “industrial solvent (other)” of the pie chart, thus claiming a share of roughly 93 ktonnes in 2017.

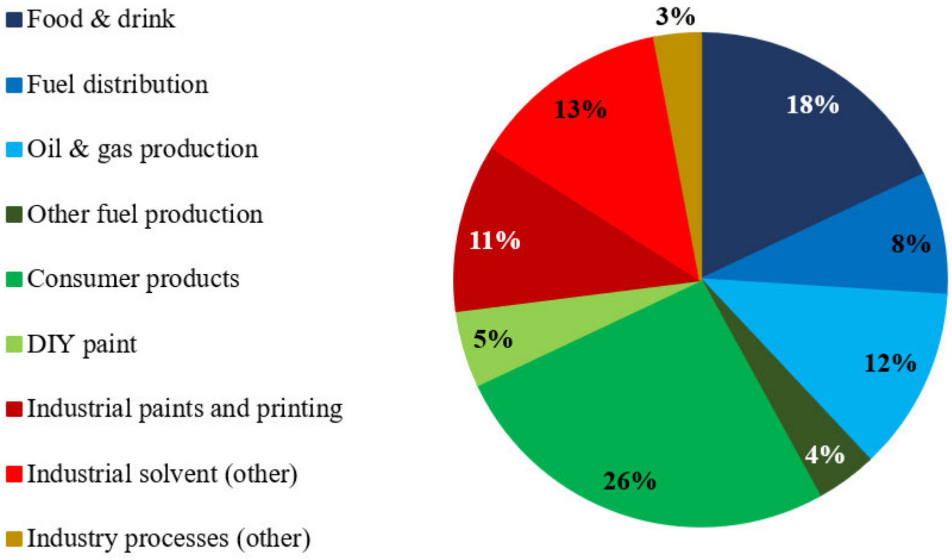

Figure 3. Industrial sectors contributions to UK VOC emissions in 2017 (data from: Department of Environment, 2023).

Figure 4 presents some key trends in VOC emission trends in China. Specifically, the pharmaceutical industry consistently contributes between 6-9% of total industrial VOC emissions between 2013-2019. The increase between 2013-2016 is attributed to increased API manufacturing and exports, while, the gradual decline from 2017 to 2019, to the enforcement of new environmental regulations (Simayi et al., 2022). Compared to the UK, China’s reported VOC emissions from industrial processes are over one order of magnitude larger.

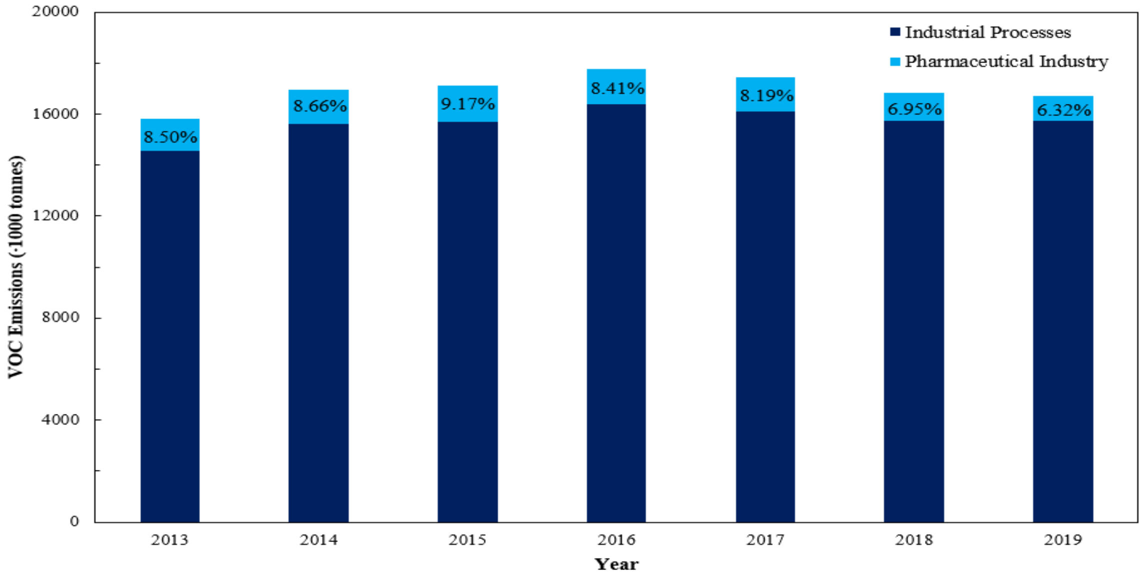

Figure 4. Industrial vs pharmaceutical sector VOC emissions in China between 2013-2019, data from: (Simayi et al., 2022).

Volatile Organic Compound emissions are known to impact both the environment and human health. From an environmental standpoint, VOCs contribute to secondary pollution in the form of tropospheric ozone formation (precursor to photochemical smog) as well as secondary organic aerosols, which in turn, leads to oxidative damage in crops (Atkinson, 2000). VOC inhalation has been shown to trigger asthma, dizziness and inflammation, while prolonged exposure could lead to cancer (Palmiotto et al., 2014), (Ma & Li, 2024),(Zhou et al., 2023).

1.1.2 VOCs in Pharmaceutical Manufacturing

In the context of pharmaceutical manufacturing, volatile organic compounds are indispensable. The stages associated with the production of a pharmaceutical product can be classified as Active Pharmaceutical Ingredient (API) synthesis, drug product formulation and packaging. In this PhD thesis, we address the first step, i.e. API synthesis. Primary pharmaceutical manufacturing typically encompasses the processes of reaction, separation, purification and drying, spread across one or multiple stages until the desired product is synthesized.

According to (Constable et al., 2007), solvents typically contribute between 85-90% to the overall process mass leading to an API on an industrial level. Their role in API synthesis is typically solubilisation (reaction medium), where they enable the reagents manipulation, as well as, extraction and crystallisation. In the extraction stage, reaction products are separated from by-products and residues usually with liquid-liquid separations between organic and inorganic phases. Finally, product purification is usually achieved through crystallisation. The careful selection of a crystallisation solvent allows the manipulation of important properties such as crystal size and/or shape which directly impact the product quality (Grodowska & Parczewski, 2010).

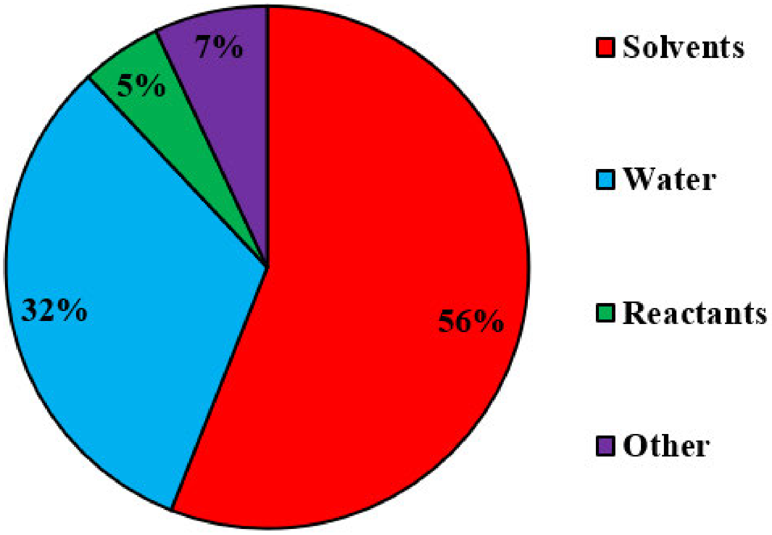

Figure 5. Materials in API manufacturing.

Volatile organic compounds (VOC) are solvents essential to primary pharmaceutical manufacturing. Their presence, ubiquitous in reactions and separations, results in a significant amount of vapour emissions from pharmaceutical production. A generally accepted measure of chemical process sustainability, is the E factor, defined as the mass ratio of waste to desired product. The greater the E factor, the more wasteful a process is and the more it negatively impacts the environment. Typical E factor values are presented in Table 1, where it becomes apparent that within the chemical industry, the pharmaceutical sector has some of the most wasteful production processes.

According to (Henderson et al., 2011) and (Sheldon, 2007), the production of 1 kg of API requires on average the contribution of 46 kg of materials. Since approximately 56% of the total process material required for the production of APIs are solvents, then almost 26 kg of solvents are required for the production of 1 kg of API. Then, according to Table 1, in a typical 1,000 tonnes per annum of API production, an approximate 26,000 tonnes of solvents will be needed. Moreover, by assuming a conservative E Factor of 50 for an API production, a 1,000 product tonnage would translate in 50,000 tonnes of waste, the majority of which, undoubtedly, would be solvents either in liquid or gaseous form.

Table 1. The E Factor in the chemical industry by sector (Sheldon, 2007).

Industry section	Product per annum (tonnes)	E Factor (kg waste/kg product)
Oil Refining	10^6 -10^8	< 0.1
Bulk Chemicals	10^4 - 10^6	< 1-5
Fine Chemicals	10^2 -10^4	5-50
Pharmaceuticals	10-10^3	25-100

The design of more sustainable production processes and/or use of "greener" solvents, although desirable, is easier said than done. As highlighted in (Henderson et al., 2011), there is no silver bullet for solvent substitution, and although efforts such as solvent selection guides in the drug development phase are being introduced, the situation for established products is more complex due to increased regulatory re-approval risks. To this end, optimisation of existing VOC controlling infrastructure at source points is critical.

Table 2 shows the VOCs in this PhD thesis, chosen based not only on their industrial relevance (heptane-decane), but specifically their use in primary pharmaceutical manufacturing recipes.

Table 2. VOC solvents examined in this PhD thesis.

Solvent	Formula	Mr (g mol^{-1})	Boiling point (°C)	Structure
Acetone (ACT)	C_3H_6O	58.08	56.08	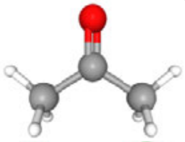
Dichloromethane (DCM)	CH_2Cl_2	84.93	39.75	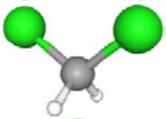
Trichloromethane (TCM)	$CHCl_3$	119.37	61.12	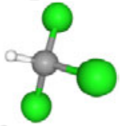
Hexane (HEX)	C_6H_{14}	86.18	68.73	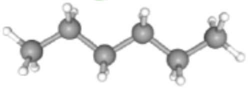
Heptane (HEP)	C_7H_{16}	100.20	98.38	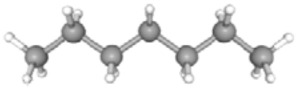
Decane (DEC)	$C_{10}H_{22}$	142.28	174.10	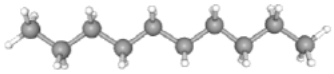
Toluene (TOL)	C_7H_8	92.14	110.60	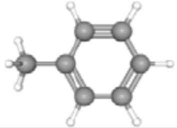

1.2 Volatile Organic Compounds Emissions Abatement via Adsorption

Volatile Organic Compound emission release has been subject to increasingly stringent regulations over the past decades. As a result, several technologies have been studied, developed, and applied over the years for VOC abatement such as, catalytic oxidation (Debono et al., 2018; Jecha et al., 2014), where VOCs are allowed to react and transformed to other chemicals, plasma treatment (Chung et al., 2018; Ikaunieks et al., 2011; Jose & Philip, 2021; Karatum & Deshusses, 2016) where VOCs are degraded via electron impact reactions, biotrickling filtration (Balasubramanian et al., 2012; San-Valero et al., 2019) where VOCs are treated by bacteria, absorption (Darracq et al., 2010; Lhuissier et al., 2022; Moufawad et al., 2022; Wantz et al., 2021) where VOCs are retained by a liquid solvent, and adsorption. Their suitability is application-specific and each method has different limitations (Y. Li et al., 2021).

Adsorption is an established VOC control method on an industrial level for several reasons. It first gained traction as a separation method in the 1970s due to its energy efficiency, as an alternative to the energy-intensive distillation (Ruthven, 1984). Firstly, it boasts easy installation and maintenance. Secondly, the technological maturity ensures a relatively low capital cost. It is further indicated for the treatment of large volumetric streams with low pollutant concentration. Furthermore, the adsorbent materials can be regenerated and reused, either in-house or by outsourcing to external contractors. This further allows the recovery of captured solvents and potential re-use, thus aiding circularity.

The need for adsorbent materials with adequate adsorption capacity has driven the research towards the development and commercial use of several material categories. Dominating practical applications are zeolites, activated alumina, silica gels, carbon molecular sieves, activated carbon and metal-organic-frameworks (Siu et al., 2023). For VOC capture, the adsorbent of choice is activated carbon, and thus this thesis will only focus on applications with this material.

Activated carbons are typically produced through the thermal decomposition of carbonaceous materials (e.g. of plant origin) followed by activation with carbon dioxide or steam at high temperature (700-1100 °C). Although specific properties of activated carbons vary, depending on the conditions of the pyrolysis and activation processes used in their synthesis, they tend to be organophilic and hydrophobic, thus making them ideal candidates for VOC capture (Navarri et al., 2001; Pui et al., 2019; Ruthven, 1984; Zhang et al., 2017).

Assuming that operation begins with a clean bed, i.e. free of adsorbates, a VOC-laden air stream is introduced to the bed and mass transfer begins from the fluid to the solid phase, thus decreasing the concentration of VOC on the fluid, all while fresh feed continues to enter the column. Eventually fluid concentration at that section of the column reaches equilibrium with the feed concentration and thus no more mass transfer occurs. Therefore, the feed stream must travel farther along the bed to reach a section that has not achieved equilibrium yet, to resume mass transfer. Thus, the fluid concentration decreases with increasing bed length, until it reaches nearly zero.

The length over which the fluid concentration changes is called the mass transfer zone. As this process continues, more and more of the bed becomes saturated (i.e. fluid concentration reaches equilibrium with the feed concentration). The mass transfer zone therefore eventually reaches the end of the column, and some VOC exits the column with the air (breakthrough onset). As the mass transfer zone exits the end of the column, the VOC presence at the column outlet gradually increases, until no more VOCs are retained and thus the fluid concentration at the bed outlet is equal to the feed concentration (Gabelman, 2017).

On a macroscopic level, adsorption usually takes place in fixed bed columns, filled with the appropriate adsorbent. Although column configurations vary across fields and applications, it is important to distinguish between systems with built-in adsorbent regeneration capabilities, such as pressure swing adsorption and temperature swing adsorption technologies (Gales et al., 2003; Han et al., 2020; Kagawa et al., 2009; Liu et al., 1998; Pak & Jeon, 2017; Suzuki et al., 2007), and those where the saturated adsorbent is removed and replaced, with regeneration outsourced. In this thesis, the focus is on the latter case. Thus, for emissions abatement typical configurations include at least two beds, where one is operated until breakthrough is achieved and the other remains idle until the first is taken off-line.

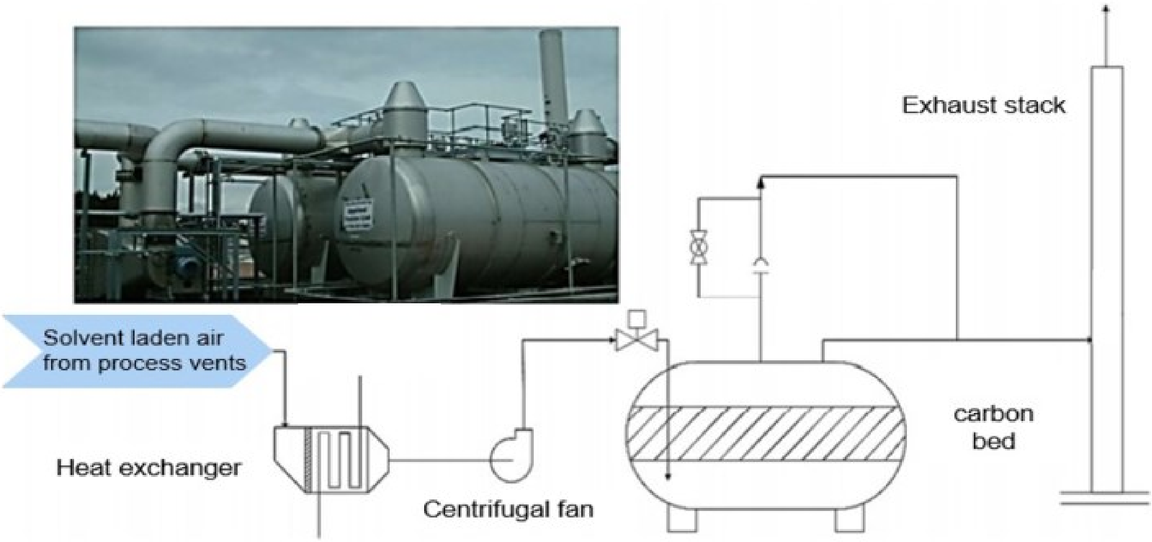

Figure 6. Industrial adsorption system configuration.

Volatile Organic Compounds, due to their relatively low boiling points, often exist in both liquid and vapour form in the process vessels. Plant-wide process vessels are connected via piping systems to the activated carbon bed responsible for VOC emissions abatement. However, in industrial operations vessels have built-in VOC-recovery measures to minimise the flow of solvent vapours to the adsorption column. For example, most vessels are equipped with nitrogen blankets and control valves that selectively allow VOC vapour flow to the activated carbon beds only if the pressure inside the vessel rises over a specific limit. Furthermore, condensers present at the distillation vessels ensure that the majority of the solvent vapour is recovered and re-used after atmospheric or vacuum distillations. The vapour emissions that manage to escape towards the adsorption column, are thus, complex trace mixtures transient in concentration and intermittent, creating an interesting modelling landscape.

Chapter 2

Project Motivation

This chapter discusses the motivation for this PhD project. First, adsorption processes and the challenges associated with volatile organic compound abatement are discussed with a focus on experimental and modelling demonstrations in the literature implemented thus far. The recent developments and applications of mixed integer linear programming in the pharmaceutical industry are then discussed to demonstrate the need for waste management steps to be included in the scheduling of batch production operations. The chapter is then concluded with the PhD thesis objectives and structure.

2.1 Dynamic modelling in VOC abatement via adsorption

The United Nations sustainable development goals (SDGs) provide a shared vision for now and the future, highlighting a responsible way forward for the global community. At the heart of this vision is tackling waste- and energy-intensive production patterns responsible for climate change and pollution (Goal 12). Leading this effort is the wider adoption of eco-friendly and innovative industrialisation practices across all manufacturing sectors (Goal 9). Integrating technology in industrial settings not only benefits the environment, but also increases productivity and resilience in crises (United Nations, 2023). In fact, Industry 4.0 paves the way to a new manufacturing paradigm, focused on increased system predictability towards efficiency maximisation and environmental impact and cost minimisation (Akbar & Irohara, 2018).

Adsorption processes have had major industrial applications in purifications and separations since the 1950s, with considerable expansions of scales and processes during the 1970s in light of soaring energy prices that deemed distillations of close boiling-point components too uneconomic (Ruthven, 1984). In the last decades, with the gradual enforcement of stricter environmental protection laws, adsorption has proven to be an effective and competitive gas waste treatment solution. Over the past 60 years adsorption has become a topic of extensive research in the chemical engineering discipline both on an experimental and, more recently, on a process modelling level, however, striking mismatches are observed for its application as a VOC emissions abatement technique in the pharmaceutical industry (Table 3).

Table 3. Recent studies including pharmaceutically relevant VOC adsorption on activated carbon.

N_{voc}	Multicomp.	Expt.	Sim.	VOC(s)	Adsorbent	Isotherm	$C_{0,max}$ (ppm)	L (m)	Lit. Ref.
1	No	Yes	Yes	DCM	Activ. Carbon	Langmuir	8,972	-	(Borkar, 2010)
1	No	Yes	Yes	Ethyl Acetate	Activ. Carbon	Langmuir	200,876	$6 \cdot 10^{-2}$	(Manjare, 2006)
1	No	Yes	Yes	n-Hexane	Activ. Carbon	Langmuir, Modified Langmuir 1-2, MSL, FH-VSM, Toth, Langmuir-Freundlich	100,000	$1 \cdot 10^{-1}$	(Shim et al., 2003)
1	No	Yes	No	Toluene	Activ. Carbon	Langmuir, Freundlich	200	$1.8 \cdot 10^{-1}$	(Yang et al., 2018)
2	Yes	Yes	Yes	Acetone, DCM	Activ. Carbon	Langmuir-Freundlich	8,000	$1 \cdot 10^{-1}$	(Talmoudi et al., 2018)
2	No	Yes	Yes	Toluene Xylene	Activ. Carbon Fiber	Sips	10,000	$1 \cdot 10^{-1}$	(Das et al., 2004)
2	No	Yes	Yes	DCM, 1,1,2-trichloro-l,2,2-trifluoroethane	Activ. Carbon	Langmuir, Sips, Freundlich	246,732	$1.5\text{-}2.5 \cdot 10^{-1}$	(Kim, 2002)
2	No	Yes	Yes	TCM, Carbon Tetrachloride	Activ. Carbon	Langmuir, Freundlich, DRK, BET	1,250	$3 \cdot 10^{-1}$	(Kalender, 2015)

Table 3 (continued)

N_{voc}	Multicomp.	Expt.	Sim.	VOC(s)	Adsorbent	Isotherm	$C_{0,max}$ (ppm)	L (m)	Lit. Ref.
2	No	Yes	No	Acetone, Benzene	Activ. Carbon Fiber Cloth	Dubinin-Ashtakhov	19,600	-	(Ramirez et al., 2005)
2	No	Yes	No	Toluene, Ethyl Acetate	Activ. Carbon	Langmuir, Freundlich, Sips, Toth, Redlich-Peterson	1,666	$2.2\cdot10^{-1}$	(Z. Li et al., 2021)
2	No	Yes	No	Toluene, n-Hexane	Activ. Carbon	Langmuir	910,000	-	(Izquierdo et al., 2011)
2	No	Yes	No	Toluene, Chlorobenzene	Activ. Carbon	-	14	-	(Ma et al., 2020)
2	No	Yes	No	Benzene, Toluene	Activ. Carbon	IAST, Toth	200	$6\text{-}10\cdot10^{-3}$	(Lillo-Ródenas et al., 2006)
3	Yes	Yes	No	Acetaldehyde, Acetone, Ethyl Acetate	Activ. Carbon	Yoon-Nelson	208	$6\cdot10^{-1}$	(Yao et al., 2020)
3	Yes	Yes	No	Toluene, MEK, MiBK	Activ. Carbon	Freundlich, Myers	250,000	-	(Kim et al., 2006)
3	Yes	Yes	Yes	Benzene, Toluene, p-Xylene	Activ. Carbon	Langmuir	3,175	$1\cdot10^{-1}$	(Yun et al., 1999)
3	No	Yes	Yes	TCM, Benzene, Carbon Tetrachloride	Activ. Carbon	Langmuir	6,966	$9\cdot10^{-3}$	(Chuang et al., 2003)
3	No	Yes	Yes	Acetone, Ethyl Formate, DCM	Activ. Carbon	Langmuir	28,322	$2\cdot10^{-1}$	(Giraudet, 2009)
3	No	Yes	Yes	Acetone, Toluene, 1,2-dichloroethane	Activ. Carbon	Langmuir	41,415	$2\cdot10^{-1}$	(Pre et al., 2002)

Table 3 (continued)

N_{voc}	Multicomp.	Expt.	Sim.	VOC(s)	Adsorbent	Isotherm	$C_{0,max}$ (ppm)	L (m)	Lit. Ref.
3	No	Yes	No	Benzene, Toluene, p-Xylene	Activ. Carbon	-	-	-	(Gu et al., 2021)
3	No	Yes	No	MCM, DCM, TCM	Activ. Carbon	Langmuir	4,000	$4\text{-}11 \cdot 10^{-2}$	(Lemus et al., 2012)
3	No	Yes	No	Acetone, TCM, Acetonitrile	Activ. Carbon, Activ. Carbon Fiber, Sludge	Langmuir, Freundlich	7,800	-	(Jiun-Horng et al., 2008)
3	No	Yes	No	Toluene, Methanol, Acetone	Activ. Carbon Fiber	-	1,263	-	(Meng et al., 2019)
3	No	Yes	No	DCM, TCM, Carbon Tetrachloride	Activ. Carbon	Langmuir, Freundlich, Temkin	5,761	-	(Saleh et al., 2015)
3	No	Yes	No	Ethyl Acetate, Acetone, Ethanol	Activ. Carbon	Langmuir	197,386	-	(Gales, 2000)
4	Yes	Yes	Yes	Acetone, Ethanol, Cyclohexane, Heptane	Activ. Carbon	Langmuir	6,000	$1 \cdot 10^{-1}$	(Vuong et al., 2016)
4	Yes	Yes	No	Acetone, MEK, Benzene, Toluene	Activ. Carbon	-	160	-	(Lee et al., 2008)
4	Yes	Yes	No	Acetone, Ethanol, Ethyl Acetate, N-propyl acetate	Activ. Carbon Fiber	-	-	-	(Zhu et al., 2019)
4	Yes	Yes	No	Benzene, Toluene, Styrene, Xylene	Activ. Carbon	Langmuir, Dubinin-Radushkevich, Freundlich, Elovich	100	$2 \cdot 10^{-2}$	(Samaddar et al., 2019)
4	No	Yes	Yes	Acetone, Benzene, TMB, Toluene	Activ. Carbon	Langmuir	1,000	$1.5 \cdot 10^{-1}$	(Tefera et al., 2013)

Table 3 (continued)

N_{voc}	Multicomp.	Expt.	Sim.	VOC(s)	Adsorbent	Isotherm	$C_{0,max}$ (ppm)	L (m)	Lit. Ref.
4	No	Yes	No	DCM, TCM, Benzene, Carbon Tetrachloride	Activ. Carbon	Langmuir	400	-	(Chiang, 2001)
5	Yes	Yes	No	Acetaldehyde, Formaldehyde, 2-Propenal, 1,3-Butadiene, Benzene	Activ. Carbon	-	1400	-	(Ouzzine et al., 2019)
6	No	Yes	Yes	Acetone, DCM, Ethyl Acetate, Isopropanol, MEK, Toluene	Activ. Carbon Fiber	Langmuir	1,050	1.64-$5\cdot10^{-3}$	(Fournel et al., 2010)
7	No	Yes	Yes	Acetone, 1,2-dichloroethane, Ethyl acetate, Ethyl alcohol, methylethyldioxolane, MEK, Toluene	Activ. Carbon	Langmuir	27,300	$2\cdot10^{-1}$	(Delage, 2000)
8	Yes	Yes	Yes	1, 2, 4-trimethylbenzene, 2, 2-dimethylpropylbenzene, Indane, Decane, Heptane, 2-butoxyethanol, 2-heptanone, n-butyl acetate, n-butanol	Activ. Carbon	Langmuir	250	$6.5\cdot10^{-2}$	(Tefera et al., 2014)
8	Yes	Yes	No	1-butanol, n-butylacetate, 2-heptanone, 2-butoxyethanol n-decane, 1,2,4-trimethylbenzene, indan, and 2,2-dimethylpropylbenzene	Activ. Carbon	-	500	-	(Lashaki et al., 2023)

Adsorption with activated carbon is an established VOC emissions control technology on an industrial level due to its easy installation and maintenance as well as energy efficiency. During adsorption, a VOC-laden air stream, from process vents across the plant, is directed towards a fixed-bed activated carbon column. There, VOCs are selectively retained in the carbon pores via attraction forces while the air stream passes through the bed and is released to the atmosphere, free from VOCs. Adsorption is often preferred due to its ability to filter large volumes of waste streams with a low concentration of pollutants. However, venting variable component and concentration waste streams to the activated carbon bed from process equipment all over the plant leads to sub-optimal performance and irregular bed saturation (Tzanakopoulou et al., 2023).

Despite the abundance of published adsorption studies, the number of papers directly addressing the adsorption of pharma-related VOCs is relatively small (Table 3). Of those, the striking majority presents purely experimental work, often to test the adsorption capabilities of a newly synthesized activated carbon material (19 studies, Table 3), while the number of studies including modelling trails behind at 16 (Table 3). The published modelling applications are limited and often restricted to the fitting of an adsorption isotherm curve on single component experimental data. The overwhelming majority investigates VOCs as single components (25 studies, Table 3), although there are eleven examples where multicomponent adsorption is studied. Although several isotherm models are encountered in the literature, the most commonly employed (24 studies, Table 3) is the Langmuir isotherm, presumably due to its ease of application and theoretical basis. Moreover, notably, many published studies do not explicitly report parameters crucial for simulation purposes (e.g. bed length, isotherm parameter values) which is critical to validation purposes. This number becomes even smaller for studies under realistic industrial operating conditions and equipment scales, as phenomena not visible in laboratory scale columns are likely to be observed at larger scales. Specifically, all column lengths reported in Table 3 are shorter than 30 cm, whereas industrial column lengths can range between 50 cm – 10 m.

One of the key characteristics of VOC gas waste streams in the pharma industry is the release of trace amounts of solvent vapours (< 1,000 ppm) depending on the recipe stage and process unit leading to multicomponent mixtures in need of abatement. Multicomponent mixture experiments are rarely reported in the literature due to their complexity, and therefore, simulation of multicomponent mixtures is essential to increasing process understanding and thus enabling optimisation on an industrial level.

Table 4. Literature studies including VOC adsorption under dynamic feed concentration conditions.

N_{voc}	Multicomp.	Expt.	Sim.	VOC(s)	Adsorbent	Isotherm	$C_{0,max}$ (ppm)	L (m)	Field	Lit. Ref.
1	No	Yes	Yes	Toluene	Activ. Carbon	Freundlich	1,000	$1\cdot10^{-2}$	Integrated Biofiltration	(Nabatilan et al., 2009)
1	No	Yes	Yes	Toluene	Activ. Carbon	-	1,000	$3.33\cdot10^{-1}$	Integrated Biofiltration	(Moe et al., 2007)
1	No	Yes	Yes	Toluene	Activ. Carbon	-	700	$2.03\cdot10^{-1}$	Integrated Biofiltration	(Kim et al., 2007)
1	No	Yes	No	Toluene	Activ. Carbon	IAST	1,000	$12.5\cdot10^{-2}$	Integrated Biofiltration	(Nabatilan & Moe, 2010)
1	No	Yes	No	Toluene	Activ. Carbon	-	4,350	$0.5\text{-}2\cdot10^{-1}$	Adsorption	(Liu et al., 2022)
2	Yes	Yes	No	n-Hexane, Benzene	Activ. Carbon	-	1,410	$2\cdot10^{-1}$	Integrated Biofiltration	(Hassan & Sorial, 2011)
2	Yes	Yes	No	Ethanol, Ethyl Acetate	Activ. Carbon	-	1,400	-	Integrated Biofiltration	(Sempere et al., 2009)
2	No	Yes	Yes	Ethanol, Xylene	Activ. Carbon	Kinetic Models	2,150	$2\text{-}8\cdot10^{-2}$	Adsorption	(Shi et al., 2023)
3	Yes	Yes	No	Acetone, m-Xylene, n-Butyl acetate	Activ. Carbon	Dubinin-Radushkevich	510	$3\cdot10^{-2}$	Integrated Biofiltration	(Palau et al., 2015)
3	Yes	Yes	No	n-Hexane, Methanol, Benzene	Activ. Carbon	Freundlich	1,749	$2.03\cdot10^{-1}$	Integrated Biofiltration	(Zehraoui & Sorial, 2015)
3	Yes	Yes	No	Toluene, m-Xylene, n-Butyl acetate	Activ. Carbon	-	1,600	-	Integrated Biofiltration	(Sempere et al., 2010)
4	Yes	Yes	No	Toluene, Styrene, MEK, MiBK	Activ. Carbon	-	700	$2.03\cdot10^{-1}$	Integrated Biofiltration	(Cai & Sorial, 2009)
5	No	Yes	No	Toluene, Xylenes, n-Butyl acetate, i-Butyl acetate Ethylbenzene, Acetone	Activ. Carbon	-	510	-	Integrated Biofiltration	(Lafita et al., 2012)

This reality leads to waste streams characterised by transient and/or intermittent feed concentration patterns of VOC mixtures which renders mixture behaviour predictions challenging. While detailed transient feed pharma-relevant VOC dynamic adsorption simulations are still elusive, Table 4 presents some key literature studies that address the existence of such feeds. However, the majority of literature studies regarding adsorption column operations under transient inlet concentration (Table 4) refer to cyclic adsorption/desorption processes as a pre-processing step before gas biofiltration. The effect of unsteady feed streams on activated carbon adsorption is only superficially examined as the focus of the studies is biofilter performance.

Implementation of integrated theoretical and modelling based approaches in the field of VOC abatement via adsorption in the pharmaceutical industry holds the key to unlocking the full potential of industrial operation optimisation, through the complex simulation scenarios necessary to capture the real time conditions of batch manufacturing and emissions abatement.

2.2 Mixed Integer Linear Programming (MILP) in the pharmaceutical industry

Production decisions in the pharmaceutical supply chain are often informed by manual planning systems due to the high degree of complexity and regulatory constraints it entails. These planning systems rely on the assumptions that operational characteristics and design parameters remain constant throughout the planning horizon, but when faced with an unexpected event, such as an unplanned downtime due to adsorption column saturation, the production plan needs to be readjusted appropriately at a short amount of time. Unfortunately, this approach leads to inflexible and economically sub-optimal operation for most pharmaceutical plants (Sampat et al., 2021).

Integrating technology in industrial settings not only benefits the environment, but also increases productivity and resilience in crises. In fact, the concept of Industry 4.0 champions a new manufacturing paradigm, reliant on augmented system monitoring, prediction and control. Modelling and simulation of pharma effluent capture systems through the development and application of advanced, first-principles based process descriptions in the form of dynamic, non-isothermal adsorption models (under both adiabatic and non-adiabatic conditions) informed by industrial data for the study of multicomponent mixture adsorption yields valuable insights into the adsorption systems’ behaviour under different operating conditions and solvent mixtures (Tzanakopoulou, 2022; Tzanakopoulou et al., 2023).

Production scheduling involves making decisions on when, where, and how to manufacture a set of products within a specific time frame, in parallel to limited resources operation and adherence to processing recipes (Floudas & Lin, 2004). The pharmaceutical industry primarily operates in the batch processing mode, which raises scheduling challenges due to the diverse processing tasks, cleaning requirements, and recipe plans (Shah, 2004). To tackle these challenges, mathematical modelling and specifically mixed-integer linear programming (MILP) models are valuable tools. MILP problems typically consist of (i) production recipes, which outline the task sequences required to manufacture specific products; (ii) available processing and storage equipment; (iii) intermediate storage policies; (iv) production requirements; (v) resource specifications, such as utilities and manpower; and (vi) a specified time horizon. The objective is to generate a schedule that includes (i) the task sequences for each piece of equipment; (ii) the timing of each task; and (iii) the batch sizes of materials to be processed. A schedule's effectiveness is evaluated based on one or more criteria, such as overall profit, operating costs, and makespan (Floudas & Lin, 2004). An optimised production schedule not only yields economic benefits, but also contributes to reducing environmental impact, energy intensity, violations of various regulations and helps cope more efficiently with uncertainties, both in production as well as in customer order levels (Harjunkoski et al., 2014).

Translating the product recipe correctly into a MILP model is essential to scheduling success, thus, several representation approaches have been developed over the years (Castro et al., 2018). Kondili et al. (1993) introduced the state-task-network (STN) concept, which is widely used in chemical batch processes. The STN diagram is an intellectual derivative of the production recipe and is formed by state nodes representing feeds, intermediates, and final products, shown as circles; task nodes representing processing steps, shown as rectangular boxes; and arcs indicating material flow. Pantelides (1993) extended the STN to include production equipment, resulting in the resource-task-network (RTN) concept. MILP-based scheduling approaches can be categorized based on the type of time domain representation used (Grunow et al., 2003), which can either be in discrete time or continuous time. Discrete time models divide the time horizon into uniform time intervals, whereas continuous time models divide the time horizon into periods of unequal and unknown lengths (Sampat et al., 2021). Both Floudas and Lin (2004) and Méndez et al. (2006) provide comprehensive reviews which highlight each method's strengths and weaknesses extensively.

A significant amount of work focuses on the pharmaceutical industry in particular, across its value chain. Papageorgiou et al. (2001) showcase a MILP model for the selection of product development and introduction strategy as well as capacity planning and investment strategy for supply chain optimisation. Siddhaye et al. (2004) focus on the early phases of pharmaceutical production, specifically proposing a MILP optimisation framework for the design of new molecules with desired properties. On the scheduling front, Castro et al. (2008) present a case study on optimal vessel allocation for an API production facility using an MILP model to tradeoff between using the minimum vessel number required to maintain plant flexibility and the potentially increased makespan due to long changeover times. Chen et al. (2012) present their combined simulation and optimisation approach on the complex landscape of clinical trial supply chain management.

Kabra et al. (2013) present an approach for multi-stage, multi-product, multi-period scheduling model for biopharmaceuticals adding on the model of Shaik and Floudas (2007) improved tightening and sequencing constraints. Moniz et al. (2014) propose a scheduling algorithm for simultaneous regular and non-regular products (i.e. campaign and short-term scheduling) in a real pharmaceutical industry example with a discrete time formulation. Vieira et al. (2017) solve a multi-objective MILP production and maintenance planning optimisation problem targeting continuous biopharmaceutical manufacturing using a continuous grid formulation. More recently, Ge and Yuan (2021) introduced a hybrid multi-stage discrete/continuous-time scheduling approach to determine the optimal production schedule of a reconfigurable modular production system, aimed for pharmaceutical manufacturing. Finally, Elekidis and Georgiadis (2022) expand to contract manufacturing organisations with a systematic MILP proposal of integrated planning and medium term scheduling for the contract appraisal problem under demand uncertainty.

2.3 Thesis Aims & Objectives

2.3.1 Langmuir Isotherm parameter estimation

Langmuir Isotherm parameters for key volatile organic compounds are calculated from published experimental data on activated carbon to address VOC simulation needs.

2.3.2 Adsorption Dynamic Model Development

This PhD thesis presents the development and validation of a dynamic, multicomponent, non isothermal adsorption model. The model simulates adsorption on the axial direction, and accounts for non isothermal conditions and pressure drop. The dynamic model uses the Linear Driving Force model to account for solid phase mass transfer and the extended Langmuir Isotherm for the equilibrium state.

2.3.3 Multicomponent Mixture Adsorption Dynamic Simulations

This PhD thesis uses the developed model to elucidate the complex adsorption relationships of multicomponent VOC mixtures on activated carbon. Specifically, several pharmaceutically-relevant VOC binary solvent mixtures are examined in order to validate the model based on published experimental data, and test the effect of key operation parameters such as mixture composition, temperature, column length and flowrate on adsorption breakthrough order, temperature profiles and pressure drop. This PhD thesis further presents the application of our model on key binary VOC mixtures under transient feed conditions on industrial-length columns. Specifically, the mixtures of hexane-toluene, dichloromethane-acetone, dichloromethane-chloroform, and dichloromethane-toluene are examined under fluctuating inlet concentration patterns which are based on industrial FTIR readings. The transient feed effects on key breakthrough metrics are analysed towards process optimisation under realistic operating scenarios. This framework can be applied not only to the field of emissions abatement via adsorption but also finds application in biofiltering, as a waste stream pre-processing step.

2.3.4 Evaluation of Theoretical Metrics Accuracy (Hodograph theory)

The present work compares our model's gPROMS$^{®}$ dynamic simulation results to Hodograph Theory metrics with a focus on breakthrough onset and maximum outlet concentration. Hodograph Theory relies on Langmuir Isotherm single component parameters of isothermal operation for predictions on multicomponent, non isothermal mixtures. Here, we provide a critical comparison of theoretical metrics against our validated model simulation results and experimental data to assess the theoretical metrics ability to inform operational decision making before the commitment of more critical resources for in-depth modelling investigation.

2.3.5 MILP Production Scheduling and Economic Evaluation

This PhD thesis develops a mixed integer linear programming (MILP) scheduling problem based on the production recipe of an API in an industrial (batch) setting while also including the VOC emissions abatement steps, with durations informed from our gPROMS$^{®}$ dynamic simulations. The problem is solved to optimality with makespan minimisation as the objective function on the CProS web application on a cloud server with GAMS code on the background. Next, a scenario-based economic evaluation of the VOC abatement system annual operating expenditure is performed based on number of material changeovers per year, VOC emission loads and mixtures, as well as, solvent prices. This framework can be extended to include more production steps and emission patterns.

2.3.6 Thesis Structure

This thesis presents a comprehensive study into multicomponent VOC adsorption modelling for emission abatement in the pharmaceutical industry. The rest of the thesis is structured as follows. Part II sees the establishment of a Langmuir Isotherm parameters database for key VOCs and Part III presents the development of a one dimensional in space, nonisothermal, multicomponent VOC adsorption model encompassing the Linear Driving Force model for solid phase mass transport and the Langmuir Isotherm for equilibrium. Part IV introduces the key simulation case studies of this PhD thesis, where the model is validated against published experimental data and the effects of temperature, heat exchange regime, flowrate, column length, and concentration of several binary VOC mixtures are examined. Furthermore, our results are compared to theoretical Hodograph Theory metrics, and the repercussions of transient feed mixtures on multicomponent adsorption are investigated. Part V presents the development of a mixed integer linear programming API production scheduling problem with adsorption characteristics derived from our gPROMS® simulations. An extensive economic evaluation of operational expenditure based on industry-informed case studies follows. Finally, Part VI summarizes the original research contributions made in this PhD thesis and conclusions of this PhD thesis. Table 5 summarises the main systems and conditions explored in this thesis.

Table 5. Thesis system investigation roadmap.

Binary	Transient Feed	Concentration Range (ppm$_v$)	Temperature T (K)	Bed Length L (m)	S. Velocity V_s (m s^{-1})	Chapter
DCM-ACT	No	500-2000	288, 293, 298	0.1	0.170	**5**
DCM-ACT	No	250	293, 300	0.065	0.914	
DCM-TCM	No	250	293, 300	0.065	0.914	
DCM-TOL	No	250	293, 300	0.065	0.914	
TCM-ACT	No	250	293, 300	0.065	0.914	
TCM-TOL	No	250	293, 300	0.065	0.914	
TOL-ACT	No	250	293, 300	0.065	0.914	
HEP-DEC	No	250	300	0.065	0.914	**6**
HEP-DEC	No	125-375	300	0.065	0.914	
ACT-TOL	No	40-160	293.15	0.019-0.021	0.332	**7**
BEN-TOL	No	40-160	293.15	0.019-0.021	0.332	
HEX-TOL	Yes	100-250	300	0.065	0.914	**9**
DCM-ACT	Yes	250-750	300	0.065	0.914	
DCM-TCM	Yes	250-750	300	0.065	0.914	

DCM-TOL	Yes	250-750	300	0.065	0.914	
HEX-ACT	No	250	300	0.25-1	0.1-0.9	**10**
HEX-DCM	No	250	300	0.25-1	0.1-0.9	
HEX-TOL	No	250	300	0.25-1	0.1-0.9	
TOL-TCM	No	50-250	300	1	0.914	**11**

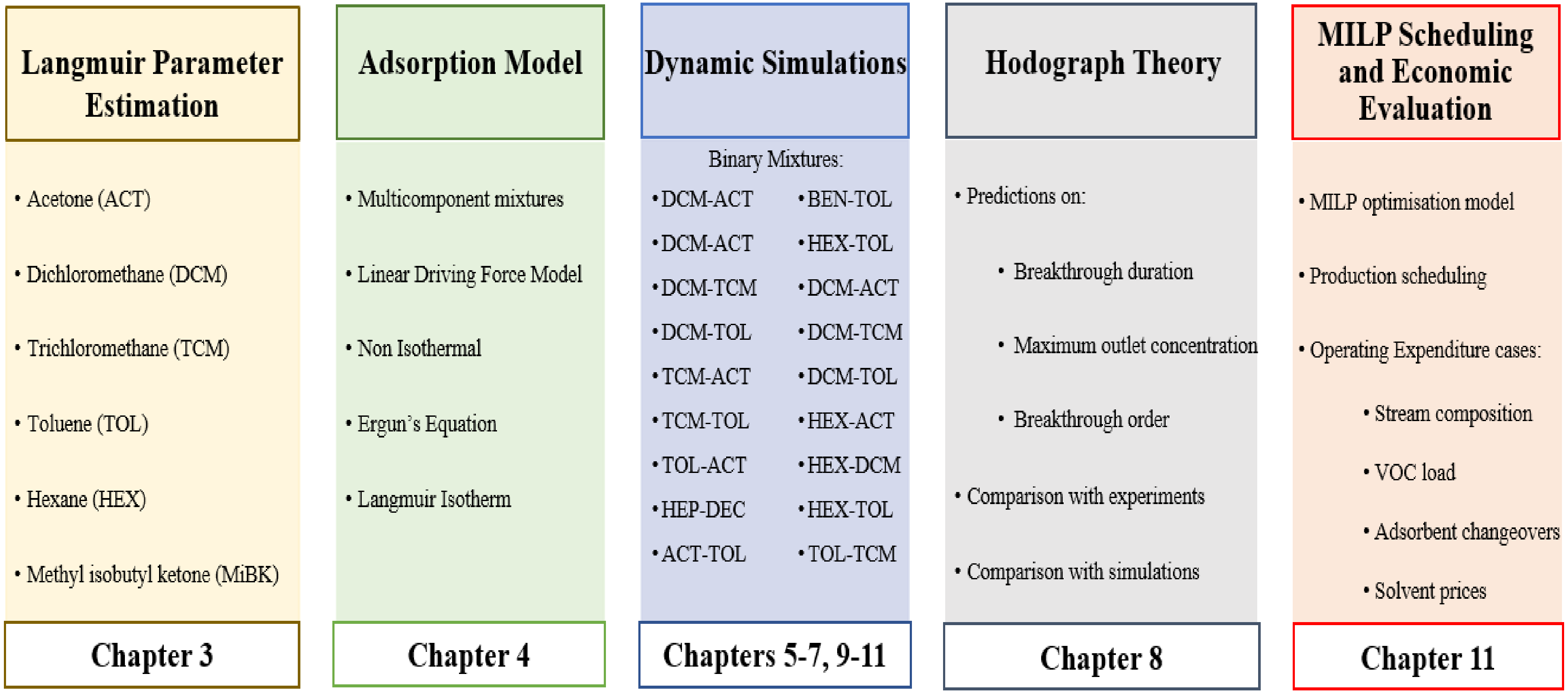

Figure 7. Thesis contents overview.

PART II

LANGMUIR PARAMETER ESTIMATION

Chapter 3

Langmuir Parameter Estimation

This chapter presents the estimation of Langmuir Isotherm parameter values for acetone, dichloromethane, chloroform, toluene, hexane and MiBK based on published experimental data for activated carbon adsorption.

The results presented in this chapter have also been published in the literature (Tzanakopoulou et al., 2023. *Comput. Chem. Eng.*, **174**, 108248); details can be found in Appendix B.

3.1 Langmuir Isotherm Parameter Estimation methodology

Published parameter values of VOC adsorption are often unreliable or pertaining to isotherm curve fits different to the Langmuir model (Figure 8). In an effort to create a database for Langmuir Isotherm parameters ($q_{m,i}$ and b_i) for volatile organic compounds of interest (toluene, acetone, dichloromethane, chloroform, hexane and MiBK) our study has focused on identifying and compiling published experimental data for single-component adsorption of these VOCs on activated carbon from multiple papers and fit them to the Langmuir Isotherm, Eq. (14), using the least square method in Origin.

$$q_{e,i} = \frac{q_{m,i} b_i C_i}{1 + b_i C_i}$$

Figure 8. The Langmuir Isotherm model.

3.2 Langmuir Isotherm Parameter Estimation Results

Figure 9 shows the results of our fit for DCM compared to published experimental data and the published model of (Talmoudi et al., 2018). The Langmuir Isotherm values obtained achieve more accurate data fit compared to the systematic over-estimation of the adsorbed amount in higher concentrations by Talmoudi et al., (2018) and have thus been used for all simulations in this paper for DCM. The y-axis of Figure 8 represents the equilibrium solid phase concentration of DCM while the x-axis represents the gas phase concentration of DCM.

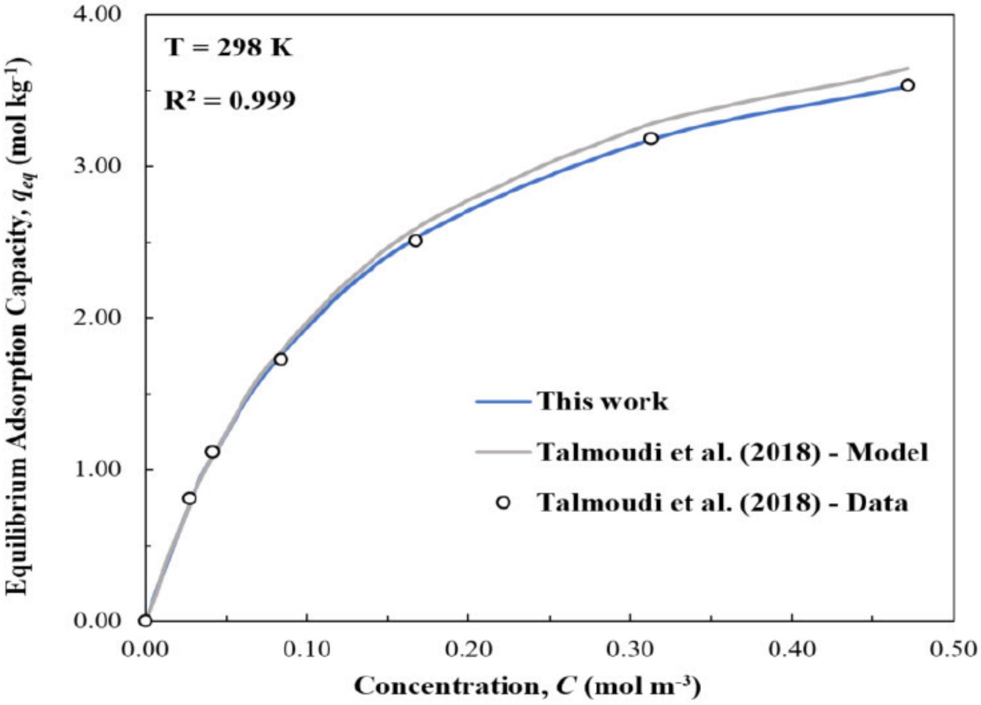

Figure 9. Langmuir Isotherm parameter estimation for DCM (data: Talmoudi et al., (2018)).

Published experimental data for toluene, acetone, dichloromethane, chloroform, hexane and MiBK have been compiled from the literature and processed in the same way, to obtain the Langmuir Isotherm parameter values presented in Table 6 and Figures 9-11.

Table 6. Langmuir Parameter Estimation Values

VOC	Author	Adsorbent	Surf. Area (m^2 g^{-1})	T (K)	q_m (mol kg^{-1})	Standard Error	b (mol m^{-3})	Standard Error	R^2
ACT (Acetone)	(Gales et al., 2000)	Commercial AC	1485.00	298.00	6.173	± 0.147	1.016	± 0.137	0.986
	(Tsai et al., 2008)	Commercial AC	807.00	303.15	3.009	± 0.334	31.832	± 13.161	0.953
				323.15	2.047	± 0.520	17.960	± 13.930	0.851
				353.15	1.632	± 0.220	17.383	± 6.926	0.966
		Sludge	757.00	303.15	2.663	± 0.441	32.351	± 19.974	0.902
				323.15	1.078	± 0.072	85.182	± 27.409	0.972
				353.15	0.733	± 0.093	74.339	± 48.339	0.930
		PAN Fiber	832.00	303.15	2.264	± 0.356	42.518	± 27.043	0.885
				323.15	1.786	± 0.639	11.818	± 11.166	0.787
				353.15	2.950	± 2.419	3.251	± 4.314	0.881

		Pitch Fiber	1518.00	303.15	5.813	±	1.700	7.880	±	5.379	0.910
				323.15	4.458	±	1.033	3.914	±	1.606	0.983
				353.15	1.875	±	0.295	5.647	±	1.744	0.989
	(Giraudet et al., 2010)	Olive stone AC	1720.00	293.15	4.377	±	0.250	24.606	±	7.056	0.942
				313.15	3.827	±	0.215	15.581	±	3.887	0.950
				333.15	2.704	±	0.192	13.116	±	3.615	0.936
				353.15	1.127	±	0.054	29.580	±	7.476	0.925
	(Tefera et al., 2013)	Commercial AC	1390.00	298.15	7.051	±	0.023	17.311	±	0.605	0.998
	(Vuong et al., 2016)	Commercial AC	950.00	298.00	4.307	±	0.263	17.684	±	2.886	0.986
	(Talmoudi et al., 2018)	Pine AC	1706.00	298.00	6.371	±	0.213	7.677	±	0.690	0.996
				313.00	4.502	±	0.153	10.394	±	1.032	0.994
				323.00	3.617	±	0.202	8.494	±	1.280	0.988
	(Zhou et al., 2020)	Commercial AC	423.00	298.00	2.668	±	0.073	0.987	±	0.171	0.881
DCM (Dichloro-methane)	(Kim et al., 2002)	Commercial AC	826.00	303.00	6.320	±	0.186	4.188	±	0.697	0.977
				318.00	5.837	±	0.108	2.260	±	0.155	0.989
				333.00	5.299	±	0.235	1.315	±	0.209	0.968
	(Borkar et al., 2010)	Commercial AC	1000.00	303.15	4.675	±	0.143	29.471	±	4.198	0.981
				318.15	4.403	±	0.153	20.522	±	2.841	0.985
				353.15	2.619	±	0.128	12.612	±	1.698	0.989
	(Giraudet et al., 2010)	Olive stone AC	1720.00	293.15	2.448	±	0.203	24.563	±	9.756	0.885
				313.15	1.998	±	0.126	19.738	±	5.423	0.934
				333.15	1.373	±	0.071	11.402	±	1.948	0.973
				353.15	0.332	±	0.034	80.437	±	67.899	0.653
	(Lemus et al., 2012)	Commercial AC	927.00	308.15	2.905	±	0.253	29.057	±	7.138	0.953
	(Talmoudi et al., 2018)	Pine AC	1706.00	298.00	4.506	±	0.054	7.610	±	0.239	0.999

				313.00	3.332	±	0.130	8.632	±	0.921	0.994
				323.00	2.611	±	0.187	8.432	±	1.625	0.981
TCM (Chloroform)	(Tsai et al., 2008)	Commercial AC	807.00	303.15	2.826	±	0.33	119.046	±	73.188	0.890
				323.15	2.738	±	0.289	20.446	±	7.078	0.967
				353.15	2.530	±	0.325	15.277	±	5.705	0.968
		Sludge	757.00	303.15	2.213	±	0.435	21.657	±	14.487	0.868
				323.15	1.077	±	0.171	29.337	±	16.959	0.908
				353.15	0.958	±	0.110	14.268	±	4.670	0.974
		PAN Fiber	832.00	303.15	2.042	±	0.098	90.631	±	21.654	0.983
				323.15	2.002	±	0.244	27.945	±	12.272	0.943
		Pitch Fiber	1518.00	303.15	5.433	±	0.617	25.004	±	10.069	0.953
				323.15	4.337	±	0.354	10.414	±	2.240	0.990
				353.15	2.500	±	0.374	15.586	±	6.822	0.956
TOL (Toluene)	(Yanxu et al., 2008)	Act. Semicoke	-	293.00	0.267	±	0.002	221.795	±	23.228	0.999
	(Tefera et al., 2013)	Commercial AC	1390.00	298.15	4.525	±	0.018	366.021	±	30.724	0.939
	(Yang et al., 2018)	Wood AC 1	1284.37	303.15	3.193	±	0.286	0.064	±	0.012	0.976
		Coal AC 2	837.97	303.15	5.183	±	0.749	0.018	±	0.004	0.990
		Coal AC 3	840.03	303.15	4.352	±	0.881	0.028	±	0.009	0.943
		Coal AC 4	687.71	303.15	4.129	±	0.885	0.020	±	0.006	0.974
		Coconut AC 5	570.72	303.15	1.680	±	0.290	0.033	±	0.010	0.965
HEX (n-Hexane)	(Izquierdo et al., 2013)	Almond Shell AC-1	1128.00	298.15	4.699	±	0.226	17.245	±	7.568	0.715
		2	626.00	298.15	2.609	±	0.060	88.802	±	30.303	0.924
		3	789.00	298.15	5.138	±	0.141	1.469	±	0.289	0.948
		4	785.00	298.15	3.301	±	0.102	3.437	±	0.994	0.914
		5	1117.00	298.15	5.166	±	0.153	1.714	±	0.299	0.928
		6	891.00	298.15	3.823	±	0.131	4.429	±	1.039	0.866
		7	926.00	298.15	4.081	±	0.233	2.77	±	1.074	0.712
		8	502.00	298.15	1.997	±	0.022	3.031	±	0.291	0.986
		9	624.00	298.15	2.654	±	0.054	5.105	±	0.706	0.946

		10	723.00	298.15	2.046	±	0.023	3.768	± 0.473	0.986
		11	990.00	298.15	4.427	±	0.185	1.476	± 0.341	0.898
	(Shim et al., 2007)	Commercial AC	1221.00	298.15	3.801	±	0.081	13.548	± 2.185	0.836
				308.15	3.576	±	0.079	13.493	± 2.153	0.866
				318.15	3.326	±	0.096	16.331	± 2.954	0.858
MiBK (Methyl-iso-butylketone)	(Kim et al., 2006)	Coconut AC	–	293.15	3.810	±	0.252	5491.742	± 1628.153	0.869
		Bituminous AC	–	293.15	2.399	±	0.053	20306.720	± 4361.015	0.763

As can be seen in Table 6, multiple activated carbon materials of different origins have been used for VOC adsorption. The surface areas of the materials demonstrate a vast variation, between 502– 1720 $m^2\ g^{-1}$, as a product of the different synthesis protocols available in the literature. Further details on the physicochemical properties/microstructures can be found on the source papers, however it is important to note that there is profound lack of harmonisation among them regarding the physicochemical properties reported.

A case indicative of the wide range of activated carbons is made by Tsai et al., (2008) which provide a comprehensive set of tests for four activated carbon materials; one commercial, one sludge-derived, one of PAN-derived fiber and one of Pitch derived fiber. It was determined that the surface of the commercial and sludge derived act. carbon tended to be acidic, while the act. carbon fiber materials tended to be neutral or basic. Moreover, important differences were noted regarding the surface oxygenated functional groups. The act. carbon fibers were dominated by carbonyl groups, while the commercial act. carbon had both carbonyl and lactone groups. Interestingly, the sludge derived carbon, of microorganism origin, was more complex, exhibiting carboxyl, phenolic and lactone surface functional groups. Based on their findings, the fibers were deemed less polar compared to the other two act. carbons.

Figure 10 (a) presents our estimated values of Langmuir Isotherm parameters for acetone. Published experimental data from acetone breakthrough experiments have been compiled from seven different papers pertaining to different types of activated carbon. The R^2 value of the fit ranges from 0.841-0.999, which indicates that the Langmuir Isotherm is a good fit for most cases. Values for the Langmuir affinity coefficient do not follow a pattern for the same material but do range within two orders of magnitude among the seven papers (Ruthven, 1984).

Figure 10 (b) shows our Langmuir Isotherm parameter estimations for DCM. Published experimental data from DCM breakthrough experiments have been compiled from five different papers pertaining to different types of activated carbon as adsorbent material. The R^2 of our fit ranges from 0.865-0.999, indicating that the Langmuir Isotherm is a good fit for most cases. Values for the Langmuir affinity coefficient do not follow a pattern for the same material but do range within one order of magnitude among these five papers. The maximum adsorbed amount decreases with increasing temperatures for each material, as expected from theory, while the variability of values for the Langmuir affinity coefficient can be attributed to the different properties of the adsorbent material which affects adsorbent-adsorbate interactions.

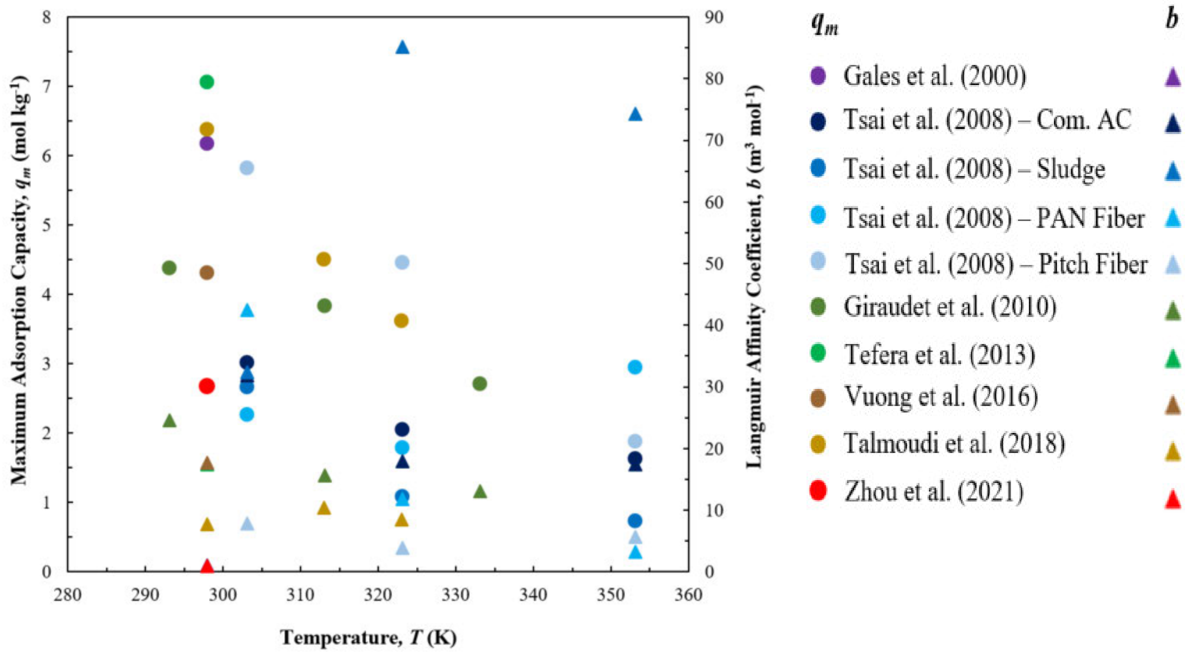

(a)

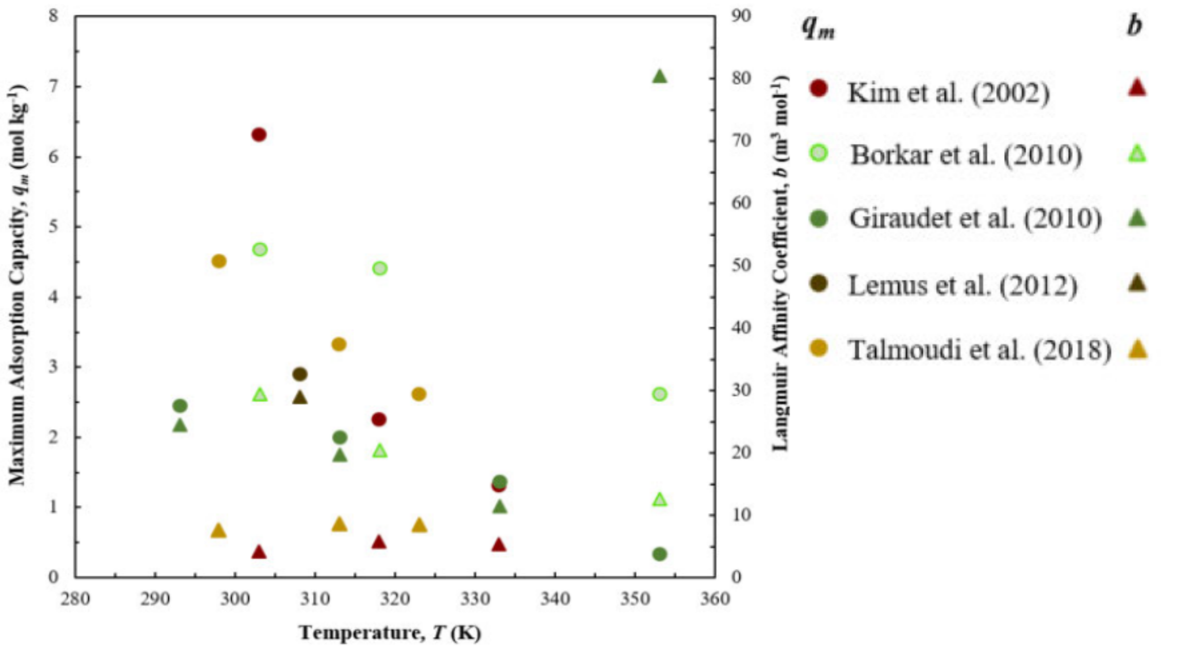

(b)

Figure 10. Langmuir Isotherm parameter estimation for Acetone (a) and DCM (b).

Figure 11(a) shows our estimated values of Langmuir Isotherm parameters for TCM based on published experimental data of breakthrough experiments from the same paper pertaining to different types of adsorbents. Moreover, values by (Chuang et al., 2003) are displayed, since they are used for simulation purposes in the present paper. The R^2 values of the fit range from 0.869-0.990. The maximum adsorption capacity values are in the same order of magnitude among the adsorbent materials while values of the Langmuir affinity coefficient do not follow a pattern for the same material but do range within one order of magnitude among the different adsorbents, possibly due to different microscopic properties. Further experimental data for chloroform adsorption on activated carbon is necessary for fitted values comparison.

Figure 11(b) presents our estimated values of Langmuir Isotherm parameters for toluene. The experimental data come from three different papers pertaining to different types of activated carbon. The R^2 values of our fit are very high, ranging from 0.940-0.999, indicating the high level of accuracy that is achieved using the Langmuir Isotherm to describe toluene adsorption. Here, the maximum adsorbed amount values range within one order of magnitude among the three papers. Values for the Langmuir affinity coefficient for experiments conducted by (Yang et al., 2018) interestingly are four orders of magnitude smaller than the other two papers, a difference attributed to the very different microscopic properties of the adsorbent materials.

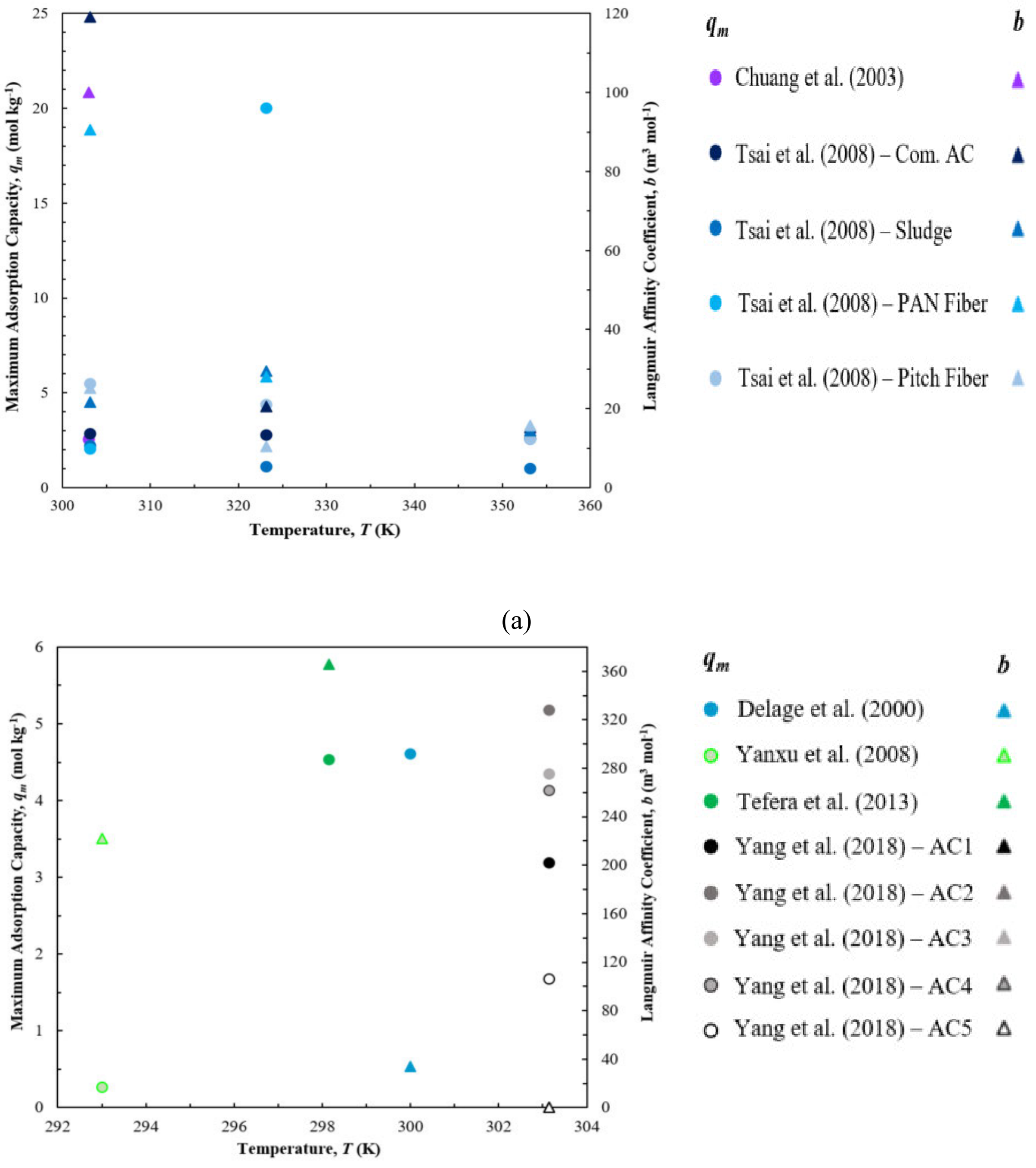

(a)

(b)

Figure 11. Langmuir Parameter Estimation for (a) Chloroform and (b) Toluene.

Maximum adsorption capacity for n-hexane, in agreement with previous results, does not follow a linear relationship with increasing surface area of the material, thus demonstrating the need for careful selection of the adsorbent in order to achieve optimal adsorption. Increasing adsorption temperature, on the other hand, results in a lower maximum adsorption capacity, consistent with thermodynamics. Langmuir adsorption affinity coefficient receives a wider range of values. For n-hexane, the values are within two orders of magnitude, while for MiBK only within one order of magnitude. Values comparison for the two VOCs highlights the broad range of values due to the different physicochemical interactions of the adsorbent-adsorbate systems and the need for more experimental data, particularly for MiBK. The complete parameter estimation results can be found in Table 6. R-squared values range between 0.712 and 0.986, while standard errors are relatively low for n-hexane and more significant for MiBK.

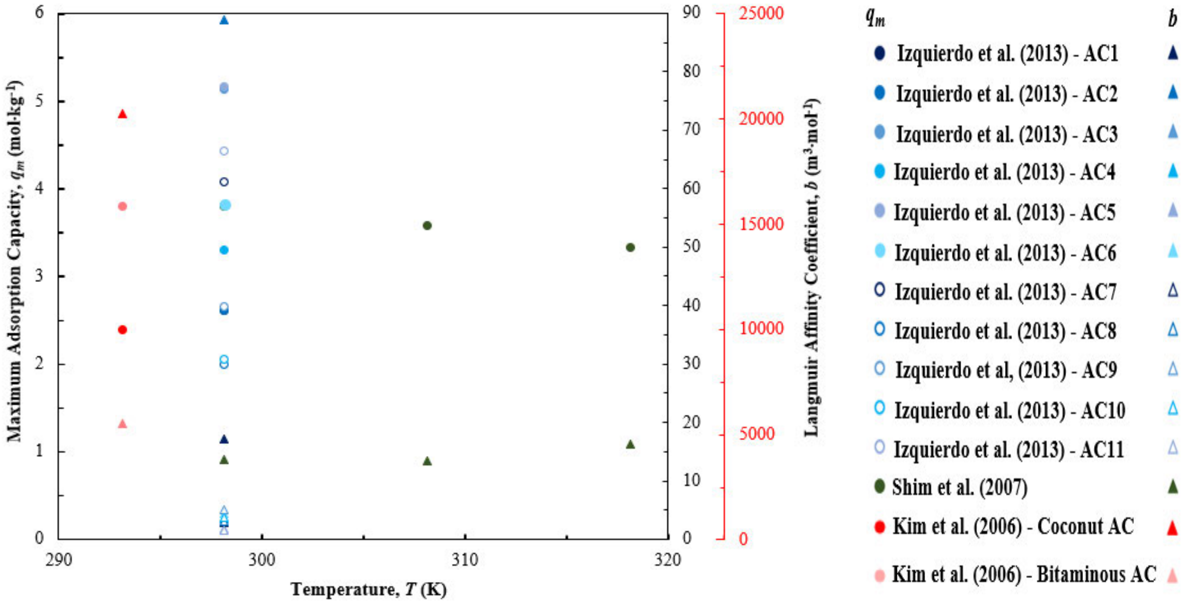

Figure 12. Langmuir parameter estimation results for n-Hexane (blue/green), MiBK (red/pink).

Surface areas of the examined activated carbons can also be found in Table 6 and range between 502 – 1221 m^2·g^{-1} for n-hexane, while the value for MiBK was not reported in the source paper.

3.3 Chapter Conclusions

The present chapter first reviews several literature studies in order to establish a database of pharma-relevant solvents (acetone, chloroform, dichloromethane, toluene, hexane, methyl isobutyl ketone) Langmuir Isotherm parameters for adsorption on activated carbon materials through parameter estimation. In several studies, Langmuir Isotherm parameter values required for simulations may have not been accurately estimated and/or explicitly reported, obstructing the validation of extremely useful experiments. Our parameter estimation results are very promising in the majority of cases and emphasise the enormous variation in certain parameter values (e.g. maximum adsorption capacity of materials, Langmuir affinity coefficient), which can be as high as 2-4 orders of magnitude, respectively. This considerable (and alarming, for modelling purposes) uncertainty reflects the extremely wide range of activated carbon (AC) material types, microstructures, processing protocols and physicochemical characteristics (many of which may similarly have not been quantified or comprehensively reported, as beyond the purpose).

PART III

ADSORPTION DYNAMIC MODEL DEVELOPMENT

Chapter 4

Adsorption Dynamic Model Development

This chapter describes the development of an adsorption dynamic model and its main assumptions. The model is multicomponent, non-isothermal and considers the Linear Driving Force model for solid phase mass transfer as well as Ergun's equation for pressure drop and the extended Langmuir Isotherm for equilibrium.

This model has been used for simulations in this thesis and all published work; details can be found in Appendix B.

Adsorption Dynamic Model Description

The validated, fixed bed, multicomponent, nonisothermal adsorption model considering mass and energy balances in the axial dimension (z) is employed to describe binary VOC mixtures adsorption under industrially relevant conditions in this PhD thesis. The mass transfer between the gas phase and the solid particles as well as heat transfer from inside the column to the environment are described using lumped equations. The mathematical model used in this PhD thesis relies on the following assumptions:

1. Radial concentration and temperature gradients are negligible (Suzuki, 1990).
2. The gas phase and adsorbent particles are in thermal equilibrium (Suzuki, 1990).
3. Wall temperature is constant and equal to the ambient temperature (Suzuki, 1990).
4. The ideal gas law applies and carrier gas adsorption is negligible (Suzuki, 1990).
5. Initially ($t = 0$ s) the column only contains carrier gas (Ruthven, 1984).
6. Equilibrium obeys the Extended Langmuir model for mixtures (Tefera et al., 2013).
7. Equations (3)-(11) and (13) are taken from (Tefera et al., 2013).

Considering all the assumptions, the overall and component mass balances are given as follows (i: component):

$$\frac{\partial C_t}{\partial t} = -\frac{\partial (uC_t)}{\partial z} - \frac{(1-\varepsilon_b)}{\varepsilon_b}\rho_p \sum \frac{\partial q_i}{\partial t} \tag{1}$$

$$\frac{\partial C_i}{\partial t} = D_{z,i}\frac{\partial^2 C_i}{\partial z^2} - \frac{\partial (uC_i)}{\partial z} - \frac{(1-\varepsilon_b)}{\varepsilon_b}\rho_p \frac{\partial q_i}{\partial t} \tag{2}$$

where C_t is the total gas phase VOC concentration, C_i is the component *i* gas phase VOC concentration, $D_{z,i}$ is the axial dispersion coefficient of component *i*, *u* is the interstitial velocity,

ε_b is the bulk bed porosity, ρ_p is the particle density and q the adsorbed phase VOC concentration.

The axial dispersion coefficient of component i is calculated by (Tefera et al., 2013):

$$D_{z,i} = \left(\alpha_0 + \frac{Sc_i Re_p}{2}\right)\frac{D_{AB,i}}{\varepsilon_b} \tag{3}$$

where Sc_i is the Schmidt number of i, Re_p the Reynolds number (adsorbent particle), $D_{AB,i}$ the molecular diffusivity and α_0 the empirical mass diffusion correction factor.

The molecular diffusivity of component i is estimated by:

$$D_{AB,i} = 10^{-3} T^{1.75} \frac{\sqrt{\left(\frac{M_{rA} + M_{rB}}{M_{rA} M_{rB}}\right)}}{P((\sum v)_A^{0.33} + (\sum v)_B^{0.33})^2} \tag{4}$$

where Σv is the sum of the atomic diffusion volumes (A: VOC, B: carrier), T is temperature, P is pressure and M_r is the molecular weight.

Solid phase adsorption is modelled by the established Linear Driving Force (LDF) model which is characterized as “simple, analytic, and physically consistent” by (Sircar & Hufton, 2000), considering a lumped overall mass transfer coefficient (Tefera et al., 2014; Tefera et al., 2013):

$$\frac{\partial q_i}{\partial t} = k_{LDF}\left(q_{e,i} - q_i\right) \tag{5}$$

where $k_{LDF,i}$ is the LDF mass transfer coefficient and $q_{e,i}$ is the inlet P and T adsorbent equilibrium capacity from the extended Langmuir Isotherm. The adsorbed phase VOC concentration (q_i) changes as the mass transfer zone progresses through the bed. Starting from a clean bed, it will be zero, and as the mass transfer zone progresses each part of the column reaches the equilibrium capacity.

The LDF mass transfer coefficient is estimated by:

$$k_{LDF} = \frac{60 \varepsilon_p C_{0,i} D_{eff,i}}{\tau_p C_{s0,i} d_p^2} \tag{6}$$

where ε_p is the particle porosity, $C_{0,i}$ is the inlet concentration of i, $D_{eff,i}$ is the effective diffusivity of i, τ_p is particle tortuosity, $C_{s0,i}$ is the adsorbed phase concentration at equilibrium with $C_{0,i}$ and d_p the particle diameter. For the purposes of this PhD Thesis particles are assumed to have the same diameters, values of which are taken from published studies used for validation purposes in the next chapters.

The particle density is given by:

$$\rho_p = \frac{\rho_b}{1-\varepsilon_b} \tag{7}$$

where ρ_b is the bed density and ε_b the bed porosity.

The bed porosity is calculated by:

$$\varepsilon_b = 0.379 + \frac{0.078}{\left(\frac{D}{d_p}\right) - 1.8} \tag{8}$$

where D is the column internal diameter and d_p is the particle diameter. This equation is used only when the paper used for validation does not disclose the ε_b of the experimental setup. When validation is not the chapter's topic, a standard value of $\varepsilon_b = 0.38$ is calculated, consistent with literature standards for adsorption (Ruthven, 1984).

The particle porosity is calculated by:

$$\varepsilon_p = V_{pore}\rho_p \tag{9}$$

where V_{pore} is the adsorbent pore volume.

The particle tortuosity is given by:

$$\tau_p = \frac{1}{\varepsilon_p^2} \tag{10}$$

where ε_p is the particle porosity.

The adsorbed phase concentration at equilibrium with $C_{0,i}$ is given by:

$$C_{s0,i} = \rho_b q_{e,i} \tag{11}$$

where ρ_b is the bed porosity.

The Knudsen diffusivity is estimated by (Ruthven, 1984):

$$D_{k,i} = 97 r_p \sqrt{\frac{T}{M_{rA}}} \tag{12}$$

where $D_{k,i}$ is the Knudsen diffusivity*,* r_p is the average pore radius, while T and M_{rA} are the temperature and VOC molecular weight.

The effective diffusivity is given by:

$$\frac{1}{D_{eff,i}} = \frac{1}{D_{AB,i}} + \frac{1}{D_{k,i}} \tag{13}$$

The Bosanquet formula of Equation (13), thus Equation (6), is verified (Krishna & van Baten, 2012) for the estimation of the effective diffusivity ($D_{eff,i}$).

Adsorption equilibrium is assumed to obey the Extended Langmuir Model, described as follows:

$$q_{e,i} = \frac{q_{m,i} b_i C_i}{1 + \sum b_i C_i} \tag{14}$$

$$b_i = b_{o,i} exp\left(\frac{-\Delta H_{ad,i}}{RT}\right) \tag{15}$$

where $q_{e,i}$ is the equilibrium adsorption capacity of i, $q_{m,i}$ is the maximum adsorption capacity of i, b_i the Langmuir affinity coefficient, $b_{o,i}$ is the pre-exponential Langmuir affinity coefficient constant and $\Delta H_{ad,i}$ is the heat of adsorption.

The energy balance for the fluid and solid phases as well as the parameter main equations based on (Ruthven, 1984), (Suzuki, 1990) and (Knox et al., 2016) are as follows:

$$\begin{aligned} \left(\rho_g C_{pg} + \frac{(1-\varepsilon_b)}{\varepsilon_b}\rho_p C_{pp}\right)\frac{\partial T}{\partial t} &= k_{ez}\frac{\partial^2 T}{\partial z^2} - \rho_g C_{pg}\frac{\partial (uT)}{\partial z} \\ &+ \frac{(1-\varepsilon_b)}{\varepsilon_b}\sum_{i=1}^{n} \Delta H_{ad,i}\frac{\partial q_i}{\partial t} - \frac{2h_o}{\varepsilon_b R_p}(T - T_w) \end{aligned} \tag{16}$$

where T_w is the wall temperature, ρ_g is the gas density, Cp_g is the specific heat capacity of the gas, Cp_p is the specific heat capacity of the particle, k_{ez} is the effective axial thermal conductivity, R_p is the particle radius, T is the temperature and h_o is the overall heat transfer coefficient.

The effective thermal conductivity is calculated by (Knox et al., 2016):

$$k_{eff} = k_g(\frac{k_p}{k_g})^n \tag{17}$$

$$n = 0.28 - 0.757\log_{10}\varepsilon_b - 0.057\log_{10}\left(\frac{k_p}{k_g}\right) \tag{18}$$

where k_{eff} is the effective thermal conductivity, k_g is the gas thermal conductivity, k_p is the particle thermal conductivity and n is the Krupickza equation parameter.

The effective axial thermal conductivity is calculated by (Knox et al., 2016):

$$k_{ez} = k_g(\frac{k_{eff}}{k_g} + 0.75PrRe) \tag{19}$$

The overall heat transfer coefficient is given by (Ruthven, 1984):

$$\frac{1}{h_o d} = \frac{1}{dh_{int}} + \frac{x}{k_w d_{lm}} \tag{20}$$

where h_{int} is the internal heat transfer coefficient, k_w is the wall thermal conductivity, x is the wall thickness and d_{lm} is the mean logarithmic column diameter.

The internal heat transfer coefficient is given by (Ruthven, 1984):

$$h_{int} = \frac{k_g}{2R}[2.03Re^{0.8}\exp\left(-6\frac{R_p}{R}\right)] \tag{21}$$

where R is the internal column radius.

The pressure drop along the column is calculated using Ergun's equation (Ruthven, 1984), (Suzuki, 1990):

$$-\frac{\partial P}{\partial z} = 150u\mu\frac{(1-\varepsilon_b)^2}{\varepsilon_b^2 d_p^2} + 1.75\rho_g u^2\frac{(1-\varepsilon_b)}{\varepsilon_b d_p} \tag{22}$$

where μ is gas viscosity and P is pressure.

The system boundary conditions at the column inlet ($z = 0$) can be written as follows:

$$D_{z,i}\frac{\partial C_i(z=0,t)}{\partial z} = -u(C_{o,i} - C_i) \tag{23}$$

$$k_{z,i}\frac{\partial T(z=0,t)}{\partial z} = -uC_{pg}\rho_g(T_{in} - T) \tag{24}$$

$$u(0) = \frac{V_s}{\varepsilon_b} \tag{25}$$

where V_s is the superficial velocity.

The boundary conditions at the column outlet ($z = L$) are:

$$\frac{\partial C_i(z=L,t)}{\partial z} = 0 \tag{26}$$

$$\frac{\partial T(z=L,t)}{\partial z} = 0 \tag{27}$$

$$\frac{\partial u(L)}{\partial z} = 0 \tag{28}$$

The initial conditions at $t = 0$ for $0 \leq z \leq L$:

$$C_i(z, t = 0) = 0 \tag{29}$$

$$q_i(z, t = 0) = 0 \tag{30}$$

$$T = (z, t = 0) = T_{in} \tag{31}$$

Moment analysis (Ruthven, 1984), and more specifically the analysis of the first moment, allows the prediction of the mean residence time of adsorbates in a given adsorption column based on the flowrate, thermodynamics of the system and flowrate, thus completely not dependent on kinetics:

$$\mu_{RT,i} = \frac{L}{u}\left[1 + \frac{(1-\varepsilon)}{\varepsilon} H_i\right] \tag{32}$$

where $\mu_{RT,i}$ is the mean residence time of component i, L is the column length, and H_i the dimensionless Henry's constant of component i.

In this PhD thesis, the dimensionless Henry's constant is calculated by:

$$H_i = \rho_p q_{m,i} b_i \tag{33}$$

With a formula similar to the mean residence time, the time required for a travelling shock to reach the column outlet can also be predicted (Ruthven, 1984 and Kotchine, 1926):

$$t_{shock,i} = \frac{L}{u}\left(1 + \frac{(1-\varepsilon)}{\varepsilon}\frac{q_{\rho e,i}}{C_i}\right) \tag{34}$$

$$q_{\rho e,i} = \rho_p \frac{q_{m,i} b_i C_i}{1 + b_i C_i} \tag{35}$$

where $t_{shock,i}$ is the shock breakthrough time of component i and $q_{\rho e,i}$ is the equilibrium concentration of component i in mol m^{-3}.

The relative errors between the mean residence time (Eq.32) and the $t_{95\%}/t_{105\%}$ are computed as follows:

$$\%RE = \frac{100(t_{95\%} - \mu_{RT,i})}{t_{95\%}} \tag{36}$$

The relative errors between the shock breakthrough time (Eq.34) and the $t_{95\%}/t_{105\%}$ are computed as follows:

$$\%RE = \frac{100(t_{95\%} - t_{shock,i})}{t_{95\%}} \tag{37}$$

PART IV

BINARY MIXTURE SIMULATIONS

Chapter 5

Validation, Binary Mixture Adsorption & Sensitivity Analysis

This chapter presents the validation of our adsorption model against published experimental data for the binary dichloromethane-acetone mixture. It is then used to perform a temperature sensitivity analysis of the same mixture. Then, the binary adsorption characteristics of the dichloromethane-acetone, dichloromethane-chloroform and dichloromethane-toluene for two different bed porosities and two adsorption temperatures are investigated.

The results presented in this chapter have also been published in the literature (Tzanakopoulou et al., 2023. *Comput.Chem.Eng.*,**174**, 108248); details can be found in Appendix B.

5.1 Case Studies of DCM-ACT, DCM-TCM, DCM-TOL, TCM-ACT, TCM-TOL and ACT-TOL

The developed model was employed to examine the adsorption of DCM-ACT according to the conditions set out by (Talmoudi et al., 2018) (Table 7 CS0) using nitrogen as the carrier gas on an activated carbon bed, with the exception of the Langmuir Isotherm parameters; the simulations use the Chapter 3 estimated Langmuir Isotherm parameter values for DCM and Tefera et al. (2013)'s for acetone for greater reliability. Then, the model was used to perform a temperature sensitivity analysis on the DCM-ACT mixture of CS0 to examine the effect of different operating temperatures on breakthrough behaviour.

The set of partial differential equations (PDEs) is solved using second order orthogonal collocation on finite elements with 30 discretisation points in the gPROMS® Process 2.0.0 software suite. For all cases considered, the DASolver DAEBDF is employed, which uses a variable time step and variable order Backward Finite Differentiation Formulae. The viscosities are computed from Wilke's equation, while densities are determined through pure component data via mixing rules (National Institute of Standards and Technology (NIST), 2023). The main system parameters are in Table 7:

Table 7. Temperature sensitivity analysis main parameters for the DCM-ACT mixture.

System	$\Delta H_{ad,i}$ (J mol^{-1})	$D_{z,i}$ (m^2 s^{-1})	T_{in} (K)	L (m)	C_0 (ppm$_v$)	V_s (m s^{-1})	q_m (mol kg^{-1})	ε_b	k_{LDF} (s^{-1})	b_0 (m^3 mol^{-1})	Fig.
DCM-ACT (CS0)	40000	0.0008	298	0.100	2000	0.170	4.51	0.39	$1.39 \cdot 10^{-4}$	$7.41 \cdot 10^{-7}$	14a
	51100	0.0008			500		7.06		$3.05 \cdot 10^{-5}$	$1.96 \cdot 10^{-8}$	

DCM-ACT	40000	0.0008	298	0.100	2000	0.170	4.51	0.39	$1.39\cdot10^{-4}$	$7.41\cdot10^{-7}$	14b
	51100	0.0008			500		7.06		$3.05\cdot10^{-5}$	$1.96\cdot10^{-8}$	
DCM-ACT	40000	0.0008	293	0.100	2000	0.170	4.51	0.39	$1.14\cdot10^{-4}$	$7.41\cdot10^{-7}$	14b
	51100	0.0008			500		7.06		$3.48\cdot10^{-5}$	$1.96\cdot10^{-8}$	
DCM-ACT	40000	0.0008	288	0.100	2000	0.170	4.51	0.39	$1.04\cdot10^{-4}$	$7.41\cdot10^{-7}$	14b
	51100	0.0008			500		7.06		$2.94\cdot10^{-5}$	$1.96\cdot10^{-8}$	

The simulation results in this PhD Thesis are presented with breakthrough curve plots. Breakthrough curves show the gas concentration at the column outlet vs time, and Figure 13 shows the derivation of the main metrics used in the analysis of this PhD Thesis. Breakthrough onset time ($t_{5\%}$) is estimated as the time needed for the outlet concentration to reach 5% of the final concentration. Breakthrough completion time is regarded as the time needed for the outlet concentration to reach 95% of the final concentration for the strongly adsorbing component ($t_{95\%}$), and 105% of the final concentration for the weakly adsorbing component ($t_{105\%}$). Finally, breakthrough duration (t_{drt}) is the difference between breakthrough completion and onset times.

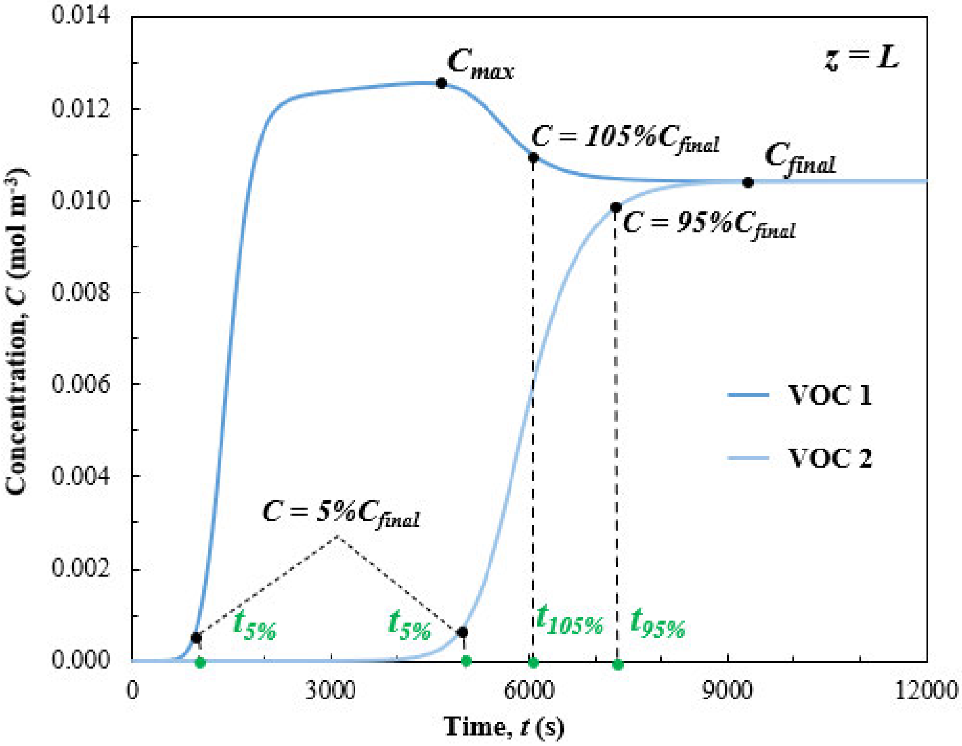

Figure 13. Breakthrough curve analysis metrics in this PhD Thesis.

Table 8 summarizes the main structural (column and adsorbent) and thermal parameter values of the systems:

Table 8. Temperature sensitivity analysis main thermal parameters for the DCM-ACT binary mixture.

System	ρ_b (kg m^{-3})	D (m)	T_{in} (K)	ε_p	d_p (m)	C_{pp} (J kg^{-1} K^{-1})	C_{pg} (J kg^{-1} K^{-1})	k_{ez} (W m^{-1} K^{-1})	h_o (W m^{-2} K^{-1})	h_{int} (W m^{-2} K^{-1})	k_w (W m^{-1} K^{-1})	x (m)	Fig.
DCM-ACT (CS0)	250	0.01	298	0.36	0.001	706.7	1039	0.21	4.55	4.56	14.2	0.001	14a
DCM-ACT	250	0.01	298	0.36	0.001	706.7	1039	0.21	4.55	4.56	14.2	0.001	14b
DCM-ACT	250	0.01	293	0.36	0.001	706.7	1039	0.22	4.52	4.53	14.2	0.001	14b
DCM-ACT	250	0.01	288	0.36	0.001	706.7	1039	0.22	4.51	4.52	14.2	0.001	14b

Next, the model has been used to explore the adsorption of binary mixtures of pharmaceutically relevant VOCs (acetone, dichloromethane, chloroform, and toluene) on an activated carbon fixed-bed column using air as the carrier gas (CS1-CS15) for two different temperatures (T = 293 K, T = 300 K) and two different bed porosities ($\varepsilon_b = 0.35$, $\varepsilon_b = 0.38$). Air is assumed a binary mixture (N_2:O_2 = 79:21 % v/v) and Langmuir Isotherm parameters ($q_{m,i}$ and b_i) are taken from (Tefera et al., 2013) for acetone, from (Chuang et al., 2003) for chloroform, and from (Delage, 2000) for toluene, respectively. Langmuir Isotherm parameters for dichloromethane ($q_{m,i}$ and b_i) are estimated from data by (Talmoudi et al., 2018). Heats of adsorption are used as per in these four papers. The main structural (column, adsorbent) and thermal parameter values are given in Table 9.

Table 9. Main thermal parameters for binary mixture Case Studies (CS) simulations.

System	ρ_b (kg m^{-3})	D (m)	T_{in} (K)	ε_p	d_p (m)	C_{pp} (J kg^{-1} K^{-1})	C_{pg} (J kg^{-1} K^{-1})	k_{ez} (W m^{-1} K^{-1})	h_o (W m^{-2} K^{-1})	h_{int} (W m^{-2} K^{-1})	k_w (W m^{-1} K^{-1})	x (m)	Fig.
DCM-ACT (CS1)	606	0.0152	300	0.56	0.00075	706.7	1013	0.67	52.90	53.08	14.2	0.001	15a
DCM-ACT (CS2)	606	0.0152	293	0.56	0.00075	706.7	1013	0.69	53.70	53.89	14.2	0.001	
DCM-ACT (CS3)	606	0.0152	300	0.53	0.00075	706.7	1013	0.67	52.90	53.08	14.2	0.001	15b
DCM-ACT (CS4)	606	0.0152	293	0.53	0.00075	706.7	1013	0.69	53.70	53.89	14.2	0.001	
DCM-TCM (CS5)	606	0.0152	300	0.56	0.00075	706.7	1012	0.67	53.16	53.35	14.2	0.001	15c
DCM-TCM (CS6)	606	0.0152	293	0.56	0.00075	706.7	1012	0.69	53.63	53.82	14.2	0.001	
DCM-TCM (CS7)	606	0.0152	300	0.53	0.00075	706.7	1012	0.67	53.16	53.35	14.2	0.001	15d
DCM-TCM (CS8)	606	0.0152	293	0.53	0.00075	706.7	1012	0.69	53.63	53.82	14.2	0.001	

System	ρ_b (kg m^{-3})	D (m)	T_{in} (K)	ε_p	d_p (m)	C_{pp} (J kg^{-1} K^{-1})	C_{pg} (J kg^{-1} K^{-1})	k_{ez} (W m^{-1} K^{-1})	h_o (W m^{-2} K^{-1})	h_{int} (W m^{-2} K^{-1})	k_w (W m^{-1} K^{-1})	x (m)	Fig.
DCM-TOL (CS9)	606	0.0152	300	0.56	0.00075	706.7	1013	0.67	37.17	37.26	14.2	0.001	15e
DCM-TOL (CS10)	606	0.0152	293	0.56	0.00075	706.7	1013	0.68	53.62	53.81	14.2	0.001	
DCM-TOL (CS11)	606	0.0152	300	0.53	0.00075	706.7	1013	0.67	40.59	40.70	14.2	0.001	15f
DCM-TOL (CS12)	606	0.0152	293	0.53	0.00075	706.7	1013	0.68	53.62	53.81	14.2	0.001	
TCM-ACT (CS13)	606	0.0152	300	0.56	0.00075	706.7	1013	0.67	37.21	37.30	14.2	0.001	15a
TCM-TOL (CS14)	606	0.0152	300	0.56	0.00075	706.7	1013	0.67	39.83	39.93	14.2	0.001	15b
TOL-ACT (CS15)	606	0.0152	300	0.56	0.00075	706.7	1014	0.67	39.78	39.88	14.2	0.001	15c

The average particle size is 0.75 mm, 99% by mass between 0.60 and 0.84 mm (Tefera et al., 2013, Lashaki et al., 2012).

The main parameters used in Case Studies (CS) simulations are in Table 10:

Table 10. Binary mixture Case Studies (CS) and main parameters for simulations.

System	$D_{z,i}$ ($m^2\ s^{-1}$)	$\Delta H_{ad,i}$ ($J\ mol^{-1}$)	T_{in} (K)	L (m)	$C_{0,i}$ (ppm_v)	V_s ($m\ s^{-1}$)	q_m ($mol\ kg^{-1}$)	ε_b	k_{LDF} (s^{-1})	b_0 ($m^3\ mol^{-1}$)	Fig.
DCM-ACT	0.0023	40,000	300	0.065	250	0.914	4.51	0.38	$2.16\cdot10^{-4}$	$7.41\cdot10^{-7}$	15a
(CS1)	0.0023	51,100			250		7.06		$8.16\cdot10^{-5}$	$1.96\cdot10^{-8}$	
DCM-ACT	0.0023	40,000	293	0.065	250	0.914	4.51	0.38	$2.34\cdot10^{-4}$	$7.41\cdot10^{-7}$	
(CS2)	0.0023	51,100			250		7.06		$5.46\cdot10^{-5}$	$1.96\cdot10^{-8}$	
DCM-ACT	0.0025	40,000	300	0.065	250	0.914	4.51	0.35	$1.87\cdot10^{-4}$	$7.41\cdot10^{-7}$	15b
(CS3)	0.0025	51,100			250		7.06		$7.08\cdot10^{-5}$	$1.96\cdot10^{-8}$	
DCM-ACT	0.0025	40,000	293	0.065	250	0.914	4.51	0.35	$1.99\cdot10^{-4}$	$7.41\cdot10^{-7}$	
(CS4)	0.0025	51,100			250		7.06		$4.63\cdot10^{-5}$	$1.96\cdot10^{-8}$	
DCM-TCM	0.0014	40,000	300	0.065	250	0.914	4.51	0.38	$4.31\cdot10^{-4}$	$7.41\cdot10^{-7}$	15c
(CS5)	0.0014	44,769			250		2.49		$3.85\cdot10^{-5}$	$1.91\cdot10^{-6}$	
DCM-TCM	0.0023	40,000	293	0.065	250	0.914	4.51	0.38	$3.92\cdot10^{-4}$	$7.41\cdot10^{-7}$	
(CS6)	0.0022	44,769			250		2.49		$3.22\cdot10^{-5}$	$1.91\cdot10^{-6}$	
DCM-TCM	0.0025	40,000	300	0.065	250	0.914	4.51	0.35	$3.65\cdot10^{-4}$	$7.41\cdot10^{-7}$	15d
(CS7)	0.0025	44,769			250		2.49		$3.29\cdot10^{-5}$	$1.91\cdot10^{-6}$	
DCM-TCM	0.0025	40,000	293	0.065	250	0.914	4.51	0.35	$3.32\cdot10^{-4}$	$7.41\cdot10^{-7}$	
(CS8)	0.0024	44,769			250		2.49		$2.73\cdot10^{-5}$	$1.91\cdot10^{-6}$	
DCM-TOL	0.0014	40,000	300	0.065	250	0.914	4.51	0.38	$2.76\cdot10^{-4}$	$7.41\cdot10^{-7}$	15e
(CS9)	0.0013	45,500			250		4.61		$5.33\cdot10^{-5}$	$4.06\cdot10^{-7}$	
DCM-TOL	0.0023	40,000	293	0.065	250	0.914	4.51	0.38	$2.21\cdot10^{-4}$	$7.41\cdot10^{-7}$	
(CS10)	0.0022	45,500			250		4.61		$3.94\cdot10^{-5}$	$4.06\cdot10^{-7}$	
DCM-TOL	0.0025	40,000	300	0.065	250	0.914	4.51	0.35	$2.39\cdot10^{-4}$	$7.41\cdot10^{-7}$	15f
(CS11)	0.0024	45,500			250		4.61		$4.48\cdot10^{-5}$	$4.06\cdot10^{-7}$	
DCM-TOL	0.0025	40,000	293	0.065	250	0.914	4.51	0.35	$1.87\cdot10^{-4}$	$7.41\cdot10^{-7}$	
(CS12)	0.0024	45,500			250		4.61		$3.34\cdot10^{-5}$	$4.06\cdot10^{-7}$	
TCM-ACT	0.0014	44,769	300	0.065	250	0.914	2.49	0.38	$4.10\cdot10^{-5}$	$1.91\cdot10^{-6}$	19a
(CS13)	0.0014	51,100			250		7.06		$1.59\cdot10^{-4}$	$1.96\cdot10^{-8}$	
TCM-TOL	0.0014	44,769	300	0.065	250	0.914	2.49	0.38	$4.42\cdot10^{-5}$	$1.91\cdot10^{-6}$	19b
(CS14)	0.0013	45,500			250		4.61		$9.50\cdot10^{-5}$	$4.06\cdot10^{-7}$	
	0.0013	45,500			250		4.61		$5.58\cdot10^{-5}$	$4.06\cdot10^{-7}$	

TOL-ACT	0.0014	51,100	300	0.065	250	0.914	7.06	0.38	$1.01\cdot10^{-4}$	$1.96\cdot10^{-8}$	19c

5.2 Dynamic Simulation (gPROMS®) Results

The developed model has been first validated against the published experimental data of Talmoudi et al., (2018) for the adsorption of binary DCM-acetone using N_2 as the carrier gas (Table 8, CS0) and then used to simulate the adsorption of binary mixtures of pharmaceutically relevant VOCs (acetone, dichloromethane, chloroform and toluene) on an activated carbon fixed-bed column using air as the carrier gas (Table 10, CS1-CS15). The binary mixtures of dichloromethane with chloroform, dichloromethane with toluene and dichloromethane with acetone are simulated in adsorption scenarios of two different temperatures and two different bed porosities each (CS1-CS3, CS7-CS15). Breakthrough curves, showing the component concentration at column outlet, of the examined binary mixture systems are presented in Figure 15-16, while key breakthrough time metrics have been summarised in Table 11-14. In all cases presented here the bed area remains constant at 0.000181 m^2 while the particle diameter remains constant at 0.00075 m based on published activated carbon particle diameter values from (Tefera et al., 2013).

The model is successfully validated (Figure 14a) against published experimental breakthrough data (dots in Fig.14) which dictated model inputs (Talmoudi et al. 2018), using the Chapter 3 estimated Langmuir Isotherm parameters. The DCM breakthrough curve has been captured with higher accuracy compared to the one published by Talmoudi et al. (2018) plot for their experimental data, while a slight mismatch is observed after breakthrough for acetone at the curve slope. The discrepancy (present in both efforts) can be attributed to one-dimensional model limitations.

The same dichloromethane-acetone mixture as the base case (CS0) is employed for a temperature sensitivity analysis in Figure 14 (b), as the temperature is one of the key parameters affecting adsorption behaviour. Three different temperatures have been investigated and in all cases, DCM exits the column outlet at a higher concentration compared to its inlet. Results indicate that with rising temperature, the maximum concentration of DCM recorded at the column outlet, declines. Moreover, as expected by adsorption theory, with rising temperature the breakthrough onset time for both VOCs becomes shorter, due to adsorption exothermicity.

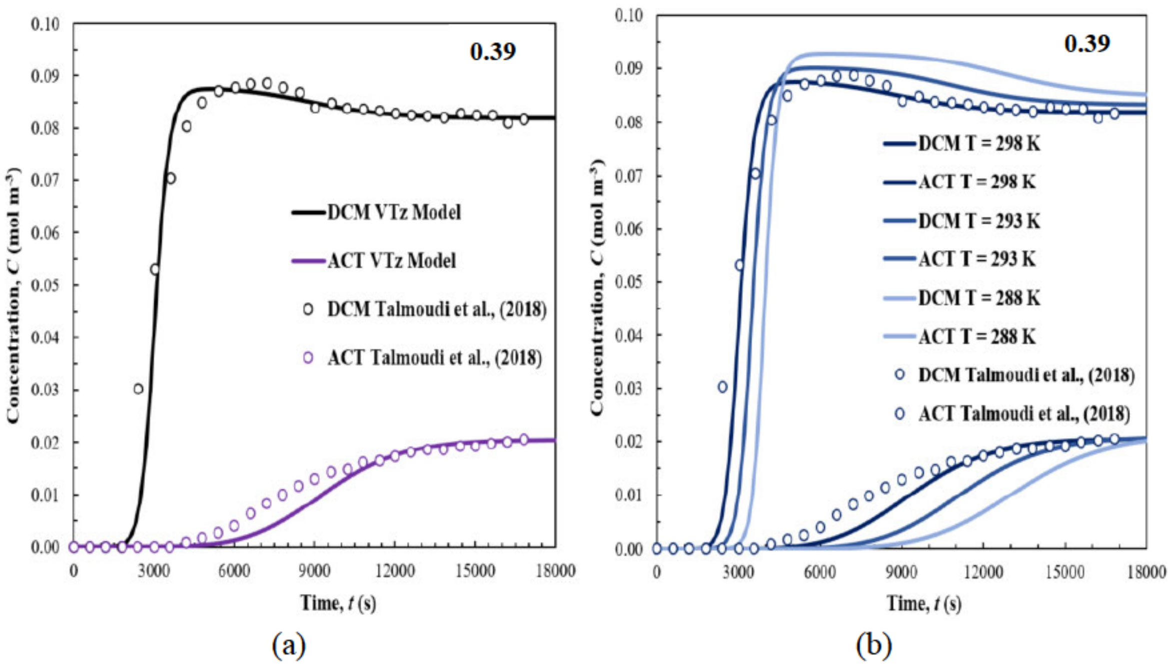

Figure 14. Model validation (a), T sensitivity analysis (b) of DCM-ACT system (bed outlet).

The mixture of dichloromethane with acetone has also been used in case studies for two different temperatures and two different bed porosities, and the relevant plots are presented in Figure 15 (a)-(b). In all scenarios considered, DCM emerges at the column outlet in a concentration higher than its inlet concentration. In all cases presented here the bed area remains constant at 0.000181 m^2 while the particle diameter remains constant at 0.00075 m based on published activated carbon particle diameter values from (Tefera et al., 2013). The changes in porosity are assumed to occur from potential raking/settling differences.

Higher temperature results in earlier breakthrough onset and shorter breakthrough duration. In Figure 15 (a), where ε_b = 0.38, breakthrough onset at 293 K is 46.05% later for DCM and 38.07% later for acetone compared to 300 K. Breakthrough duration at ε_b = 0.38 for DCM is 27.08% longer at 293 K than at 300 K, whereas acetone's at 293 K is 37.10% longer than at 300 K. In Figure 15 (b), where ε_b = 0.35, the breakthrough onset time of DCM is 46.89% later at 293 K than 300 K, and 36.70% later for acetone. Regarding breakthrough duration at ε_b = 0.35, DCM's is 21.96% longer at 293 K compared to 300 K, while acetone's is 35.71% longer at 293 K compared to 300 K.

Bulk bed porosity also affects breakthrough times. At T = 293 K and ε_b = 0.35 (Fig. 12b), DCM and acetone reach breakthrough at t = 1206 s and t = 4112 s respectively, values which are 1.94% and 2.14% larger compared to the breakthrough onset times at bed porosity ε_b = 0.38 (Figure 15a). At 300 K and ε_b = 0.35 (Figure 15b), the same trend is observed, with DCM's breakthrough onset being 1.36% later compared to 0.38, and acetone's 3.16% compared to 0.38 (Figure 15a). Breakthrough duration for DCM is 9.54% larger and for acetone 2.07% larger at 293 K and ε_b = 0.35 compared to 0.38. At 300 K and ε_b = 0.35, the trend persists, with DCM's breakthrough duration 15.49% longer and acetone's 3.11% longer compared to 0.38.

The mixture of dichloromethane with chloroform (TCM) was also employed for case studies at two different temperatures and two different bed porosities which can be seen in Figure 15 (c)-(d). In all scenarios considered, the order of affinity persists with DCM being weakly adsorbed. For the same ε_b (Figure 15c) breakthrough onset at 293 K is 71.20% later for DCM and 2.16% earlier for TCM compared to 300 K. In Figure 15 (d), the breakthrough onset time of DCM is 35.96% later at 293 K than at 300 K, and 13.67% later for TCM. In Figure 15 (c), the breakthrough duration of DCM is 1.09% longer at 293 K than at 300 K, whereas TCM's at 293 K is 75.87% longer than at 300 K. In Figure 15 (d), DCM breakthrough duration is 13.72% longer at 293 K compared to 300 K, while TCM's is 11.98% longer at 293 K compared to 300 K.

The breakthrough behaviour of the binary mixture of DCM-TCM is also clearly affected by bulk bed porosity (Figure 15c vs. d). At 293 K and ε_b = 0.35 (Figure 15d), DCM and TCM reach breakthrough at t = 1240 s and t = 5537 s respectively, values which are 23.60% sooner and 13.00% later compared to the VOCs breakthrough onset times at bed porosity 0.38 (Figure 15c) and 293 K. At 300 K and ε_b = 0.35 (Figure 15b), DCM's breakthrough onset is 3.80% earlier and TCM's 2.74% earlier compared to ε_b = 0.38 at the same temperature (Figure 15c). Breakthrough duration at 293 K and ε_b = 0.35 is for DCM 17.40% longer and for TCM 24.70% shorter compared to 0.38. At 300 K and ε_b = 0.35, DCM's breakthrough duration is 5.31% longer and TCM's 18.26% longer compared to 0.38.

The mixture of dichloromethane with toluene has been similarly used in case studies for two different temperatures and two different bed porosities (Figure 15 e-f). In all scenarios considered the order of affinity remains with DCM exiting the column in concentrations higher than its inlet's. In Figure 15 (e), where ε_b = 0.38, breakthrough onset at 293 K is 36.13% later for DCM and 29.02% later for toluene compared to 300 K. Moreover, breakthrough duration of DCM is 19.97% longer at 293 K than at 300 K, whereas toluene's breakthrough duration at 293 K is 37.84% longer than at 300 K. In Figure 15 (f), where ε_b = 0.35, the breakthrough onset time of DCM is 46.89% later at 293 K than at 300 K, and 36.70% later for acetone.

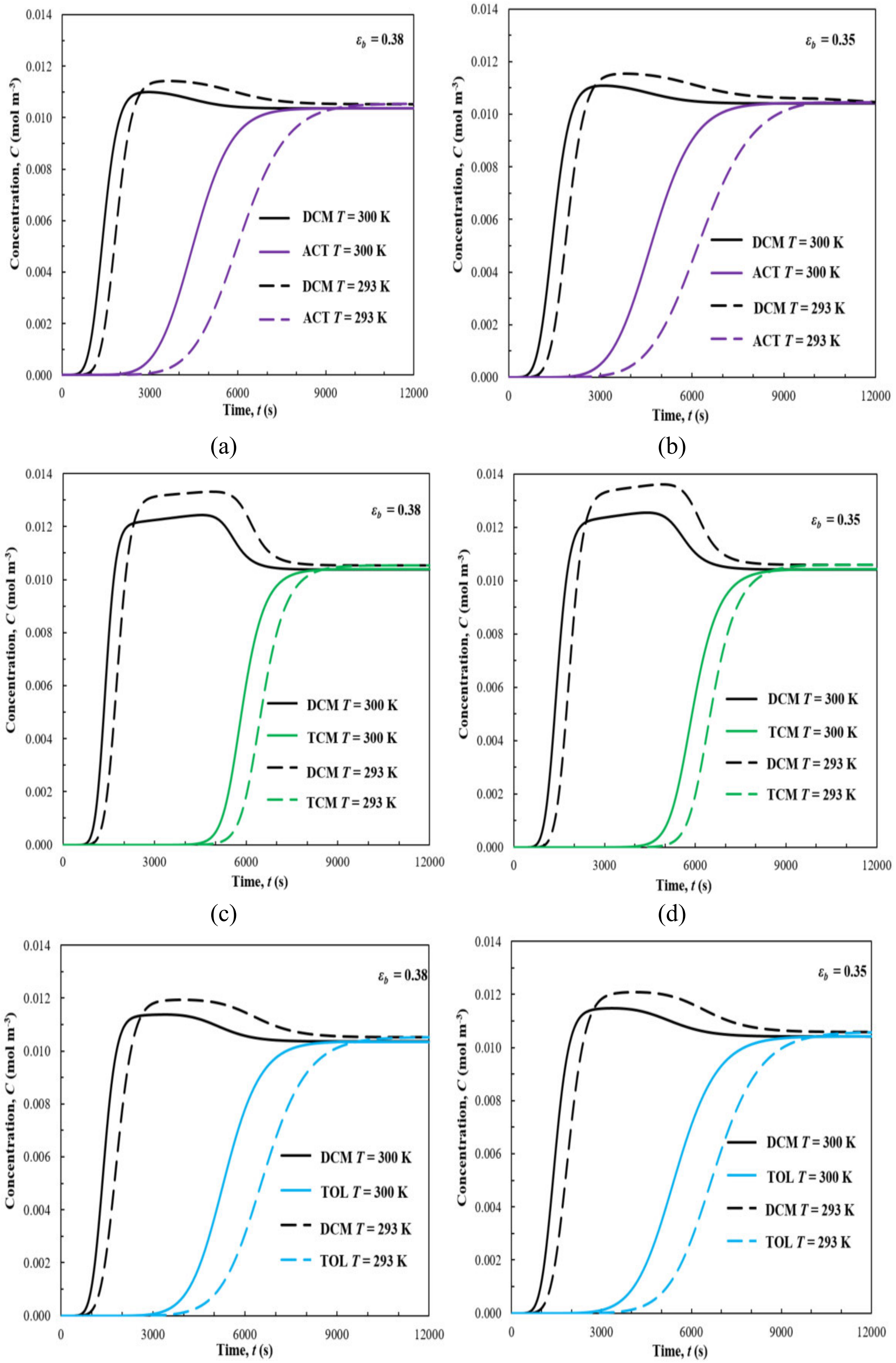

(a) (b)

(c) (d)

(e) (f)

Figure 15. Breakthrough comparison at T = 300, 293 K and ε_b = 0.38, 0.35 (bed outlet).

Regarding breakthrough duration, at $\varepsilon_b = 0.35$, DCM's is 11.71% longer at 293 K compared to 300 K, while toluene's is 23.02% longer at 293 K compared to 300 K.

Finally, breakthrough behaviour of the dichloromethane-toluene mixture shows slight differences with varying bulk bed porosity (Figure 15e vs. f). At 293 K and $\varepsilon_b = 0.35$ (Figure 15f), DCM and toluene reach breakthrough at t = 1168 s and t = 4766 s respectively, values which are 1.57% and 0.44% larger compared to the VOCs breakthrough onset times at bed porosity $\varepsilon_b = 0.38$ (Figure 15e) and 293 K. At 300 K and $\varepsilon_b = 0.35$ (Figure 15 f), the trend is reversed, with DCM's breakthrough onset being 3.05% earlier compared to 0.38, and toluene's 3.25% earlier compared to 0.38 at the same temperature (Figure 15e). Breakthrough duration at 293 K and $\varepsilon_b = 0.35$ is for DCM 6.20% longer and for toluene 2.42% longer compared to 0.38. At 300 K and $\varepsilon_b = 0.35$, the trend persists, with DCM's breakthrough duration being 14.97% longer and toluene's 14.77% longer compared to 0.38.

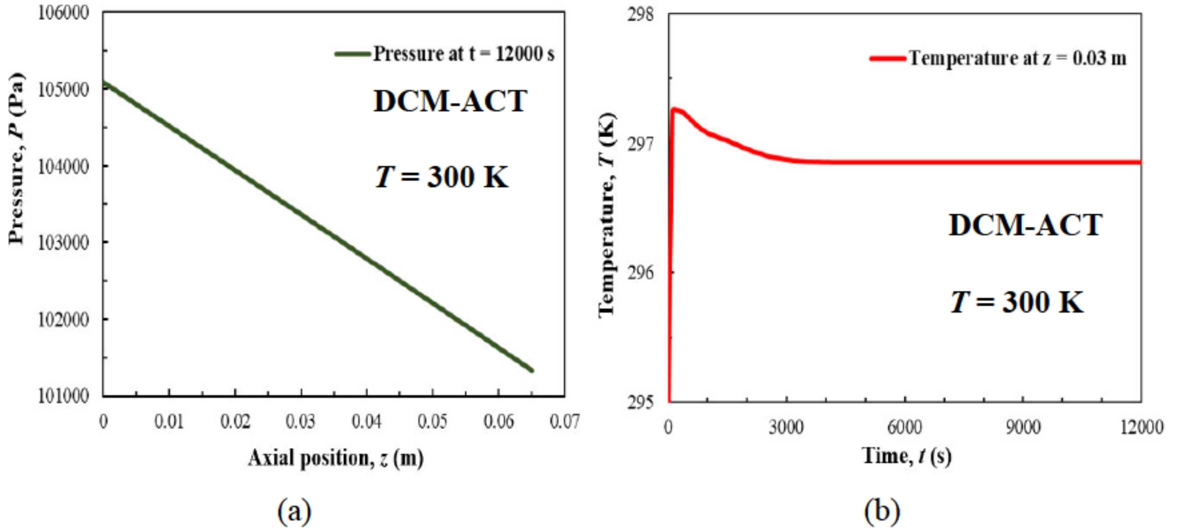

Figure 16. Pressure at t = 12000 s (a) and temperature at z = 0.03 m (b) for DCM-ACT (CS1).

Figure 16-18 introduce the pressure drop profile at t = 12000 s and the temperature profile at z = 0.03 m for the mixtures of DCM-ACT, DCM-TCM and DCM-TOL at T_{in} = 300 K and ε_b = 0.38 (CS1, CS5 and CS 9 of Table 10). For all cases presented, pressure drop, which follows Ergun's equation, is linear, as expected from the literature. Regarding the temperature profiles at z = 0.03 m, it is obvious that the temperature sharply rises when the gas mixture arrives, and immediately starts to drop as we approach the column outlet given the fact that the gas stream has an inlet temperature of 300 K and the column walls 295 K. The plateaus observed at the beginning of the graph are a result of adsorption exothermicity and correspond to adsorption taking place at this axial position (z = 0.03 m).

Figure 16 (a)-(b) correspond to the DCM-ACT mixture (CS1). The pressure drop a t = 12000 s is equal to 3755.6 Pa. In Figure 16 (b), the maximum temperature reached is 297.26 K.

Figure 17 (a) shows the pressure drop of DCM-TCM (CS5), which is equal to 3755.52 Pa, while the maximum temperature observed in Figure 17 (b) is 297.23 K.

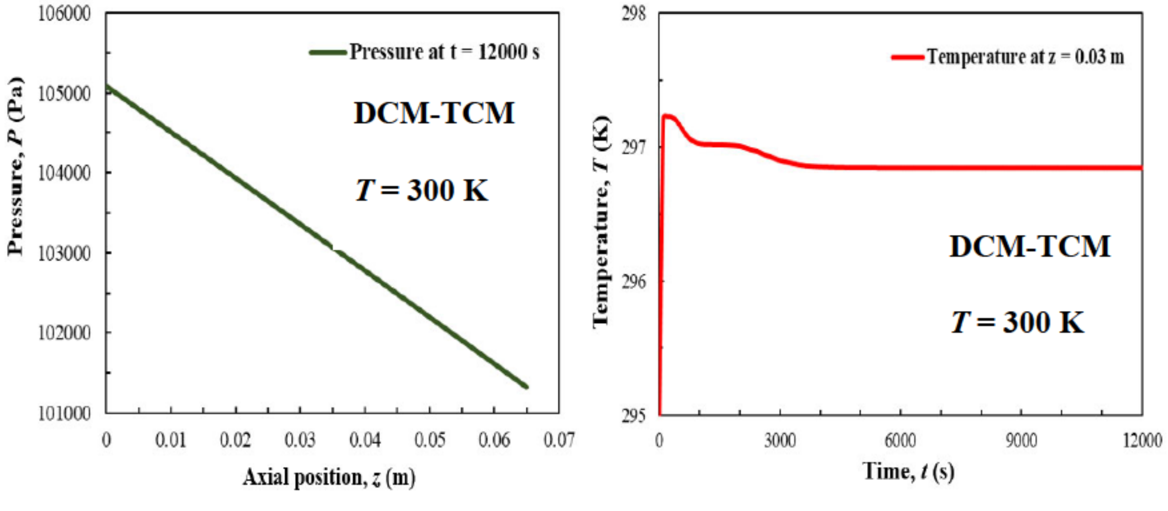

(a) (b)

Figure 17. Pressure at t = 12000 s (a) and temperature at z = 0.03 m (b) for DCM-TCM (CS5).

Finally, the DCM-TOL (CS9) pressure and temperature profiles are presented in Figure 18 (a-b). Pressure drop is 3758.40 Pa and T_{max} = 297.43 K.

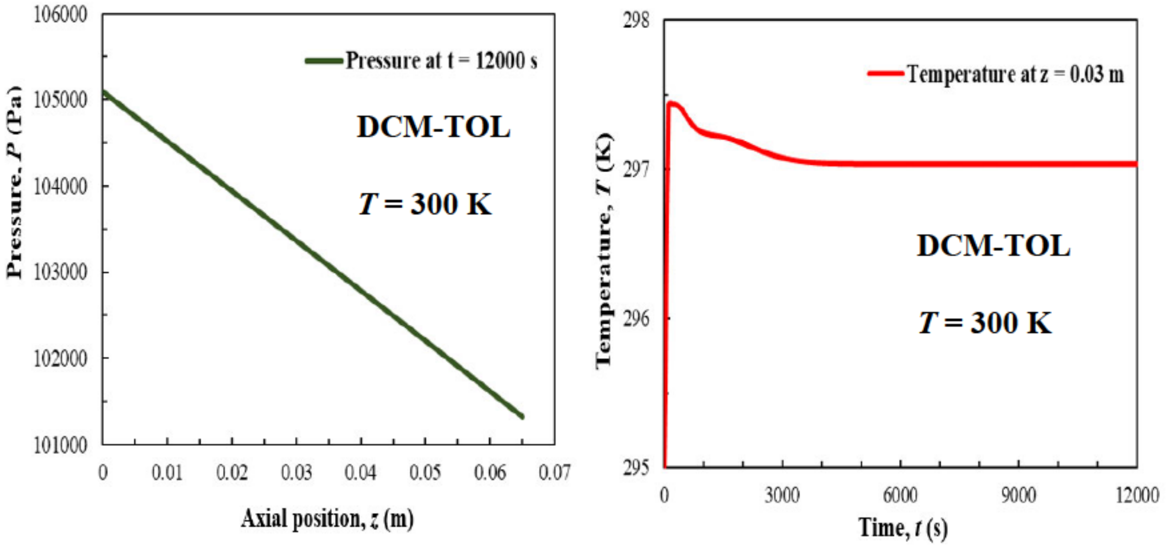

(e) (f)

Figure 18. Pressure at t = 12000 s (a) and temperature at z = 0.03 m (b) for DCM-TCM (CS9).

The case studies show that the pressure drops are about 3.76 kPa under the examined conditions in laboratory scale columns while the temperature profiles show only but small temperature plateaus. These effects however would be magnified under industrial conditions and thus require careful flow adjustments to ensure process safety and operational expenditure minimisation.

The adsorption of the binary mixtures of chloroform with acetone (Figure 19a), chloroform with toluene (Figure 19b) and toluene with acetone (Figure 19c) has also been investigated at 300 K and ε_b = 0.38. Amongst the three mixtures breakthrough characteristics, solvent-to-carbon affinity is correlated with molecular weight, with increasing molecular weight leading to higher affinity for the activated carbon. Therefore, chloroform (TCM) is the most strongly adsorbed mixture component, followed by toluene and then acetone. Chloroform (TCM), a solvent whose emissions are tightly regulated by the Scottish Environmental Protection Agency (SEPA), exits the column earlier when in a mixture with toluene, compared with one with acetone.

Harnessing simulation results to aid in production scheduling optimisation is essential to sustainable manufacturing (Akbar & Irohara, 2018, Giret et al., 2015). Understanding VOC breakthrough patterns paves the way to emissions reduction and designing production scheduling paradigms not only in a way that satisfies demand, but also respecting the environment by minimising impact. The combination of solvents in a mixture, their quantities and the operational parameters could be the key to sustainably improving existing underperforming processes. This in turn translates into less waste-intensive end-of-pipe solutions for emissions control and unit operations that meet environmental and societal demands.

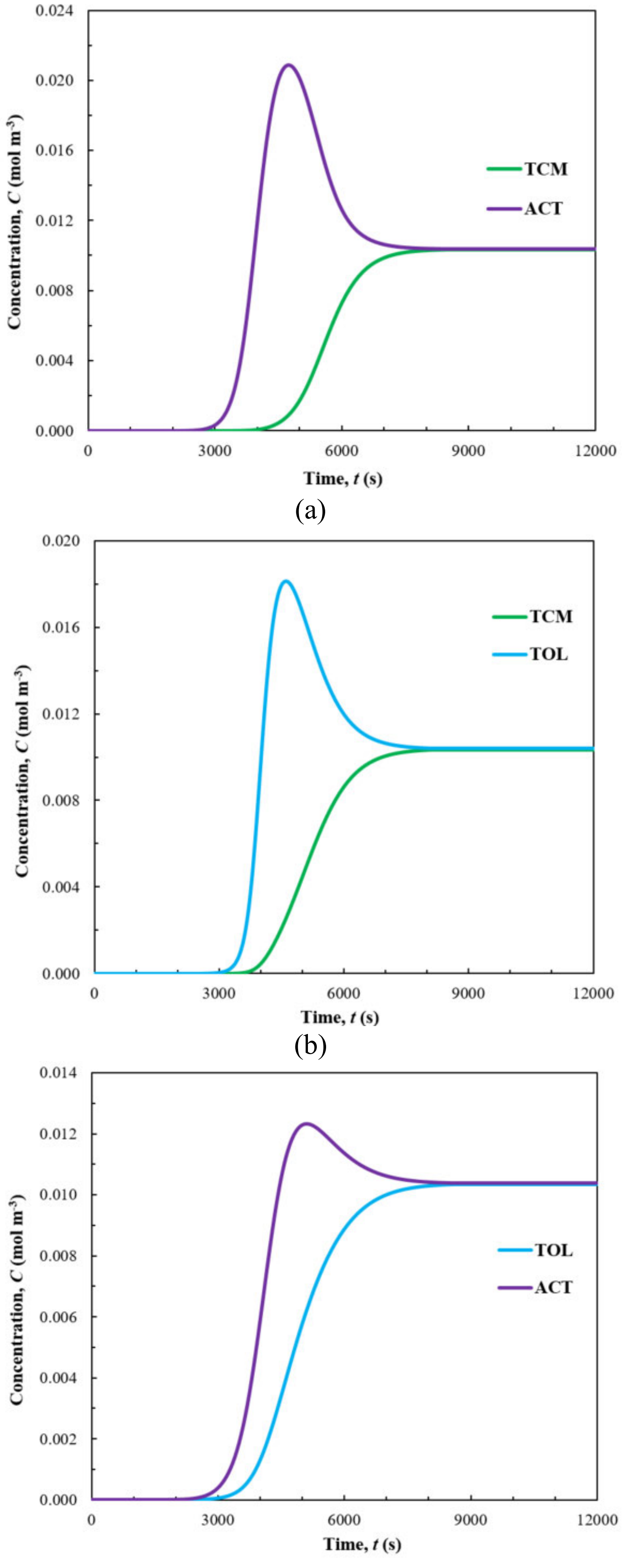

(a)

(b)

(c)

Figure 19. Binary mixture breakthrough characteristics at T = 300 K and $\varepsilon_b = 0.38$ (bed outlet).

Table 11 presents key breakthrough metrics of the dichloromethane-acetone system in the cases investigated. Two theoretically derived predictive formulas (Eqs. 32 and 34) can help us determine the shock breakthrough time (how long a single component's concentration front reaches the bed outlet) and the mean residence time (required for a single component to achieve breakthrough through a column). The breakthrough duration time, $t_{drt,i}$, is here defined as the time span between 5% breakthrough and 95% breakthrough, from dynamic simulations. Our simulation breakthrough completion times ($t_{95\%}$), from Figure 15 plots, are used to define and compute relative errors compared with each of the two foregoing metrics (Eq.36 and 37). Results for DCM exhibit notable discrepancies from both theoretical time metrics of Eq. 32 and 34; closer agreement is achieved for acetone. The relative error for the mean residence time has a consistently smaller discrepancy compared to the shock breakthrough time error. These discrepancies are attributed to the fact that both theoretical metrics (Eqs. 32 and 34) are derived for isothermal conditions and single-component Langmuir Isotherm adsorption, while our dynamic simulations concern the case of binary mixture (DCM-acetone) adsorption. However, theoretical predictive formulas clearly provide good order-of-magnitude estimates.

Table 11. Key time metrics of the dichloromethane-acetone mixture.

DCM-ACT									
	T (K)	ε_b	**t_{shock} (s) Eq. 34**	**μ_{RT} (s) Eq. 32**	**$t_{5\%}$ (s) Fig. 15 a-b**	**$t_{95\%}$ /$t_{105\%}$ (s) Fig. 15a-b**	**t_{drt} (s) Fig. 15 a-b**	**%R.E. t_{shock}**	**%R.E. μ_{RT}**
DCM	293	0.35	1,760	1,950	1,206	6,749	5,543	73.92	71.11
ACT			6,115	7,690	4,112	8,607	4,495	28.95	10.65
DCM	293	0.38	1,756	1,945	1,183	6,197	5,014	71.66	68.61
ACT			6,103	7,671	4,026	8,283	4,257	26.32	7.39
DCM	300	0.35	1,245	1,329	825	5,151	4,326	75.83	74.20
ACT			4,063	4,714	3,018	6,455	3,437	37.06	26.97
DCM	300	0.38	1,242	1,326	810	4,466	3,656	72.19	70.31
ACT			4,052	4,702	2,916	6,195	3,279	34.59	24.10

Table 12 presents the same breakthrough metrics for the dichloromethane-chloroform system. Dynamic simulation results (Figure 15 c-d) are again compared with mean residence and shock breakthrough time predictions (Eqs. 32 and 34) via relative error calculations (Eqs. 36-37). Similarly to both previous binary system cases, we clearly observe that error metrics for DCM are considerably high (but within the same order of magnitude) for both theoretical metrics.

Conversely, error metrics for chloroform display a more complicated landscape: the relative error for the shock breakthrough time is very promising and smaller than any other mixture (below 19% or better), implying the approximate predictive formula (Eq. 34) is quite suitable. Nevertheless, the mean residence time error is large - in fact larger than in both other systems. Also, relative errors are consistently negative, implying mean residence time overprediction. Once again, the discrepancies observed differ by metric as well as by component, and they can be attributed to the isothermal conditions and single-component Langmuir Isotherm adsorption which have been used in the literature for deriving Eqs. 32 and 24. Nevertheless, these formulas can offer useful fast industrial predictions without/before dynamic simulations.

Table 12. Key time metrics of the dichloromethane-chloroform mixture.

DCM-TCM									
	T (K)	ε_b	t_{shock} (s) Eq. 34	μ_{RT} (s) Eq. 32	$t_{5\%}$ (s) Fig. 15 c-d	$t_{95\%}$ /$t_{105\%}$ (s) Fig. 15 c-d	t_{drt} (s) Fig. 15 c-d	%R.E. t_{shock}	%R.E. μ_{RT}
DCM	293	0.35	1,751	1,949	1,240	7,896	6,656	77.82	75.32
TCM			6,764	19,651	5,537	7,865	2,328	14.00	-149.85
DCM	293	0.38	1,746	1,944	1,379	6,877	5,498	74.61	71.73
TCM			6,750	19,601	5,592	7,758	2,166	12.99	-152.66
DCM	300	0.35	1,232	1,480	912	6,655	5,743	81.49	77.76
TCM			5,788	14,442	4,871	7,115	2,244	18.65	-102.98
DCM	300	0.38	1,229	1,477	948	6,386	5,438	80.75	76.87
TCM			5,773	14,405	5,008	6,892	1,884	16.24	-109.01

Table 13 presents the key breakthrough metrics for the dichloromethane-toluene system. Dynamic simulation breakthrough times (Figure 15 e-f) are compared with mean residence and shock breakthrough time predictions (from Eqs. 32 and 34). Errors computed for DCM indicate clear discrepancy from both theoretical metrics, but acceptable and quite reliable predictions are clearly achieved for both the mean residence and the shock breakthrough times. For toluene, the mean residence time shows consistently smaller discrepancies compared to the shock breakthrough time. Once again, all (small and larger) discrepancies can be safely attributed to the isothermal conditions and single-component Langmuir Isotherm adsorption used for Eqs. 32 and 24, but the latter can provide good first estimates for industrial operation.

Table 13. Key time metrics of the dichloromethane-toluene mixture.

DCM-TOL									
	T (K)	ε_b	t_{shock} (s) Eq. 34	μ_{RT} (s) Eq. 32	$t_{5\%}$ (s) Fig. 15 e-f	$t_{95\%}$ /$t_{105\%}$ (s) Fig. 15 e-f	t_{drt} (s) Fig. 15 e-f	%R.E. t_{shock}	%R.E. μ_{RT}
DCM	293	0.35	1,765	1,950	1,168	7,494	6,326	76.45	73.98
TOL			6,757	10,441	4,766	8,881	4,115	23.92	-17.57
DCM	293	0.38	1,761	1,945	1,150	7,084	5,934	75.14	72.54
TOL			6,736	10,414	4,745	8,637	3,892	22.01	-20.57
DCM	300	0.35	1,242	1,329	858	6,443	5,585	80.73	79.37
TOL			5,023	6,752	3,694	7,333	3,639	31.50	7.92
DCM	300	0.38	1,239	1,326	885	5,634	4,749	78.01	76.46
TOL			5,008	6,735	3,818	6,950	3,132	27.94	3.09

Table 14 introduces a set of key breakthrough metrics (Eq. 32 and 34) for the systems of chloroform (TCM) with acetone, chloroform with toluene and toluene with acetone for T = 300 K and bulk bed porosity of 0.38 in all cases. Shock breakthrough time and mean residence time relative errors (Eq. 36 and 37) are compared to Figure 19 (a-c) plots characteristics. For each system, the mean residence time relative error shows larger differences between components compared to their shock breakthrough time relative errors. The mismatch between theoretically derived metrics and results could be attributed to the assumptions upon which the theoretical estimations rely.

Table 14. Key time metrics of the TCM-ACT, TCM-TOL and TOL-ACT systems.

	T (K)	ε_b	t_{shock} (s) Eq.34	μ_{RT} (s) Eq.32	$t_{5\%}$ (s) Fig.19	$t_{95\%}$ /$t_{105\%}$ (s) Fig. 19	t_{drt} (s) Fig.19	%R.E. t_{shock}	%R.E. μ_{RT}
TCM-ACT									
TCM	300	0.38	5,798	12,767	4,538	6,830	2,292	15.11	-86.93
ACT			4,052	4,702	3,097	6,881	3,784	41.11	31.67
TCM-TOL									
TCM	300	0.38	5,786	12,792	4,024	6,553	2,529	11.69	-95.21
TOL			5,018	6,749	3,626	6,944	3,318	27.74	2.81
TOL-ACT									
TOL	300	0.38	5,018	6,749	3,663	6,541	2,878	23.28	-3.18
ACT			4,071	4,711	3,080	6,893	3,813	40.94	31.66

5.3 Chapter Conclusions

Dynamic simulations of VOC adsorption for three industrially critical binary systems (namely mixtures of dichloromethane with acetone, toluene and chloroform) revealed that the VOC breakthrough order off the industrial activated carbon bed is: dichloromethane (DCM), then acetone, toluene and chloroform, i.e. trichloromethane (TCM). Our gPROMS® dynamic model is validated against experimental data by (Talmoudi et al., 2018).

Furthermore, the temperature sensitivity analysis via dynamic simulation revealed that higher operating temperatures lead to shorter breakthrough times, while the effect of bed porosity on binary mixture behaviour is more complex, and system-specific. Theoretical prediction formulas from the literature (mean residence and shock breakthrough times, Eqs. 32 and 34) have been compared to our gPROMS® dynamic simulation results, showing that the former (albeit originally derived for single-component, isothermal conditions) can provide quick, useful estimates to inform industrial operation, before committing resources in pursuit of the latter. Discrepancies of max. 30% are observed for all but one (DCM) components in most cases, implying the said Eqs. are extremely useful before undertaking detailed dynamic simulations. Dichloromethane (DCM), however, yields higher discrepancies (80%) in the said comparison, indicating that order-of-magnitude estimates are still possible, but dynamic simulation is very much justified for VOC capture intensification, especially as it is the first gas to break through.

Axial dispersion is accounted for in our model in Eqs. (2-3). Fixed bed adsorbers suffer from their tendency to develop axial dispersion, a phenomenon which reduces process efficiency (Ruthven, 1984) as it prevents adsorbates from diffusing into the adsorbent material due to axial mixing and therefore could have an influence on breakthrough completion time. Kinetic effects have been ignored in accordance with literature, but must be revisited in subsequent studies. Moreover, pressure drop is modelled via Ergun's Equation, considered preferable compared to other methods due to its direct dependence on bed voidage (Ruthven, 1984). Pressure directly affects the adsorption of contaminants on activated carbon and can increase the time needed for adsorbent saturation (thus breakthrough completion), especially in larger beds. Numerical dispersion is another potential cause of discrepancies: when numerical discretization is applied to analyse physical processes, even if many of them are modelled by nondispersive PDEs, typically a small dispersion emerges in results (Griffiths, 2016).

Chapter 6

Validation & Heat Transfer Case Study on Binary Mixture

This chapter first presents the validation of our non isothermal and multicomponent adsorption model for the binary mixture of heptane-decane against published experimental data. Then the effect of flowrate, mixture composition and column length is investigated. Furthermore, the effect of different heat transfer boundary conditions (isothermal vs adiabatic) is explored.

The results presented in this chapter have also been published in the literature (Tzanakopoulou et al., 2022. *Comput.Aided Chem.Eng.*, **51**, 331-336); details can be found in Appendix B.

6.1 Case Studies of HEP-DEC

The developed model is used to simulate key cases of multicomponent VOC adsorption under varying heat transfer scenarios (adiabatic and non-adiabatic). The set of PDEs is solved using orthogonal collocation on finite elements in gPROMS® Process 2.0.0. The adsorption of binary heptane – decane mixture, with air as the carrier, has been examined on beaded activated carbon (Tefera et al., 2014) under both isothermal and adiabatic BC (C.S.0), different flowrate, composition, bed length (C.S. 1–3). The system viscosities are computed from Wilke's equation for binary mixtures, while densities are determined through pure component data via mixing rules (T = 300 K and P = 1 atm) (NIST, 2021). Air is assumed as a binary mixture (N_2:O_2 = 79:21 % v/v). In all cases considered in this chapter the bed area remains constant at 0.000181 m^2. Table 15-Table 17 present the values for the calculation of the axial dispersion coefficients, energy balance parameters and main simulation parameters respectively. The average particle size is 0.75 mm, 99% by mass between 0.60 and 0.84 mm (Tefera et al., 2013, Lashaki et al., 2012).

Table 15. Parameters for heptane-decane scenarios.

Case Study	ρ (kg m^{-3})	μ (Pa s^{-1})	*Re*	*Sc*	$D_{AB,i}$ (m^2 s^{-1})	*R* (m)
0	1.52	$2.19 \cdot 10^{-5}$	47.64	1.96	$7.34 \cdot 10^{-6}$	0.0076
				2.37	$6.08 \cdot 10^{-6}$	0.0076
1	1.52	$2.19 \cdot 10^{-5}$	23.82	1.96	$7.34 \cdot 10^{-6}$	0.0076
				2.37	$6.08 \cdot 10^{-6}$	0.0076
2	1.53	$2.20 \cdot 10^{-5}$	47.74	1.96	$7.34 \cdot 10^{-6}$	0.0076
				2.36	$6.08 \cdot 10^{-6}$	0.0076
3	1.52	$2.19 \cdot 10^{-5}$	47.64	1.96	$7.34 \cdot 10^{-6}$	0.0076
				2.37	$6.08 \cdot 10^{-6}$	0.0076

Table 16. Thermal properties parameters for heptane-decane mixture case studies.

Case Study	k_{ez} (W m^{-2} K^{-1})	T_{in} (K)	h_o (W m^{-2} K^{-1})	k_p (W m^{-1} K^{-1})	C_{pp} (J kg^{-1} K^{-1})	Pr	x (m)	ρ_b (kg m^{-3})
0	0.85	300	43.57	0.17	706.7	1.1	0.001	606
1	0.46	300	25.07	0.17	706.7	1.1	0.001	606
2	0.86	300	43.65	0.17	706.7	1.1	0.001	606
3	0.85	300	43.57	0.17	706.7	1.1	0.001	606

Table 17. Main simulation parameters for heptane-decane mixture case studies.

Case Study	$D_{z,i}$ (m^2 s^{-1})	T_w (K)	L (m)	x_{VOC}	V_s (m s^{-1})	q_m (mol kg^{-1})	ε	k_{LDF} (s^{-1})	b_0 (m^3 mol^{-1})	Figure 20
CS0	0.00129	295	0.065	0.000250	0.914	3.69	0.38	19.2	$5.02 \cdot 10^{-13}$	(a)-(d)
	0.00122			0.000250		3.16		16.1	$8.65 \cdot 10^{-14}$	
CS1	0.00083	295	0.065	0.000250	0.457	3.69	0.38	19.2	$5.02 \cdot 10^{-13}$	(e)-(f)
	0.00077			0.000250		3.16		16.1	$8.65 \cdot 10^{-14}$	
CS2	0.00129	295	0.065	0.000125	0.914	3.69	0.38	19.2	$5.02 \cdot 10^{-13}$	(g)
	0.00122			0.000375		3.16		16.1	$8.65 \cdot 10^{-14}$	
CS3	0.00129	295	0.080	0.000250	0.914	3.69	0.38	19.4	$5.02 \cdot 10^{-13}$	(h)
	0.00122			0.000250		3.16		16.3	$8.65 \cdot 10^{-14}$	

6.2 gPROMS® Dynamic Simulation Results

Breakthrough curves, temperature and pressure variations of the examined systems are shown in Figure 20. The model was succesfully validated vs. published experimental breakthrough curves, Figure 20 (a), which dictated our inputs (CS0) in Figure 20 (a)-(d) (Tefera et al., 2014). Figure 20(a) shows a breakthrough onset predicted with 13% rel. error for heptane and -3% for decane; the rel. error for $C_{max}(z = L, t)$ is -22% for heptane and 0% for decane. Discrepancies could be attributed to the limitations of the 1-D model. Subsequently, we consider three case studies (CS 1-3) of different flowrate (CS1), composition (CS2) and bed length (CS3), depicted in Figure 20 (e)-(h). Adiabatic BCs of the base case, Figure 20(d), clearly induce a heat buildup within the bed, compared to the isothermal BCs of Figure 20 (c). A linear ΔP profile is seen in Figure 20 (b), consistent with reported trends (Tefera et al., 2013).

Figure 20(e) presents the heptane-decane binary mixture behaviour at a flowrate 50% smaller than the base case (CS1). The order of affinity strength remains (decane > heptane), but the onset of breakthrough occurs later and the duration is longer compared to the base case. The

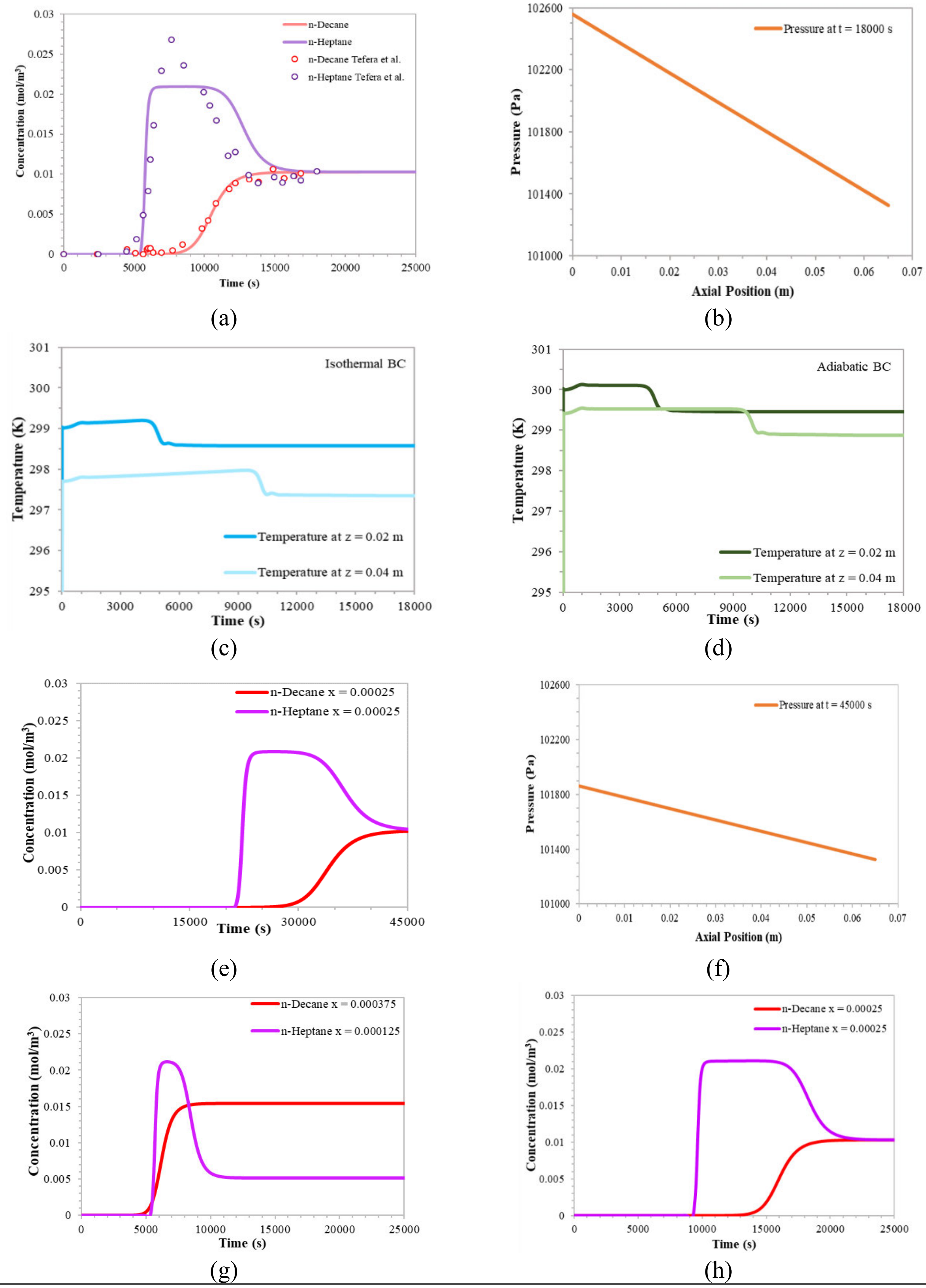

(a) (b)

(c) (d)

(e) (f)

(g) (h)

Figure 20. Model validation (a) and operation profiles (b)-(d) vs case studies (e)-(h).

lower flowrate is directly associated with a 56% pressure drop reduction presented in Figure 20 (f), i.e. roughly half the pressure drop observed in Figure 20 (b) for CS0.

The effect of mixture composition is explored next where decane concentration is 3 times larger than that heptane (CS2). While displacement of heptane persists, Figure 20 (g) reveals a later breakthrough onset of heptane as well as an earlier breakthrough onset of decane, combined with a clearly shorter duration for both VOCs compared to the base case (CS0). Finally, Figure 20 (h) presents the effect of a 23% larger bed length (CS3). Decane displaces heptane, but breakthrough onset occurs later and slower due to the increased bed size.

6.3 Chapter Conclusions

In this chapter, a comparison between adiabatic vs non adiabatic heat transfer conditions takes place. To simulate adiabatic conditions, the energy balance (Equation 16) of the model presented in Chapter 4 loses the final term which corresponds to heat losses to the environment. Differences between isothermal and adiabatic BC are critical considering the exothermic nature of the process. The simulations revealed roll–up of heptane under varying flowrate, composition and bed length, with decane demonstrating preferential adsorption in all cases considered, possibly due to its larger molecular weight.. A decrease in the flowrate resulted in a later onset and larger duration of breakthrough and reduction of pressure drop compared to the base case, while the mixture composition caused an almost simultaneous onset & faster duration of breakthrough compared to the base case. In view of industrial applications, a larger bed length investigation resulted in a later onset and longer duration of breakthrough. Reliable modelling of multicomponent, nonisothermal VOC adsorption paves the way for technoeconomic optimisation efforts.

Chapter 7

Validation of Binary Adsorption under Limited Information

This chapter demonstrates the validation of our adsorption model against published experimental data of the binary mixtures of acetone-toluene, benzene-toluene across three concentration pairs and a set of different porosities and corresponding bed lengths. This investigation was prompted by the lack of bed length and porosity reporting in the experimental publication.

The results presented in this chapter have also been published in the literature (Tzanakopoulou et al., 2024. *Ind. Eng. Chem. Res.*, 63, **16**, 7281-7299); details can be found in Appendix B.

7.1 Main Model Parameters & Case Studies

The developed model was employed to investigate the adsorption characteristics of binary VOC mixtures (with air as the carrier gas) as published in the work of (Lee et al., 2008). The model examines specifically the mixtures of Acetone-Toluene and Benzene-Toluene in an initially clean, coconut based activated carbon fixed bed at three different concentration pairs each. As the calculation of Langmuir Isotherm parameters was outside the scope of the original publication by (Lee et al., 2008), in this PhD thesis, the necessary Langmuir Isotherm parameter values were taken from (Tefera et al., 2013) for all components, shown on Table 18:

Table 18. Langmuir Isotherm parameters used in this PhD thesis.

BINARY	$q_{m,i}$ (mol kg^{-1})	b_0 (m^3 mol^{-1})	$\Delta H_{ad,i}$ (J mol^{-1})	Lit. Ref.
ACT-TOL	7.06	$1.96\cdot10^{-8}$	51,125	(Tefera et al., 2013)
	4.56	$1.27\cdot10^{-8}$	59,722	(Tefera et al., 2013)
BEN-TOL	5.38	$1.13\cdot10^{-8}$	56,027	(Tefera et al., 2013)
	4.56	$1.27\cdot10^{-8}$	59,722	(Tefera et al., 2013)

In order to perform the model validation for the published experimental data by (Lee et al., 2008) on coconut-based activated carbon and given that the bed porosity and bed density were not reported, an initial estimation was performed by assuming the value of 528.61 kg m^{-3} based on commercial coconut-based activated carbon specifications by (Servapure, 2023) over a range of typical bed porosity fractions (ε_b = 0.38-0.45). Determination of the column length was performed based on the activated carbon mass reported by (Lee et al., 2008), by solving the equation system (Eq. 38-39):

$$m_{AC} = N_{pellets} \frac{4}{3} \pi R_p^3 \rho_p \tag{38}$$

$$N_{pellets} = \frac{(1 - \varepsilon_b)(\pi R^2 L)}{\frac{4}{3} \pi R_p^3} \tag{39}$$

The results of the estimated column length based on different bed porosities and a coconut based activated carbon density are presented in Table 19:

Table 19. Column structural properties calculation results.

R_p (m)	R (m)	ε_b	ρ_b (kg m^{-3})	ρ_p (kg m^{-3})	m_{ac} (kg)	L (m)
0.001	0.008	0.38	528.61	852.60	0.002	0.019
0.001	0.008	0.40	528.61	881.02	0.002	0.019
0.001	0.008	0.42	528.61	911.40	0.002	0.020
0.001	0.008	0.45	528.61	961.11	0.002	0.021

In all cases considered in this chapter the bed area remains constant at 0.000201 m^2. The set of partial differential equations (PDEs) is solved using second order orthogonal collocation on finite elements with 50 discretisation points in the gPROMS® Process 2.0.0 software suite. For all cases considered in this PhD thesis onwards, the DASolver SRADAU is employed, which uses a variable time step fully implicit Runge-Kutta method, instead of DAEBDF, due to its efficiency in solving highly dispersive PDEs with steep gradients and reducing the computational time from hours to minutes.

The viscosities are computed from Wilke's equation, while densities are determined through pure component data via mixing rules (National Institute of Standards and Technology (NIST), 2023). Each of the six binary mixtures is solved for four different cases corresponding to four different bed porosities (ε_b = 0.38, 0.40, 0.42 and 0.45) and their corresponding bed lengths as resulting from calculations on Table 19. The main simulation parameters for all Acetone-Toluene cases examined in this PhD thesis are in Table 20:

Table 20. Model parameter values for the acetone-toluene binary simulations.

System	$C_{0,i}$ (ppm)	$D_{z,i}$ ($m^2\ s^{-1}$)	T_{in} (K)	L (m)	V_s ($m\ s^{-1}$)	ε_b	k_{LDF} (s^{-1})	Fig.
ACT-TOL	160	$1.43\cdot10^{-3}$	293.15	0.019	0.332	0.38	$9.91\cdot10^{-6}$	21-23
	40	$1.30\cdot10^{-3}$					$5.52\cdot10^{-7}$	
ACT-TOL	160	$1.35\cdot10^{-3}$	293.15	0.019	0.332	0.40	$1.09\cdot10^{-5}$	21-23
	40	$1.23\cdot10^{-3}$					$6.09\cdot10^{-7}$	
ACT-TOL	160	$1.29\cdot10^{-3}$	293.15	0.020	0.332	0.42	$1.21\cdot10^{-5}$	21-23
	40	$1.17\cdot10^{-3}$					$6.74\cdot10^{-7}$	
ACT-TOL	160	$1.20\cdot10^{-3}$	293.15	0.021	0.332	0.45	$1.42\cdot10^{-5}$	21-23
	40	$1.09\cdot10^{-3}$					$7.91\cdot10^{-7}$	
ACT-TOL	100	$1.43\cdot10^{-3}$	293.15	0.019	0.332	0.38	$1.62\cdot10^{-5}$	21-23
	100	$1.30\cdot10^{-3}$					$9.02\cdot10^{-7}$	
ACT-TOL	100	$1.35\cdot10^{-3}$	293.15	0.019	0.332	0.40	$1.79\cdot10^{-5}$	21-23
	100	$1.23\cdot10^{-3}$					$9.95\cdot10^{-7}$	
ACT-TOL	100	$1.29\cdot10^{-3}$	293.15	0.020	0.332	0.42	$1.98\cdot10^{-5}$	21-23
	100	$1.17\cdot10^{-3}$					$1.10\cdot10^{-6}$	
ACT-TOL	100	$1.20\cdot10^{-3}$	293.15	0.021	0.332	0.45	$2.32\cdot10^{-5}$	21-23
	100	$1.09\cdot10^{-3}$					$1.29\cdot10^{-6}$	
ACT-TOL	40	$1.43\cdot10^{-3}$	293.15	0.019	0.332	0.38	$2.25\cdot10^{-5}$	21-23
	160	$1.30\cdot10^{-3}$					$1.25\cdot10^{-6}$	
ACT-TOL	40	$1.35\cdot10^{-3}$	293.15	0.019	0.332	0.40	$2.48\cdot10^{-5}$	21-23
	160	$1.23\cdot10^{-3}$					$1.38\cdot10^{-6}$	
ACT-TOL	40	$1.29\cdot10^{-3}$	293.15	0.020	0.332	0.42	$2.74\cdot10^{-5}$	21-23
	160	$1.17\cdot10^{-3}$					$1.53\cdot10^{-6}$	
ACT-TOL	40	$1.20\cdot10^{-3}$	293.15	0.021	0.332	0.45	$3.22\cdot10^{-5}$	21-23
	160	$1.09\cdot10^{-3}$					$1.79\cdot10^{-6}$	

Table 21 introduces the main simulation parameters for all Benzene-Toluene mixtures examined in this PhD thesis:

Table 21. Main parameter values for the benzene-toluene binary simulations.

System	$C_{0,i}$ (ppm)	$D_{z,i}$ ($m^2\ s^{-1}$)	T_{in} (K)	L (m)	V_s ($m\ s^{-1}$)	ε_b	k_{LDF} (s^{-1})	Fig.
BEN-TOL	160	$1.34 \cdot 10^{-3}$	293.15	0.019	0.332	0.38	$3.29 \cdot 10^{-6}$	21-23
	40	$1.30 \cdot 10^{-3}$					$6.99 \cdot 10^{-7}$	
BEN-TOL	160	$1.27 \cdot 10^{-3}$	293.15	0.019	0.332	0.40	$3.63 \cdot 10^{-6}$	21-23
	40	$1.23 \cdot 10^{-3}$					$7.71 \cdot 10^{-7}$	
BEN-TOL	160	$1.21 \cdot 10^{-3}$	293.15	0.020	0.332	0.42	$4.02 \cdot 10^{-6}$	21-23
	40	$1.17 \cdot 10^{-3}$					$8.53 \cdot 10^{-7}$	
BEN-TOL	160	$1.13 \cdot 10^{-3}$	293.15	0.021	0.332	0.45	$4.72 \cdot 10^{-6}$	21-23
	40	$1.09 \cdot 10^{-3}$					$1.00 \cdot 10^{-6}$	
BEN-TOL	100	$1.34 \cdot 10^{-3}$	293.15	0.019	0.332	0.38	$4.68 \cdot 10^{-6}$	21-23
	100	$1.30 \cdot 10^{-3}$					$9.93 \cdot 10^{-7}$	
BEN-TOL	100	$1.27 \cdot 10^{-3}$	293.15	0.019	0.332	0.40	$5.17 \cdot 10^{-6}$	21-23
	100	$1.23 \cdot 10^{-3}$					$1.10 \cdot 10^{-6}$	
BEN-TOL	100	$1.21 \cdot 10^{-3}$	293.15	0.020	0.332	0.42	$5.72 \cdot 10^{-6}$	21-23
	100	$1.17 \cdot 10^{-3}$					$1.21 \cdot 10^{-6}$	
BEN-TOL	100	$1.13 \cdot 10^{-3}$	293.15	0.021	0.332	0.45	$6.71 \cdot 10^{-6}$	21-23
	100	$1.09 \cdot 10^{-3}$					$1.42 \cdot 10^{-6}$	
BEN-TOL	40	$1.34 \cdot 10^{-3}$	293.15	0.019	0.332	0.38	$6.07 \cdot 10^{-6}$	21-23
	160	$1.30 \cdot 10^{-3}$					$1.29 \cdot 10^{-6}$	
BEN-TOL	40	$1.27 \cdot 10^{-3}$	293.15	0.019	0.332	0.40	$6.70 \cdot 10^{-6}$	21-23
	160	$1.23 \cdot 10^{-3}$					$1.42 \cdot 10^{-6}$	
BEN-TOL	40	$1.21 \cdot 10^{-3}$	293.15	0.020	0.332	0.42	$7.42 \cdot 10^{-6}$	21-23
	160	$1.17 \cdot 10^{-3}$					$1.57 \cdot 10^{-6}$	
BEN-TOL	40	$1.13 \cdot 10^{-3}$	293.15	0.021	0.332	0.45	$8.70 \cdot 10^{-6}$	21-23
	160	$1.09 \cdot 10^{-3}$					$1.84 \cdot 10^{-6}$	

Table 22 summarizes the main structural (column and adsorbent) and thermal parameter values of the Acetone-Toluene simulations. Values for C_{pp} and k_w are taken from (Tefera et al., 2013) for coconut-based activated carbon.

Table 22. Main structural and thermal parameter values of the systems.

System	$C_{0,i}$ (ppm)	D (m)	T_w (K)	ε_p	d_p (m)	C_{pp} (J kg^{-1} K^{-1})	C_{pg} (J kg^{-1} K^{-1})	k_{ez} (W m^{-1} K^{-1})	h_o (W m^{-2} K^{-1})	h_{int} (W m^{-2} K^{-1})	k_w (W m^{-1} K^{-1})	x (m)	Fig.
ACT-TOL	160 40	0.016	293.15	0.52	0.002	706.7	1,013	0.66	31.54	31.60	14.2	0.001	21-23
ACT-TOL	160 40	0.016	293.15	0.54	0.002	706.7	1,013	0.66	31.54	31.60	14.2	0.001	21-23
ACT-TOL	160 40	0.016	293.15	0.56	0.002	706.7	1,013	0.66	31.54	31.60	14.2	0.001	21-23
ACT-TOL	160 40	0.016	293.15	0.59	0.002	706.7	1,013	0.66	31.54	31.60	14.2	0.001	21-23
ACT-TOL	100 100	0.016	293.15	0.52	0.002	706.7	1,013	0.66	31.56	31.63	14.2	0.001	21-23
ACT-TOL	100 100	0.016	293.15	0.54	0.002	706.7	1,013	0.66	31.56	31.63	14.2	0.001	21-23
ACT-TOL	100 100	0.016	293.15	0.56	0.002	706.7	1,013	0.66	31.56	31.63	14.2	0.001	21-23
ACT-TOL	100	0.016	293.15	0.59	0.002	706.7	1,013	0.66	31.56	31.63	14.2	0.001	21-23

	100												
ACT-TOL	$\frac{40}{160}$	0.016	293.15	0.52	0.002	706.7	1,013	0.66	31.58	31.65	14.2	0.001	21-23
ACT-TOL	$\frac{40}{160}$	0.016	293.15	0.54	0.002	706.7	1,013	0.66	31.58	31.65	14.2	0.001	21-23
ACT-TOL	$\frac{40}{160}$	0.016	293.15	0.56	0.002	706.7	1,013	0.66	31.58	31.65	14.2	0.001	21-23
ACT-TOL	$\frac{40}{160}$	0.016	293.15	0.59	0.002	706.7	1,013	0.66	31.58	31.65	14.2	0.001	21-23

Table 23 introduces the thermal and column structural properties for the benzene-toluene mixture cases. Values for C_{pp} and k_w are taken from (Tefera et al., 2013) for coconut based activated carbon. The average particle size value is based on the statement at (Lee et al., 2008) that the particle size is 8-12 mesh.

Table 23. Thermal and structural properties for benzene-toluene binary simulations.

System	$C_{0,i}$ (ppm)	D (m)	T_w (K)	ε_p	d_p (m)	C_{pp} (J kg^{-1} K^{-1})	C_{pg} (J kg^{-1} K^{-1})	k_{ez} (W m^{-1} K^{-1})	h_o (W m^{-2} K^{-1})	h_{int} (W m^{-2} K^{-1})	k_w (W m^{-1} K^{-1})	x (m)	Fig.
BEN-TOL	$\frac{160}{40}$	0.016	293.15	0.52	0.002	706.7	1,013	0.66	31.56	31.63	14.2	0.001	21-23
BEN-TOL	$\frac{160}{40}$	0.016	293.15	0.54	0.002	706.7	1,013	0.66	31.56	31.63	14.2	0.001	21-23
BEN-TOL	$\frac{160}{40}$	0.016	293.15	0.56	0.002	706.7	1,013	0.66	31.56	31.63	14.2	0.001	21-23
BEN-TOL	$\frac{160}{40}$	0.016	293.15	0.59	0.002	706.7	1,013	0.66	31.56	31.63	14.2	0.001	21-23
BEN-TOL	$\frac{100}{100}$	0.016	293.15	0.52	0.002	706.7	1,013	0.66	31.56	31.63	14.2	0.001	21-23
BEN-TOL	$\frac{100}{100}$	0.016	293.15	0.54	0.002	706.7	1,013	0.66	31.56	31.63	14.2	0.001	21-23
BEN-TOL	100	0.016	293.15	0.56	0.002	706.7	1,013	0.66	31.56	31.63	14.2	0.001	21-23

	100												
BEN-TOL	$\frac{100}{100}$	0.016	293.15	0.59	0.002	706.7	1,013	0.66	31.56	31.63	14.2	0.001	21-23
BEN-TOL	$\frac{40}{160}$	0.016	293.15	0.52	0.002	706.7	1,013	0.66	31.60	31.66	14.2	0.001	21-23
BEN-TOL	$\frac{40}{160}$	0.016	293.15	0.54	0.002	706.7	1,013	0.66	31.60	31.66	14.2	0.001	21-23
BEN-TOL	$\frac{40}{160}$	0.016	293.15	0.56	0.002	706.7	1,013	0.66	31.60	31.66	14.2	0.001	21-23
BEN-TOL	$\frac{40}{160}$	0.016	293.15	0.59	0.002	706.7	1,013	0.66	31.60	31.66	14.2	0.001	21-23

The average particle size value is based on the statement at (Lee et al., 2008) that the particle size is 8-12 mesh.

7.2 Dynamic Simulation (gPROMS®) Results

The developed model was validated against published experimental data from (Lee et al., 2008) for the adsorption of trace binary mixtures of Acetone-Toluene (ACT-TOL) and Benzene-Toluene (BEN-TOL) on coconut based activated carbon for three concentration pairs each (160-40 ppm, 100-100 ppm, 40-160 ppm) using air as the non-adsorbing carrier gas. Each of the six binaries was simulated for four different bed porosity fractions (ε_b = 0.38, 0.40, 0.42 and 0.45) and theirs corresponding bed lengths as calculated by Eq. (38-39) in Table 19.

Breakthrough curve (concentration at the column exit vs time) plots of the acetone-toluene and benzene-toluene binary mixtures are presented on Figure 21, while Figure 22-Figure 23 introduce the simulation results for temperature evolution in the middle of the adsorption columns and pressure drops respectively. Table 24-Table 25 show key breakthrough time metrics.

Table 24. Key simulation results and time metrics for the acetone-toluene mixtures.

	ε_b	C_0 (ppm)	$t_{5\%}$ (s)	$t_{105\%}$ / $t_{95\%}$ (s)	t_{drt} (s)	T_{max} (K)	ΔP (Pa)	Fig. 21-23
ACT	0.38	160	2042	9515	7472	293.4275	54.86	a
TOL		40	20413	55739	35326			
ACT	0.40	160	2084	9465	7381	293.4266	44.71	
TOL		40	20930	55099	34169			
ACT	0.42	160	2282	9788	7506	293.4260	38.59	
TOL		40	23060	56675	33615			
ACT	0.45	160	2507	10057	7550	293.4252	30.38	
TOL		40	25456	57967	32512			
ACT	0.38	100	2142	6748	4606	293.4279	54.86	c
TOL		100	16353	29638	13284			
ACT	0.40	100	2178	6748	4571	293.4254	44.71	
TOL		100	16623	29297	12674			
ACT	0.42	100	2371	7068	4697	293.4235	38.59	
TOL		100	18033	30197	12164			
ACT	0.45	100	2592	7383	4791	293.4211	30.38	
TOL		100	19555	30945	11390			
ACT	0.38	40	2190	6021	3831	293.4386	54.86	e
TOL		160	13055	19984	6929			
ACT	0.40	40	2219	6036	3817	293.4374	44.71	
TOL		160	13216	19766	6550			
ACT	0.42	40	2413	6360	3947	293.4372	38.59	
TOL		160	14217	20424	6207			
ACT	0.45	40	2623	6683	4060	293.4369	30.38	
TOL		160	15274	21010	5735			

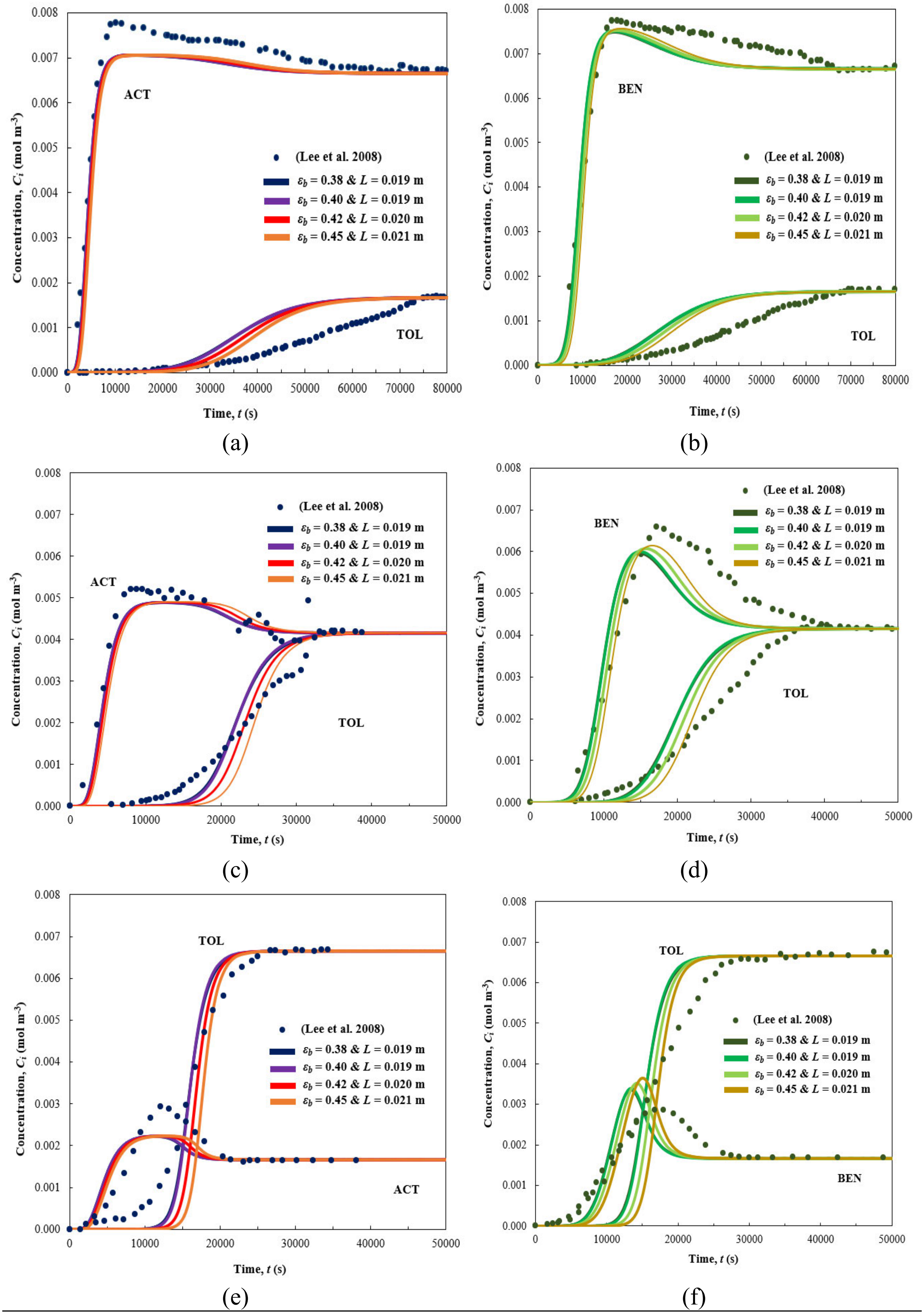

(a) (b) (c) (d) (e) (f)

Figure 21. Breakthrough curves of (a-b: 160-40 ppm), (c-d: 100-100 ppm), (e-f: 40-160 ppm).

Specifically, breakthrough onset time ($t_{5\%}$) is estimated as the time needed for the outlet concentration to reach 5% of the final concentration. Breakthrough completion time is here regarded as the time needed for the outlet concentration to reach 95% of the final concentration for the strongly adsorbing component ($t_{95\%}$), and 105% of the final concentration for the weakly adsorbing component ($t_{105\%}$). Finally, breakthrough duration (t_{drt}) is the difference between breakthrough completion and onset times.

Figure 21 (a) presents the mixture of acetone-toluene at inlet concentration of 160-40 ppm respectively. Our model accurately captures the breakthrough onset and final concentrations for both components. For acetone, the slope of the breakthrough curve is successfully captured, whereas a slight mismatch is observed for toluene's after breakthrough onset. The predicted maximum overshoot concentration observed at the column outlet for acetone is slightly underpredicted by the model compared to experimental data. Specifically, the difference between the experimental maximum outlet concentration for acetone and the simulation results is below 9.5% for all four potential porosities and corresponding bed lengths. For increasing bed porosity and thus column lengths, the breakthrough onset comes later for both components. For $\varepsilon_b = 0.38$, breakthrough onset time for acetone comes at $t_{5\%} = 2042$ s, while for toluene at $t_{5\%} = 20413$ s. Breakthrough completion for acetone takes place at $t_{105\%} = 9515$ s and for toluene, at $t_{95\%} = 55739$ s.

The results for the mixture of acetone-toluene in 100 ppm of inlet concentration each can be found Figure 21 (c). Good agreement is observed for both acetone and toluene, while a steeper slope for the sigmoidal concentration curve of toluene is predicted compared to experimental data. The maximum acetone concentration predicted at column exit is within a remarkable 6% of relative error compared to experimental results for all four porosities and corresponding bed lengths. With increasing bed porosity, a longer column length is calculated (L = 0.019-0.021 m), and thus the breakthrough onset metrics for both components increase, with increasing bed porosity. Comparing the $\varepsilon_b = 0.38$ case of 100-100 ppm and 160-40 ppm, it is noted that the breakthrough onset time for acetone increases for the 100 ppm inlet concentration by ≈ 5 %, while for toluene it deceases by ≈ 20%. Breakthrough completion times for the same set of comparisons, decreased by 29 % for acetone and 47 % for toluene. Thus, the overall duration for acetone decreased by 39 % and for toluene by 63 % for the $\varepsilon_b = 0.38$ case at 100-100 ppm compared to 160-40 ppm.

The results of the 40-160 ppm pair of concentrations for the acetone-toluene mixture are found in Figure 21 (e). In this scenario, the model accurately predicts the breakthrough onset time of acetone, while for toluene the model curve is steeper than the experimental. The higher acetone concentration observed at the column outlet is predicted with a relative error below 25 % for all bed porosity and corresponding bed lengths examined in this PhD thesis. Comparison between the 40-160 ppm and 100-100 ppm concentrations pair for ε_b = 0.38, shows the breakthrough onset time taking place ≈ 2 % later for acetone and ≈ 20 % earlier for toluene at

Table 25. Key simulation results and time metrics for the benzene-toluene mixtures.

	ε_b	C (ppm)	$t_{5\%}$ (s)	$t_{105\%}$ / $t_{95\%}$ (s)	t_{drt} (s)	T_{max} (K)	ΔP (Pa)	Fig. 21-23
BEN	0.38	160	5658	12869	7211	293.4645	54.86	b
TOL		40	14341	47117	32775			
BEN	0.40	160	5765	12782	7017	293.4651	44.71	
TOL		40	14706	46619	31913			
BEN	0.42	160	6304	13250	6946	293.4666	38.59	
TOL		40	16209	47992	31783			
BEN	0.45	160	6893	13687	6794	293.4682	30.38	
TOL		40	17923	49145	31222			
BEN	0.38	100	5898	10909	5011	293.4720	54.86	d
TOL		100	13339	28747	15409			
BEN	0.40	100	5997	10920	4923	293.4724	44.71	
TOL		100	13591	28440	14849			
BEN	0.42	100	6537	11479	4942	293.4737	38.59	
TOL		100	14776	29270	14495			
BEN	0.45	100	7125	12052	4926	293.4750	30.38	
TOL		100	16099	30034	13935			

BEN	0.38	40	6056	10272	4216	293.4863	54.86
TOL		160	12126	20077	7951		
BEN	0.40	40	6149	10315	4166	293.4869	44.71
TOL		160	12280	19859	7578		
BEN	0.42	40	6700	10929	4229	293.4880	38.59
TOL		160	13222	20538	7316		
BEN	0.45	40	7295	11564	4270	293.4888	30.38
TOL		160	14228	21111	6882		

f

the 40-160 ppm concentrations. Breakthrough completion between the same cases happens ≈ 11 % earlier for acetone and ≈ 33 % earlier for toluene at the 40-160 ppm compared to the 100-100 ppm concentrations. Breakthrough duration hence is shorter by ≈ 17 % for acetone and ≈ 48 % for toluene at 40-160 ppm compared to 100-100 ppm.

Figure 21 (b) presents the results for the benzene-toluene mixture at an inlet concentration of 160-40 ppm respectively. The model predicts in excellent agreement the breakthrough onset and curve slope for benzene, even capturing the maximum outlet concentration within ≈ 3 % relative error. For toluene, while the breakthrough onset and final concentration is accurately predicted, there is a small mismatch with the curve's slope. Breakthrough onset for benzene takes place at $t_{5\%}$ = 5658 s for ε_b = 0.38 with a duration of t_{drt} = 7211 s. For toluene, breakthrough onset starts later, at $t_{5\%}$ = 14341 s and lasts longer than acetone, with a duration of 32775 s. For increasing bed porosity and thus column lengths, the breakthrough onset comes later for both components.

Figure 21 (d) shows the breakthrough curve results for the binary mixture of benzene-toluene at 100-100 ppm inlet concentrations respectively. The model accurately captures benzene breakthrough onset and approaches the maximum outlet concentration with a relative error below 10 %. Despite a small mismatch, observed for the toluene curve slope and by association for the toluene breakthrough onset, the final toluene outlet concentration is accurately captured. Comparing the ε_b = 0.38 case of 100-100 ppm with 160-40 ppm, shows that the breakthrough onset of benzene is ≈ 4 % later and toluene's ≈ 7 % earlier than in 160-40 ppm. Breakthrough completion is ≈ 15 % earlier for benzene and ≈ 39 % earlier for toluene at the 100-100 ppm

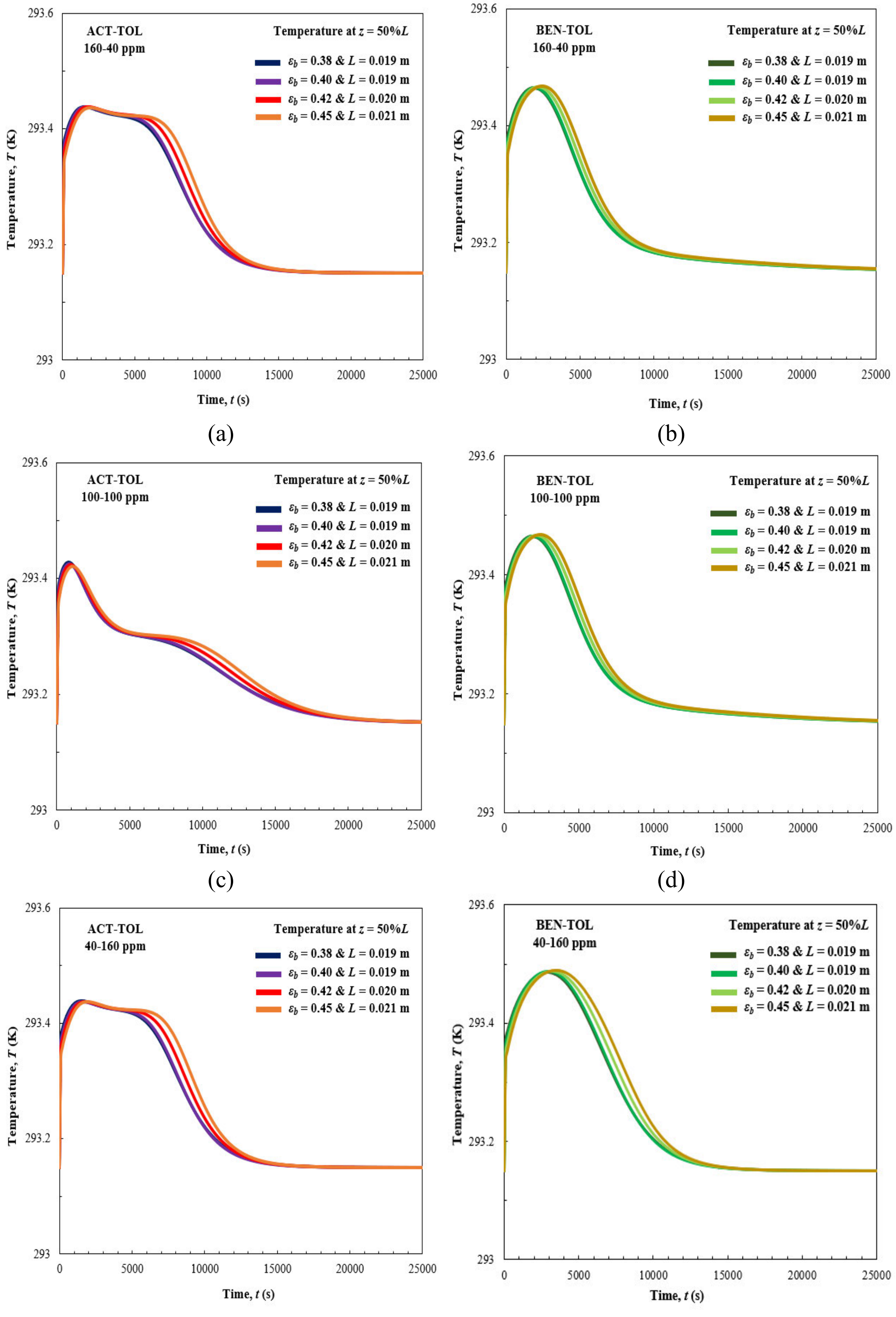

(a) (b)

(c) (d)

(e) (f)

Figure 22. Temperature variation at z = 50%L results from binary mixtures simulations.

inlet concentration case compared to the 160-40 ppm binary for $\varepsilon_b = 0.38$. Finally, breakthrough duration for benzene is ≈ 31 % shorter and for toluene ≈ 53 % shorter in the 100-100 ppm inlet concentration case, compared to the 160-40 ppm case.

Figure 21 (f) presents the breakthrough curves for the 40-160 ppm benzene-toluene mixture. While the model sufficiently captures the breakthrough onset time and final concentrations of benzene and toluene, it overestimates the maximum outlet concentration of benzene by less than 30 % relative error. For toluene, the model predicts a steeper curve than the experiment suggests, thus affecting the prediction of breakthrough onset and completion times. For $\varepsilon_b = 0.38$, breakthrough onset time for benzene is ≈ 3 % later and for toluene ≈ 9 % earlier at the 40-160 ppm inlet concentrations compared to the 100-100 ppm. Breakthrough completion, for the same comparison, comes ≈ 6 % earlier for benzene and ≈ 30 % earlier for toluene. Finally, breakthrough duration for benzene is ≈ 16 % shorter and for toluene ≈ 51 % shorter at 40-160 ppm inlet concentration, compared to the 100-100 ppm inlet concentration for $\varepsilon_b = 0.38$.

Figure 22 introduces the temperature variation in the middle of the column for all scenarios investigated in this chapter. At a first glance, the temperature profiles of the two binaries follow different trends, with acetone-toluene mixtures forming two peaks and the benzene-toluene mixtures forming a single peak. Adsorption is an exothermic process; thus, temperature peaks are expected and signify adsorption taking place at a specific part of the column. Due to the trace VOC concentrations examined in this PhD thesis (up to 200 ppm) the magnitude of the temperature rises is below 1 K. Each concentration pair is examined for four potential bed porosity fractions and their corresponding bed lengths. For the acetone-toluene mixture, increasing bed porosity (and thus bed length) leads to the observation of a decreasing maximum temperature, while interestingly, for the benzene-toluene mixtures, the opposite is observed; increasing bed porosity leads to an increasing maximum temperature in the middle of the column. The higher T_{max} of the benzene-toluene mixtures compared to acetone-toluene, are attributed to the higher heat of adsorption of benzene compared to acetone (Table 18).

Figure 23 presents the pressure drop profiles for all binary mixtures considered in this paper. Pressure drops follow a linear profile, and, in accordance to the Ergun's equation is equal for corresponding concentrations and bed porosity fractions between the acetone-toluene and benzene-toluene mixtures. The overall values are low, as expected from the column length ad flow conditions. The largest pressure drop, 54.86 Pa, is observed for the smallest bed porosity ($\varepsilon_b = 0.38$), which then decreases to 30.38 Pa for the largest bed porosity examined ($\varepsilon_b = 0.45$)

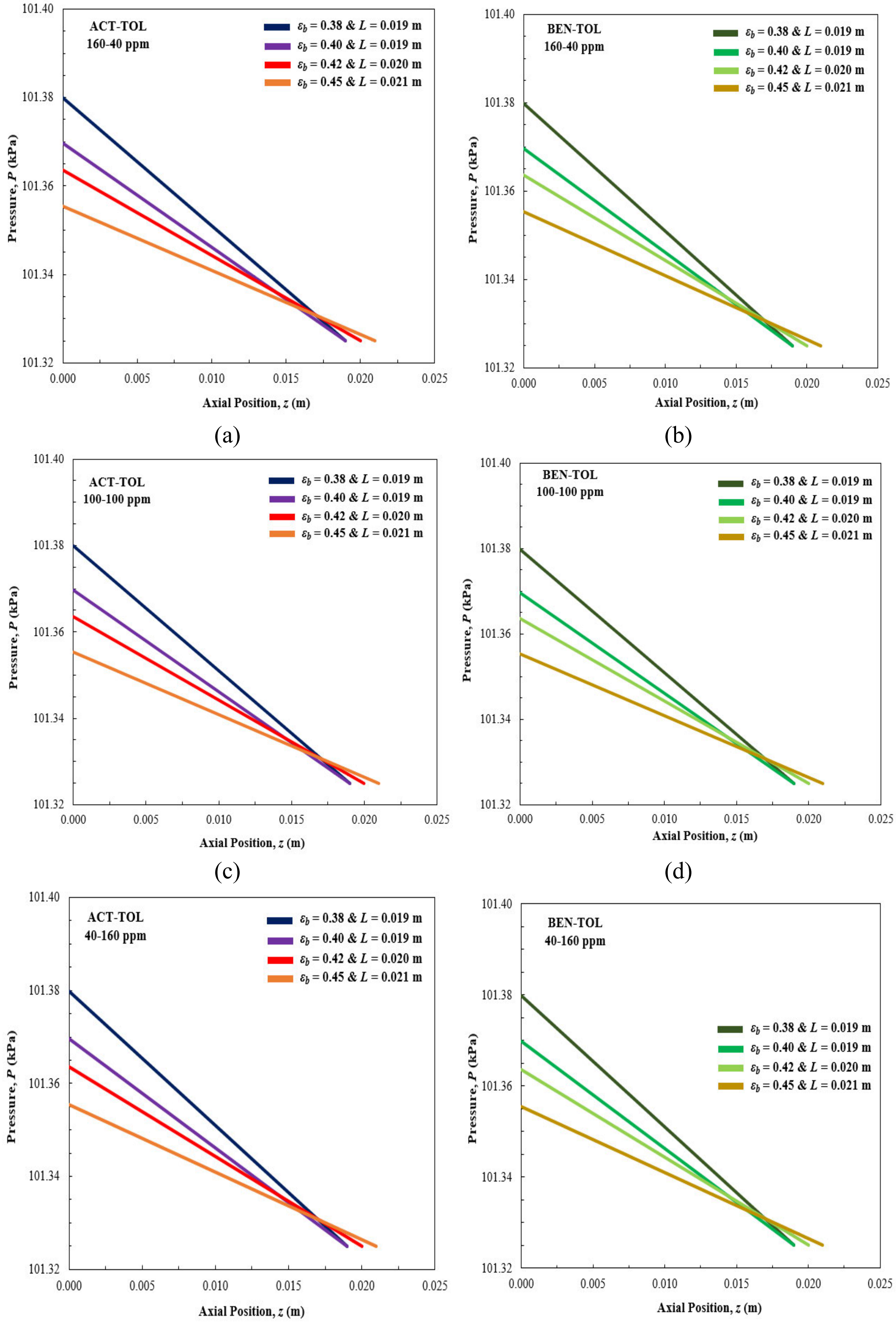

(a) (b)

(c) (d)

(e) (f)

Figure 23. Pressure drop profile results from binary mixtures simulations.

regardless of mixture composition and component concentration.

7.3 Chapter Conclusions

The present chapter continues to demonstrate the application of a validated (Tzanakopoulou et al., 2023), multicomponent, nonisothermal dynamic adsorption model for the simulation of published experimental data by (Lee et al., 2008). The mixtures of acetone-toluene and benzene-toluene with air as the inert carrier gas are studied under the same three inlet concentration pairs of 160-40 ppm, 100-100 ppm and 40-160 ppm at T = 293.15 K. Firstly, an estimation of the column length is performed for four different potential bed porosities (ε_b = 0.38, 0.40, 0.42 and 0.45) which results in column lengths of L = 0.019 – 0.021 m. Based on these calculations, key breakthrough metrics highlight trends observed across all three mixtures concerning column exit behaviour. Specifically, acetone and benzene emerge at the column at a higher concentration compared to their inlet, across all concentration pairs examined, thus confirming them as the weakly adsorbed components.

The earliest breakthrough onset times occur for acetone when in a mixture with toluene. Toluene demonstrates earlier breakthrough onset when in a mixture with benzene, compared to the acetone mixtures. As expected, breakthrough onset times decrease for increasing inlet concentration for all three components. The discrepancies between experimental data and simulation results are possibly due to the incomplete knowledge of the experimental system details as well as our model limitations. The discrepancies between experimental breakthrough data and simulation results are attributed to the incomplete knowledge of the experimental system details as well as our model limitations.

Moreover, simulation results shed light in temperature variations and pressure drop of multicomponent mixtures. Specifically, due to the trace concentrations of the feed streams studied in this PhD thesis, temperature rises in the middle of the column, occurring due to adsorption exothermicity, are minute, and slightly higher for the benzene-toluene mixtures compared to the acetone-toluene owing to the higher heat of adsorption for benzene as opposed to acetone. Pressure drop, computed via Ergun's equation, in the columns examined is minimal, ranging from 30.38 to 54.86 Pa among all mixtures. Higher values are reported for the smallest bed porosity (0.38) and corresponding bed length (0.019 m) which decline as the bed porosity and corresponding calculated bed length increase. These results emphasize the importance of reliable dynamic modelling with respect to adsorption column efficiency and unlock the potential for process optimisation in the industrial scale.

Chapter 8

Hodograph Theory Investigation

This chapter introduces the basics of Hodograph Theory and then proceeds to investigate its applicability to multicomponent mixture adsorption characteristics predictions, regarding breakthrough duration and maximum outlet concentration. The case studies here are taken from the simulations of Chapter 5 and Chapter 7.

The results presented in this chapter have also been published in the literature (Tzanakopoulou et al., 2023. *Comput. Chem. Eng.*,**174**, 108248) and (Tzanakopoulou et al., 2024. *Ind. Eng. Chem. Res.*, 63, **16**, 7281-7299); details can be found in Appendix B.

8.1 Hodograph Theory

Multicomponent adsorption equilibrium theory allows the qualitative prediction of the equilibrium behaviour of isothermal, Langmuir isotherm-obeying systems. Glueckauf's work connected chromatographic theory and kinematic waves in a similar manner which resulted in the ability to predict multicomponent mixture dynamic behaviour. The foundation of the theory is the concept of coherence, which assumes that a front of multicomponent fluid is travelling along the column as a front of constant composition and can transition either as a continuous wave or a shock. For example, the feeding of an initially clean bed with a ternary mixture (two low-concentration adsorbable species with an inert carrier gas) generates a front travelling as a shock along the column, whose behaviour is critical during industrial operation.

In such a ternary mixture, the equilibrium of each adsorbable component depends on both components, which, also due to the coherence of waves, gives rise to the fundamental quadratic equation (Eq. (40)):

$$\frac{\partial q_2}{\partial C_1}\left(\frac{\partial C_1}{\partial C_2}\right)^2 + \left(\frac{\partial q_2}{\partial C_2} - \frac{\partial q_1}{\partial C_1}\right)\frac{\partial C_1}{\partial C_2} - \frac{\partial q_1}{\partial C_2} = 0 \qquad (40)$$

Glueckauf's approach (1949) (Ruthven, 1984) enables the binary Langmuir isotherm analysis simplification by the introduction of the p_1, p_2 variables, where component 2 is assumed to be the strongly adsorbed. Therefore, b_2 is always larger than b_1 and Equation (40) becomes:

$$p_1 = \frac{b_1 b_2 C_1}{b_2 - b_1} \qquad (41)$$

$$p_2 = \frac{b_1 b_2 C_2}{b_2 - b_1} \tag{42}$$

$$\lambda = \frac{\partial C_1}{\partial C_2} \tag{43}$$

$$p_2 \lambda^2 + (p_2 - p_1 - 1)\lambda - p_1 = 0 \tag{44}$$

Equation 44 has two roots, where *M* is the positive and *N* is the negative. The transition of a system between the bed's initial and final (feed concentration) state can be described qualitatively on a hodograph plot of p_1 vs. p_2. This plot contains two points corresponding to the initial and final state of the bed respectively, as well as, four straight lines passing through them which correspond to the characteristic curves of p_1 and p_2 coherence equation's (Eq. 44) roots for each point, as follows:

$$p_1 = p_2 M - \frac{M}{1 + M} \tag{45}$$

$$p_1 = p_2 N - \frac{N}{1 + N} \tag{46}$$

Hodograph interpretation relies on 2 rules to predict the system's dynamic behaviour when transitioning from the bed's initial state to the bed's final (feed concentration) state (Glueckauf, 1949 and Basmadjian, 1997):

1. One departs from the initial composition point on a positive root characteristic line and arrives at the final (feed) composition point on a negative root characteristic curve.

2. Whenever the more strongly adsorbed solute increases in concentration along the column we have a diffuse boundary while where the concentration of the more strongly adsorbed component decreases along the column we have a shock transition.

8.2 Hodograph Theory Case Studies from Chapter 5

The two simple rules of Hodograph Theory enable the prediction of binary mixture dynamic adsorption on a qualitative level. To this end, the adsorption of mixtures of dichloromethane with chloroform, dichloromethane with toluene and dichloromethane with acetone were studied at five different temperatures (T = 293 K–313 K) and two different bed states (clean and used) each, as described in Chapter 5. The API manufacturing site has an internal emissions limit for combined chloroform and dichloromethane of 18 ppm, so an initial concentration of 9 ppm per VOC was assumed for the used bed scenarios.

For each scenario, the coherence equation (Eq. 44) is solved twice. Once for the initial state of the bed and once for the feed (final state). For the clean bed scenario, p_1 and p_2 are zero. Only one pair of M, N values are therefore computed and thus, 2 curves, corresponding to the feed state roots of the coherence equation are drawn on the clean bed hodographs (Figure 25a, Figure 26a, Figure 26a). For the used bed scenario, the solution of the coherence equation gives 2 pairs of M, N values, corresponding to the four characteristic curves present on the used bed hodographs (Figure 25b, Figure 26b, Figure 26b).

Table 26 shows the results of the coherence equation solution for the DCM-TCM system.

Table 26. Coherence equation solutions for the DCM-TCM system for clean/used bed.

System	T **(K)**	**State**	p_1	p_2	M	N
DCM-TCM (CLEAN BED)	293	Initial	0	0	-	-
		Feed	0.1100	0.1100	9.1830	-0.1090
	298	Initial	0	0	-	-
		Feed	0.0826	0.0824	12.2110	-0.0821
	303	Initial	0	0	-	-
		Feed	0.0620	0.0622	16.1340	-0.0617
	308	Initial	0	0	-	-
		Feed	0.0474	0.0474	21.1300	-0.0473
	313	Initial	0	0	-	-
		Feed	0.0366	0.0363	27.5340	-0.0365
DCM-TCM (USED BED)	293	Initial	0.0039	0.0039	254.9140	-0.0039
		Feed	0.1100	0.1100	9.1830	-0.1086
	298	Initial	0.0029	0.0029	336.7910	-0.0029
		Feed	0.0826	0.0824	12.2109	-0.0820
	303	Initial	0.0022	0.0022	446.3244	-0.0022
		Feed	0.0619	0.0622	16.1343	-0.0617
	308	Initial	0.0017	0.0017	585.6890	-0.0017
		Feed	0.0474	0.0474	21.1409	-0.0473
	313	Initial	0.0013	0.0013	763.3631	-0.0013

		Feed	0.0365	0.0363	27.5339	-0.0365

Table 27 shows the results of the coherence equation solution for the DCM-TOL system.

Table 27. Coherence equation solutions for the DCM-TOL system for clean/used bed.

System	*T* (K)	State	p_1	p_2	*M*	*N*
DCM-TOL (CLEAN BED)	293	Initial	0	0	-	-
		Feed	0.1284	0.1291	7.8664	-0.1264
	298	Initial	0	0	-	-
		Feed	0.0972	0.0968	10.4278	-0.0962
	303	Initial	0	0	-	-
		Feed	0.0734	0.0740	13.5667	-0.0731
	308	Initial	0	0	-	-
		Feed	0.0566	0.0565	17.7338	-0.0564
	313	Initial	0	0	-	-
		Feed	0.0440	0.0440	22.7682	-0.0439
DCM-TOL (USED BED)	293	Initial	0.0046	0.0045	218.7553	-0.0046
		Feed	0.1283	0.1291	7.8664	-0.1263
	298	Initial	0.0034	0.0035	285.4714	-0.0034
		Feed	0.0972	0.0968	10.4278	-0.0962
	303	Initial	0.0025	0.0023	417.9689	-0.0025
		Feed	0.0734	0.0740	13.5666	-0.0731
	308	Initial	0.0020	0.0018	535.7988	-0.0020
		Feed	0.0566	0.0565	17.7338	-0.0564
	313	Initial	0.0015	0.0014	681.1179	-0.0015
		Feed	0.0440	0.0440	22.7682	-0.0439

Table 28 shows the results of the coherence equation solution for the DCM-ACT system.

Table 28. Coherence equation solutions for the DCM-ACT system for clean/used bed.

System	***T*** **(K)**	**State**	p_1	p_2	M	N
DCM-ACT (CLEAN BED)	293	Initial	0	0	-	-
		Feed	0.1729	0.1712	6.0186	-0.1678
	298	Initial	0	0	-	-
		Feed	0.1358	0.1358	7.4963	-0.1334
	303	Initial	0	0	-	-
		Feed	0.1082	0.1082	9.3459	-0.1070
	308	Initial	0	0	-	-
		Feed	0.0884	0.0875	11.5227	-0.0877
	313	Initial	0	0	-	-
		Feed	0.0734	0.0734	13.7035	-0.0730
DCM-ACT (USED BED)	293	Initial	0.0066	0.0049	200.8863	-0.0066
		Feed	0.1729	0.1712	6.0186	-0.1678
	298	Initial	0.0053	0.0039	250.6769	-0.0053
		Feed	0.1358	0.1358	7.4963	-0.1334
	303	Initial	0.0043	0.0032	308.3027	-0.0043
		Feed	0.1082	0.1082	9.3459	-0.1070
	308	Initial	0.0035	0.0026	373.5492	-0.0035
		Feed	0.0884	0.0875	11.5227	-0.0876
	313	Initial	0.0029	0.0022	445.5996	-0.0029
		Feed	0.0733	0.0733	13.7034	-0.0729

Figure 24 (a) shows the clean bed hodographs of the dichloromethane–acetone system. In this system, acetone is the strongly adsorbed component and DCM is the weakly adsorbed component due to the smaller Langmuir Isotherm parameter values. For the clean bed scenario, five different temperatures were examined while the concentration remained the same at 250 ppm per VOC. For each temperature, the initial point is at the bottom left of the plot (0,0) while the feed point, corresponding to the final state of the bed, is moving closer to (0,0) with increasing temperature. That is due to the definitions of p_1, p_2 which include the Langmuir affinity coefficients. The Langmuir affinity coefficients are temperature dependent, as can be seen in Eq. (15), and more specifically, they decrease as temperature increases. Hence, the feed points on the hodograph for a specific system will be receiving smaller values with increasing temperature. This system demonstrates the highest p_1-p_2 values compared to the others.

The used bed hodographs of the dichloromethane–acetone system are shown in Figure 24(b), for five different temperatures and an initial bed concentration of 9 ppm per VOC. The feed concentration remained at 250 ppm per VOC. The gradual decline of the feed point values is due to the increased temperature, as in the clean bed cases. According to Rule 1, departure from the initial point occurs on a positive characteristic (M) line, therefore, for T = 293 K we depart from the initial point on the continuous purple line and, we arrive at the feed point on the dashed purple line which corresponds to the negative characteristic. Thus, if C is the point where the positive root characteristic (continuous purple line) and the negative root characteristic curve (dashed purple line) intersect, the route could be summarized as going to the feed point, from the initial point via C. Since the concentration of the strongly adsorbed component is decreasing due to an amount of it being adsorbed throughout the column, a shock transition occurs, as set out by Rule 2, and thus a sharp rise in the concentration of the weakly adsorbed component occurs, leading to its exit in a higher concentration compared to its inlet. The hodograph plots of all temperatures are interpreted in a similar manner. It is observed that with rising operating temperature, the amount of displaced dichloromethane decreases thus corroborating our results shown in Figure 14 (b), where the temperature sensitivity analysis of the same system clearly shows a decline in the maximum DCM concentration at the column outlet with rising temperature.

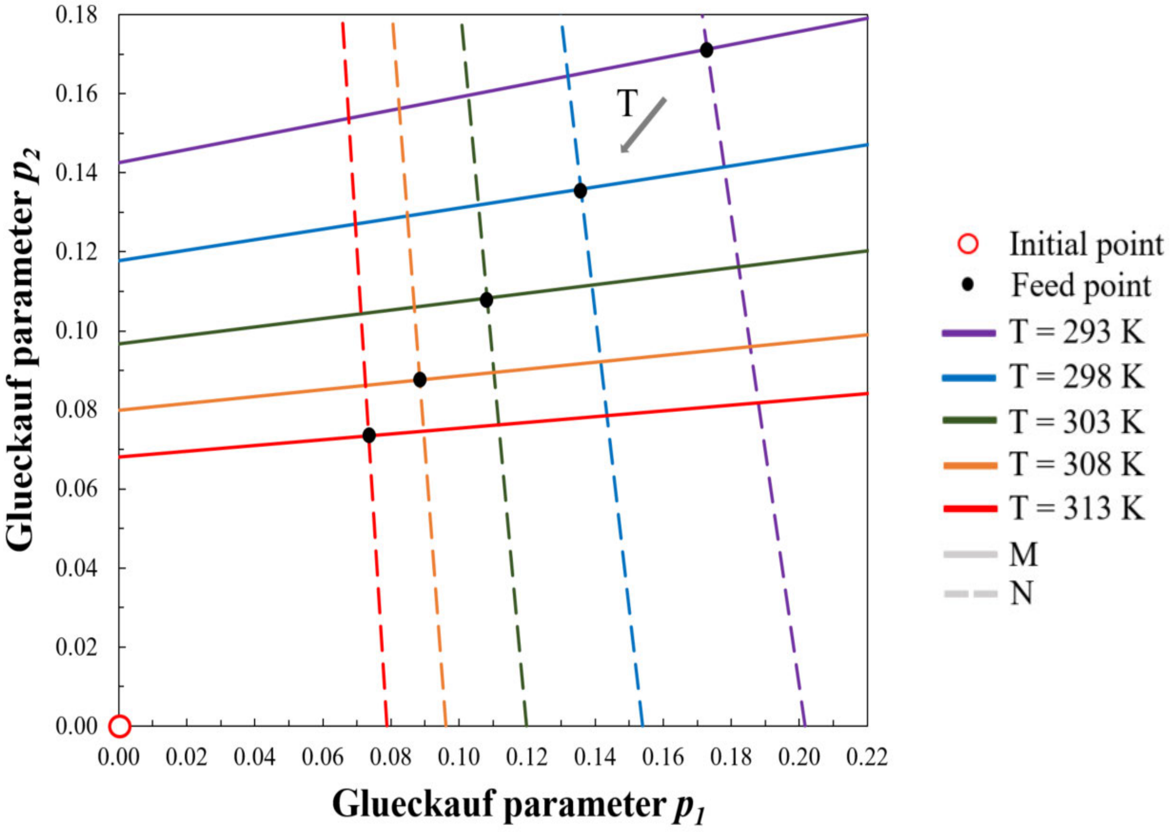

(a) DCM-ACT mixture, clean bed

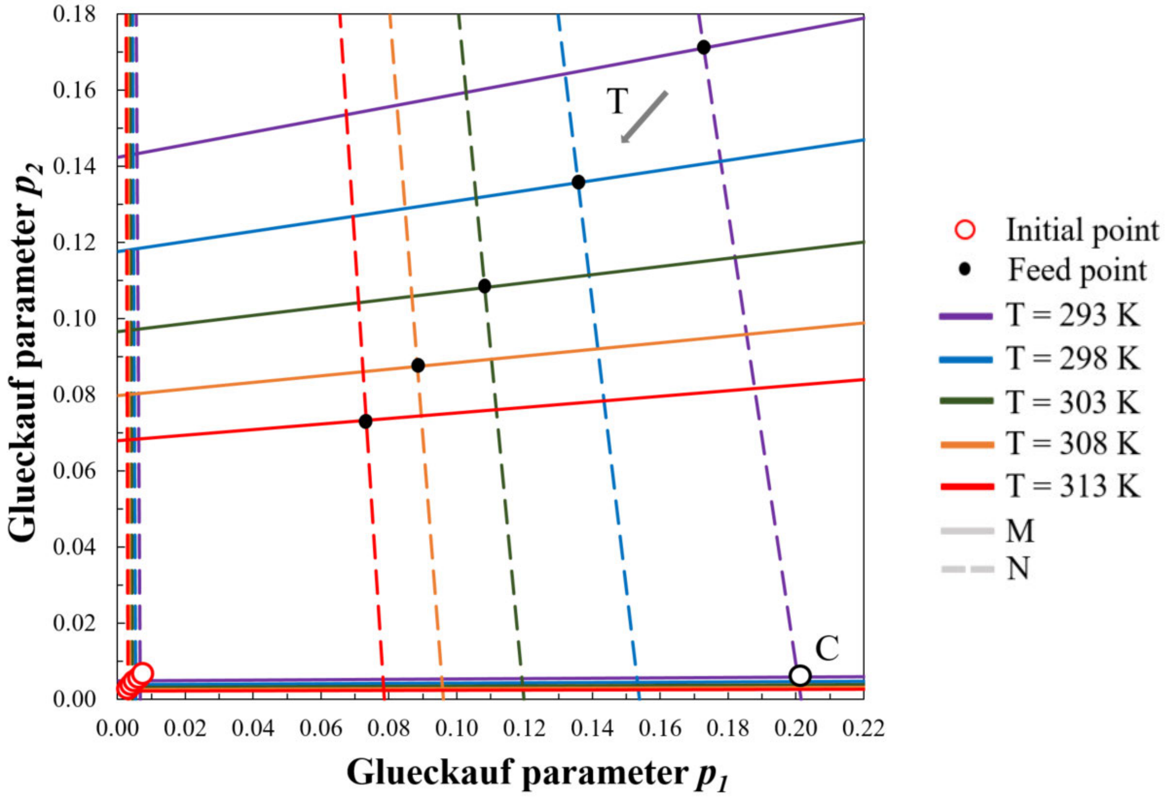

(b) DCM-ACT mixture, used bed

Figure 24. Hodograph plots for the DCM-ACT system on a (a) clean and (b) used bed.

The clean bed hodographs of the dichloromethane–chloroform system are presented in Figure 25a. In this system, TCM is the strongly adsorbed component and DCM is the weakly adsorbed component due to the larger Langmuir Isotherm parameter values of TCM compared to DCM. For the clean-bed scenario, 5 different temperatures were examined while the concentration remains the same at 250 ppm per VOC. For each temperature, the initial point is at the bottom left of the plot (0,0) while the feed point, corresponding to the final state of the bed, is moving closer to (0,0) with increasing temperature. That is due to the definitions of p_1, p_2 which include the Langmuir affinity coefficients. The Langmuir affinity coefficients are temperature dependent, as can be seen in Eq. (15), and more specifically, they decrease as temperature increases. Hence, the feed points on the hodograph for a specific system will be receiving smaller values with increasing temperature.

The used bed hodographs of the dichloromethane–chloroform system are shown in Figure 25b. Here, the same five different temperatures are explored but the beds have an initial concentration of 9 ppm per VOC while the feed concentration remains at 250 ppm per VOC. The gradual decline of the feed point values is due to the increased temperature, as in the clean bed cases. However, here, the predictive capabilities of hodograph theory can be displayed since there are now four lines on the p_1-p_2 plane, corresponding to the two pairs of roots of the coherence equation. As Rule 1 states, we depart from the initial point on a positive characteristic (M) line, therefore, for T = 293 K, we depart from the initial point on the continuous purple line and, we arrive at the feed point on the dashed purple line which corresponds to the negative characteristic. Therefore, if C is the point where the positive root characteristic (continuous purple line) and the negative root characteristic curve (dashed purple line) intersect, the route could be summarized as going to the feed point, from the initial point via C. Since the concentration of the strongly adsorbed component is decreasing due to an amount of it being adsorbed throughout the column, a shock transition occurs, as set out by Rule 2, and thus there is a sharp rise in the concentration of the weakly adsorbed component, which exits the column in a higher concentration compared to its inlet. The hodograph plots of all temperatures are interpreted in a similar manner. What is interestingly deducted by this method, is not only the prediction of the component to be displaced but also the observation that with rising operating temperature, the amount of displaced weakly adsorbed component decreases. This corroborates our simulations which clearly show that as temperature rises, the maximum concentration of the displaced component encountered at the column outlet declines.

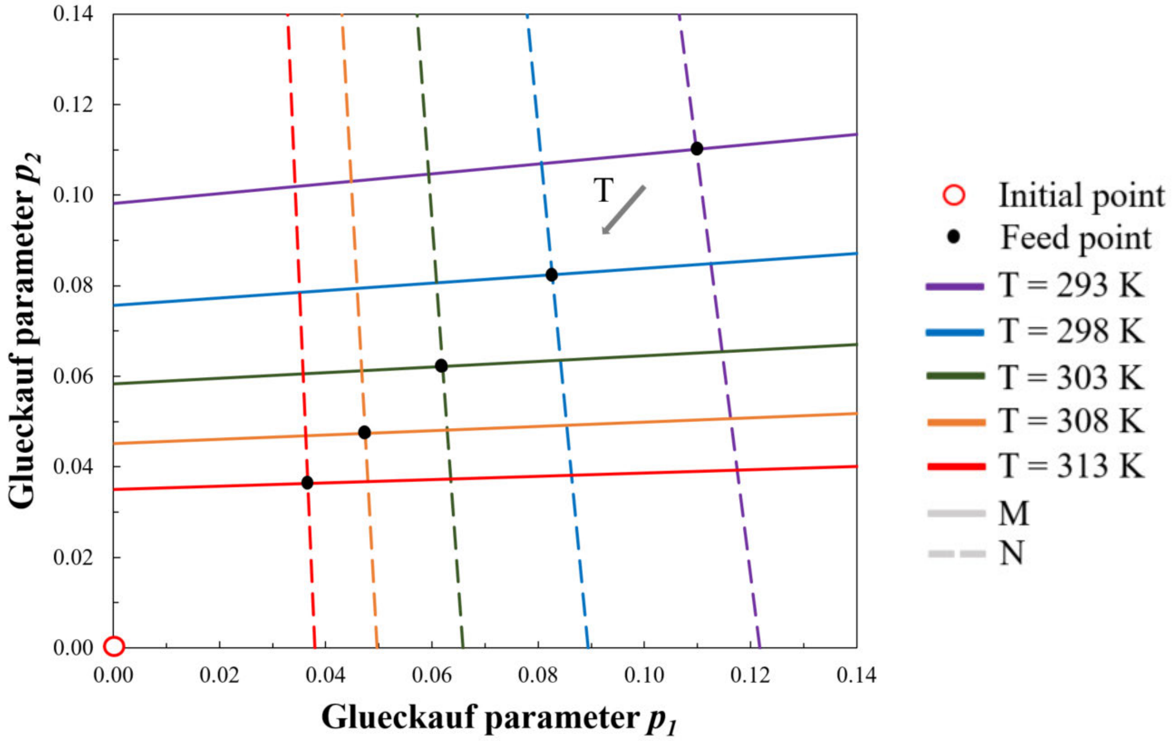

(a) DCM-TCM mixture, clean bed

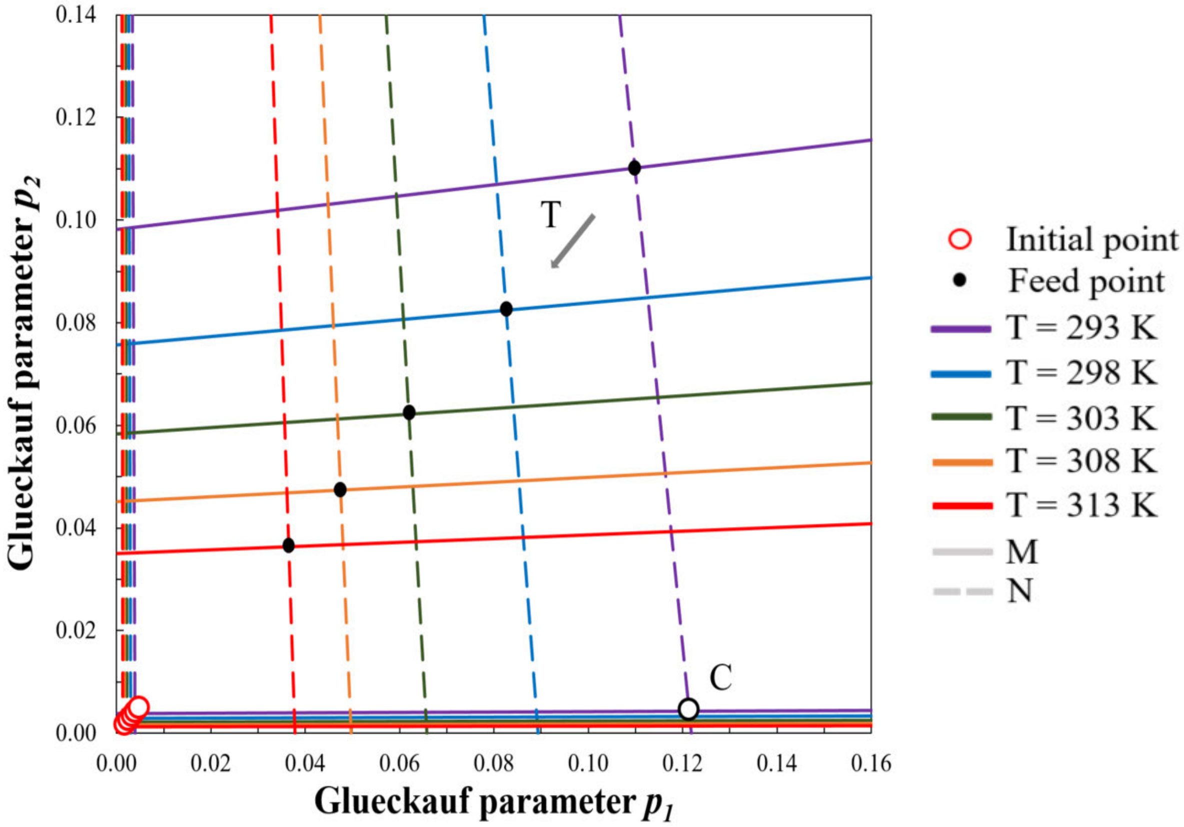

(b) DCM-TCM mixture, used bed

Figure 25. Hodograph plots for the DCM-TCM system on a (a) clean and (b) used bed.

Figure 26a shows the clean bed hodographs of the dichloromethane–toluene system. In this system, toluene is the strongly adsorbed component and DCM is the weakly adsorbed component due to the smaller Langmuir Isotherm parameter values. For the clean bed scenario, 5 different temperatures were examined while the concentration remained the same at 250 ppm per VOC. For each temperature, the initial point is at the bottom left of the plot (0,0) while the feed point, corresponding to the final state of the bed, is moving closer to (0,0) with increasing temperature. That is due to the definitions of p_1, p_2 which include the Langmuir affinity coefficients. The Langmuir affinity coefficients are temperature dependent, as can be seen in Eq. (15), and more specifically, they decrease as temperature increases. Hence, the feed points on the hodograph for a specific system will be receiving smaller values with increasing temperature. This system has the lowest values on the hodograph for p_1 and p_2.

The used bed hodographs of the dichloromethane–toluene system are shown in Figure 26b. Here, the same five different temperatures were explored but the beds had an initial concentration of 9 ppm per VOC while the feed concentration remained at 250 ppm per VOC. The gradual decline of the feed point values is due to the increased temperature, as in the clean bed cases. According to Rule 1, departure from the initial point occurs on a positive characteristic (M) line, therefore, for T = 293 K we depart from the initial point on the continuous purple line and, we arrive at the feed point on the dashed purple line which corresponds to the negative characteristic. Thus, if C is the point where the positive root characteristic (continuous purple line) and the negative root characteristic curve (dashed purple line) intersect, the route could be summarized as going to the feed point, from the initial point via C. Since the concentration of the strongly adsorbed component is decreasing due to an amount of it being adsorbed throughout the column, a shock transition occurs, as set out by Rule 2, and thus a sharp rise in the concentration of the weakly adsorbed component occurs, leading to its exit in a higher concentration compared to its inlet. The hodograph plots of all temperatures are interpreted in a similar manner. What is interestingly deducted by this method, is not only the prediction of the component to be displaced, but also the observation that with rising operating temperature, the amount of displaced weakly adsorbed component decreases.

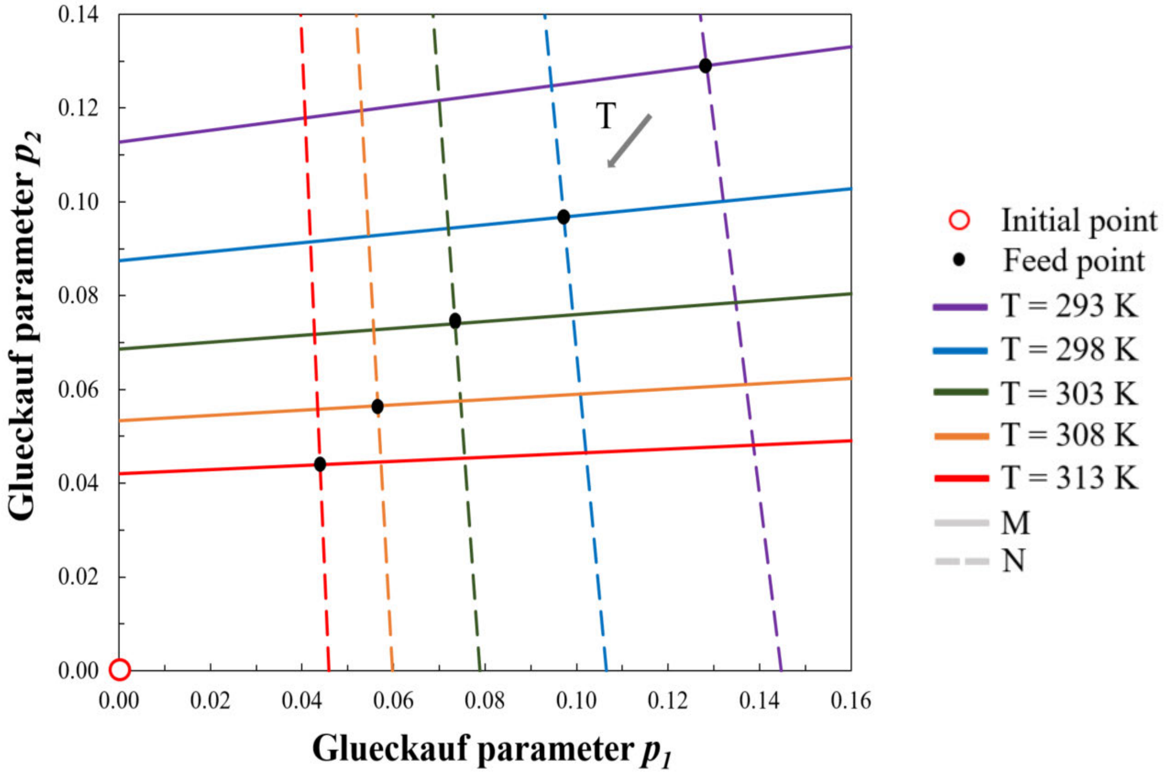

(a) DCM-TOL mixture, clean bed

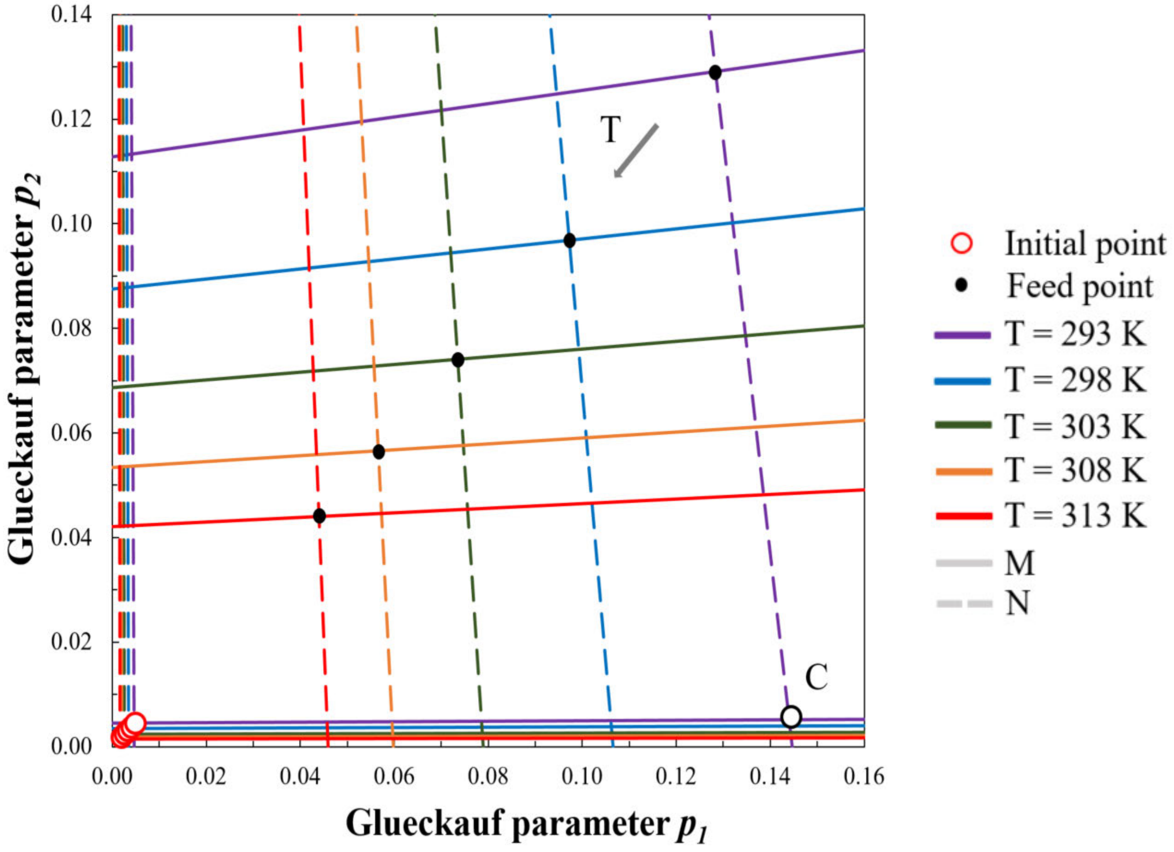

(b) DCM-TOL mixture, used bed

Figure 26. Hodograph plots for the DCM-TOL system on a (a) clean and (b) used bed.

8.3 Hodograph Theory Case Studies from Chapter 7

The two simple rules of Hodograph Theory enable the prediction of overshoot concentration in a binary mixture dynamic adsorption. To this end, the adsorption of mixtures of acetone with toluene and benzene with toluene (both with air as the inert carrier gas) were studied at three different concentration pairs (160-40, 100-100, 40-160 ppm) each on a clean bed and T = 293.15 K.

For each mixture and inlet concentration pair, the coherence equation (Eq. 44) is solved twice. Once for the initial state of the bed and once for the final (feed) state. For the clean bed scenario, p_1 and p_2 are zero, hence the p_1 and p_2 axes are considered as the initial state solutions. Only one pair of M, N values are therefore computed and thus, 2 curves, corresponding to the final (feed) state roots of the coherence equation are drawn on the clean bed hodographs (Figure 27).

Table 29 shows the results of the coherence equation solution for the binary mixtures.

Table 29. Coherence equation solutions for binary mixture hodograph plots construction.

System	T (K)	C_0 (ppm$_v$)	State	p_1	p_2	M	N	Fig. 26
ACT-TOL (CLEAN BED)	293.15	160	Initial	0	0	-	-	a
		40	Feed	0.175927	0.043982	25.89115	-0.15449	
	293.15	100	Initial	0	0	-	-	a
		100	Feed	0.109955	0.109955	9.203321	-0.10866	
	293.15	40	Initial	0	0	-	-	a
		160	Feed	0.043982	0.175927	4.984322	-0.05016	
BEN-TOL (CLEAN BED)	293.15	160	Initial	0	0	-	-	b
		40	Feed	0.899281	0.224820	7.951076	-0.50308	
	293.15	100	Initial	0	0	-	-	b
		100	Feed	0.562050	0.562050	2.228027	-0.44883	
	293.15	40	Initial	0	0	-	-	b
		160	Feed	0.224820	0.899281	0.712753	-0.35075	

The clean bed hodographs for the mixtures of acetone-toluene and benzene-toluene at three concentration pairs (160-40 ppm, 100-100 ppm and 40-160 ppm) are found in Figure 27. Hodograph plots only rely on pure component Langmuir Isotherm parameters for their construction; thus, each plot is agnostic to bed porosities, lengths, and flow conditions. The predictive capabilities of hodograph theory can be displayed by referring to Figure 27 (a). As Rule 1 states, one departs from the initial point on a positive characteristic (M) line, therefore, we depart from the initial point on the p_1 axis and, arrive at the final (feed) point on the dashed line which corresponds to the negative characteristic (N) line. Hence, if the triangle point is the point where the positive root characteristic (p_1 axis) line and the negative root characteristic line (dashed line) intersect, the route could be summarized as heading to the final (feed) point, from the initial point via the triangle point. Since the concentration of the strongly adsorbed

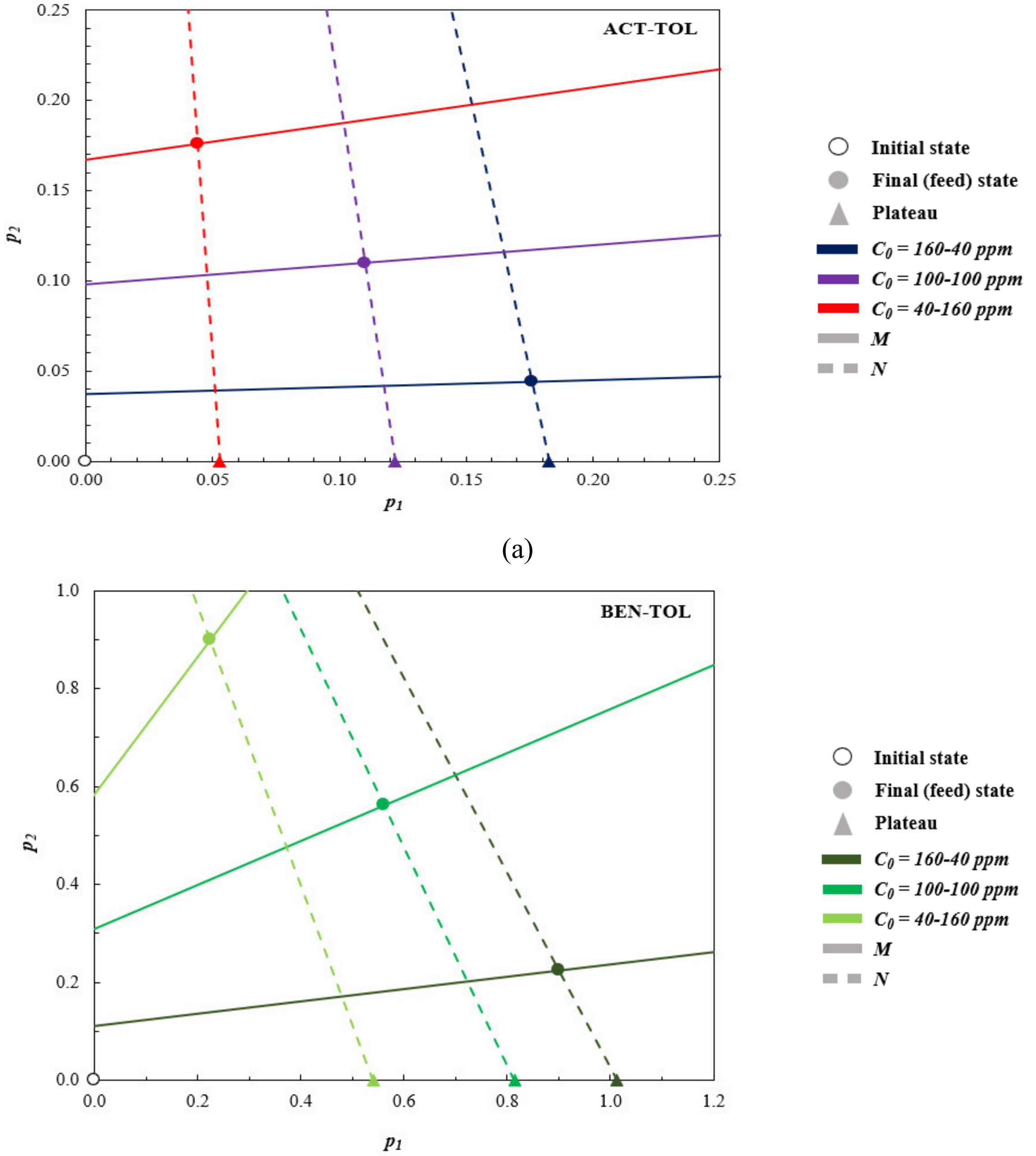

(a)

(b)

Figure 27. Hodograph plots for binary mixtures breakthrough theoretical predictions.

component is decreasing due to an amount of it being adsorbed throughout the column, a shock transition occurs, as set out by Rule 2, and thus there is a sharp rise in the concentration, namely the plateau, of the weakly adsorbed component (acetone/benzene), which exits the column in a higher concentration compared to its inlet.

The hodograph plots of all binary mixtures can be interpreted in an analogous manner. It is interesting to note is that the estimated plateau point (triangle) can predict the maximum concentration of the weakly adsorbed component in the column outlet (overshoot). Table 30 summarizes and compares the plateau concentrations derived as predictions from hodograph theory (H), from the experimental data of (Lee et al., 2008) (E) and from the simulations (S) in this PhD thesis. Relative errors are estimated based on Equations (47)-(49).

$$\%R.E.\ S-H = 100\left(\frac{c_{MAX,S} - c_{MAX,H}}{c_{MAX,H}}\right) \tag{47}$$

$$\%R.E.\ S-E = 100\left(\frac{c_{MAX,S} - c_{MAX,E}}{c_{MAX,E}}\right) \tag{48}$$

$$\%R.E.\ H-E = 100\left(\frac{c_{MAX,H} - c_{MAX,E}}{c_{MAX,E}}\right) \tag{49}$$

As can be seen in Table 30, maximum concentration at column outlet for the weakly adsorbing component (acetone or benzene) slightly increases for the different bed porosities of the simulations carried out in the present paper.

Table 30. Overshoot concentrations predictions of displaced components from mixtures.

System	C_0 (ppm$_v$)	ε_b	$C_{max,H}$ (mol m^{-3})	$C_{max,E}$ (mol m^{-3})	$C_{max,S}$ (mol m^{-3})	%R.E. S-H	%R.E. S-E	%R.E. H-E
ACT	160	0.38	0.006909	0.007786	0.007055	2.119	-9.392	-11.272
	160	0.40	0.006909	0.007786	0.007056	2.133	-9.380	-11.272
	160	0.42	0.006909	0.007786	0.007058	2.167	-9.350	-11.272
	160	0.45	0.006909	0.007786	0.007060	2.191	-9.328	-11.272
	100	0.38	0.004609	0.005213	0.004891	6.107	-6.192	-11.592
	100	0.40	0.004609	0.005213	0.004892	6.141	-6.163	-11.592
	100	0.42	0.004609	0.005213	0.004895	6.210	-6.101	-11.592
	100	0.45	0.004609	0.005213	0.004898	6.263	-6.055	-11.592

	40	0.38	0.001997	0.002931	0.002222	11.311	-24.183	-31.887
	40	0.40	0.001997	0.002931	0.002224	11.405	-24.119	-31.887
	40	0.42	0.001997	0.002931	0.002228	11.588	-23.994	-31.887
	40	0.45	0.001997	0.002931	0.002231	11.750	-23.884	-31.887
BEN	160	0.38	0.007488	0.007732	0.007484	-0.062	-3.212	-3.152
	160	0.40	0.007488	0.007732	0.007500	0.151	-3.006	-3.152
	160	0.42	0.007488	0.007732	0.007530	0.557	-2.613	-3.152
	160	0.45	0.007488	0.007732	0.007561	0.965	-2.217	-3.152
	100	0.38	0.006023	0.006598	0.005957	-1.103	-9.720	-8.713
	100	0.40	0.006023	0.006598	0.005995	-0.473	-9.145	-8.713
	100	0.42	0.006023	0.006598	0.006072	0.802	-7.981	-8.713
	100	0.45	0.006023	0.006598	0.006151	2.126	-6.772	-8.713
	40	0.38	0.003996	0.002864	0.003349	-16.191	16.949	39.542
	40	0.40	0.003996	0.002864	0.003399	-14.952	18.678	39.542
	40	0.42	0.003996	0.002864	0.003511	-12.128	22.619	39.542
	40	0.45	0.003996	0.002864	0.003641	-8.896	27.128	39.542

For the binary mixture of acetone-toluene, with acetone at C_0 = 160 ppm, the relative errors between simulation and hodograph theory prediction are ≈ 2 %, between simulation and experiment ≈ 9 %, and between hodograph theory prediction and experiment ≈ –11 %. When acetone is fed in the column at C_0 = 100 ppm in a mixture with toluene, the relative errors between simulation and hodograph theory prediction are ≈ 6 %, between simulation and experiment ≈ –6 %, and between hodograph theory prediction and experiment ≈ –11 %. Finally, for the lowest acetone inlet concentration of 40 ppm in a mixture with toluene, the relative errors between simulation and hodograph theory prediction are ≈ 11 %, between simulation and experiment ≈ –24 %, and between hodograph theory prediction and experiment ≈ –32 %.

For the mixture of benzene-toluene, containing benzene at C_0 = 160 ppm, the relative errors between simulation and hodograph theory prediction are < 1 %, between simulation and experiment ≈ –3 %, and between hodograph theory prediction and experiment also ≈ –3 %. For the same mixture, but with components at C_0 = 100 ppm, the relative errors for the overshoot concentration of benzene between simulation and hodograph theory prediction are < 2 %, between simulation and experiment < – 9 %, and between hodograph theory prediction and experiment also ≈ –9 %. Finally, for the benzene-toluene mixture containing benzene at C_0 = 40 ppm, the relative errors for the overshoot concentration of benzene between simulation and hodograph theory prediction are < –16 %, between simulation and experiment < 27 %, and between hodograph theory prediction and experiment also ≈ 40 %.

From the conducted comparisons it appears that the developed model can successfully capture component exit concentration overshoot in competitive adsorption. Interestingly, the largest mismatch among all relative error metrics is encountered for the case of low concentration (40 ppm) of acetone or benzene. There, the largest discrepancies are encountered between the hodograph theory prediction and the experimental data of (Lee et al., 2008), possibly owning to the foundations of hodograph theory, which rely on the Langmuir parameters of the pure components for the predictions. The simulation results demonstrate a better agreement with experimental data even on the 40 ppm inlet concentration cases, compared to hodograph theory predictions.

8.4 Chapter conclusions

In this chapter, hodograph theory was applied to demonstrate the prediction capabilities of this simple, fast, and yet first-principles consistent concept, enabling binary mixture dynamic behaviour predictions. Hodograph theory results corroborate Chapter 5 simulations not only regarding the order of VOC affinity to the bed, but also in that with rising temperature the maximum concentration of the weak component at the column outlet decreases.

Moreover, hodograph theory estimations have been compared to gPROMS® dynamic simulation results of Chapter 7, showing that the former (albeit originally derived for single-component, isothermal conditions) can provide quick, useful estimates to inform industrial operation, before committing resources in pursuit of the latter. However, discrepancies between hodograph theory predictions and experimental data are higher in all cases examined compared to gPROMS® simulation results.

Chapter 9

Transient Feed Simulations of Binary Mixtures

This Chapter presents the application of our model to the investigation of adsorption characteristics of binary mixtures under transient feed conditions. First the mixtures of hexane-toluene are examined, and the rest of the chapter addresses the mixtures of dichloromethane-acetone, dichloromethane-chloroform and dichloromethane-toluene.

The results presented in this chapter have also been published in the literature (Tzanakopoulou et al., 2024. *Comput. Aided Chem. Eng.*, in press) and (Tzanakopoulou et al., 2024. *Comput. Chem. Eng.*, accepted for publication); details can be found in Appendix B.

9.1 Case Study of HEX-TOL

Herein presented is the application of a validated dynamic, nonisothermal adsorption model (Tzanakopoulou et al., 2023) to study a binary mixture (hexane-toluene) under industrial conditions. This study therefore considers two dynamic VOC feed concentration patterns, in order to examine relevant breakthrough trends in an Activated Carbon (AC) adsorption column. The VOC concentration range (100-250 ppm) emulates realistic industrial (multi-unit) feed conditions for both cases, aiming to probe the effect of component/concentration sequencing on bed breakthrough time, cost implications and wider environmental impact.

The developed model is used to simulate multicomponent VOC adsorption under dynamic inlet concentration. The set of PDEs is solved using RADAU solver and orthogonal collocation on finite elements for space discretization in gPROMS® Process 2.0.0. The adsorption of binary hexane – toluene mixture, with air as the carrier, has been examined on beaded activated carbon (Tefera et al., 2014) and a wall temperature of 295 K. The system viscosities are computed from Wilke's equation for binary mixtures, while Langmuir isotherm parameters are taken from (Delage et al., 2000) and (Shim et al., 2003) for toluene (TOL) and hexane (HEX) respectively. Air is assumed as a binary mixture (N_2:O_2 = 79:21 % v/v). Table 31 presents the values for the main simulation parameters. In all cases considered in this chapter the bed area remains constant at 0.000181 m^2. The average particle size is 0.75 mm, 99% by mass between 0.60 and 0.84 mm (Tefera et al., 2013, Lashaki et al., 2012).

Table 31. Main model parameter values for HEX-TOL dynamic input simulations.

	V_s (m s^{-1})	L (m)	R (m)	ε_b	x (m)	ρ_b (kg m^{-3})	T_{in} (K)	T_w (K)
HEX	0.914	0.065	0.0076	0.38	0.001	606	300	295
TOL								

	C_{pp} (J kg^{-1} K^{-1})	k_w (W m^{-1} K^{-1})	k_p (W m^{-1} K^{-1})	ε_p	b_0 (m^3 mol^{-1})	ΔHad (J mol^{-1})	q_m (mol kg^{-1})
HEX	706.7	14.2	0.17	0.56	$2.35 \cdot 10^{-8}$	50,000	3.801
TOL					$4.06 \cdot 10^{-7}$	45,500	4.610

Table 32 presents the main dynamic inlet parameter values employed for both patterns.

Table 32. Pattern 1 and 2 parameter values for HEX-TOL dynamic input simulations.

Pattern 1	$C_{0,i}$ (ppm$_v$)	k_{LDF} (s^{-1})	$D_{z,i}$ (m^2 s^{-1})	C_{pg} (J kg^{-1} K^{-1})	h_o (W m^{-2} K^{-1})	k_{ez} (W m^{-1} K^{-1})
HEX	200	$1.88 \cdot 10^{-4}$	$1.32 \cdot 10^{-3}$	1,014	37.17	0.67
TOL	250	$5.43 \cdot 10^{-5}$	$1.34 \cdot 10^{-3}$			
HEX	230	$1.94 \cdot 10^{-4}$	$1.32 \cdot 10^{-3}$	1,014	37.17	0.67
TOL	250	$5.50 \cdot 10^{-5}$	$1.34 \cdot 10^{-3}$			
HEX	250	$1.95 \cdot 10^{-4}$	$1.32 \cdot 10^{-3}$	1,014	37.17	0.67
TOL	250	$5.53 \cdot 10^{-5}$	$1.34 \cdot 10^{-3}$			
HEX	165	$1.82 \cdot 10^{-4}$	$1.32 \cdot 10^{-3}$	1,014	37.17	0.67
TOL	250	$5.38 \cdot 10^{-5}$	$1.34 \cdot 10^{-3}$			
HEX	150	$1.85 \cdot 10^{-4}$	$1.32 \cdot 10^{-3}$	1,014	37.16	0.67
TOL	250	$5.33 \cdot 10^{-5}$	$1.34 \cdot 10^{-3}$			
HEX	130	$1.83 \cdot 10^{-4}$	$1.32 \cdot 10^{-3}$	1,014	37.16	0.67
TOL	250	$5.32 \cdot 10^{-5}$	$1.34 \cdot 10^{-3}$			
Pattern 2	$C_{0,i}$ (ppm$_v$)	k_{LDF} (s^{-1})	$D_{z,i}$ (m^2 s^{-1})	C_{pg} (J kg^{-1} K^{-1})	h_o (W m^{-2} K^{-1})	k_{ez} (W m^{-1} K^{-1})
HEX	200	$1.59 \cdot 10^{-4}$	$1.32 \cdot 10^{-3}$	1,014	37.19	0.67
TOL	100	$4.63 \cdot 10^{-5}$	$1.34 \cdot 10^{-3}$			
HEX	230	$1.62 \cdot 10^{-4}$	$1.32 \cdot 10^{-3}$	1,014	37.19	0.67
TOL	100	$4.69 \cdot 10^{-5}$	$1.34 \cdot 10^{-3}$			
HEX	250	$1.65 \cdot 10^{-4}$	$1.32 \cdot 10^{-3}$	1,014	37.19	0.67
TOL	100	$4.73 \cdot 10^{-5}$	$1.34 \cdot 10^{-3}$			
HEX	165	$1.57 \cdot 10^{-4}$	$1.32 \cdot 10^{-3}$			

TOL	100	$4.58\cdot10^{-5}$	$1.34\cdot10^{-3}$	1,014	37.19	0.67
HEX	150	$1.58\cdot10^{-4}$	$1.32\cdot10^{-3}$	1,014	37.19	0.67
TOL	100	$4.54\cdot10^{-5}$	$1.34\cdot10^{-3}$			
HEX	130	$1.52\cdot10^{-4}$	$1.32\cdot10^{-3}$	1,014	37.19	0.67
TOL	100	$4.50\cdot10^{-5}$	$1.34\cdot10^{-3}$			

9.1.1 Transient Feed Results for HEX-TOL

Figure 28 presents the breakthrough curves (outlet concentration vs time) and temperature and pressure variations of the examined binary system (hexane-toluene). In this PhD thesis the adsorption behaviour of the binary mixture hexane-toluene (with air as the carrier gas) has been examined, for an activated carbon column, under two different dynamic inlet concentration cases (Patterns 1, 2) of industrial relevance. For both scenarios considered, hexane undergoes a series of inlet concentration step changes (as occurring from upstream batch production steps), accompanied by a toluene stream of steady inlet concentration. The latter is fixed at a high (250 ppm) or low (100 ppm) level, for the said Patterns 1-2.

The breakthrough onset time ($t_{5\%}$) is calculated as the time that the component's outlet concentration reaches 5% of its equilibrium outlet concentration (after all transitions). Breakthrough completion for toluene ($t_{95\%}$) is considered to occur at the time that the outlet concentration of the VOC reaches a 95% fraction of the equilibrium (final) value. For hexane (the weakly adsorbing component), the $t_{105\%}$ value is taken to be the breakthrough completion time (as it is approached from higher values after an overshoot). The breakthrough intervals are thus defined as 5-95% for toluene, and 5-105% for hexane.

Figure 28 (a-b) present the inlet and outlet concentrations for the Pattern 1 case, respectively. Hexane breaks through the column outlet first at t = 1,037 s, while toluene breaks through the column second at t = 3,190 s. Breakthrough completion comes after the indicative points of $t_{95\%}$ = 6,769 s for toluene, and $t_{105\%}$ = 5,200 s for hexane (due to a clear overshoot).

Figure 28 (c-d) present the inlet and outlet concentrations of pattern two. As observed in pattern one, hexane breakthrough onset precedes toluene's, at $t_{5\%}$ = 1,021 s followed by toluene at $t_{5\%}$ = 3,368 s. Breakthrough completion for toluene is at $t_{95\%}$ = 8,220 s, which makes it's duration in pattern 2, 18 % longer than in pattern 1, due to the lower concentration of toluene in the mixture. For hexane, breakthrough completion is $t_{105\%}$ = 5,038 s, 3 % shorter than in pattern 1. Interestingly, in pattern 2 the breakthrough onset time for hexane is 2 % quicker than in pattern one, despite the lower toluene concentration, while toluene's breakthrough onset is 5 % larger

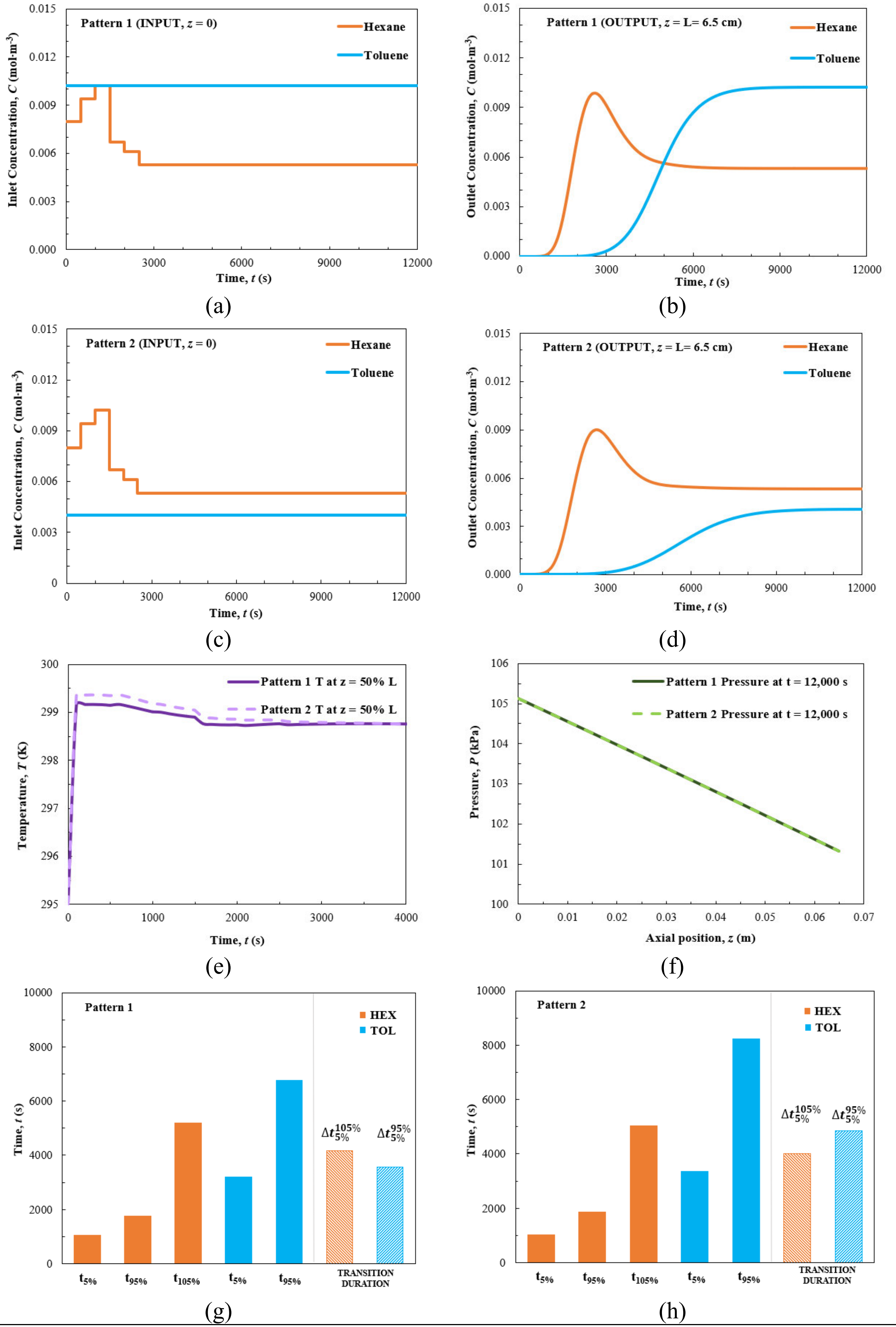

(a) (b)

(c) (d)

(e) (f)

(g) (h)

Figure 28. Simulation results for dynamic inlet patterns 1 and 2 of the hexane-toluene mixture.

compared to pattern one, as expected due to the decrease in inlet concentration between the two scenarios.

Figure 28 (e-f) show temperature and pressure variations for both said Patterns investigated. Continuous dark lines denote Pattern 1, while dashed light lines correspond to Pattern 2. As can be seen in plot (e), adsorption causes a temperature rise when taking place due to its exothermicity. Interestingly, the temperature rise of Pattern 1 leads to a marginally higher temperature rise (T_{max} = 299.37 K) compared to Pattern 2 (T_{max} = 299.17 K), in which toluene concentration is lower, before stabilising once the mass transfer zone has moved to later parts of the bed. The pressure drop, depicted in panel 1(f), is nearly the same for the two patterns, as expected due to flow conditions and feed concentrations.

Figure 28 (g-h) present the key metrics of breakthrough, quantifying the transition intervals. All breakthrough time metrics for both cases are summarised in Figure 28 (g-h) histograms.

Breakthrough durations therein are denoted by respective Δt symbols and lighter shading. For Pattern 2, where we have considered toluene at a 60% lower inlet concentration vs. Pattern 1, the breakthrough duration is 74% shorter; for hexane, it is only 4% shorter.

A remarkable observation emerges: though Pattern 1 has a clearly heavier VOC load vs. Pattern 2 (due only to the higher toluene level, as the hexane transient is kept invariant), the adsorption breakthrough duration is shorter for Pattern 1 vs. Pattern 2, for which it is longer. The strongly adsorbing component (toluene) affects the time to reach steady state.

9.2 Case Studies of DCM-ACT, DCM-TCM, DCM-TOL

The developed model was employed to examine the adsorption characteristics of binary VOC mixtures (with air as the carrier gas) under concentrations occurring in industrial settings. The validated model examines specifically the mixtures of DCM-Acetone, DCM-TCM, DCM-Toluene. Langmuir isotherm parameters for acetone (ACT) are taken from (Tefera et al., 2013), for trichloromethane (TCM) from (Chuang et al., 2003), for toluene (TOL) from (Delage et al., 2000) and for dichloromethane (DCM) are estimated based on data from (Talmoudi et al., 2018). Firstly, the effect of dynamic inlet concentrations is explored over four different pattern scenarios for each mixture. The inlet concentration patterns examined are in Table 33:

Table 33. Dynamic inlet concentration patterns in this PhD thesis.

		Inlet concentration, $C_{0,i}$ (ppm)		
Pattern	**Change timepoints**	**$0 < t < 1{,}000$ s**	**$1{,}000 \leq t < 3{,}000$ s**	**$t \geq 3{,}000$ s**
1	VOC 1	750	250	250
	VOC 2	250	750	750
2	VOC 1	250	750	750
	VOC 2	750	250	250
3	VOC 1	250	500	750
	VOC 2	250	250	250
4	VOC 1	250	250	250
	VOC 2	250	500	750

During patterns 1 and 2 the inlet concentrations of the VOCs change only once, at $t = 1{,}000$ s. For patterns 3 and 4, inlet concentration changes are examined in two timepoints; one at $t = 1{,}000$ s and one at $t = 3{,}000$ s. In patterns 1 and 2, both VOC's inlet concentrations change, while in patterns 3 and 4, one VOC's inlet concentration changes while the other one's remains constant. In all cases considered in this chapter the bed area remains constant at 0.000181 m^2.

The set of PDEs is solved using second order orthogonal collocation on finite elements with 30 discretisation points in the gPROMS® Process 2.0.0 software suite. For all cases considered, the DASolver SRADAU is employed, which uses a variable time step fully implicit Runge-Kutta method. The viscosities are computed from Wilke's equation, while densities are determined through pure component data via mixing rules (Coker, 2007; National Institute of Standards and Technology (NIST), 2023). The average particle size is 0.75 mm, 99% by mass between 0.60 and 0.84 mm (Tefera et al., 2013, Lashaki et al., 2012).

The main system parameters for all cases examined in this PhD thesis are in Table 34:

Table 34. Model parameter values for dynamic input simulations.

System	$C_{0,i}$ (ppm)	$D_{z,i}$ (m^2 s^{-1})	$\Delta H_{ad,i}$ (J mol^{-1})	T_{in} (K)	L (m)	V_s (m s^{-1})	q_m (mol kg^{-1})	k_{LDF} (s^{-1})	b_0 (m^3 mol^{-1})	Fig.
DCM-ACT	750	$1.47 \cdot 10^{-3}$	40,000	300	0.065	0.914	4.51	$2.70 \cdot 10^{-4}$	$7.41 \cdot 10^{-7}$	29-30
	250	$1.48 \cdot 10^{-3}$	51,100				7.06	$9.23 \cdot 10^{-5}$	$1.96 \cdot 10^{-8}$	
DCM-ACT	250	$1.47 \cdot 10^{-3}$	40,000	300	0.065	0.914	4.51	$3.01 \cdot 10^{-4}$	$7.41 \cdot 10^{-7}$	29-30
	750	$1.48 \cdot 10^{-3}$	51,100				7.06	$1.02 \cdot 10^{-4}$	$1.96 \cdot 10^{-8}$	
DCM-ACT	250	$1.47 \cdot 10^{-3}$	40,000	300	0.065	0.914	4.51	$2.69 \cdot 10^{-4}$	$7.41 \cdot 10^{-7}$	29-30
	500	$1.48 \cdot 10^{-3}$	51,100				7.06	$9.17 \cdot 10^{-5}$	$1.96 \cdot 10^{-8}$	
DCM-ACT	500	$1.47 \cdot 10^{-3}$	40,000	300	0.065	0.914	4.51	$2.52 \cdot 10^{-4}$	$7.41 \cdot 10^{-7}$	29-30
	250	$1.48 \cdot 10^{-3}$	51,100				7.06	$8.58 \cdot 10^{-5}$	$1.96 \cdot 10^{-8}$	
DCM-ACT	250	$1.48 \cdot 10^{-3}$	40,000	300	0.065	0.914	4.51	$2.39 \cdot 10^{-4}$	$7.41 \cdot 10^{-7}$	29-30
	250	$1.48 \cdot 10^{-3}$	51,100				7.06	$8.10 \cdot 10^{-5}$	$1.96 \cdot 10^{-8}$	
DCM-TCM	750	$1.48 \cdot 10^{-3}$	40,000	300	0.065	0.914	4.51	$4.70 \cdot 10^{-4}$	$7.41 \cdot 10^{-7}$	31-32
	250	$1.40 \cdot 10^{-3}$	44,769				2.49	$4.14 \cdot 10^{-5}$	$1.91 \cdot 10^{-6}$	
DCM-TCM	250	$1.48 \cdot 10^{-3}$	40,000	300	0.065	0.914	4.51	$8.61 \cdot 10^{-4}$	$7.41 \cdot 10^{-7}$	31-32
	750	$1.40 \cdot 10^{-3}$	44,769				2.49	$8.02 \cdot 10^{-5}$	$1.91 \cdot 10^{-6}$	
DCM-TCM	250	$1.48 \cdot 10^{-3}$	40,000	300	0.065	0.914	4.51	$6.46 \cdot 10^{-4}$	$7.41 \cdot 10^{-7}$	31-32
	500	$1.40 \cdot 10^{-3}$	44,769				2.49	$5.94 \cdot 10^{-5}$	$1.91 \cdot 10^{-6}$	
DCM-TCM	500	$1.48 \cdot 10^{-3}$	40,000	300	0.065	0.914	4.51	$4.49 \cdot 10^{-4}$	$7.41 \cdot 10^{-7}$	31-32
	250	$1.40 \cdot 10^{-3}$	44,769				2.49	$4.00 \cdot 10^{-5}$	$1.91 \cdot 10^{-6}$	
DCM-TCM	250	$1.47 \cdot 10^{-3}$	40,000	300	0.065	0.914	4.51	$4.31 \cdot 10^{-4}$	$7.41 \cdot 10^{-7}$	31-32
	250	$1.40 \cdot 10^{-3}$	44,769				2.49	$3.88 \cdot 10^{-5}$	$1.91 \cdot 10^{-6}$	
DCM-TOL	750	$1.47 \cdot 10^{-3}$	40,000	300	0.065	0.914	4.51	$3.04 \cdot 10^{-4}$	$7.41 \cdot 10^{-7}$	33-34
	250	$1.34 \cdot 10^{-3}$	45,500				4.61	$5.75 \cdot 10^{-5}$	$4.06 \cdot 10^{-7}$	
DCM-TOL	250	$1.48 \cdot 10^{-3}$	40,000	300	0.065	0.914	4.51	$4.31 \cdot 10^{-4}$	$7.41 \cdot 10^{-7}$	33-34
	750	$1.34 \cdot 10^{-3}$	45,500				4.61	$7.83 \cdot 10^{-5}$	$4.06 \cdot 10^{-7}$	
DCM-TOL	250	$1.48 \cdot 10^{-3}$	40,000	300	0.065	0.914	4.51	$3.45 \cdot 10^{-4}$	$7.41 \cdot 10^{-7}$	33-34
	500	$1.34 \cdot 10^{-3}$	45,500				4.61	$6.52 \cdot 10^{-5}$	$4.06 \cdot 10^{-7}$	
DCM-TOL	500	$1.47 \cdot 10^{-3}$	40,000	300	0.065	0.914	4.51	$2.87 \cdot 10^{-4}$	$7.41 \cdot 10^{-7}$	33-34
	250	$1.34 \cdot 10^{-3}$	45,500				4.61	$5.49 \cdot 10^{-5}$	$4.06 \cdot 10^{-7}$	
DCM-TOL	250	$1.47 \cdot 10^{-3}$	40,000	300	0.065	0.914	4.51	$2.72 \cdot 10^{-4}$	$7.41 \cdot 10^{-7}$	33-34
	250	$1.34 \cdot 10^{-3}$	45,500				4.61	$5.23 \cdot 10^{-5}$	$4.06 \cdot 10^{-7}$	

Table 35 summarizes the main structural (column and adsorbent) and thermal parameter values of the systems:

Table 35. Main structural and thermal parameter values of the systems.

System	$C_{0,i}$ (ppm)	ρ_b (kg m^{-3})	D (m)	T_{in} (K)	ε_b	ε_p	d_p (m)	C_{pp} (J kg^{-1} K^{-1})	C_{pg} (J kg^{-1} K^{-1})	k_{ez} (W m^{-1} K^{-1})	h_o (W m^{-2} K^{-1})	h_{int} (W m^{-2} K^{-1})	k_w (W m^{-1} K^{-1})	x (m)	Fig.
DCM-ACT	750 250	606	0.0152	300	0.38	0.56	0.00075	706.7	1,012	0.67	52.74	52.92	14.2	0.001	29-30
DCM-ACT	250 750	606	0.0152	300	0.38	0.56	0.00075	706.7	1,013	0.67	52.78	52.96	14.2	0.001	29-30
DCM-ACT	250 500	606	0.0152	300	0.38	0.56	0.00075	706.7	1,013	0.67	52.74	52.92	14.2	0.001	29-30
DCM-ACT	500 250	606	0.0152	300	0.38	0.56	0.00075	706.7	1,013	0.67	52.71	52.89	14.2	0.001	29-30
DCM-ACT	250 250	606	0.0152	300	0.38	0.56	0.00075	706.7	1,013	0.67	52.90	53.08	14.2	0.001	29-30
DCM-TCM	750 250	606	0.0152	300	0.38	0.56	0.00075	706.7	1,012	0.67	53.24	53.43	14.2	0.001	31-32
DCM-TCM	250 750	606	0.0152	300	0.38	0.56	0.00075	706.7	1,011	0.67	53.52	53.71	14.2	0.001	31-32
DCM-TCM	250 500	606	0.0152	300	0.38	0.56	0.00075	706.7	1,012	0.67	53.33	53.52	14.2	0.001	31-32
DCM-TCM	500 250	606	0.0152	300	0.38	0.56	0.00075	706.7	1,012	0.67	53.21	53.40	14.2	0.001	31-32
DCM-TCM	250 250	606	0.0152	300	0.38	0.56	0.00075	706.7	1,012	0.67	53.16	53.35	14.2	0.001	31-32
DCM-TOL	750 250	606	0.0152	300	0.38	0.56	0.00075	706.7	1,012	0.67	53.18	53.37	14.2	0.001	33-34
DCM-TOL	250 750	606	0.0152	300	0.38	0.56	0.00075	706.7	1,012	0.67	53.74	53.93	14.2	0.001	33-34
DCM-TOL	250 500	606	0.0152	300	0.38	0.56	0.00075	706.7	1,012	0.67	53.65	53.84	14.2	0.001	33-34
DCM-TOL	500 250	606	0.0152	300	0.38	0.56	0.00075	706.7	1,012	0.67	53.18	53.37	14.2	0.001	33-34
DCM-TOL	250 250	606	0.0152	300	0.38	0.56	0.00075	706.7	1,013	0.67	53.33	53.52	14.2	0.001	33-34

9.2.1 Transient Feed Results for DCM-ACT, DCM-TCM, DCM-TOL

The adsorption of three binary VOC mixtures (with air as the carrier gas) was studied under conditions of dynamic inlet concentrations. The breakthrough curves, depicting each component's concentration at the column outlet over time, as well as, temperature and pressure plots, are presented in Figure 29-Figure 34 and key breakthrough metrics are summarized in

Table **36**-Table 38 and Figure 35. Breakthrough onset time is calculated as the time required for the outlet concentration to reach 5% of the final concentration. Breakthrough completion time ($t_{95\%}$ / $t_{105\%}$) are calculated as the time required for the outlet concentration to reach 95% of the final concentration for the strongly adsorbing component and 105% of the final concentration for the component that exits the bed first.

Dynamic input simulation results for the mixture of dichloromethane-acetone are found in Figure 29-Figure 30 while key metrics are presented in Table 36. In Figure 29 (a–b), pattern 1, DCM starts at 250 ppm and acetone at 750 ppm. At t = 1,000 s, DCM's inlet concentration rises to 750 ppm and acetone's drops to 250 ppm. DCM is the first component to break through the column exit at t = 1,011 s (0.3 h) and acetone follows at t = 2,193 s (0.6 h). Interestingly, the breakthrough onset of DCM is 31 % later in pattern 1 where DCM's inlet concentration rises, compared to pattern 2 where it decreases over time. The duration of DCM's breakthrough is now 1,489 s (0.4 h), 62 % shorter than in pattern two. For acetone, the breakthrough duration becomes 1,025 s (0.3 h), which is 42% shorter compared to pattern two.

In Figure 29 (c–d), pattern two, DCM starts at 750 ppm and acetone at 250 ppm. At t = 1000 s, DCM's inlet concentration falls to 250 ppm and acetone's rises to 750 ppm. DCM quickly starts to break through the column first at t = 698 s (0.2 h) while acetone follows at t = 3,169 s (0.9 h). Duration of breakthrough is 3,877 s (1.1 h) for DCM and 1,782 s (0.5 h) for ACT.

In Figure 29 (e–f), pattern 3, the inlet concentration of DCM starts at 250 ppm, at t = 1,000s it rises to 500 ppm and at t = 3,000 s it further increases to 750 ppm while acetone's inlet concentration remains constant at 250 ppm throughout the simulation horizon. DCM starts to break through the column exit first at t =1,035 s (0.3 h) and acetone follows at t = 2,851 s (0.8 h). Although the initial and final concentration of DCM at pattern 3 are identical to pattern one, breakthrough onset is 4 % slower and duration is 59 % longer, possibly due to the intermediate concentration (500 ppm) step at t = 1,000 s. Acetone's breakthrough duration on the other hand, is 54 % longer than in pattern one where DCM's concentration increased without an intermediate concentration (500 ppm) step.

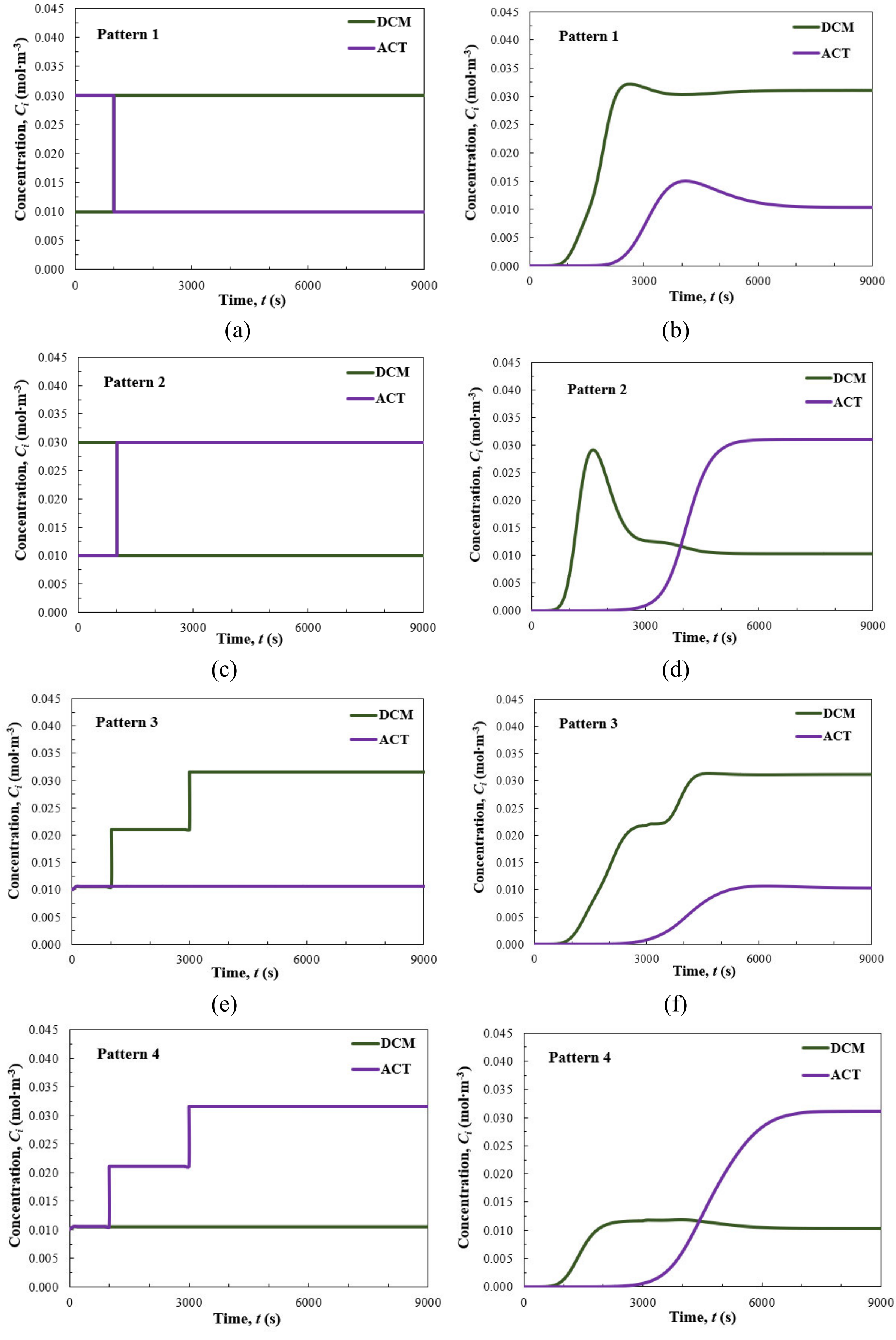

(a) (b)

(c) (d)

(e) (f)

(g) (h)

Figure 29. Dynamic inlet simulation results for DCM-Acetone: inlet (left) and outlet (right).

Figure 30 shows the temperature (*z*=50%*L)* and pressure profiles of the DCM-ACT mixtures.

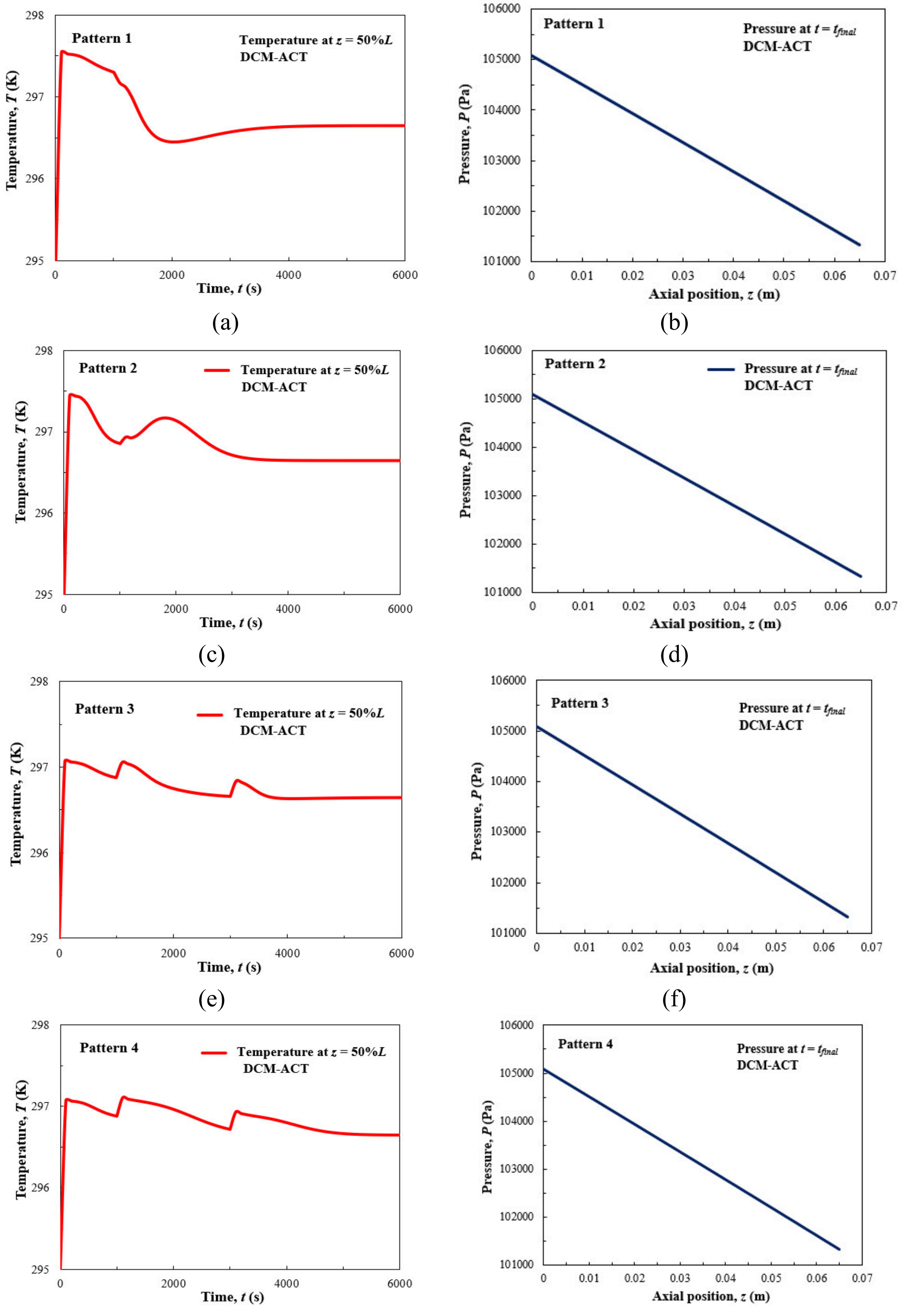

(a) (b)

(c) (d)

(e) (f)

(g) (h)

Figure 30. Temperature (left) and pressure (right) profiles of the DCM-ACT mixtures.

In Figure 29 (g–h), pattern four, the inlet concentration of DCM remains constant while acetone's increases from 250 ppm to 500 ppm and then 750 ppm at t = 1,000 s and t = 3,000 s respectively. DCM again exits the column first at t = 853 s (0.2 h), followed by acetone t = 3,363 s (0.9 h). In pattern two where acetone's inlet concentration increases, DCM has the fastest breakthrough onset, while the intermediate concentration step of acetone at 500 ppm seems to delay the breakthrough onset of DCM by 18 %. DCM's breakthrough duration is the longest among all other patterns at 4,797 s (1.3 h), while acetone also exhibits the longest duration among all patterns considered at 2,803 s (0.8 h).

Figure 35 (a–d) summarizes the key breakthrough outcomes for the DCM-ACT mixtures. It becomes apparent that the shortest breakthrough onset time for DCM occurs at the highest ACT concentration (pattern two), and thus is mainly dictated by the amount of stronger adsorbing component in the mixture. Moreover, breakthrough duration is longest for DCM with increased amounts of ACT (patterns 2 and 4), while ACT requires the longest in pattern 4.

Figure 30 (a) shows the temperature profile of pattern 1, (b) of pattern 2, (c) of pattern 3 and (d) of pattern 4. As expected, due to adsorption exothermicity, the temperature peaks indicate adsorption taking place at that specific part of the activated carbon bed. Patterns 1 and 2 have a distinct peak temperature profile compared to patterns 3 and 4. Specifically, patterns 1 and 2 exhibit two temperature peaks, while patterns 3 and 4, three, corresponding to the inlet concentration changes of each profile. Interestingly, pattern one demonstrates the highest peak temperature (T_{max} = 297.54 K) among all cases, while, pattern 3 the lowest (T_{max} = 297.07 K) even though in both cases, the inlet concentration of DCM reaches the same value (750 ppm), leading to the conclusion that acetone's high inlet concentration in pattern one, despite brief, significantly contributes to the heat release.

Figure 30 (b, d, f, h) presents the pressure profiles for all patterns examined for the DCM-ACT mixture. It becomes apparent that the inlet concentration fluctuations examined here do not impact the pressure drop encountered during component breakthrough.

Key breakthrough metrics (breakthrough onset, completion and duration) for the DCM-ACT mixture are summarized in

Table **36** and Figure 35. Due to the overshoot of DCM in DCM-ACT pattern 3 Figure 29 (d–f) not reaching 105 % of the final outlet concentration, the breakthrough completion, and thus breakthrough duration, of this case only has been calculated at the time of 102.5 % of outlet concentration ($\Delta t_{5\%}^{102.5\%}$).

Table 36. Key breakthrough metrics for the DCM-ACT mixture.

	Pattern	$t_{5\%}$ (s)	$t_{95\%}$ (s)	$t_{105\%}$ (s)	$\Delta t_{5\%}^{95\%}$ (s)	$\Delta t_{5\%}^{105\%}$ (s)	T_{max} (K)	ΔP (Pa)	Fig. 29-30
DCM	1	1,011	2,207	2,500	-	1,489	297.54	3,763.00	a-b
ACT		2,193	3,218	-	1,025	-			
DCM	2	698	1,079	4,575	-	3,877	297.44	3,763.00	c-d
ACT		3,169	4,951	-	1,782	-			
DCM	3	1,035	4,081	4,700	-	3,665	297.07	3,763.00	e-f
ACT		2,851	5,073	-	2,222	-			
DCM	4	853	1,786	5,650	-	4,797	297.10	3,763.00	g-h
ACT		3,363	6,166	-	2,803	-			

The results for the dynamic inlet simulation of the DCM-TCM mixture are presented in Figure 31-Figure 32 while key breakthrough metrics are presented in Table 37.

Table 37. Key breakthrough metrics for the DCM-TCM mixture.

	Pattern	$t_{5\%}$ (s)	$t_{95\%}$ (s)	$t_{105\%}$ (s)	$\Delta t_{5\%}^{95\%}$ (s)	$\Delta t_{5\%}^{105\%}$ (s)	T_{max} (K)	ΔP (Pa)	Fig. 31-32
DCM	1	1023	1,791	3,696	-	2,673	297.44	3,762.90	a-b
TCM		2833	4,276	-	1,443	-			
DCM	2	759	1,061	3,509	-	2,750	297.42	3,762.80	c-d
TCM		3166	3,694	-	528	-			
DCM	3	1068	3,632	5,744	-	4,675	297.04	3,762.90	e-f
TCM		4583	6,537	-	1,954	-			
DCM	4	926	1,583	4,221	-	3,295	297.04	3,762.80	g-h
TCM		3775	4,387	-	612	-			

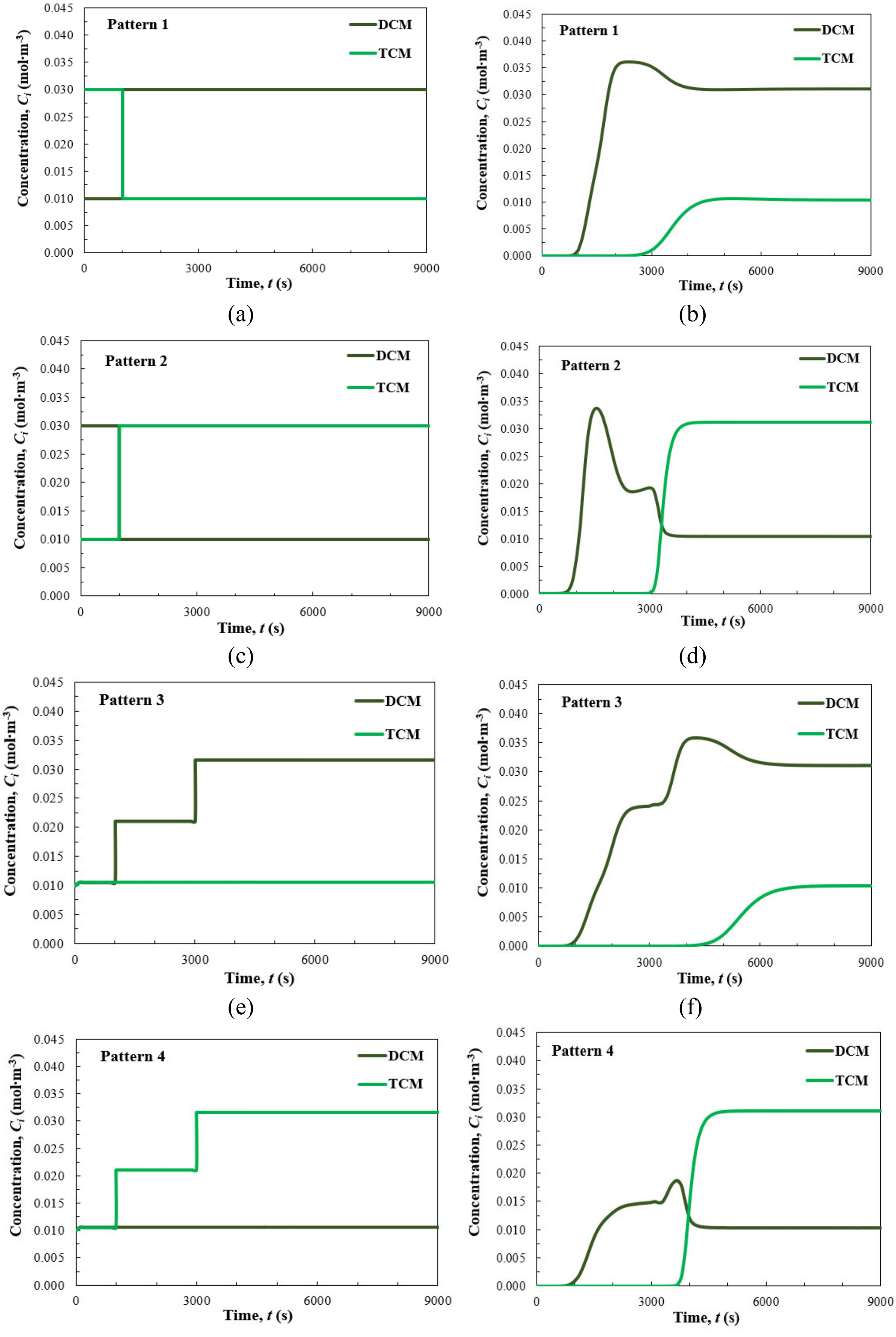

(a) (b)

(c) (d)

(e) (f)

(g) (h)

Figure 31. Dynamic inlet simulation results for DCM-TCM: inlet (left) outlet (right).

In Figure 31 (a–b), pattern one, the inlet concentration of DCM is initially 250 ppm and at t = 1000 s it rises to 750 ppm in contrast to chloroform's inlet concentration which starts at 750 ppm and is reduced to 250 ppm at t = 1,000 s. Here, DCM exits the column at t = 1,023 s (0.3 h), while chloroform on the other hand starts to break through the column at t = 2,833 s (0.8 h). Interestingly, chloroform's breakthrough onset is 11 % earlier compared to pattern two, where chloroform's inlet concentration increases over time. Breakthrough duration decreases compared to pattern two for DCM, being 3 % shorter at Δt = 2,673 s (0.7 h), whereas it increases for chloroform by 63 % at Δt = 1,443 s (0.4 h).

In Figure 31 (c–d), pattern two, DCM starts at the high inlet concentration of 750 ppm, and then at t = 1,000 s falls to 250 ppm, while the opposite change occurs for the inlet concentration of chloroform (TCM). In this scenario breakthrough duration is 2,750 s (0.8 h) for DCM and 528 s (0.1 h) for chloroform. DCM exits the column first at t = 759 s (0.2 h) and chloroform follows later at t = 3,166 s (0.9 h). As observed with the DCM-ACT mixture, DCM's breakthrough onset time is 26 % earlier than in pattern one, where DCM'S inlet concentration increases over time.

In Figure 31 (e–f), pattern 3, the inlet concentration of chloroform remains constant while the inlet concentration of DCM undergoes step increases at t = 1,000 s and t = 3,000 s, from 250 ppm to 500 ppm and 750 ppm respectively. In this scenario, DCM exits the column first at t = 1,068 s (0.3 h) while chloroform follows at t = 4,583 s (1.3 h), thus demonstrating the latest breakthrough onset times among all patterns considered for this mixture. Specifically, DCM's breakthrough onset is 4 % later compared to pattern one whereas chloroform's 38 % later. The breakthrough durations of both components are also the longest with DCM requiring 4,675 s (1.3 h) and chloroform 1,954 s (0.5 h) to complete breakthrough.

In Figure 31 (g–h), pattern 4, DCM's inlet concentration remains the constant at 250 ppm while the inlet concentration of chloroform rises from 250 ppm to 500 ppm and finally to 750 ppm at t = 1,000 s and t = 3,000 s respectively. DCM starts to exit the column first at t = 926 s (0.3 h), 18 % later than in pattern two, possibly due to the intermediate step increase of the TCM's inlet concentration, while TCM follows at t = 3,775 s (1 h), 16 % later compared to pattern two. Compared to pattern two, breakthrough duration is longer; the value for DCM is 17 % larger and for chloroform 14 % larger.

Figure 32 (a, c, e, g) present the temperature profiles at the column middle for the DCM-TCM mixtures. The temperature profile trends observed for the DCM-TCM mixtures are in

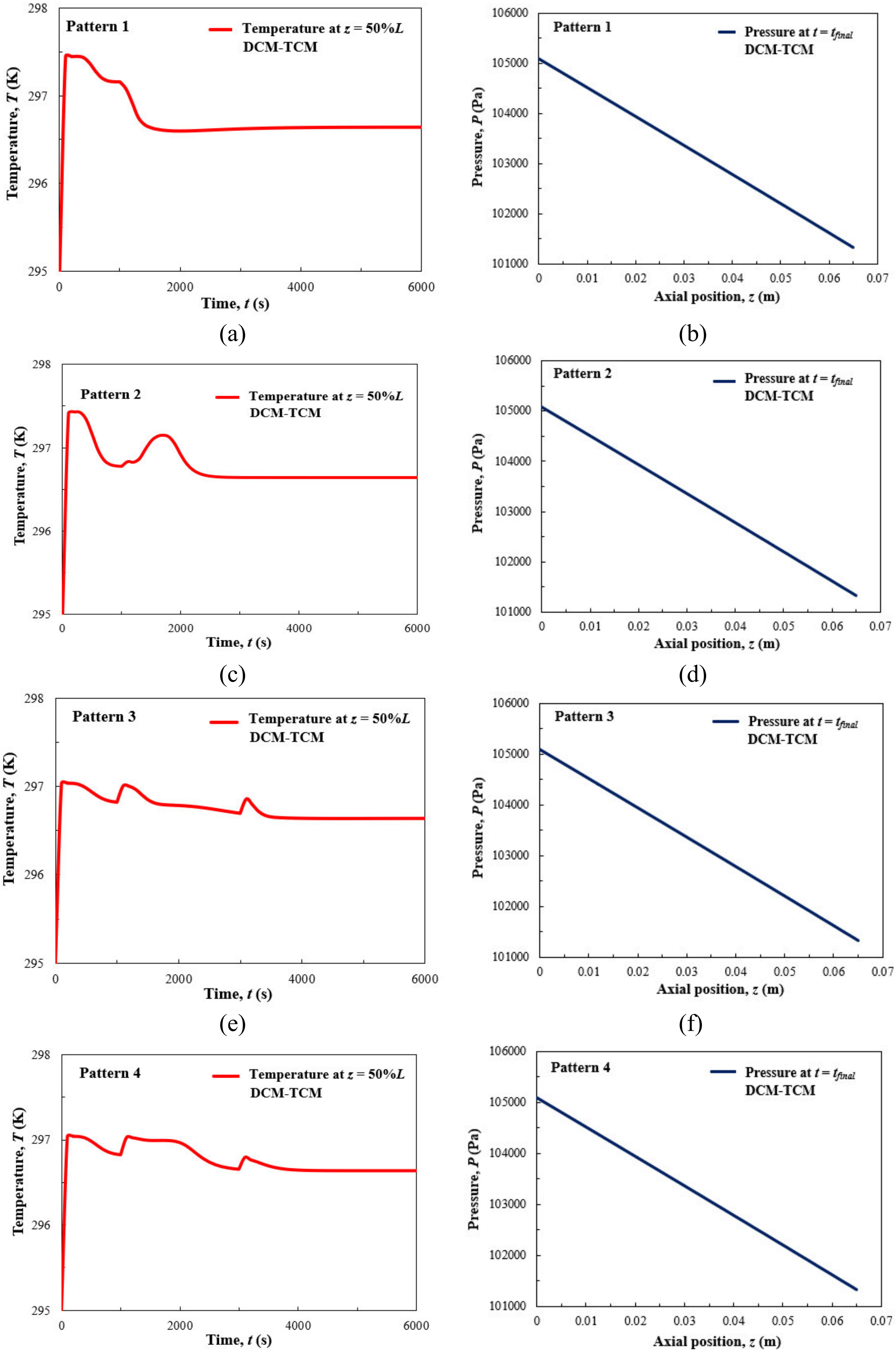

(a) (b)

(c) (d)

(e) (f)

(g) (h)

Figure 32. Temperature (left) and pressure (right) profiles of the DCM-TCM mixtures.

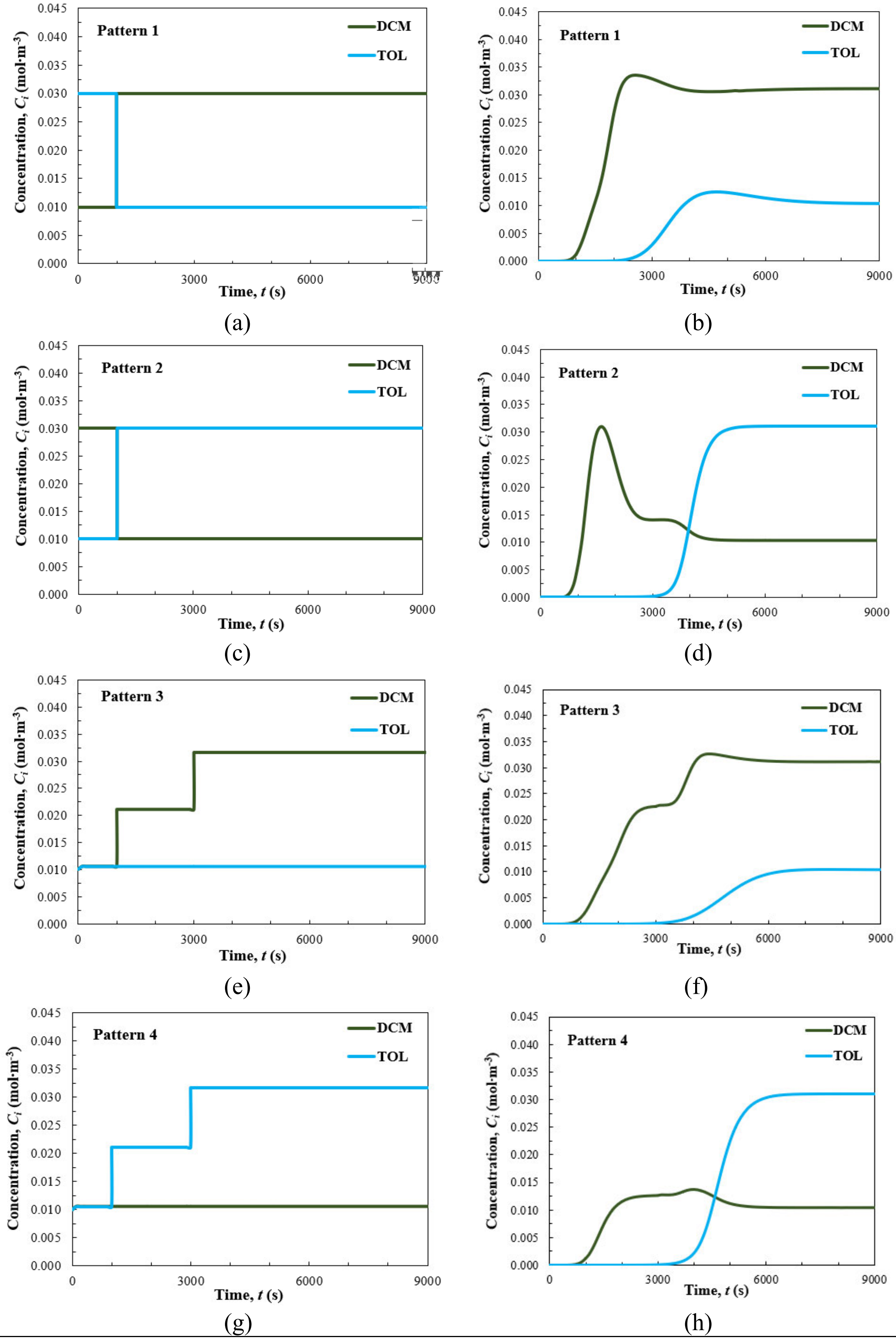

(a) (b)

(c) (d)

(e) (f)

(g) (h)

Figure 33. Dynamic inlet simulation results for DCM-Toluene: inlet (left) outlet (right).

agreement with the corresponding DCM-ACT mixtures. As with the DCM-ACT mixtures, here, pattern one demonstrates again the highest peak temperature (T_{max} = 297.44 K) among all cases. However, interestingly patterns 3 and 4 both exhibit the lowest (T_{max} = 297.04 K) temperature peak, despite the opposite inlet concentration changes. For the DCM-TCM mixtures the peak temperatures among all patterns are lower compared to their DCM-ACT mixtures equivalents due to the lower value of heat of adsorption of trichloromethane compared to acetone's.

Figure 32 (b, d, f, h) present the pressure profiles of the four dynamic inlet concentration patterns for the DCM-TCM mixtures. The linear profiles are in agreement with the DCM-ACT mixtures and have only a minute difference in values. Furthermore, the inlet concentration changes have little effect on pressure drop as seen from Table 37 values.

Figure 35 (e–h) summarizes the breakthrough metrics for all DCM-TCM mixtures examined. DCM starts to exit the column faster when in a mixture with high concentrations with TCM (patterns 2 and 4), whereas the longest breakthrough duration occurs, interestingly, for pattern three for both DCM and TCM.

The results for DCM-TOL are found in Figure 33-Figure 34 and key metrics in Table 38.

In Figure 33 (a–b), pattern 1, the inlet concentration of DCM initially is 250 ppm and then rises to 750 ppm at t = 1,000 s, whereas the opposite happens for toluene's. DCM's breakthrough onset starts 30 % later compared to pattern two, at t = 1,023 s (0.3 h), whereas TOL starts to breakthrough 30% earlier than in pattern two, at t = 2,451 s (0.7 h). While breakthrough duration for DCM decreases by 31 % compared to pattern 2, to 2,296 s (0.6 h), for TOL it is 10 % longer at 1,326 s (0.4 h).

Figure 33 (c–d), pattern 2, sees DCM's inlet concentration start at 750 ppm and drop to 250 ppm at t = 1,000 s while the opposite happens for TOL. DCM exits the column first, at t = 714 s (0.2 h), while TOL follows at t = 3,488 s (1 h). Breakthrough duration is 3,697 s (1 h) for DCM and 1,176 s (0.3 h) for TOL.

Table 38. Key breakthrough metrics for the DCM-TOL mixture.

	Pattern	**$t_{5\%}$ (s)**	**$t_{95\%}$ (s)**	**$t_{105\%}$ (s)**	**$\Delta t_{5\%}^{95\%}$ (s)**	**$\Delta t_{5\%}^{105\%}$ (s)**	**T_{max} (K)**	**ΔP (Pa)**	**Fig. 33-34**
DCM	1	1,023	2,076	3,319	-	2,296	297.45	3,762.90	a-b
TOL		2,451	3,777	-	1,326	-			
DCM	2	714	1,081	4,411	-	3,697	297.41	3,762.80	c-d

TOL		3,488	4,664	-	1,176	-			
DCM	3	1,042	3,900	4,976	-	3,934	297.04	3,763.00	e-f
TOL		3,528	6,071	-	2,543	-			
DCM	4	873	1,716	5,304	-	4,431	297.04	3,762.90	g-h
TOL		3,901	5,578	-	1,678	-			

Figure 33 (e–f), pattern 3, finds the inlet concentration of toluene constant at 250 ppm and DCM's sustaining step increases from 250 ppm, to 500 ppm and 750 ppm at t = 1,000 s and t = 3,000 s respectively. DCM starts to exit the column first, at t = 1,042 s (0.3 h), later by 2 % compared to pattern one, whereas toluene follows at t = 3,528 s (1 h), later by 31 % compared to pattern one. As with the previous binary mixtures, pattern three demonstrates the latest breakthrough onset for DCM among all cases, despite the significant increase in concentration. Breakthrough durations of are 42 % longer, Δt = 3,934 s (1.1 h), for DCM, and 48 % longer, Δt = 2,543 s (0.7 h), for toluene compared to pattern one.

Figure 33 (g–h), pattern four, shows the inlet concentration of DCM constant at 250 ppm, while toluene's increases to first 500 ppm and then to 750 ppm at t = 1,000 s and t = 3,000 s respectively. It is noted that DCM starts to exit the column first, at t = 873 s (0.2 h), which is 18 % later compared to pattern two. Therefore, the intermediate concentration step (500 ppm) during the inlet concentration increase promotes the later onset of DCM's breakthrough. Toluene's breakthrough onset also starts 11 % later compared to pattern two at $t_{5\%}$ = 3,901 s (1.1 h). Breakthrough durations of both components are longer than pattern two; by 17 % for dichloromethane and 30 % for toluene.

Figure 34 shows the temperature (mid-column) and pressure profiles for the dichloromethane-toluene mixtures. The temperature profile trends of all four patterns examined agree with the DCM-ACT and DCM-TCM mixtures. Pattern one once more exhibits the highest temperature peak among all dynamic inlet concentration patterns (T_{max} = 297.45 K) while patterns 3 and 4 the lowest at T_{max} = 297.04 K. Finally, the pressure drops of the DCM-TOL mixtures in Figure 34 (b, d, f, h) concur with values reported for the other two binaries and show minimal fluctuation among the inlet patterns.

Figure 35 (i–l) summarises the breakthrough metrics for all DCM-TOL mixtures. For both DCM and TOL, the earliest breakthrough onset occurs for at the highest TOL concentration (pat. 2), while the shortest duration interestingly occurs for pat. 1 for DCM and pat. 2 for TOL.

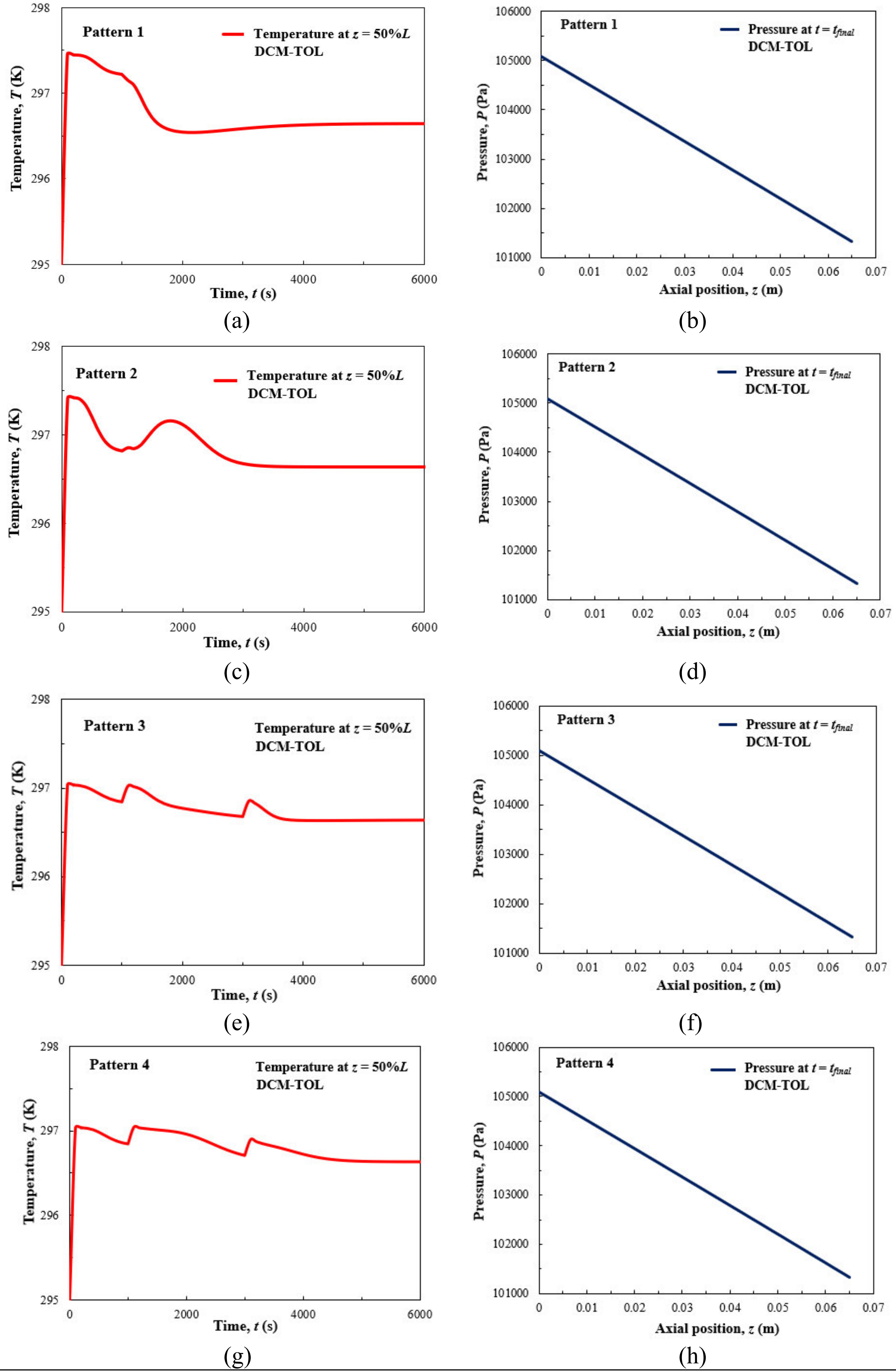

(a) (b)

(c) (d)

(e) (f)

(g) (h)

Figure 34. Temperature (left) and pressure (right) profiles for the DCM-TOL mixtures.

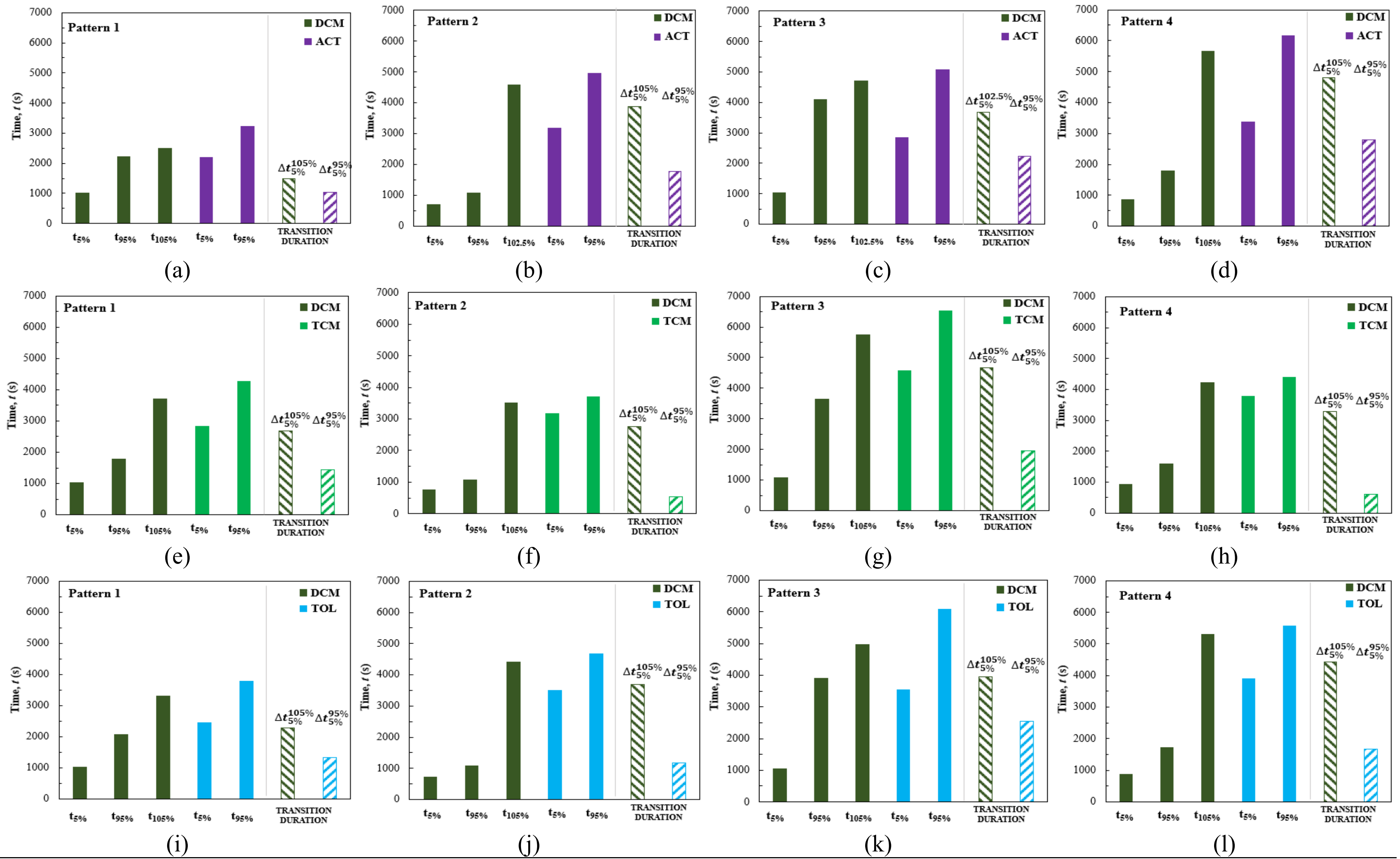

Figure 35. Breakthrough metrics for all case studies.

9.3 Chapter Conclusions

The mixture of hexane-toluene with air as the carrier gas is studied under inlet conditions informed by industrial data. Two VOC inlet patterns are studied where hexane undergoes a series of inlet concentration changes and toluene remains at a constant high (250 ppm) inlet concentration in one scenario and toluene remains at a constant low (100 ppm) inlet concentration in the second scenario. Results reveal a later breakthrough onset time for hexane when in a mixture with a high (250 ppm) toluene inlet concentration, while the opposite happens for toluene. The transient duration is longer for the lower VOC load. Temperature rises in the bed as well as pressure drop increase with increased VOC solvent stream load. This PhD thesis paves the way for waste stream sequencing efforts, not only under batch, but also future continuous pharmaceutical manufacturing optimisation efforts.

Three mixtures, namely DCM-Acetone, DCM-Chloroform and DCM-Toluene, with air as the carrier gas are studied under the same four dynamic inlet concentration patterns on an activated carbon bed. First, in pattern one, component one starts at a high (750 ppm) inlet concentration and component two at a low (250 ppm) inlet concentration, and at t = 1,000 s they switch to 250 ppm and 750 ppm inlet concentrations respectively. In pattern two, the opposite happens. In pattern three, component one starts at a low (250 ppm) feed concentration which at t = 1,000 s increases to 500 ppm and at t = 3,000 s rises to the high 750 ppm feed concentration, all while component two feed concentration remains constant at 250 ppm. In pattern four, the feed concentration of component two undergoes the same changes, while the feed concentration of component one remains constant at 250 ppm.

Key breakthrough metrics highlight trends observed across all three mixtures concerning column exit behaviour. Specifically, for all binary mixtures, the fastest breakthrough onset time for DCM is observed in pattern two, whereas the slowest in pattern three. Thus, maintaining a low feed concentration of the last to exit the bed mixture component (ACT/TCM/TOL) is essential in prolonging the breakthrough onset time of DCM even if that exists in the feed stream in a higher load. The latest breakthrough onset for the strongly retained component (ACT/TCM/TOL) occurs, surprisingly, due to their high load, for pattern four for acetone and toluene and for pattern three for chloroform.

Transient duration for DCM is longest with the lowest feed concentration (pattern four) when in a mixture with acetone or toluene, but in pattern three when in a mixture with chloroform. For chloroform and toluene, transient duration is longer in the lowest feed load (pattern three), whereas for acetone in pattern four with an increasing feed load. Interestingly, while input transitions only last for 1,000 s (patterns 1, 2) and 3,000 s (patterns 3, 4), the output transitions well surpass those durations for most cases. Pattern one demonstrates the highest temperature peaks across all binary mixtures, whereas the lowest peak temperatures are found in patterns three and four. In contrast with temperature, pressure drop remains almost unaffected by mixture composition changes.

Chapter 10

Binary Mixture Sensitivity Analysis: Column Length and Velocity

This Chapter demonstrates the application of our model to the examination of the effect of different superficial velocities on different activated carbon fixed bed columns, ranging from laboratory to industrial for the binary mixtures of hexane-acetone, hexane-dichloromethane and hexane-toluene. Furthermore, in this chapter a new breakthrough onset metric is introduced to elucidate the relationship between column length, superficial velocity and multicomponent mixture composition for potential column operation design applications.

The results presented in this chapter have also been submitted for publication in the literature (Tzanakopoulou et al., 2024. *Processes*, submitted for publication); details can be found in Appendix B.

10.1 Case Studies ACT-HEX, DCM-HEX, TOL-HEX

The developed model was employed to examine the adsorption characteristics of binary VOC mixtures (with air as the carrier gas) under six different superficial velocities (V_s = 0.1, 0.2, 0.3, 0.5, 0.7, 0.9 m s^{-1}) and four different bed lengths (L = 0.25, 0.50, 0.75, 1 m) ranging from laboratory (L = 0.25 m) to industrial (L = 1 m) scale. The validated model examines specifically the mixtures acetone-hexane (ACT-HEX), dichloromethane-hexane (DCM-HEX) and toluene-hexane (TOL-HEX). Langmuir isotherm parameters for acetone (ACT) are taken from (Tefera et al., 2013), for hexane (HEX) from (Chuang et al., 2003; Shim et al., 2003), for toluene (TOL) from (Delage, 2000) and for dichloromethane (DCM) are estimated based on data from (Talmoudi et al., 2018). The present paper presents detailed simulation results for the boundary cases of bed length (L = 0.25 m and L = 1 m) and three velocities (V_s = 0.1, 0.5, 0.9 m s^{-1}) for brevity.

The set of PDEs is solved using second order orthogonal collocation on finite elements in the gPROMS® Process 2.0.0 software suite. For all cases considered, the DASolver SRADAU is employed, which uses a variable time step fully implicit Runge-Kutta method. The viscosities are computed from Wilke's equation, while densities are determined through pure component data via mixing rules (Coker, 2007; National Institute of Standards and Technology (NIST), 2023),(Coker, 2007). The average particle size is 0.75 mm, 99% by mass between 0.60 and 0.84 mm (Tefera et al., 2013, Lashaki et al., 2012). The main system parameters for all cases presented in this PhD thesis are in Table 39-Table 40:

Table 39. Model parameters for dynamic simulations.

System	$C_{0,i}$ (ppm)	$D_{z,i}$ ($m^2\ s^{-1}$)	$\Delta H_{ad,i}$ ($J\ mol^{-1}$)	T_{in} (K)	L (m)	V_s ($m\ s^{-1}$)	q_m ($mol\ kg^{-1}$)	ε_b	k_{LDF} (s^{-1})	b_0 ($m^3\ mol^{-1}$)	Fig.
HEX-ACT	250	$0.68 \cdot 10^{-3}$	51,100	300	0.25-1	0.1	7.060	0.38	$8.45 \cdot 10^{-5}$	$1.96 \cdot 10^{-8}$	36-37
	250	$0.52 \cdot 10^{-3}$	50,000				3.801		$1.66 \cdot 10^{-4}$	$2.35 \cdot 10^{-8}$	
HEX-ACT	250	$1.07 \cdot 10^{-3}$	51,100	300	0.25-1	0.5	7.060	0.38	$8.45 \cdot 10^{-5}$	$1.96 \cdot 10^{-8}$	36-37
	250	$0.91 \cdot 10^{-3}$	50,000				3.801		$1.66 \cdot 10^{-4}$	$2.35 \cdot 10^{-8}$	
HEX-ACT	250	$1.47 \cdot 10^{-3}$	51,100	300	0.25-1	0.9	7.060	0.38	$8.45 \cdot 10^{-5}$	$1.96 \cdot 10^{-8}$	36-37
	250	$1.31 \cdot 10^{-3}$	50,000				3.801		$1.66 \cdot 10^{-4}$	$2.35 \cdot 10^{-8}$	
HEX-DCM	250	$0.67 \cdot 10^{-3}$	40,000	300	0.25-1	0.1	4.510	0.38	$2.32 \cdot 10^{-4}$	$7.41 \cdot 10^{-7}$	36-37
	250	$0.52 \cdot 10^{-3}$	50,000				3.801		$1.55 \cdot 10^{-4}$	$2.35 \cdot 10^{-8}$	
HEX-DCM	250	$1.07 \cdot 10^{-3}$	40,000	300	0.25-1	0.5	4.510	0.38	$2.32 \cdot 10^{-4}$	$7.41 \cdot 10^{-7}$	36-37
	250	$0.91 \cdot 10^{-3}$	50,000				3.801		$1.55 \cdot 10^{-4}$	$2.35 \cdot 10^{-8}$	
HEX-DCM	250	$1.46 \cdot 10^{-3}$	40,000	300	0.25-1	0.9	4.510	0.38	$2.32 \cdot 10^{-4}$	$7.41 \cdot 10^{-7}$	36-37
	250	$1.31 \cdot 10^{-3}$	50,000				3.801		$1.55 \cdot 10^{-4}$	$2.35 \cdot 10^{-8}$	
HEX-TOL	250	$0.54 \cdot 10^{-3}$	45,500	300	0.25-1	0.1	4.610	0.38	$5.36 \cdot 10^{-5}$	$4.06 \cdot 10^{-7}$	36-37
	250	$0.52 \cdot 10^{-3}$	50,000				3.801		$1.91 \cdot 10^{-4}$	$2.35 \cdot 10^{-8}$	
HEX-TOL	250	$0.93 \cdot 10^{-3}$	45,500	300	0.25-1	0.5	4.610	0.38	$5.36 \cdot 10^{-5}$	$4.06 \cdot 10^{-7}$	36-37
	250	$0.91 \cdot 10^{-3}$	50,000				3.801		$1.91 \cdot 10^{-4}$	$2.35 \cdot 10^{-8}$	
HEX-TOL	250	$1.33 \cdot 10^{-3}$	45,500	300	0.25-1	0.9	4.610	0.38	$5.36 \cdot 10^{-5}$	$4.06 \cdot 10^{-7}$	36-37
	250	$1.31 \cdot 10^{-3}$	50,000				3.801		$1.91 \cdot 10^{-4}$	$2.35 \cdot 10^{-8}$	

Table 40 summarizes the main structural (column and adsorbent) and thermal parameter values of the systems:

Table 40. Main structural and thermal parameter values for the systems.

System	$C_{0,i}$ (ppm)	ρ_b (kg m^{-3})	D (m)	T_{in} (K)	ε_p	d_p (m)	C_{pp} (J kg^{-1} K^{-1})	C_{pg} (J kg^{-1} K^{-1})	k_{ez} (W m^{-1} K^{-1})	h_o (W m^{-2} K^{-1})	h_{int} (W m^{-2} K^{-1})	k_w (W m^{-1} K^{-1})	x (m)	Fig.
HEX-ACT	250 250	606	0.0152	300	0.56	0.00075	706.7	1,014	0.13	9.05	9.05	14.2	0.001	36-37
HEX-ACT	250 250	606	0.0152	300	0.56	0.00075	706.7	1,014	0.39	32.75	32.82	14.2	0.001	36-37
HEX-ACT	250 250	606	0.0152	300	0.56	0.00075	706.7	1,014	0.66	52.33	52.52	14.2	0.001	36-37
HEX-DCM	250 250	606	0.0152	300	0.56	0.00075	706.7	1,013	0.13	9.04	9.05	14.2	0.001	36-37
HEX-DCM	250 250	606	0.0152	300	0.56	0.00075	706.7	1,013	0.39	32.74	32.81	14.2	0.001	36-37
HEX-DCM	250 250	606	0.0152	300	0.56	0.00075	706.7	1,013	0.66	52.32	52.50	14.2	0.001	36-37
HEX-TOL	250 250	606	0.0152	300	0.56	0.00075	706.7	1,014	0.13	9.06	9.06	14.2	0.001	36-37
HEX-TOL	250 250	606	0.0152	300	0.56	0.00075	706.7	1,014	0.39	32.80	32.87	14.2	0.001	36-37
HEX-TOL	250 250	606	0.0152	300	0.56	0.00075	706.7	1,014	0.66	52.41	52.60	14.2	0.001	36-37

10.2 Results of Dynamic Simulations

The adsorption of three binary VOC mixtures (with air as the carrier gas) was examined at two bed lengths (L = 0.25, 1 m) and three superficial velocities (V_s = 0.1, 0.5, 0.9 m s^{-1}). The breakthrough curves, depicting each component's concentration at the column outlet over time, are presented in Figure 36 and key breakthrough metrics are summarized in Table 41-Table 43 and Figure 38. Breakthrough onset time is calculated as the time required for the outlet concentration to reach 5% of the final concentration. Breakthrough completion times ($t_{95\%}$ - $t_{105\%}$) are calculated as the time required for the outlet concentration to reach 95% of the final concentration for the strongly adsorbing component and 105% of the final concentration for the component that exits the bed first. Each colour corresponds to one superficial velocity and two sets of lines; one set for L = 0.25 m and one set for L = 1 m. In all cases considered in this chapter the bed area remains constant at 0.000181 m^2 while superficial velocities change up to 0.9 m s^{-1} to avoid fluidization phenomena.

Figure 36 (a) presents the breakthrough curves for the mixture of hexane-acetone (HEX-ACT). Breakthrough curves represent the concentration at the column outlet vs. time. It becomes apparent that the greater the superficial velocity, the sooner the breakthrough onset time. For each colour, the first set of lines, corresponding to L = 0.25 m, demonstrates a faster breakthrough onset compared to the second set of lines of same colour which represent the case of L = 1 m. It is interesting to note that for L = 1 m, the peak concentration of hexane increases with increasing superficial velocity.

At L = 0.25 m, for V_s = 0.1 m s^{-1}, the breakthrough onset time of hexane is 66,240 s, which is 81% later compared to V_s = 0.5 m s^{-1}, and 90% later compared to V_s = 0.9 m s^{-1}. At L = 1 m, for V_s = 0.1 m s^{-1}, breakthrough onset time of hexane is 303,888 s, which is 82% later compared to V_s = 0.5 m s^{-1}, and 92% later compared to V_s = 0.9 m s^{-1}. For V_s = 0.1 m s^{-1}, the breakthrough onset of hexane at L = 0.25 m is 78% earlier compared to L = 1 m while for V_s = 0.5 m s^{-1}, 76% earlier and for V_s = 0.9 m s^{-1}, 75% earlier.

The breakthrough onset time of acetone at L = 0.25 m is $t_{5\%}$ = 135,185 s, which is 80% later compared to V_s = 0.5 m s^{-1}, and one order of magnitude later compared to V_s = 0.9 m s^{-1}. For V_s = 0.1 m s^{-1}, the breakthrough onset of acetone is 78% sooner at L = 0.25 m compared to L = 1 m, while for V_s = 0.5 m s^{-1}, acetone's onset is 76% earlier at L = 0.25 m vs. L = 1 m, and for V_s = 0.9 m s^{-1}, 73% earlier.

Moreover, Figure 36 (a) also informs regarding breakthrough duration of the HEX-ACT mixtures. At L = 0.25 m, the breakthrough duration of hexane is 101,249 s for V_s = 0.1 m s^{-1}, which is 82% longer than for V_s = 0.5 m s^{-1}, and one order of magnitude longer than for V_s = 0.9 m s^{-1}. For V_s = 0.1 m s^{-1}, the breakthrough duration of hexane is 72% shorter for L = 0.25 m, compared to L =1 m and for V_s = 0.5 m s^{-1}, 70% shorter for L = 0.25 m, compared to L =1 m. Finally, for V_s = 0.9 m s^{-1}, the breakthrough duration for hexane is 65% quicker for L = 0.25 m than for L = 1 m.

For acetone, at L = 0.25 m, the breakthrough duration at V_s = 0.1 m s^{-1} is 51,622 s, which is 86% longer compared to V_s = 0.5 m s^{-1} and 91% compared to V_s = 0.9 m s^{-1}. For V_s = 0.1 m s^{-1}, the breakthrough duration for acetone is 23% shorter for L = 0.25 m compared to L = 1 m. For V_s = 0.5 m s^{-1}, the breakthrough duration for acetone is 4% shorter for L = 0.25 m compared to L = 1 m and for V_s = 0.9 m s^{-1}, 2% shorter for L = 0.25 m than L = 1 m.

Figure 37 (a) also presents key temperature and pressure drop metrics for the ACT-HEX mixtures. Specifically, the highest temperature peak is observed for L = 0.25 m at T_{max} = 296.58 K for V_s = 0.9 m s^{-1} , and the lowest T_{max} = 295.26 K for V_s = 0.1 m s^{-1} , but a 1 m long column. Pressure drop, as predicted by Ergun's equation, is lowest for the smallest velocity (V_s = 0.1 m s^{-1}) at 0.91 kPa for L = 0.25 m and 3.75 kPa for L = 1 m.

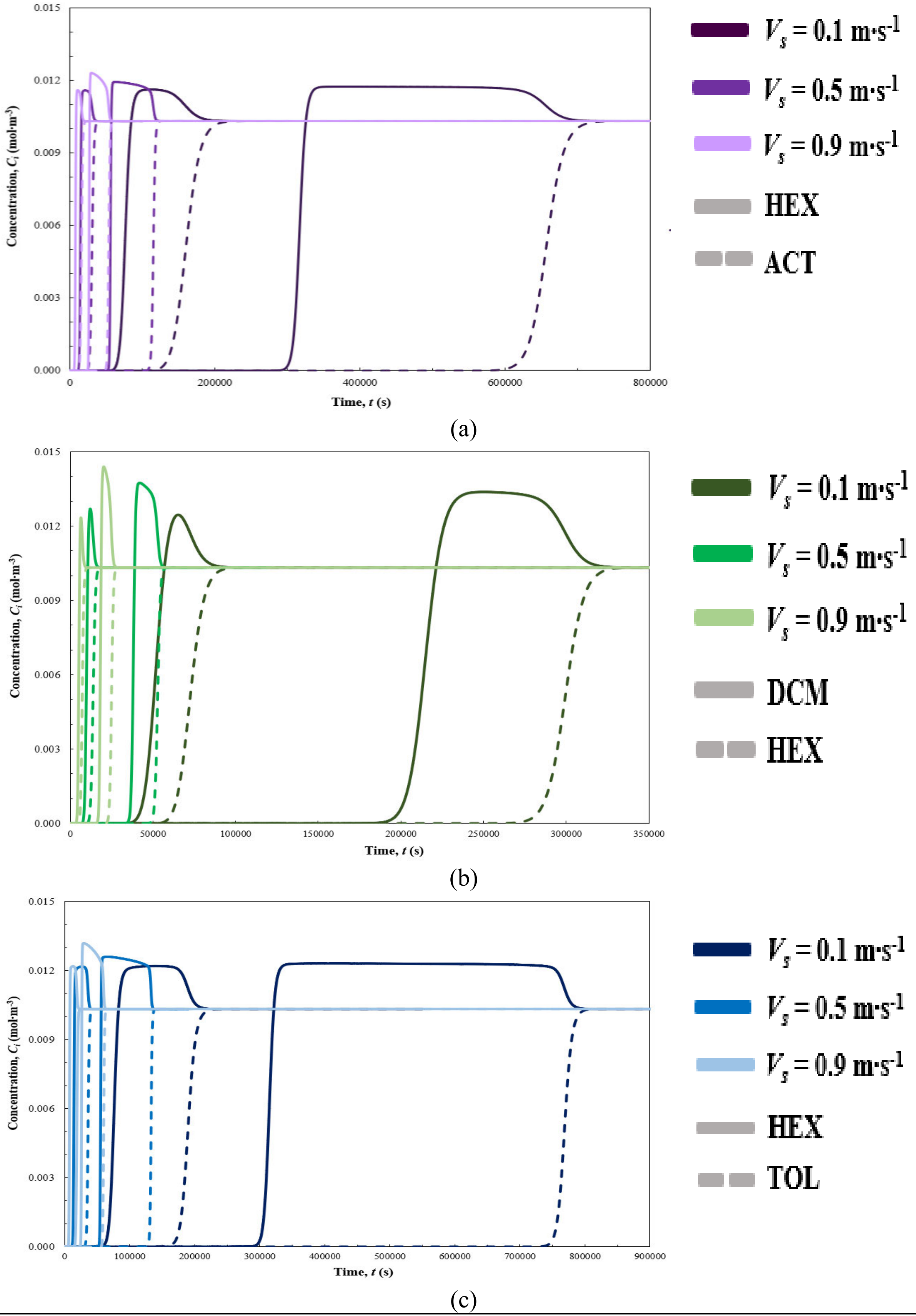

(a)

(b)

(c)

Figure 36. Breakthrough curves of binary mixtures at L = 0.25 m (left) and L = 1 m (right).

Table 41-Table 43 present key breakthrough metrics for the examined mixtures.

Table 41. Key breakthrough metrics for the HEX-ACT mixture.

	V_s (m s^{-1})	$t_{5\%}$ (s)	$t_{95\%}$ (s)	$t_{105\%}$ (s)	$\Delta t_{5\%}^{95\%}$ (s)	$\Delta t_{5\%}^{105\%}$ (s)	T_{max} (K)	ΔP (kPa)	Fig. 36-37
				L = 0.25 m					
ACT	0.1	135,185	186,806	-	51,622	-	295.80	0.91	(a)
HEX		66,240	82,722	167,489	-	101,249			
ACT	0.5	26,858	34,048	-	7,190	-	296.33	6.26	(a)
HEX		12,801	15,504	31,357	-	18,556			
ACT	0.9	13,617	18,349	-	4,732	-	296.58	15.15	(a)
HEX		6,448	8,292	16,517	-	10,069			
	V_s (m s^{-1})	**$t_{5\%}$ (s)**	**$t_{95\%}$ (s)**	**$t_{105\%}$ (s)**	**$\Delta t_{5\%}^{95\%}$ (s)**	**$\Delta t_{5\%}^{105\%}$ (s)**	**T_{max} (K)**	**ΔP (kPa)**	**Fig. 36-37**
				L = 1 m					
ACT	0.1	622,722	689,812	-	67,089	-	295.26	3.75	(a)
HEX		303,888	323,394	666,333	-	362,445			
ACT	0.5	111,102	118,558	-	7,457	-	295.40	28.41	(a)
HEX		54,223	56,818	115,936	-	61,714			
ACT	0.9	50,841	55,686	-	4,846	-	295.55	77.92	(a)
HEX		25,375	26,999	53,942	-	28,567			

Figure 36(b) presents the breakthrough curves for the mixture of hexane-dichloromethane (HEX-DCM). Key metrics are summarized in Table 42 and Figure 38(d-f). At L = 0.25 m, for V_s = 0.1 m s^{-1}, the breakthrough onset time of hexane is 62,155 s, which is 81% later compared to V_s = 0.5 m s^{-1}, and 90% later compared to V_s = 0.9 m s^{-1}. At L = 1 m, for V_s = 0.1 m s^{-1}, breakthrough onset time of hexane is 283,768 s, which is 82% later compared to V_s = 0.5 m s^{-1}, and 92% later compared to V_s = 0.9 m s^{-1}. For V_s = 0.1 m s^{-1}, the breakthrough onset of hexane at L = 0.25 m is 78% earlier compared to L = 1 m while for V_s = 0.5 m s^{-1}, 76% earlier and for V_s = 0.9 m s^{-1}, 74% earlier.

The breakthrough onset time of DCM at L = 0.25 m, for V_s = 0.1 m s^{-1}, is 42,484 s, which is 80% later compared to V_s = 0.5 m s^{-1}, and one order of magnitude later compared to V_s = 0.9 m s^{-1}. For V_s = 0.1 m s^{-1}, the breakthrough onset of DCM is 79% sooner at L = 0.25 m compared to L = 1 m, while for V_s = 0.5 m s^{-1} dichloromethane's onset is 77% earlier at L = 0.25 m vs. L = 1 m, and for V_s = 0.9 m s^{-1}, 75% earlier.

Breakthrough duration of the HEX-DCM mixtures can also be deduced from Figure 36(b). At $L = 0.25$ m, the breakthrough duration of hexane is 21,949 s for $V_s = 0.1$ m s^{-1}, which is 83% longer than for $V_s = 0.5$ m s^{-1}, and 88% longer than for $V_s = 0.9$ m s^{-1}. For $V_s = 0.1$ m s^{-1}, the breakthrough duration of hexane is 28% shorter for $L = 0.25$ m, compared to $L =1$ m and for $V_s = 0.5$ m s^{-1}, 5% shorter for $L = 0.25$ m, compared to $L =1$ m. Finally, for $V_s = 0.9$ m s^{-1}, the breakthrough duration for hexane is 17% quicker for $L = 0.25$ m than for $L = 1$ m.

For dichloromethane, at $L = 0.25$ m, the breakthrough duration at $V_s = 0.1$ m s^{-1} is 37,949 s, which is 83% longer compared to $V_s = 0.5$ m s^{-1} and one order of magnitude longer compared to $V_s = 0.9$ m s^{-1}. For $V_s = 0.1$ m s^{-1}, the breakthrough duration for dichloromethane is 63% shorter for $L = 0.25$ m compared to $L = 1$ m. For $V_s = 0.5$ m s^{-1}, the breakthrough duration for DCM is again 63% shorter for $L = 0.25$ m compared to $L = 1$ m and for $V_s = 0.9$ m s^{-1}, 57% shorter for $L = 0.25$ m than $L = 1$ m.

Temperature and pressure drop metrics for the HEX-DCM mixtures are presented in Figure 37. Specifically, the highest temperature peak is observed for $L = 0.25$ m at $T_{max} = 296.57$ K for $V_s = 0.9$ m s^{-1}, and the lowest $T_{max} = 295.20$ K for $V_s = 0.1$ m s^{-1}, and a 1 m long column. Pressure drop, as expected, is lowest for the smallest velocity ($V_s = 0.1$ m s^{-1}) at 0.93 kPa for $L = 0.25$ m and 3.75 kPa for $L = 1$ m.

Table 42. Key breakthrough metrics for the HEX-DCM mixture.

	V_s (m s^{-1})	$t_{5\%}$ (s)	$t_{95\%}$ (s)	$t_{105\%}$ (s)	$\Delta t_{5\%}^{95\%}$ (s)	$\Delta t_{5\%}^{105\%}$ (s)	T_{max} (K)	ΔP (kPa)	Fig. 36-37
					$L = 0.25$ m				
DCM	0.1	42,484	55,960	80,433	-	37,949	295.80	0.93	(b)
HEX		62,155	84,074	-	21,919	-			
DCM	0.5	8,404	10,517	14,999	-	6,595	296.32	6.37	(b)
HEX		11,961	15,695	-	3,734	-			
DCM	0.9	4,243	5,606	8,039	-	3,796	296.57	15.15	(b)
HEX		6,018	8,550	-	2,532	-			
	V_s (m s^{-1})	**$t_{5\%}$ (s)**	**$t_{95\%}$ (s)**	**$t_{105\%}$ (s)**	**$\Delta t_{5\%}^{95\%}$ (s)**	**$\Delta t_{5\%}^{105\%}$ (s)**	**T_{max} (K)**	**ΔP (kPa)**	**Fig. 36-37**
					$L = 1$ m				
DCM	0.1	199,347	219,975	309,736	-	110,389	295.20	3.75	(b)
HEX		283,768	314,348	-	30,579	-			
DCM	0.5	36,236	38,780	54,261	-	18,025	295.36	28.41	(b)
HEX		50,523	54,470	-	3,948	-			
DCM	0.9	17,133	18,586	25,943	-	8,811	295.52	77.92	(b)
HEX		23,409	26,467	-	3,059	-			

Figure 36 (c) presents the breakthrough curves for the mixture of hexane-toluene (HEX-TOL). Key metrics are summarized in Table 43 and Figure 38(g-i). At $L = 0.25$ m, for $V_s = 0.1$ m s^{-1}, the breakthrough onset time of hexane is 66,179 s, which is 81% later compared to $V_s = 0.5$ m s^{-1}, and 90% later compared to $V_s = 0.9$ m s^{-1}. At $L = 1$ m, for $V_s = 0.1$ m s^{-1}, breakthrough onset time of hexane is 302,704 s, which is 82% later compared to $V_s = 0.5$ m s^{-1}, and 92% later compared to $V_s = 0.9$ m s^{-1}. For $V_s = 0.1$ m s^{-1}, the breakthrough onset of hexane at $L = 0.25$ m is 78% earlier compared to $L = 1$ m while for $V_s = 0.5$ m s^{-1}, 76% earlier and for $V_s = 0.9$ m s^{-1}, 74% earlier.

For toluene, the breakthrough onset time at $L = 0.25$ m, for $V_s = 0.1$ m s^{-1}, is 174,107 s, which is 81% later compared to $V_s = 0.5$ m s^{-1}, and 90% later compared to $V_s = 0.9$ m s^{-1}. For $V_s = 0.1$ m s^{-1}, the breakthrough onset of TOL is 77% sooner at $L = 0.25$ m compared to $L = 1$ m, while for $V_s = 0.5$ m s^{-1} toluene's onset is 74% earlier at $L = 0.25$ m vs. $L = 1$ m, and for $V_s = 0.9$ m s^{-1}, 71% earlier.

Breakthrough duration metrics of the HEX-TOL mixtures can also be inferred from Figure 36 (c). At $L = 0.25$ m, the breakthrough duration of hexane is 131,173 s for $V_s = 0.1$ m s^{-1}, which is 81% longer than for $V_s = 0.5$ m s^{-1}, and one order of magnitude longer than for $V_s = 0.9$ m s^{-1}. For $V_s = 0.1$ m s^{-1}, the breakthrough duration of hexane is 72% shorter for $L = 0.25$ m, compared to $L =1$ m and for $V_s = 0.5$ m s^{-1}, 70% shorter for $L = 0.25$ m, compared to $L =1$ m. Finally, for $V_s = 0.9$ m s^{-1}, the breakthrough duration for hexane is 63% quicker for $L = 0.25$ m than for $L = 1$ m.

For toluene, at $L = 0.25$ m, the breakthrough duration at $V_s = 0.1$ m s^{-1} is 32,120 s, which is 83% longer compared to $V_s = 0.5$ m s^{-1} and 87% longer compared to $V_s = 0.9$ m s^{-1}. For $V_s = 0.1$ m s^{-1}, the breakthrough duration for toluene is 2% longer for $L = 0.25$ m compared to $L = 1$ m. For $V_s = 0.5$ m s^{-1}, the breakthrough duration for TOL is again 17% longer for $L = 0.25$ m compared to $L = 1$ m and for $V_s = 0.9$ m s^{-1}, 12% longer for $L = 0.25$ m than $L = 1$ m.

Temperature and pressure drop metrics for the HEX-TOL mixtures are presented in Figure 37. Specifically, the highest temperature peak is observed for $L = 0.25$ m at $T_{max} = 296.56$ K for $V_s = 0.9$ m s^{-1}, and the lowest $T_{max} = 295.27$ K for $V_s = 0.1$ m s^{-1}, and a 1 m long column. Pressure drop, as expected, is lowest for the smallest velocity ($V_s = 0.1$ m s^{-1}) at 0.93 kPa for $L = 0.25$ m and 3.75 kPa for $L = 1$ m.

Table 43. Key breakthrough metrics for the HEX-TOL mixture.

	V_s (m s^{-1})	$t_{5\%}$ (s)	$t_{95\%}$ (s)	$t_{105\%}$ (s)	$\Delta t_{5\%}^{95\%}$ (s)	$\Delta t_{5\%}^{105\%}$ (s)	T_{max} (K)	ΔP (kPa)	Fig. 36-37
					L = 0.25 m				
TOL	0.1	174,107	206,227	-	32,120	-	295.77	0.93	(c)
HEX		66,179	81,570	197,352	-	131,173			
TOL	0.5	33,483	38,827	-	5,344	-	296.31	6.37	(c)
HEX		12,864	15,170	37,191	-	24,327			
TOL	0.9	16,902	20,982	-	4,079	-	296.56	15.15	(c)
HEX		6,505	8,102	19,644	-	13,139			
	V_s (m s^{-1})	**$t_{5\%}$ (s)**	**$t_{95\%}$ (s)**	**$t_{105\%}$ (s)**	**$\Delta t_{5\%}^{95\%}$ (s)**	**$\Delta t_{5\%}^{105\%}$ (s)**	**T_{max} (K)**	**ΔP (kPa)**	**Fig. 36-37**
					L = 1 m				
TOL	0.1	752,898	784,410	-	31,512	-	295.27	3.75	(c)
HEX		302,704	320,280	775,966	-	473,262			
TOL	0.5	130,518	134,963	-	4,445	-	295.42	28.41	(c)
HEX		53,973	56,165	133,890	-	79,917			
TOL	0.9	58,333	61,930	-	3,597	-	295.59	77.92	(c)
HEX		25,170	26,488	60,772	-	35,602			

Figure 38 summarizes key breakthrough metrics for all three binary component systems at three superficial velocities (V_s = 0.1, 03, 0.5 m s^{-1}) and two bed lengths (L = 0.25, 1 m). It becomes apparent that the slowest velocity (V_s = 0.1 m s^{-1}) corresponds to the longest breakthrough onset times, which increase with the increasing superficial velocity case studies. Breakthrough onset times are earlier for the laboratory scale column (L = 0.25 m) compared to the industrial column (L = 1 m).

Breakthrough duration, however, has more mixture specific characteristics. For the hexane-acetone mixture both components' breakthrough durations are shorter for the laboratory scale column and decrease with increasing superficial velocity. For the hexane-dichloromethane mixture the same trends are observed for both components. For the hexane-toluene mixture, however, while the trend holds true for hexane's breakthrough duration, it does not for toluene's. Toluene demonstrates shorter duration in the industrial scale column which decreases with increasing superficial velocity. Finally, temperature peaks increase in value with increasing superficial velocity, with higher peaks occurring for the shortest column (L = 0.25 m). Furthermore, pressure drops follow the opposite trend; smallest are demonstrated in short columns with the lowest superficial velocity.

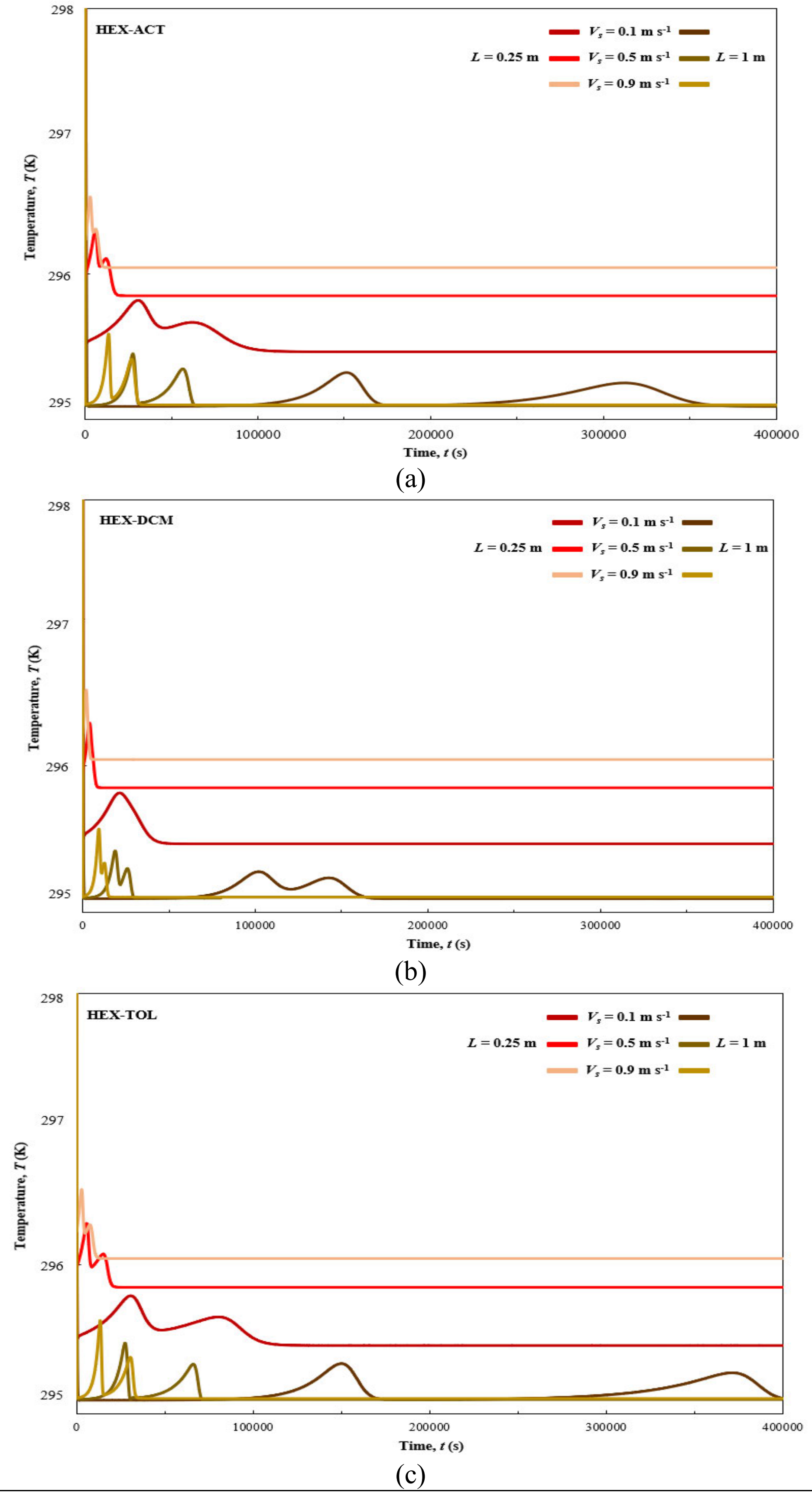

Figure 37. Temperature trends of (a) HEX-ACT (b) HEX-DCM (c) HEX-TOL.

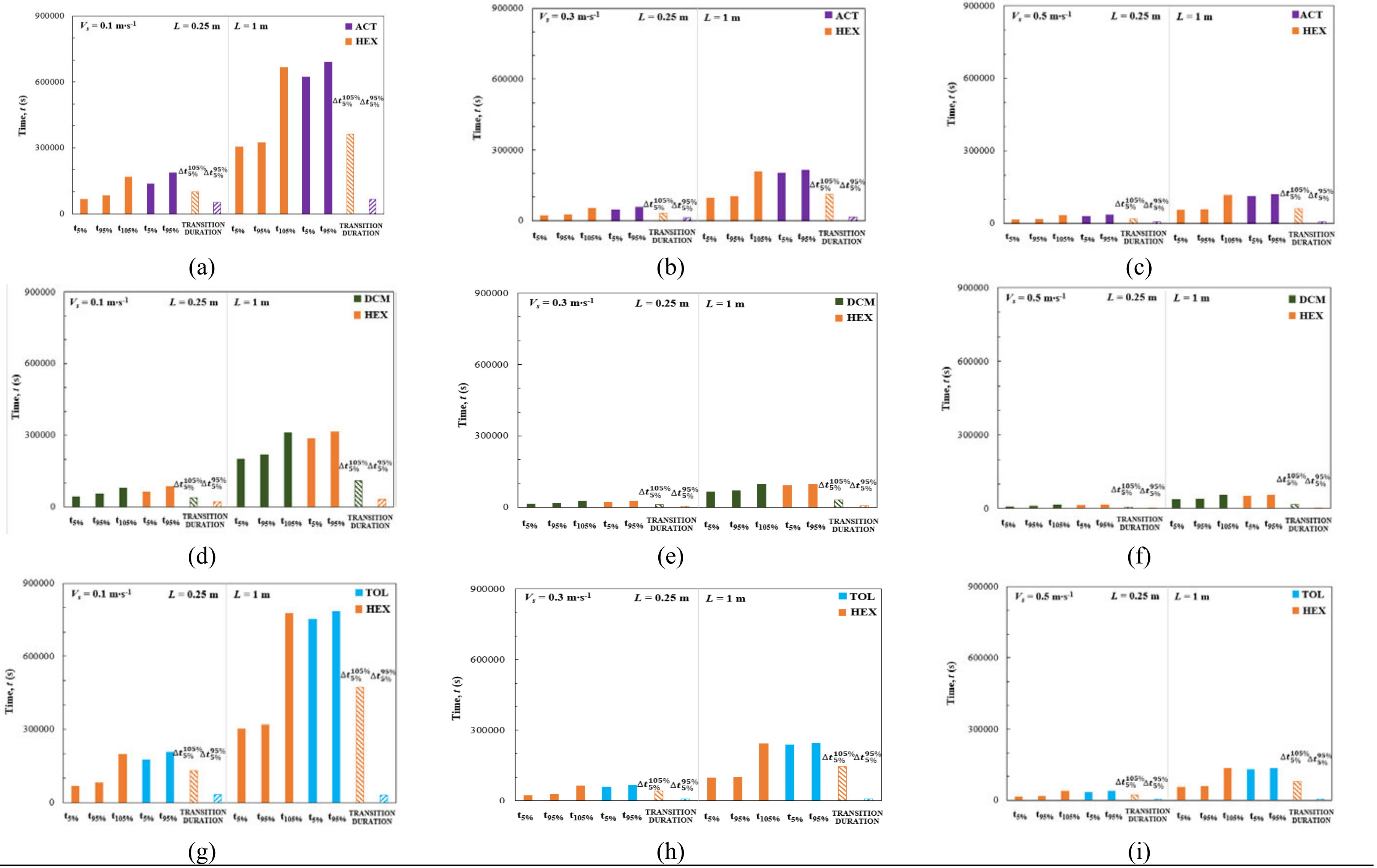

(a) (b) (c)

(d) (e) (f)

(g) (h) (i)

Figure 38. Breakthrough metrics for V_s = 0.1, 0.3, 0.5 m s^{-1} for (a) ACT-HEX, (b) DCM-HEX, (c) HEX-TOL.

10.3 Column Length and Velocity Influence on Breakthrough

One of the key parameters to consider upon designing an industrial adsorption column for emissions abatement is the breakthrough onset time ($t_{5\%}$). Thus, shedding light on how it is impacted by various mixtures and operating conditions is of great importance to stakeholders. A metric called normalised time (t^*) is introduced to quantify the effect of bed length scale up on breakthrough onset time. Normalised time (t^*) is breakthrough onset time divided by the column length.

The adsorption behaviour of mixtures of hexane-acetone (HEX-ACT), hexane-dichloromethane (HEX-DCM) and hexane-toluene (HEX-TOL) is examined for four bed lengths (L = 0.25, 0.50, 0.75, 1 m) and six superficial velocities (V_s = 0.1, 0.2, 0.3, 0.5, 0.7, 0.9 m s^{-1}), under the same conditions as found in Figure 36 and Figure 37, to determine the correlation between breakthrough onset time, column length and velocity as a potential adsorption bed design tool. In all cases considered, the bed area remains constant at 0.000181 m^2.

Figure 38 shows the normalised time metrics vs. column length for all components and superficial velocities. Figure 38 (a) refers to the hexane-acetone mixture, Figure 38 (b) to the hexane-dichloromethane mixture and Figure 38 (c) to the hexane-toluene mixture. Interestingly, common trends emerge for all systems considered in this PhD thesis. As expected, the weakly adsorbing mixture component demonstrates lower values of normalised time due to earlier breakthrough onset.

Furthermore, it is noted that with increasing superficial velocity, normalised time metrics not only shift to lower values but are also demonstrating a smaller gap, therefore a smaller change in breakthrough onset. Thus, there is a velocity range for which the trade-off among process energy consumption (for turbines maintaining the pressure), cost savings from more efficient use of the bed (longer periods of usage between adsorbent regeneration) and process recipe volume constraints is optimal.

Another trend is observed pertaining to length scale up and velocities. Specifically, at high superficial velocities, the normalised time values reported for increasing bed lengths tend to follow a straight line, thus indicating an analogous relationship of length scale up and breakthrough onset times. However, a different story unfolds for lower superficial velocity values where it is observed that the rate of change of normalised time increases with increasing bed length until a certain length, after which it seems to plateau. This observation gives rise to the conclusion that when increasing superficial velocity, the rate of change of breakthrough onset by column length becomes linear, thus highlighting the effect of superficial velocity on breakthrough onset is different for lower superficial velocities and shorter columns. Based on these differences, operational protocol and design interventions could potentially balance the cost of constructing a very long column with no added operational benefit in terms of breakthrough onset.

Table 44. Breakthrough onset times for superficial velocities 0.2, 0.3 and 0.7 m s^{-1}.

		$t_{5\%}$ (s)					
V_s (m s^{-1})	**L (m)**	**HEX**	**ACT**	**HEX**	**DCM**	**HEX**	**TOL**
0.2	**0.25**	33,597	69,512	31,469	21,845	33,619	87,770
	0.50	72,803	149,991	67,930	47,647	72,683	183,365
	0.75	111,529	229,683	104,243	73,573	111,228	276,469
	1	149,461	307,725	139,910	99,142	148,910	367,014
0.3	**0.25**	22,161	46,164	20,741	14,503	22,228	58,203
	0.50	47,818	98,816	44,587	31,444	47,801	120,317
	0.75	72,796	150,078	67,946	48,156	72,679	179,796
	1	96,970	199,526	90,643	64,544	96,557	236,853
0.7	**0.25**	8,726	18,384	8,145	5,738	8,785	22,865
	0.50	18,534	38,348	17,196	12,233	18,560	46,203
	0.75	27,520	56,359	25,515	18,312	27,459	66,563
	1	35,669	72,429	33,080	23,925	35,472	84,252

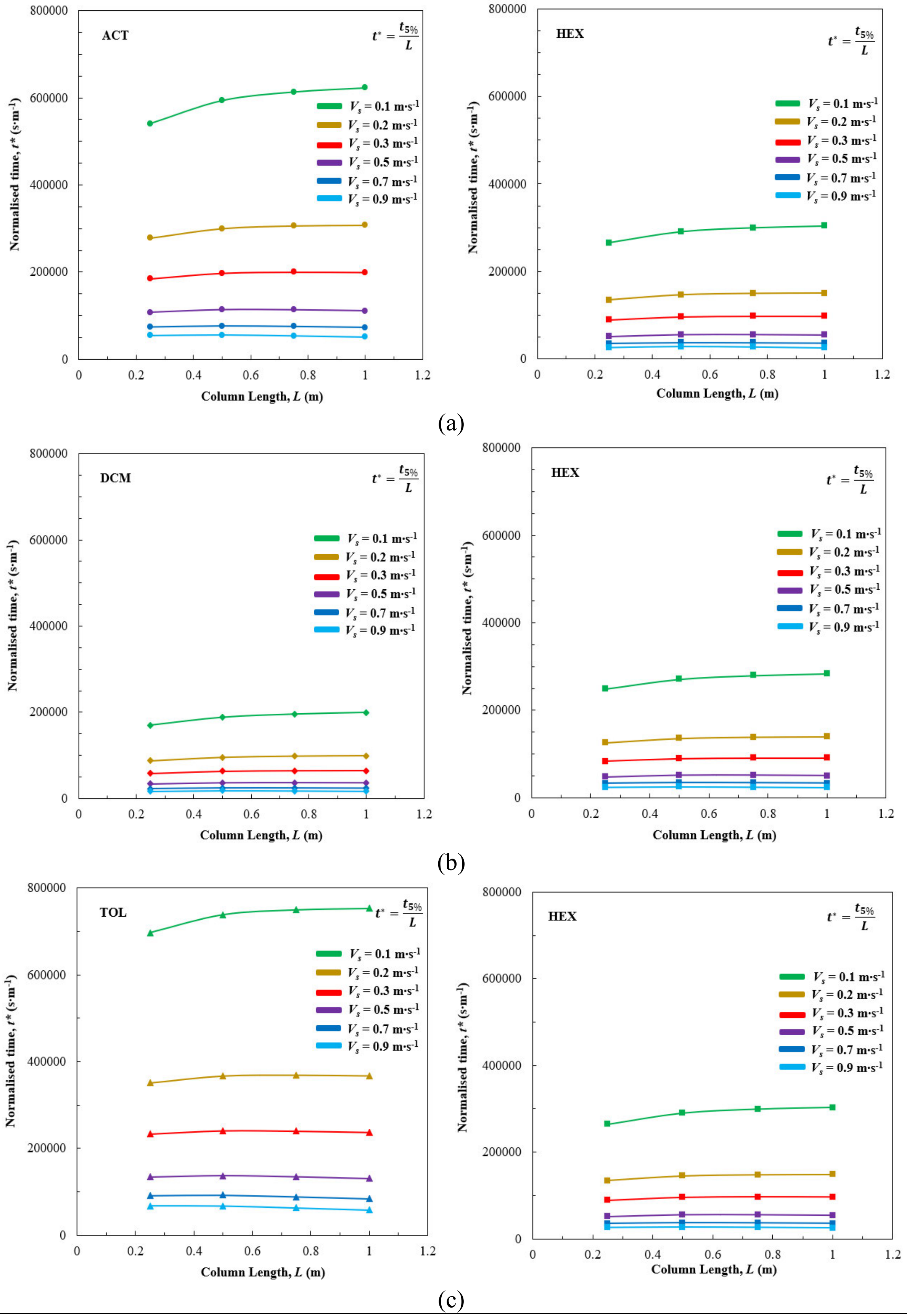

(a)

(b)

(c)

Figure 39. Bed design metrics for the (a) HEX-ACT, (b) HEX-DCM, (c) HEX-TOL mixtures.

10.4 Chapter Conclusions

The present chapter demonstrates the application of a validated, multicomponent, nonisothermal adsorption model to investigate the effect of superficial velocity and column length on multicomponent VOC mixture adsorption. Specifically, the breakthrough behaviour of three trace binary VOC mixtures (hexane-acetone, hexane-dichloromethane, and hexane-toluene), with air as the carrier gas, is examined on an activated carbon column for four bed lengths ranging from laboratory to industrial scale ($L = 0.25, 0.50, 0.75, 1$ m) and six superficial velocities ($V_s = 0.1, 0.2, 0.3, 0.5, 0.7, 0.9$ m s^{-1}) each. Extensive breakthrough behaviour results are presented for the cases of $L = 0.25$ m and $L = 1$ m (min-max) at $V_s = 0.1, 0.5, 0.9$ m s^{-1} (min-mid-max). Finally, the concept of normalised time is introduced as detailed component breakthrough onset over bed length metrics for all cases considered and examined as a tool for column design decision-making.

The detailed breakthrough behaviour study has shown interesting relationships between the VOCs and process parameters. Specifically, among all cases considered, the latest breakthrough onset times are reported with the lowest superficial velocity and longest column. Breakthrough duration on the other hand, demonstrates mixture-specific characteristics. For the hexane-acetone and hexane-dichloromethane mixtures as well as for hexane in the hexane-toluene mixture breakthrough durations are shorter for the laboratory scale column and decrease with increasing superficial velocity. For toluene, shorter duration is observed in the industrial scale column which decreases with increasing superficial velocity. Temperature peaks tend to be the highest at the shortest columns with the largest superficial velocity, while the smallest pressure drops occur in the short-column, low-superficial velocity scenarios.

Moreover, the concept of normalised time, is proposed as an adsorption column utilisation tool. Specifically, the increasing proximity of the plot lines in Figure 39 with increasing superficial velocity indicates that there is a velocity range which ensures balance among process energy consumption (for compressors maintaining the flow), and plant emissions constraints. In tandem with an optimised velocity range, there seems to also be a potential economic trade-off between the linear change on breakthrough onset rate and the cost of designing and operating an extra-long column with potentially no added operational benefits, i.e. total adsorbent mass and/or adsorbent changeover frequency.

PART V

MIXED INTEGER LINEAR PROGRAMMING OPTIMISATION SCHEDULING MODEL & ECONOMIC EVALUATION

Chapter 11

MILP & Economic Evaluation

In this Chapter a Mixed Integer Linear Programming (MILP) model is formulated and applied in a pharmaceutical manufacturing context, not only to meet demand but also to include gas waste capture via adsorption. Specifically, the MILP model finds the optimal API production schedule for a 35-statess, 16-tasks State-Task-Network (STN). The STN includes the gas abatement tasks and examines five binary VOC (chloroform- toluene) emission mixtures (ranging from 50 to 250 ppm), informed by gPROMS® dynamic simulation results for adsorption task duration. Based on the MILP schedules and industrial data, VOC abatement system annual Operating Expenditure projections are presented and compared for two VOC emission mixture compositions, two solvent mass, three adsorbent changeover scenarios, three makespans and two solvent price cases.

The results presented in this chapter have also been submitted for publication (Tzanakopoulou et al., 2024. *Chem. Eng. Res. Des.*, submitted for publication); details can be found in Appendix B.

11.1 Mathematical Formulation

In this chapter, the web based application CProS of (Misra et al., 2022) is employed to solve the optimisation problem. The mathematical formulation relies on the work of (Shah et al., 1993) the presentation of which follows as per (Misra et al., 2022) for completeness. Discreet time formulations divide the production time horizon in equal intervals of desired duration. The beginning and end of events (tasks) are bound by the limits of these time intervals. This results in a shared time grid for all operations competing for the same resources, such as equipment units. The relationships stemming from the production recipe, like material flows and process conditions are then implemented via a set of equations, the constraints. The structure of the network is represented using the following sets and subsets:

- $i \in \mathbf{I}$: tasks

- $j \in \mathbf{J}$: units

- $k \in \mathbf{K}$: materials

- $\boldsymbol{I_k^+}/\boldsymbol{I_k^-}$: tasks producing/consuming material k

- $\boldsymbol{J_i}$: units that can process task *i*

- $\boldsymbol{n}$: time

The binary decision variables, X_{ijn}, are responsible for the assignment of units to tasks. This set of binary variables determine whether a task *i* starts in unit *j* at the beginning of time interval *n*, by taking the value 1, and 0 if otherwise. The unit allocation constraint of Eq. (50) expresses the restriction that for any unit *j*, at most one task *i* can start at the beginning of each time interval *n*. Moreover, this constraint also ensures that if a task *i* is selected to start at unit *j* at the beginning of time interval *n*, then no other task can start in the same unit *j* until this task *i* is completed.

$$\sum_{i\in I_j}\sum_{n'\geq n-\tau_{ij}+1}^{n} X_{ijn'} \leq 1, \ \forall j,n \tag{50}$$

The MILP model further includes the variable families B_{ijn} and S_{kn}. B_{ijn} represents the material amount, or batch size, which starts undergoing task *i* in unit *j* at the beginning of time interval *n and* S_{kn} the amount of material k during time interval *n*. The batch size of a task is related to the assignment variable through the unit capacity constraint shown in Eq. (51).

$$\beta_j^{MIN} X_{ijn} \leq B_{ijn} \leq \beta_j^{MAX} X_{ijn} \quad \forall\, i,j\, \in\, J_i, n \tag{51}$$

where $\beta_j^{MIN}/\beta_j^{MAX}$ are the minimum /maximum capacity of unit *j*.

The mass balance is expressed by establishing the relationships between inventory levels at two consecutive time intervals, as in Eq. (52):

$$S_{kn} = \ S_{k(n-1)} + \sum_{i\in I_k^+} \rho_{ik} \sum_{j\in J_i} B_{ij(n-\tau_{ij})} + \sum_{i\in I_k^-} \rho_{ik} \sum_{j\in J_i} B_{ijn} + \xi_{kn} \ \forall\, k,n \tag{52}$$

where τ_{ij} is the processing time for task *i* in unit *j*, ρ_{ik} is the fraction of material *k* produced (>0) or consumed (<0) in task *i and* ξ_{kn} is the amount of raw material *k* delivered at time *n* (>0) / demand for material *k* at time *n* (<0).

The material storage constraints are enforced by an upper limit bound on the S_{sn} variables.

$$0 \ \leq\ S_{kn} \leq \gamma_k^{MAX} \ \forall\, k,n \tag{53}$$

where γ_k^{MAX} is the storage vessel capacity for material *k*.

The objective function utilized in this PhD thesis is the makespan minimisation, expressed by Eqs. (54) and (55)

$$MS \geq \sum_{i \in I_j} (n + \tau_{ij}) X_{ijn} \quad \forall j, n \tag{54}$$

$$\min MS \tag{55}$$

where MS represents the makespan.

11.2 Active Pharmaceutical Ingredient Production Process

Material S1 is dissolved in solvent S8 and stirred while a mixture of S2, S3, S4 and S8 is prepared in a separate vessel and cooled. The two mixtures are combined to react for approximately 2 hours and produce intermediate S5. The reaction mixture is then washed with solvent S8. Solvent S6 is added to the batch and the mixture is refluxed for approximately 24 hours until intermediate S7 is formed. The batch then undergoes distillation until solvent S8 distils off. Solvent S10 is then added to the batch mixture and another distillation follows until solvent S10 is distilled off. The batch then undergoes a cascade of washes and solvent separations followed by mixing with solvent S8 which leads to the formation of the target compound S9. The batch finally undergoes crystallization and filtration through which the target compound is isolated and kegged. Vessel washes conclude the production schedule.

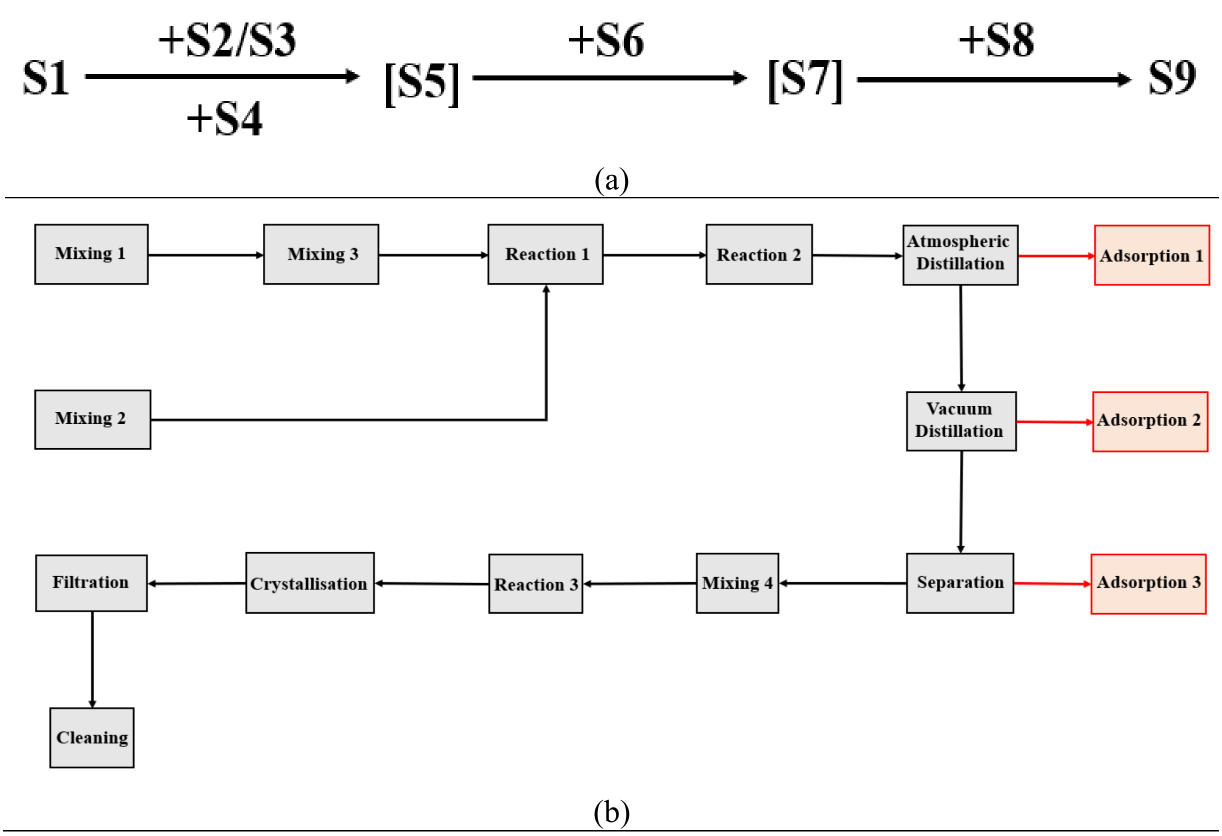

(a)

(b)

Figure 40. API production reaction scheme (a) and flow diagram (b).

Figure 40 summarises the reaction scheme and presents the process flow diagram.

Recipe steps involving material charges, material transfer between vessels, reactions and separations are modelled as tasks. This formulation leads to a model consisting of sixteen tasks processing thirty-five states in twelve units. VOC emissions from the two distillations (tasks I6-I7) and the separation (task I8) are vented to the activated carbon bed. In this schedule, emission release is modelled as tasks which take place or not, depending on the recipe. Emission release tasks are then scheduled in such a way to create the minimum impact possible on the carbon bed. This minimum impact strategy is informed by detailed process simulation results from gPROMS® corresponding to VOC mixture breakthrough behaviour. Specifically, drawing from the knowledge of VOC affinity to the activated carbon bed and the breakthrough onset times involved with VOC mixtures forms the VOC release scenarios while still meeting production targets. Periodic resource restrictions caused by limited holding times and workforce availability are also considered in the total time horizon.

11.3 State Task Network Formulation

The successful deployment of a MILP problem relies on forming a State-Task Network (STN) which balances between computational efficiency and depth of detail for process representability. The STN represents an intellectual derivative of the production recipe, in the form of a diagram where materials are depicted as circles and actions/production steps as rectangles. The STN further accounts for intermediate material additions as well as product separations. The orange colour of states/circles signifies volatile organic compound emissions. The red arrows indicate the connection of the VOC emitting tasks with the adsorption tasks. If/when a connection is selected to be made by the algorithm, then emissions are sent to the carbon bed for abatement.

To this end, the production recipe described in section 2 was translated to an STN diagram consisting of 16 tasks and 35 materials. At first, three mixing tasks (tasks I1-I3) are performed in order to prepare the solvent mixtures, which are followed by the two first reactions (tasks I4-I5). After them, two distillations (tasks I6-I7) and a separation (task I8) take place to purify the streams. Next, further mixing (task I9) takes place followed by the third and final reaction (task I10). After that, crystallisation (task I11), and filtering (task I12) leads to the desired product (material K26), followed by cleaning and disposal activities (task I13).

VOC emissions are primarily generated during the distillations and separation tasks (I6-I8). The red arrows indicate the feeding of VOC emissions to the carbon bed for abatement. To overcome the unit allocation constraint which dictates that a unit is occupied by only one task at a time period, the carbon bed is represented by units J10-J12, undergoing the adsorption tasks (I14-I16). This way, the problem became easier to conceptualize and solve. Main problem parameters are presented in Table 45-Table 46.

Volatile Organic Compound emissions generated by tasks I6-I8 are directed to tasks I14-I16. Therefore, gPROMS® simulations are performed to determine the appropriate breakthrough onset time to avoid breaching of emission limits. This gPROMS® derived breakthrough onset time is manually applied as the adsorption task (I14-I16) duration on CProS. The solvent quantities sent for abatement are calculated as 2% of the total process solvent consumption and equal to 30 kg, which are modelled as 10 kg of solvent mixture escaping from each of the distillations and separation tasks. The solvent mixture encountered in this process is the binary toluene-chloroform (TOL-TCM) with air as the carrier gas. The VOC concentrations vary and therefore five concentration scenarios have been selected for gPROMS® simulation informed by industrial emissions monitoring reports.

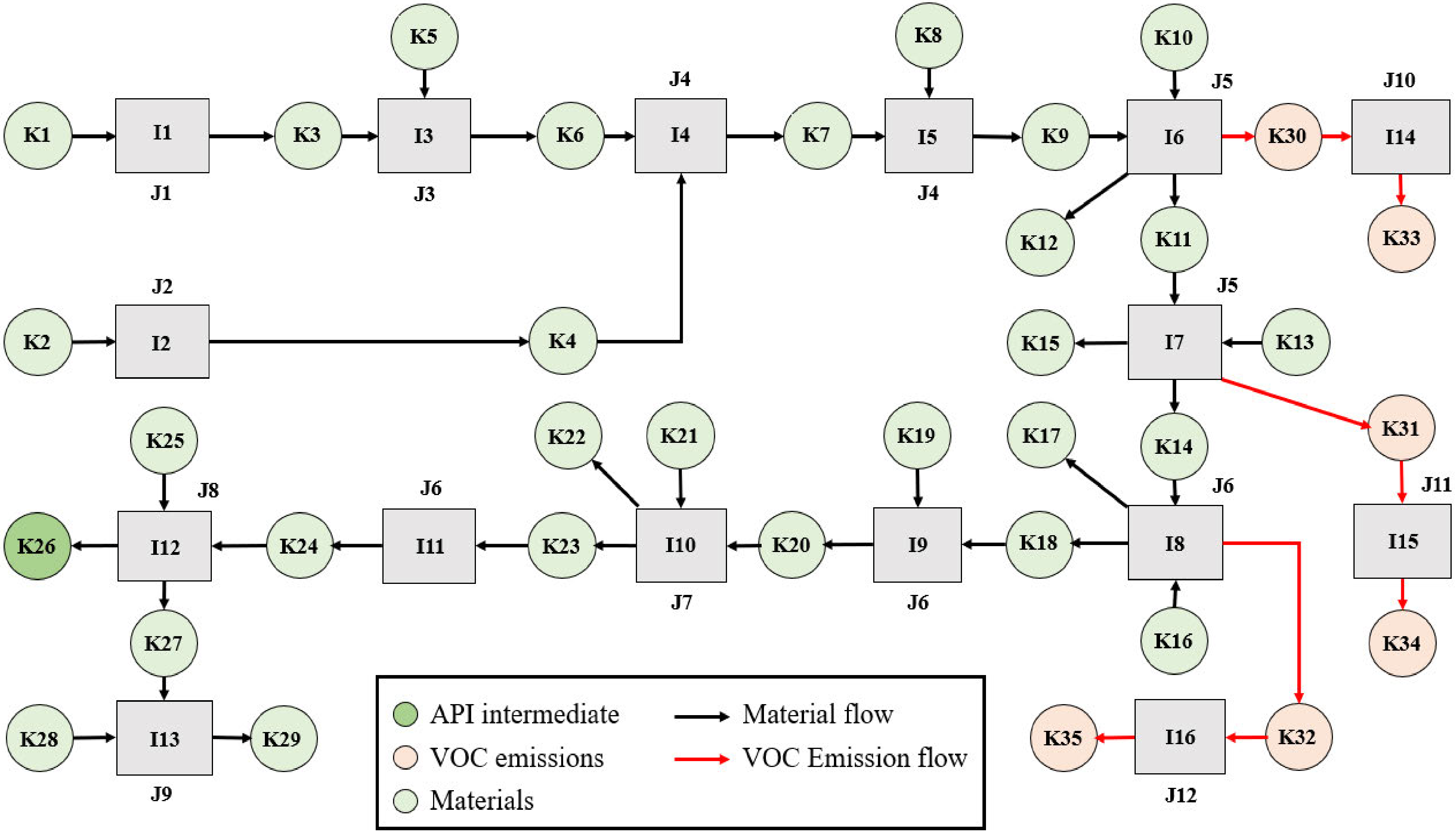

Figure 41. State-Task-Network diagram for stage 2 API production.

Table 45. Parameter values of task duration and vessel capacity for the MILP problem.

Step	Task	Unit	Consumes	Produces	Duration (h)	Capacity (kg)	
						Min	Max
Mixing 1	I1	J1	K1	K3	16	0	2,000
Mixing 2	I2	J2	K2	K4	2	0	2,000
Mixing 3	I3	J3	K3, K5	K6	2	0	2,000
Reaction 1	I4	J4	K4, K6	K7	3	0	2,000
Reaction 2	I5	J4	K7, K8	K9	24	0	2,000
Atmospheric Distillation	I6	J5	K9, K10	K11, K12, K30	22	0	2,000
Vacuum Distillation	I7	J5	K11, K13	K14, K15, K31	2	0	2,000
Separation	I8	J6	K14, K16	K17, K18, K32	2	0	2,000
Mixing 4	I9	J6	K18, K19	K20	1	0	2,000
Reaction 3	I10	J7	K20, K21	K22, K23	2	0	2,000
Crystallisation	I11	J6	K23	K24	42	0	2,000
Filtration	I12	J8	K24, K25	K26, K27	7	0	2,000
Cleaning	I13	J9	K27, K28	K29	2	0	2,000
Adsorption 1	I14	J10	K30	K33	gPROMS®	0	10
Adsorption 2	I15	J11	K31	K34	gPROMS®	0	10
Adsorption 3	I16	J12	K32	K35	gPROMS®	0	10

The duration of adsorption tasks is determined via gPROMS® dynamic simulations. The five binary mixture scenarios result in five breakthrough profiles. Breakthrough onset, which is the appearance of the VOCs at the column outlet, signals the unsuitability of the bed to carry on the adsorption task without environmental risks. Based on the UK Department for Environment, Food and Rural Affairs, and internal industry limits, the threshold of 18 ppm of combined VOC presence at the column outlet is chosen as the point where a new bed must come in operation. Therefore, the time required for each VOC to reach 9 ppm at the column outlet is chosen as the duration of the corresponding adsorption task. The time horizon of this scheduling problem is 150 h, and it discretised in 15-minute increments. Therefore, adsorption task duration, as calculated from gPROMS® dynamic simulation results, is rounded to the lower, closest 0.25 h increment and can be found in Table 50.

Table 46. Parameter values for the mass balance of the MILP problem.

Material (K)	Mass (kg)	Fraction of material (ρ_{ik})		Storage Capacity (kg)	Material (kg)	
		Produced	**Consumed**		**Delivery**	**Demand**
1	372	-	-1	1,000	372	-
2	802	-	-1	1,000	802	-
3	372	1	-0.56	1	-	-
4	802	1	-0.55	1	-	-
5	289	-	-0.44	1,000	289	-
6	661	1	-0.45	1	-	-
7	1462	1	-0.89	1	-	-
8	182	-	-0.11	1,000	182	-
9	1645	1	-0.96	1	-	-
10	74	-	-0.04	1,000	74	-
11	543	0.3159	-0.89	1	-	-
12	1166	0.6783	-	2,000	-	-50
13	65	-	-0.11	1,000	65	-
14	511	0.8405	-0.54	1	-	-
15	87	0.1431	-	2,000	-	-50
16	429	-	-0.46	1,000	429	-
17	508	0.5404	-	2,000	-	-50
18	422	0.4489	-0.83	1	-	-
19	86	-	-0.17	1,000	86	-
20	508	1	-0.52	1	-	-
21	475	-	-0.48	1,000	475	-
22	308	0.31	-	2,000	-	-50
23	675	0.69	-1	1	-	-
24	675	1	-0.63	1	-	-
25	390	-	-0.37	1,000	390	-
26	159	0.15	-	2,000	-	-150
27	906	0.85	-0.64	1	-	-
28	511	-	-0.36	1,000	511	-
29	1417	1	-	2,000	-	-100
30	10	0.0058	-1	0	-	-
31	10	0.0164	-1	0	-	-
32	10	0.0106	-1	0	-	-
33	$5\cdot10^{-6}$	1	-	10	-	$-5\cdot10^{-6}$
34	$5\cdot10^{-6}$	1	-	10	-	$-5\cdot10^{-6}$
35	$5\cdot10^{-6}$	1	-	10	-	$-5\cdot10^{-6}$

11.4 gPROMS® Dynamic Simulation Results

The validated, dynamic, non-isothermal, multicomponent adsorption model (Tzanakopoulou et al., 2023) developed was employed to investigate the adsorption characteristics of a binary

VOC mixture (with air as the carrier gas). Specifically, the mixture of Toluene-Chloroform (TOL-TCM) in an initially clean, coconut based activated carbon fixed bed at five different concentration pairs informed by industrial data.

The set of partial differential equations (PDEs) is solved using second order orthogonal collocation on finite elements with 110 discretisation points in the gPROMS® Process 2.0.0 software suite. For all cases considered, the DASolver SRADAU is employed, which uses a variable time step fully implicit Runge-Kutta method. The viscosities are computed from Wilke's equation, while densities are determined through pure component data via mixing rules (National Institute of Standards and Technology (NIST), 2023). The main simulation parameters for all cases examined in this PhD thesis are in Table 47-Table 49:

Table 47. Langmuir Isotherm parameters used in this PhD thesis.

BINARY	$q_{m,i}$ **(mol kg^{-1})**	b_0 **(m^3 mol^{-1})**	$\Delta H_{ad,i}$ **(J mol^{-1})**	**Lit. Ref.**
TOL-TCM	4.61	$4.06 \cdot 10^{-7}$	45,500	(Delage et al., 2000)
	2.49	$1.91 \cdot 10^{-6}$	44,769	(Chuang et al., 2003)

The concentration pairs examined in this PhD thesis are: 50-250 ppm, 130-250 ppm, 250-250 ppm, 250-130 ppm and 250-50 ppm.

Table 48. Main gPROMS® simulation parameters in this PhD thesis.

System	$C_{0,i}$ **(ppm)**	$D_{z,i}$ **(m^2 s^{-1})**	T_{in} **(K)**	L **(m)**	V_s **(m s^{-1})**	ε_b	k_{LDF} **(s^{-1})**	**Fig.**
TOL-TCM	50	$1.34 \cdot 10^{-3}$	300	1	0.914	0.38	$8.34 \cdot 10^{-5}$	38a
	250	$1.40 \cdot 10^{-3}$					$3.88 \cdot 10^{-5}$	
TOL-TCM	130	$1.34 \cdot 10^{-3}$	300	1	0.914	0.38	$8.74 \cdot 10^{-5}$	38b
	250	$1.40 \cdot 10^{-3}$					$4.07 \cdot 10^{-5}$	
TOL-TCM	250	$1.34 \cdot 10^{-3}$	300	1	0.914	0.38	$9.35 \cdot 10^{-5}$	38c
	250	$1.40 \cdot 10^{-3}$					$4.36 \cdot 10^{-5}$	
TOL-TCM	250	$1.34 \cdot 10^{-3}$	300	1	0.914	0.38	$7.22 \cdot 10^{-5}$	38d
	130	$1.40 \cdot 10^{-3}$					$3.36 \cdot 10^{-5}$	
TOL-TCM	250	$1.34 \cdot 10^{-3}$	300	1	0.914	0.38	$5.81 \cdot 10^{-5}$	38e
	50	$1.40 \cdot 10^{-3}$					$2.70 \cdot 10^{-5}$	

Table 49. Main thermal and structural parameter values in this chapter.

System	$C_{0,i}$ (ppm)	D (m)	T_w (K)	ε_p	d_p (m)	C_{pp} (J kg^{-1} K^{-1})	C_{pg} (J kg^{-1} K^{-1})	k_{ez} (W m^{-1} K^{-1})	h_o (W m^{-2} K^{-1})	h_{int} (W m^{-2} K^{-1})	k_w (W m^{-1} K^{-1})	x (m)	Fig.
TOL-TCM	50 250	0.0152	283	0.56	0.00075	706.7	1,013	0.67	53.00	53.18	14.2	0.001	38a
TOL-TCM	130 250	0.0152	283	0.56	0.00075	706.7	1,013	0.67	53.02	53.21	14.2	0.001	38b
TOL-TCM	250 250	0.0152	283	0.56	0.00075	706.7	1,013	0.67	53.07	53.25	14.2	0.001	38c
TOL-TCM	250 130	0.0152	283	0.56	0.00075	706.7	1,013	0.67	53.01	53.19	14.2	0.001	38d
TOL-TCM	250 50	0.0152	283	0.56	0.00075	706.7	1,013	0.67	52.97	53.16	14.2	0.001	38e

The average particle size is 0.75 mm, 99% by mass between 0.60 and 0.84 mm (Tefera et al., 2013, Lashaki et al., 2012).

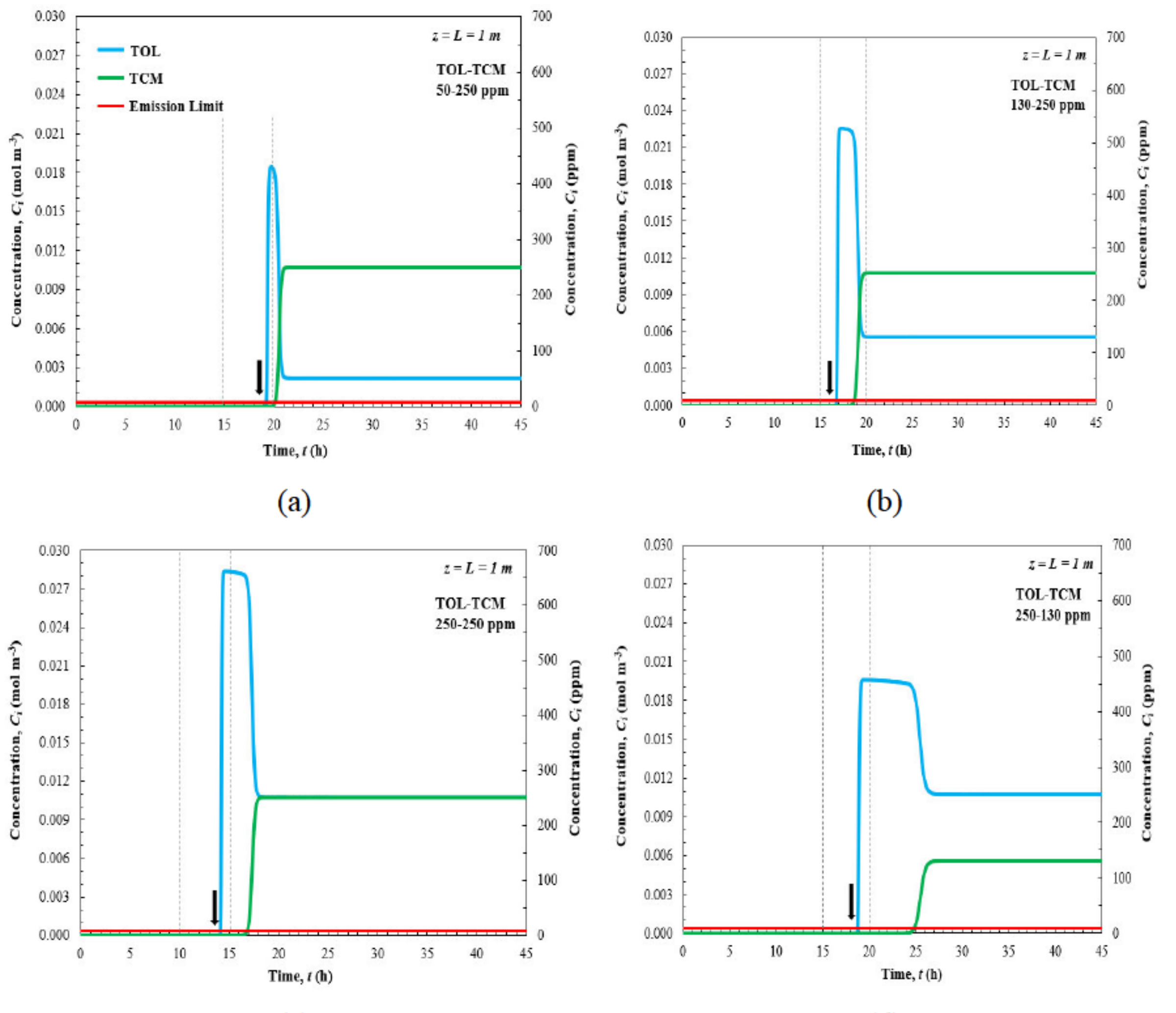

(a) (b)

(c) (d)

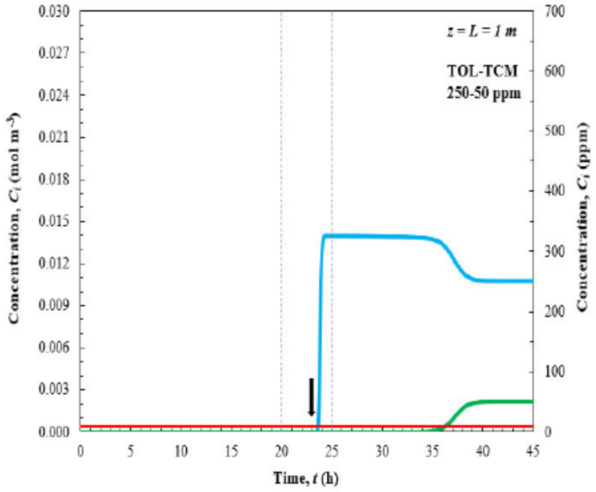

(e)

Fig. 42	$t_{5\%, TOL}$ (h)	$\Delta t_{9\ ppm, TOL}$ (h)
(a)	19.18	19.22
(b)	16.75	16.76
(c)	14.16	14.15
(d)	18.79	18.78
(e)	23.67	23.65

(f)

Figure 42. Breakthrough profiles of (a) 50-250, (b) 130-250, (c) 250-250 (d) 250-130, (e) 250-50 ppm TOL-TCM mixtures and (f) main breakthrough onset metrics.

Table 50. Breakthrough onset and task duration values for binary adsorption.

System	$C_{0,i}$ (ppm)	$t_{5\%}$ (h)	$\Delta t_{9\,ppm}$ (h)	$\Delta t_{CProS\ TASK}$ (h)	t_{CPU} (s)	Figure 42
TOL-TCM	50	19.18	19.22	19.00	17.630	(a)
	250	20.17	20.13			
TOL-TCM	130	16.75	16.76	16.75	22.757	(b)
	250	18.74	18.70			
TOL-TCM	250	14.16	14.15	14.00	14.800	(c)
	250	16.92	16.87			
TOL-TCM	250	18.79	18.78	18.75	16.876	(d)
	130	24.74	24.90			
TOL-TCM	250	23.67	23.65	23.50	15.500	(e)
	50	35.40	36.29			

11.5 CProS MILP Scheduling Results

The API production and emissions abatement scheduling problem described in this PhD thesis is optimised by the CProS framework. The MILP models are solved using the CProS tool (Misra et al., 2022), which utilizes the GAMS software suite to solve the problem instances to optimality via the described mathematical model, adsorption task duration of which is informed by gPROMS® dynamic simulation results for five case studies of different VOC emission mixture concentrations. Figure 43 showcases the Gantt charts emerging from the optimal solution of the five scenarios and Table 51 summarizes main metrics of the solution of each scenario.

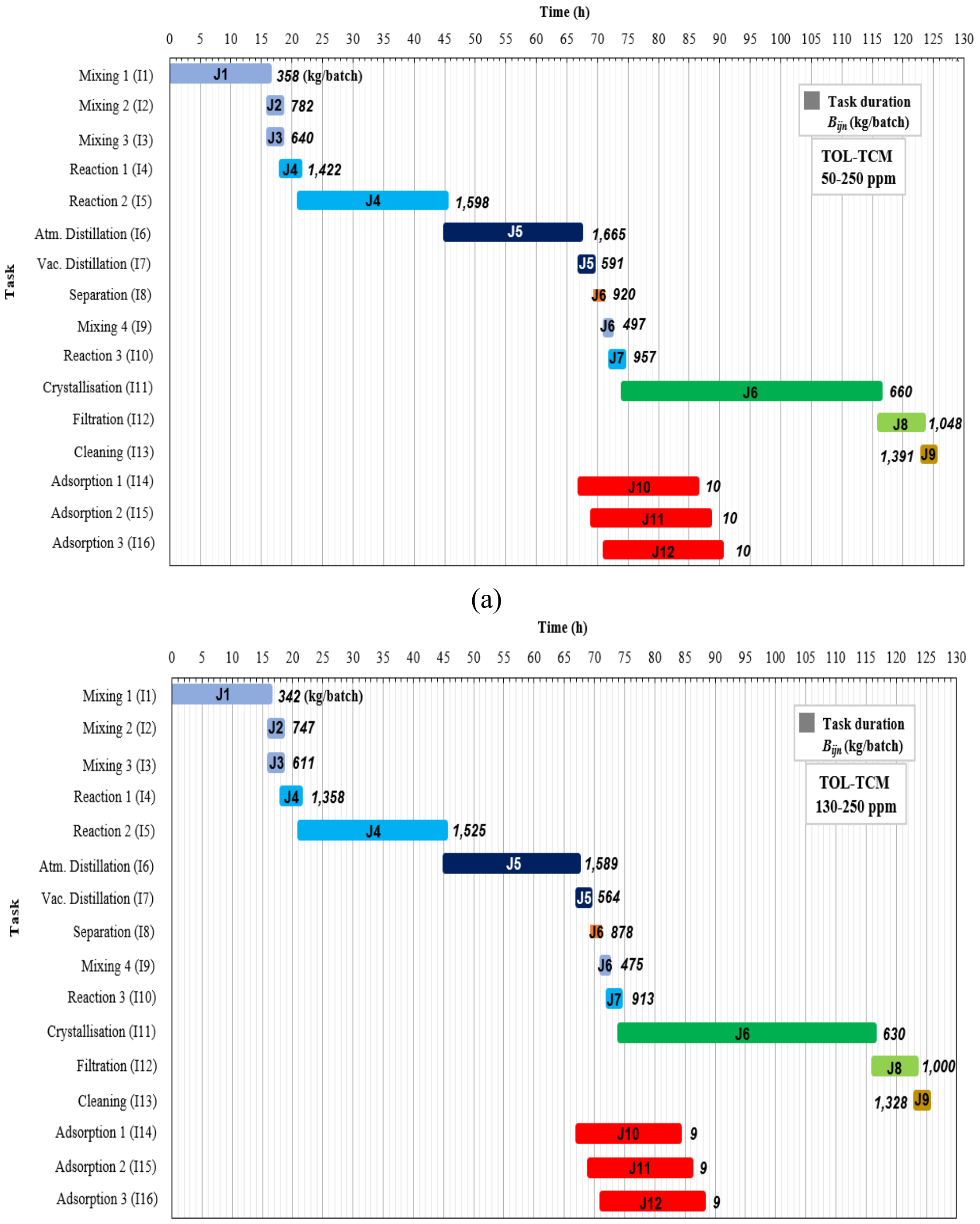
Time (h)
0 5 10 15 20 25 30 35 40 45 50 55 60 65 70 75 80 85 90 95 100 105 110 115 120 125 130
Task
Mixing 1 (I1)
Mixing 2 (I2)
Mixing 3 (I3)
Reaction 1 (I4)
Reaction 2 (I5)
Atm. Distillation (I6)
Vac. Distillation (I7)
Separation (I8)
Mixing 4 (I9)
Reaction 3 (I10)
Crystallisation (I11)
Filtration (I12)
Cleaning (I13)
Adsorption 1 (I14)
Adsorption 2 (I15)
Adsorption 3 (I16)
J1 358 (kg/batch)
J2 782
J3 640
J4 1,422
J4 1,598
J5 1,665
J5 591
J6 920
J6 497
J7 957
J6 660
J8 1,048
1,391 J9
J10 10
J11 10
J12 10
Task duration
B_{ijn} (kg/batch)
TOL-TCM
50-250 ppm
J1 342 (kg/batch)
J2 747
J3 611
J4 1,358
J4 1,525
J5 1,589
J5 564
J6 878
J6 475
J7 913
J6 630
J8 1,000
1,328 J9
J10 9
J11 9
J12 9
Task duration
B_{ijn} (kg/batch)
TOL-TCM
130-250 ppm

(a)

(b)

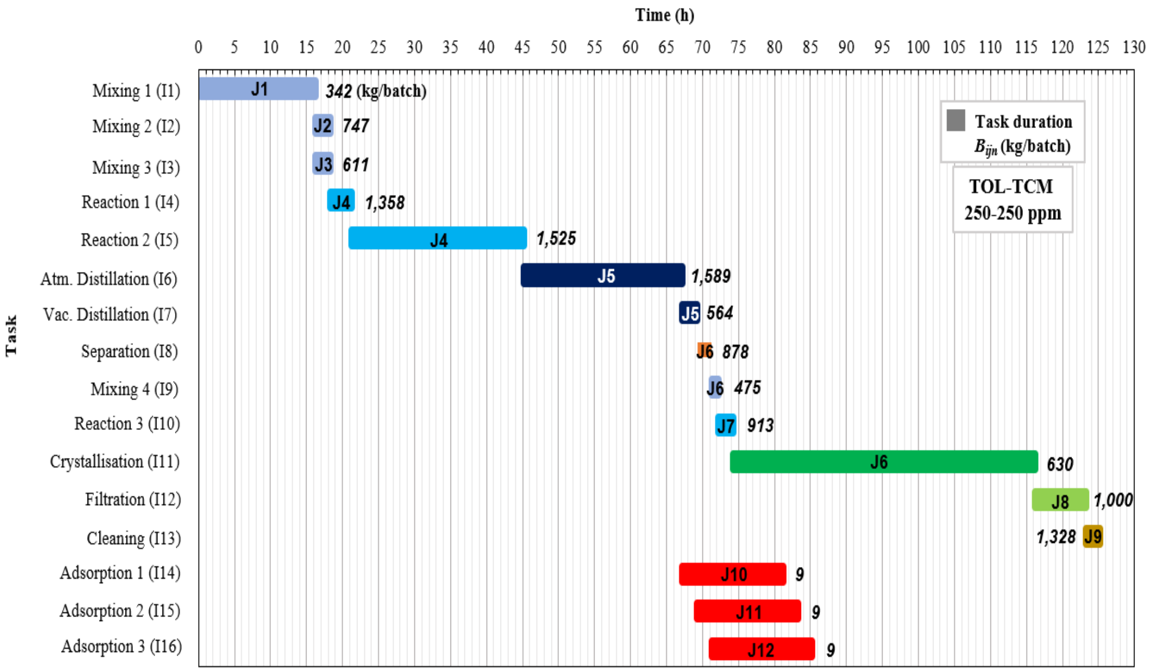
Time (h)
0 5 10 15 20 25 30 35 40 45 50 55 60 65 70 75 80 85 90 95 100 105 110 115 120 125 130
Task
Mixing 1 (I1)
Mixing 2 (I2)
Mixing 3 (I3)
Reaction 1 (I4)
Reaction 2 (I5)
Atm. Distillation (I6)
Vac. Distillation (I7)
Separation (I8)
Mixing 4 (I9)
Reaction 3 (I10)
Crystallisation (I11)
Filtration (I12)
Cleaning (I13)
Adsorption 1 (I14)
Adsorption 2 (I15)
Adsorption 3 (I16)
J1 342 (kg/batch)
J2 747
J3 611
J4 1,358
J4 1,525
J5 1,589
J5 564
J6 878
J6 475
J7 913
J6 630
J8 1,000
1,328 J9
J10 9
J11 9
J12 9
Task duration
B_{ijn} (kg/batch)
TOL-TCM
250-250 ppm

(c)

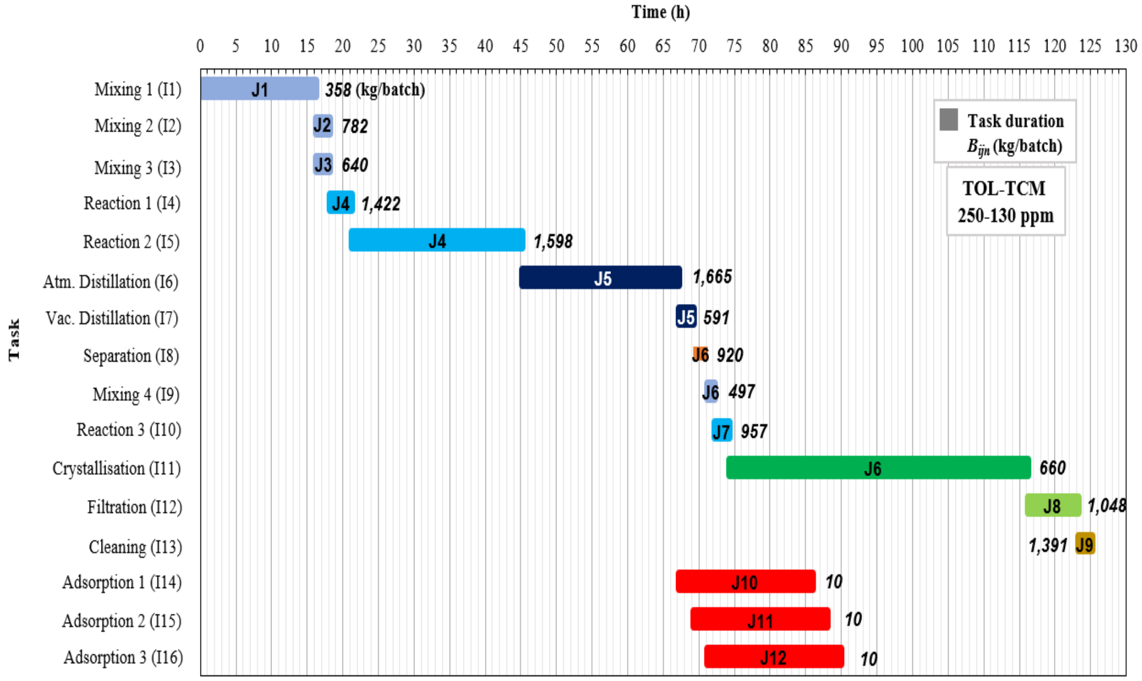
Time (h)
0 5 10 15 20 25 30 35 40 45 50 55 60 65 70 75 80 85 90 95 100 105 110 115 120 125 130
Task
Mixing 1 (I1)
Mixing 2 (I2)
Mixing 3 (I3)
Reaction 1 (I4)
Reaction 2 (I5)
Atm. Distillation (I6)
Vac. Distillation (I7)
Separation (I8)
Mixing 4 (I9)
Reaction 3 (I10)
Crystallisation (I11)
Filtration (I12)
Cleaning (I13)
Adsorption 1 (I14)
Adsorption 2 (I15)
Adsorption 3 (I16)
J1 358 (kg/batch)
J2 782
J3 640
J4 1,422
J4 1,598
J5 1,665
J5 591
J6 920
J6 497
J7 957
J6 660
J8 1,048
1,391 J9
J10 10
J11 10
J12 10
Task duration
B_{ijn} (kg/batch)
TOL-TCM
250-130 ppm

(d)

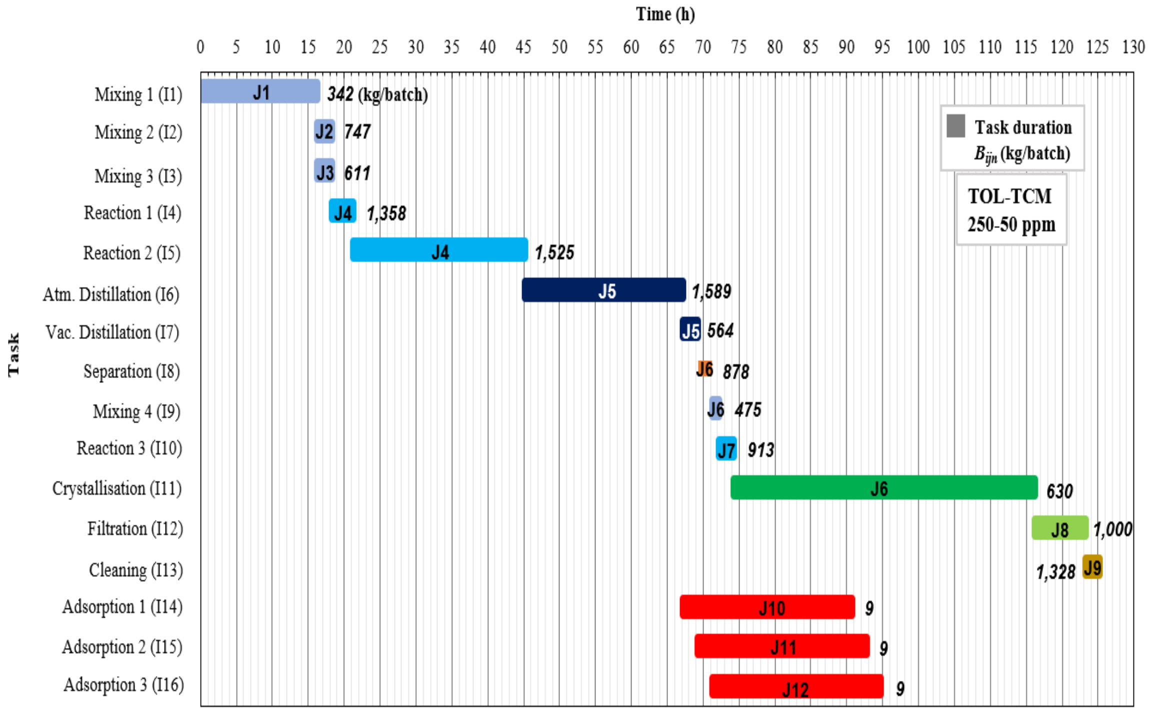

(e)

Figure 43. Gantt chart results for the five scenarios of MILP scheduling.

The makespan minimisation problem presented in this PhD thesis is solved five times for different durations of the adsorption tasks. The Gantt charts emerging from the solution of the MILP makespan minimisation problem follow a similar pattern. Specifically, production steps are performed in a sequential manner, in line with the recipe, with adsorption tasks (I14-I16) starting at the end of each emission producing task (I6-I8) and in parallel to the rest of the recipe steps.

Interestingly, what differs among the five scenarios examined are the material quantities processed in each step. Specifically, the values of variables B_{ijn}, the material quantities processed at unit j at the start of time period n, for the cases of TOL-TCM 50-250 ppm and 250-130 ppm are slightly higher compared to the cases of TOL-TCM 130-250, 250-250 and 250-50 ppm. Furthermore, small quantities of feed material remain unreacted at the end of the production horizons in all case studies. Although all five scenarios examined result in the same total makespan of 125 h per batch, it is likely that in an STN where more production stages take place and/or the solvent load is higher/lower, the makespan and Gantt charts would show differences.

Table 51. MILP solution metrics for the five scenarios.

System	$C_{0,i}$ (ppm)	*Obj. Value* (h)	$t_{execution}$ (s)	$t_{solution}$ (s)	$N_{variables}$	$N_{constraints}$	RAM (MB)	Fig.42
TOL-TCM	50 250	125	17.630	5.79	40,269	76,463	42	(a)
TOL-TCM	130 250	125	22.757	10.82	40,269	76,436	41	(b)
TOL-TCM	250 250	125	14.800	4.67	40,269	76,403	40	(c)
TOL-TCM	250 130	125	16.876	6.70	40,269	76,460	42	(d)
TOL-TCM	250 50	125	15.500	5.17	40,269	76,517	43	(e)

11.6 Economic Evaluation

Systematic economic analysis is essential to informed process intervention decisions. The examined adsorption process is implemented at an existing pharmaceutical manufacturing site with essential auxiliary structures already in place. Despite the batch operation of the API production, the adsorption column operates continuously and 7680 h of operation per year are considered. As the process is already installed and operational, capital expenditure is not an object of this investigation.

This study focuses on the effect of different VOC emissions load and mixtures, number of activated carbon changeovers, solvent prices and the makespan in the total annual operating expenses. Specifically, we assume two VOC mixture compositions (A, B) corresponding to two binary mixtures each, of dichloromethane-toluene (250-250 ppm) and toluene-chloroform (50-250 ppm) as mixture A and of dichloromethane-toluene (250-250 ppm) and toluene-chloroform (250-50 ppm) as mixture B, for two different VOC emission loads. In case study 0, the base case, the emissions escaping from vessel vents to the adsorption unit are assumed to represent 2% of the total VOC solvent mass of each API production stage based on the product recipe. We then investigate the effect on solvent load on OpEx by assuming that VOC emissions to the bed represent 5% of the total VOC solvent mass of each API production stage instead of 2% (case study 1). Next, we examine the effect of solvent prices on the OpEx by examining the 2% solvent load case with 50% of the original solvent prices (case study 2).

Finally, as reducing the amount of emissions, will lead to less frequent need for adsorbent changeovers, we examine the scenario where both VOC emissions load and number of adsorbent changeovers per year change by ± 50% simultaneously.

For each of these three cases, we examine the effect of 18, 20 and 22 adsorbent material changeovers per year, as well as, 120 h, 125 h and 130 h of total makespan on the annual OpEx. The number of API batches per year remains constant at 131 across all cases.

Table 52. VOC solvent prices.

VOC	Price (GBP kg^{-1})	Vendor
DCM	8.78	Spectrum Chemical MFG Corp (2024)
TCM	10.55	Spectrum Chemical MFG Corp (2024)
TOL	6.26	Spectrum Chemical MFG Corp (2024)

Table 53 summarises the VOC mixture compositions and material loads examined in the thesis.

Table 53. VOC mixture compositions and loads for OpEx calculation cases.

VOC mixture A composition							
Emissions fraction of total solvent mass				**2%**		**5%**	
	VOC	Mr (g mol^{-1})	$C_{0,i}$ (ppm)	Mass / batch (kg)	Mass / year (kg)	Mass / batch (kg)	Mass / year (kg)
Stage 1	DCM	84.93	250	6	817	16	2,042
	TOL	92.14	250	7	886	17	2,215
Stage 2	TOL	92.14	50	4	526	10	1,314
	TCM	119.37	250	26	3,404	65	8,511
VOC mixture B composition							
Emissions fraction of total solvent mass				**2%**		**5%**	
	VOC	Mr (g mol^{-1})	$C_{0,i}$ (ppm)	Mass / batch (kg)	Mass / year (kg)	Mass / batch (kg)	Mass / year (kg)
Stage 1	DCM	84.93	250	6	817	16	2,042
	TOL	92.14	250	7	886	17	2,215
Stage 2	TOL	92.14	250	24	3,121	60	7,803

TCM	119.37	50	6	809	15	2,022

11.7 Operating expenditure (OpEx) methodology

As only the operating expenditure (OpEx) is considered in this PhD thesis, the following methodology is assumed. Annual operating expenditure ($OpEx_{annual}$) is calculated as the sum of annual material (solvent emissions) (MAT_{annual}), utilities (U_{annual}), labour (L_{annual}), maintenance (M_{annual}) and adsorbent changeover (AC_{annual}) costs. Utilities, labour and maintenance costs calculation is based on (Couper, 2003):

$$L_{annual} = t_{operation,annual} Wage_{hourly} \tag{56}$$

$$M_{annual} = 0.06 CapEx \tag{57}$$

$$OpEx_{annual} = MAT_{annual} + U_{annual} + L_{annual} + M_{annual} + AC_{annual} \tag{58}$$

The utility required by the adsorption unit is only electricity, at an annual consumption of 250,000 kWh, inclusive of auxiliary equipment (pumping, compression, heat exchanger) based on (Sorrels, 2018). The adsorbent changeover cost is per changeover according to industry quotes for this facility. Average hourly wage data and industrial electricity prices are taken from the UK Office of National Statistics (UK Office for National Statistics (ONS), 2023) and UK Department of Energy Security and Net Zero respectively (UK Department Energy Security and Net Zero, 2024). CapEx is an estimate based on (Sorrels, 2018) and solvent pricing from (Spectrum Chemical Manufacturing Mfg Corp, 2024) .

Table 54. OpEx components pricing.

Electricity (GBP kWh^{-1})	AC Changeover (GBP)	Average Wage (GBP h^{-1})	CapEx (GBP)
0.1416	20,473	15.88	623,000

11.8 OpEx Results

In the first case study examined in this PhD thesis the OpEx corresponding to VOC mixtures A and B, at a solvent load corresponding to 2% of total solvent mass per API production stage have been estimated for three makespans (120 h, 125 h and 130 h) and three material changeover instances (18, 20 and 22 per year). Our findings are summarised in Figure 44 and Table 55. There are two colour palettes; greens for VOC mixture A and blues for VOC mixture

B. Solid colours represent 18 adsorbent changeovers per year (N_{AC}), the dotted 20 and the striped 22.

Table 55. Annual OpEx results for all cases in this PhD thesis.

Case Study	Makespan, *MS* (h)	VOC Mix	N_{AC}	OpEx (GBP yr^{-1})	Figure 44
0	120, 125, 130	A	18	615,200	(a)
0	**120, 125, 130**	**A**	**20**	**656,100**	**(a)**
0	120, 125, 130	A	22	697,000	(a)
0	120, 125, 130	B	18	604,000	(a)
0	**120, 125, 130**	**B**	**20**	**645,000**	**(a)**
0	120, 125, 130	B	22	685,900	(a)
1	120, 125, 130	A	18	693,000	(b)
1	120, 125, 130	A	20	734,000	(b)
1	120, 125, 130	A	22	774,900	(b)
1	120, 125, 130	B	18	665,200	(b)
1	120, 125, 130	B	20	706,200	(b)
1	120, 125, 130	B	22	747,100	(b)
2	120, 125, 130	A	18	589,200	(c)
2	120, 125, 130	A	20	630,200	(c)
2	120, 125, 130	A	22	671,100	(c)
2	120, 125, 130	B	18	583,600	(c)
2	120, 125, 130	B	20	624,600	(c)
2	120, 125, 130	B	22	665,500	(c)

Although the batch makespan did not change for the scenarios tested in the MILP problem described in this PhD thesis, it is possible that for different material loads and or more stages of API production, the makespan calculated by the MILP problem would be different, hence we have tested the 120 h and 130 h hour scenarios apart from the MILP solution of 125 h. However, despite the batch operation of API production stages, the VOC abatement system utilities and staff work continuously, even when the bed only treats VOC-free air. Therefore, labour and utilities calculations are based on the total operating hours per year, which explains why the API production makespan does not influence the OpEx calculations and results for the adsorption system.

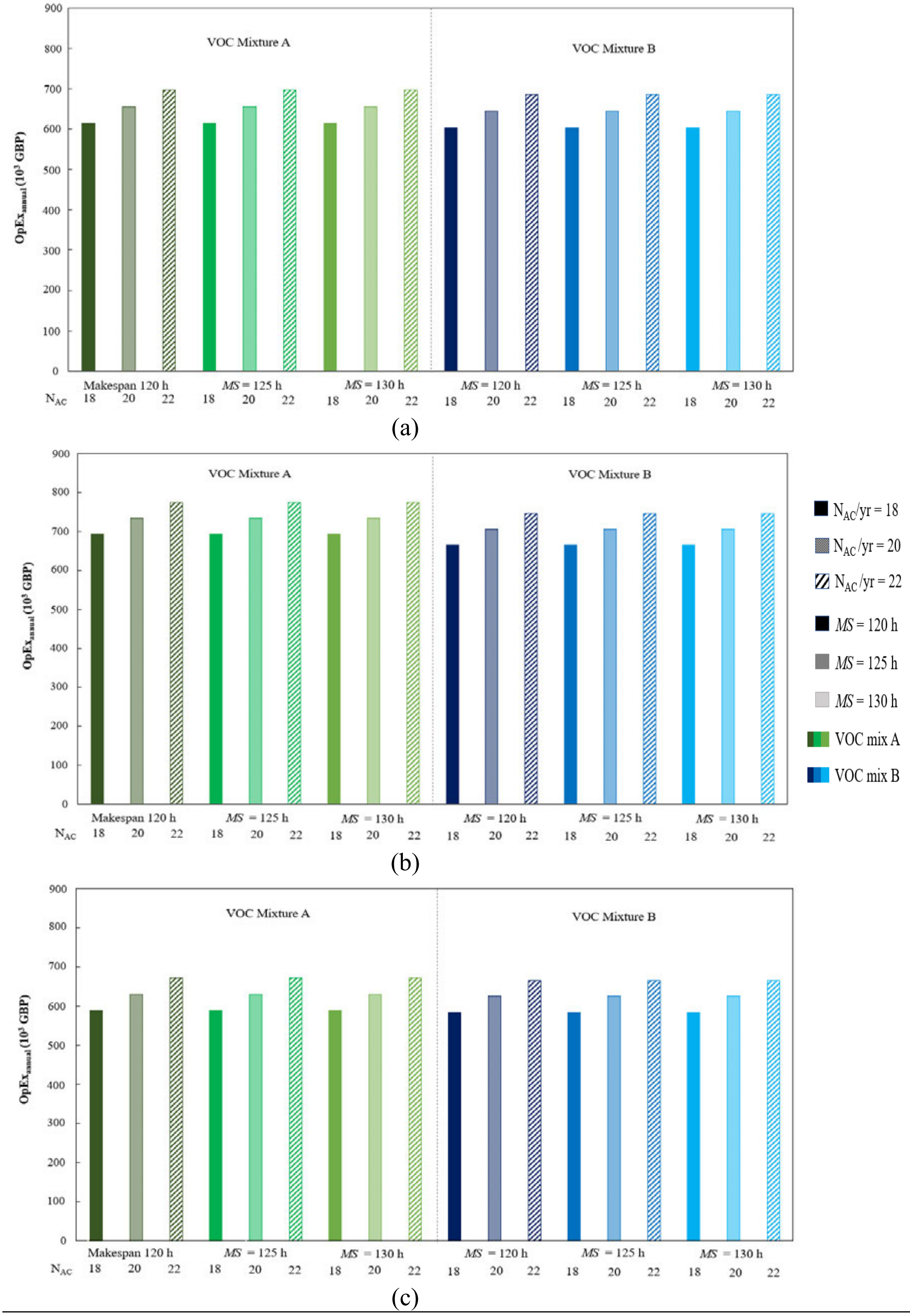

Figure 44. Annual OpEx for (a) base case CS0, (b) 5% solvent mass, CS1, (c) -50% solvent price, CS2.

Figure 44 (a) shows the OpEx results for the case study 0. In all cases examined, VOC mixture A has a higher OpEx compared to VOC mixture B. Specifically, for 18 adsorbent changeovers per year, OpEx of mix A is 1.83% higher than for mix B, for 20 adsorbent changeovers per year, 1.71% and for 22 adsorbent changeovers per year, 1.61%. It is further observed that OpEx for both mixtures increases with the number of adsorbent changeovers. For mixture A, OpEx is 6.44% lower for 18 changeovers per year compared to 20 changeovers per year, while for mixture B 6.56%. When comparing the case of 18 changeovers per year vs. 22, the OpEx is 12.48% lower for mixture A, and 12.70% lower for mixture B respectively. Finally, for mixture A, OpEx is 6.05% lower for 20 changeovers per year compared to 22, and for mixture B, 6.15% for 20 changeovers per year compared to 22.

Figure 44 (b) presents the OpEx calculated for the case study 1, where the total VOC emissions directed to the adsorption column represent 5% of the process total solvent mass instead of 2%. The operational expenditure associated with VOC mixture A is higher in all cases compared to the ones for VOC mixture B. For 18 adsorbent changeovers per year, OpEx for VOC mixture A is 4.10% higher than for mixture B. For 20 changeovers per year, OpEx is 3.86% higher for mixture A than for mixture B. Finally, for 22 changeovers per year, OpEx is 3.66% higher for mixture A compared to mixture B. OpEx also increases with the number of changeovers per year. Specifically, for mixture A, the OpEx is 5.74% lower, and for mixture B, 5.97% lower for 18 compared to 20 changeovers per year respectively. For VOC mixture A, OpEx is 11.16% lower for 18 changeovers per year compared to 22, while for VOC mixture B, it is 11.60% lower. Finally, OpEx is 5.43% lower for 20 changeovers per year compared to 22, for mixture A, and 5.63% lower for mixture B.

Figure 44 (c) presents the OpEx estimated for case study 2, where solvent prices are 50% lower than the base case. This case study shows the lowest difference in OpEx between mixtures A and B, with mixture A’s OpEx again, marginally higher. Specifically, for 18 changeovers per year, mixture A’s OpEx is 0.95% higher than mixture B’s, for 20 changeovers per year, 0.89% and for 22 changeovers per year, 0.83%. For mixture A, the OpEx corresponding to 18 adsorbent changeovers per year is 6.72% lower than for 20 changeovers per year, while for mixture B, 6.78% lower for 18 vs. 20 changeovers per year. When comparing the difference between 18 and 22 changeovers per year, the OpEx for mixture A is 13% lower and for mixture B 13.11% lower. Finally, the OpEx for mixture A is 6.29% lower and for mixture B 6.35% lower for 20 changeovers per year, compared to 22 changeovers.

Figure 45 (a) summarises the comparison between case study 0 and case study 1, where the VOC emissions mass increases from 2% to 5% of the total process solvent mass. The makespan shown is 120 h, as no differences are observed among the three makespan cases. The comparison shows clear OpEx increase for all case study 1 scenarios. Specifically, VOC mixture A at 18 changeovers per year in case study 0 has 11.91% lower OpEx compared to case study 1. For mixture A, for 20 changeovers per year, the OpEx in case study 0 is 11.20% lower and for 22 changeovers per year, 10.58% lower in case study 0, compared to the respective case study 1 results. For mixture B, the calculated OpEx for 18 changeovers is 9.64%, for 20 changeovers 9.06% and for 22 changeovers 8.54% lower in case study 0 compared to case study 1 respectively.

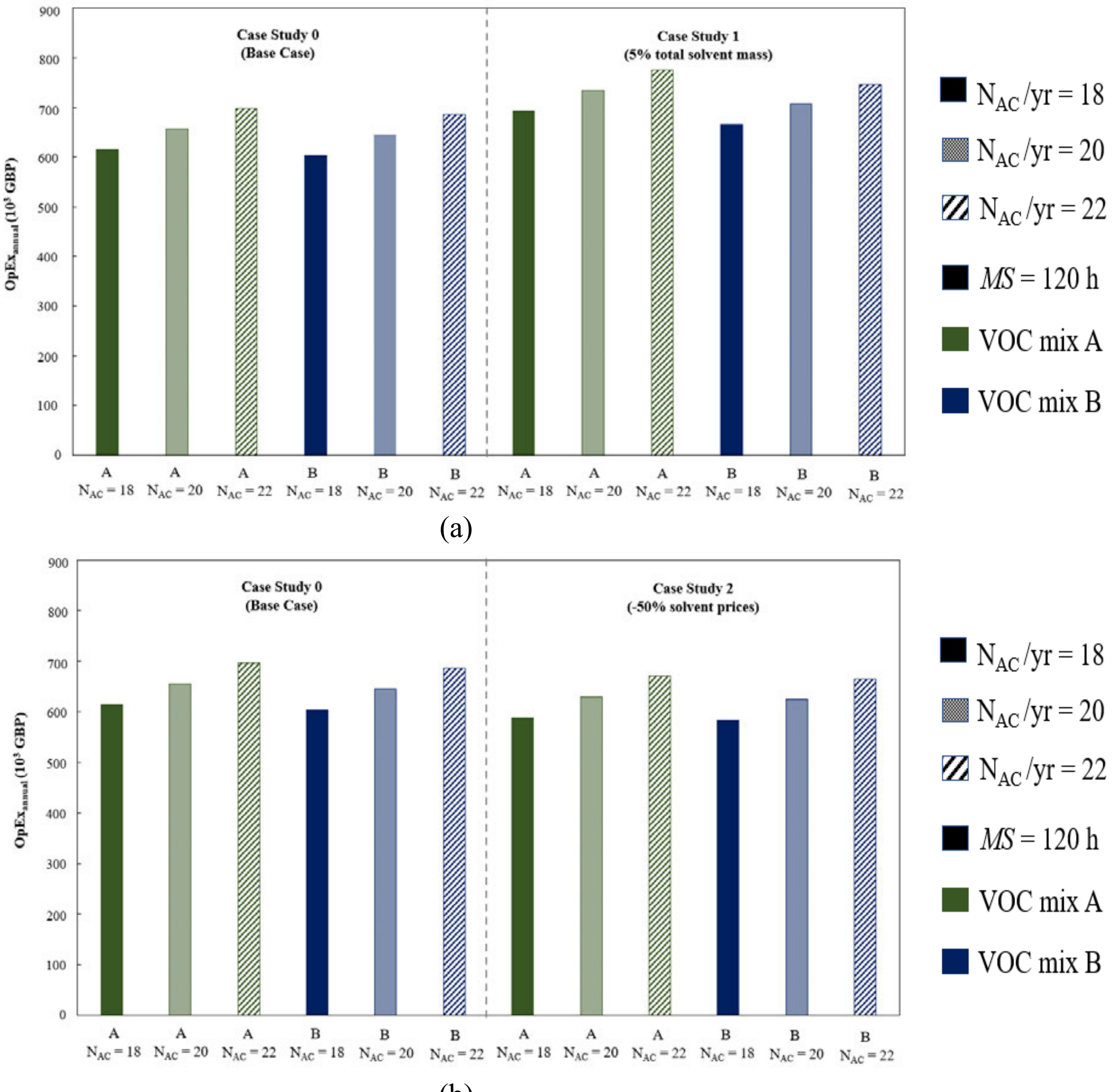

(a)

(b)

Figure 45. Case study comparisons (a) CS0 vs. CS1, (b) CS0 vs. CS2.

Figure 45 (b) the results of the OpEx comparison of case study 0 and case study 2, where the effect of solvent price on OpEx cost is investigated, by the assumption of 50% lower solvent prices. As expected, case study 2 has lower OpEx in all cases considered. The makespan shown is 120 h, as no differences are observed among the three makespan cases. Specifically, for mixture A, 18 changeovers per year result 4.31% lower OpEx, 20 changeovers per year results in 4.04% lower OpEx, and 22 changeovers per year result in 3.79% lower OpEx, for case study 2 compared to case study 0. For mixture B, the OpEx calculated for 18 changeovers per year is 3.43% lower, for 20 changeovers per year 3.21% lower and for 22 changeovers per year 3.02% lower in case study 0 compared to case study 2 respectively.

Figure 46 summarises the OpEx cost comparisons of the different cases studies examined in this PhD thesis, with respect to the base case (VOC emissions represent 2% of total solvent load, 125 h makespan and 20 adsorbent changeovers per year). Both VOC mixtures (composition A and composition B) follow the same trend. The combined effect of reducing the emissions load and the number of adsorbent changeovers per year by 50% is causing a remarkable 35% reduction in OpEx, thus proving that increased process sustainability and economic benefits can be achieved simultaneously. Total VOC emission load plays a significant role in OpEx fluctuation, as a 3% increase results in OpEx increases of over 75,000 GBP for mixture A and over 50,000 GBP for mixture B. Next, the effect of number of adsorbent changeovers per year is examined. The left side of the chart (18 changeovers per year) shows OpEx savings over 40,000 GBP for both solvent loads and VOC mixture compositions.

Finally, the last bar in the chart shows the effect on OpEx from a ± 50% change in solvent prices. The greater cost savings and cost increases are observed for VOC mixture A, at over 25,000 GBP per year, while, for mixture B the OpEx changes are over 20,000 GBP per year. Undoubtedly, the OpEx fluctuations become more significant than 10% when multiple factors contribute in parallel (such as high emission loads and 22 adsorbent changeovers per year). This analysis underscores the importance of accurate emission measurements and the economic benefits brought on by potential waste stream manipulation strategies, such as delaying toluene breakthrough onset by pairing it with low chloroform concentration flows.

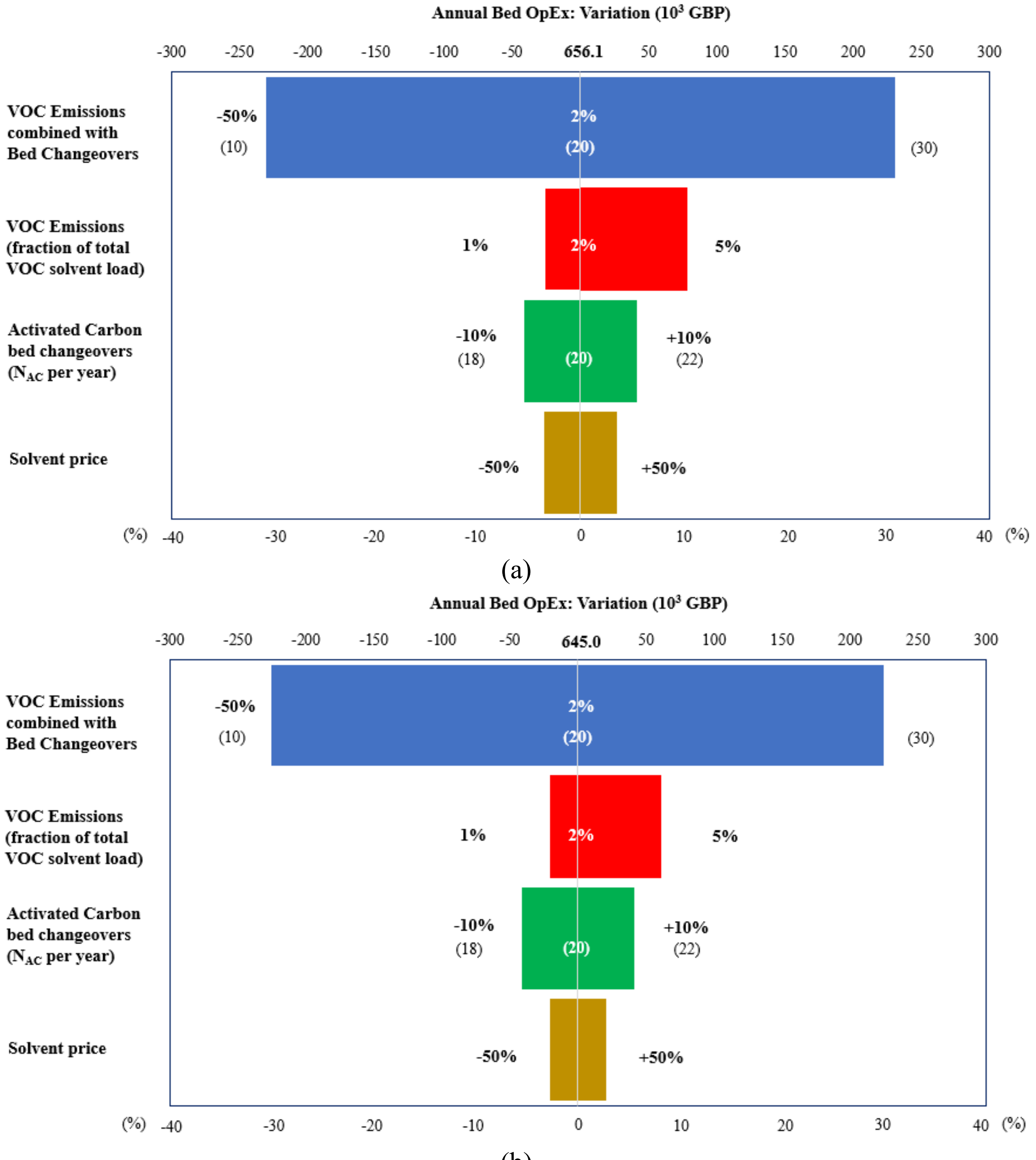

(a)

(b)

Figure 46. OpEx case study factor effect assessment for (a) mixture A and (b) mixture B.

11.9 Chapter Conclusions

In this chapter, an industrial case study of API production is formulated as a MILP scheduling model informed by both the production recipe and dynamic gPROMS® simulation results from multicomponent VOC adsorption.

First, our validated (Tzanakopoulou et al., 2023), multicomponent, nonisothermal dynamic adsorption model is used to examine breakthrough characteristics, specifically breakthrough onset time, for five binary VOC mixtures. The mixture of toluene-chloroform (TOL-TCM) is investigated for five concentration pairs (50-250, 130-250, 250-250, 250-130, 250-50 ppm) the ranges of which are informed by industrial FTIR measurements. Breakthrough onset times range between 14 and 24 hours, with earlier breakthrough onset observed at higher load mixtures due to competitive adsorption phenomena and adsorbent saturation. The 9 ppm breakthrough time is used as the cut-off limit for the adsorption column and thus the adsorption task duration in the MILP model, based on UK environmental protection regulations and plant operating parameters.

The MILP scheduling model example is formulated and solved in the CProS web application of Misra et al. (2022) for the five different VOC emission concentration scenarios. While in the real world there is one adsorption column capturing the VOC emissions simultaneously, due to task allocation constraints in the MILP model the adsorption column has been modelled as three different units. The solution results in five Gantt charts with identical task sequence and total makespan of 125 h. Material balances are the same for two and for three of the total five scenarios while feed materials are not used completely. Adsorption tasks are scheduled to run in parallel immediately after the VOC-producing tasks are completed. Despite the makespan not being impacted by the different VOC emission mixtures in this scenario, it is likely that adding more API production stages and/or different VOC emission pattern would yield different makespans.

Finally, this PhD thesis continues to present the estimation of annual operating expenditure (OpEx) of the VOC abatement system. The API recipe and industrial data are used to investigate the effect of two different VOC emission patterns, three different makespans, three different numbers of adsorbent changeovers per year, two different total emission loads and two sets of industrial solvent prices on OpEx. Our results reveal that makespan does not impact the OpEx because even though API production is batch, the VOC abatement system works continuously in the background even though it might not be adsorbing VOCs all the time. On the contrary, the number of adsorbent changeovers per year increases the OpEx in all cases examined, by ≈5-13%. Moreover, VOC emissions mixture A demonstrates higher OpEx in all cases considered by ≈1-4%, due to the higher concentration of chloroform in the mix. Interestingly, the solvent load, i.e. the VOC emissions total mass, plays a significant role in

OpEx, as a 3% increase in solvent mass leads to OpEx that is higher by ≈8-11%. Solvent prices appear to play a secondary role, as a 50% change in solvent prices results in a ≈3-4% difference in OpEx. Finally, the biggest OpEx savings are achieved through a combined reduction in solvent emissions load and total number of adsorbent changeovers per year by 50% which leads to 35% lower OpEx.

This PhD thesis underlines the importance combined process modelling and optimisation for improved process efficiency. Moreover, it highlights the need of the inclusion of waste management tasks in optimisation models to align with sustainability targets and environmental protection laws in a more systematic way. Furthermore, possibly prompting the creation of new VOC waste management protocols based on VOC release timing and task-solvent sequencing to ensure minimal impact on and maximum lifespan of the activated carbon fixed bed column used as the VOC effluent capture system. This way the operating expenditure savings stemming from the less frequent activated carbon bed changeovers as well as lower total VOC emission loads, renders the process even more economic, thus paving the way for more affordable access to life-saving APIs.

PART VI

RESEARCH CONTRIBUTIONS & THESIS CONCLUSIONS

Chapter 12

Research Contributions

This thesis makes several novel research contributions which merit summarising. The most remarkable contributions include the illumination of adsorption characteristics of multicomponent volatile organic compound emissions, such as breakthrough order, as well as the effect of temperature, superficial velocity, heat boundary conditions, concentration, mixture composition, transient feeds, and column length on breakthrough onset metrics for the first time. Moreover, this PhD thesis demonstrates the predictive abilities of Hodograph Theory for multicomponent VOC mixtures as an operational decision tool and establishes a Langmuir Isotherm Parameter database for single component VOC adsorption. Finally, mixed integer linear programming models for scheduling optimisation are employed for API production including waste management tasks and the factors impacting operating expenditure are highlighted via detailed OpEx projections for the first time.

12.1 Extensive literature review and Langmuir Isotherm parameter estimation for VOCs in pharma.

First, this PhD thesis compiles a comprehensive body of published literature studies that focus on activated carbon volatile organic compound adsorption across several concentrations and operating conditions, under an experimental, or less often, modelling perspective. Furthermore, this PhD thesis is the first concentrated effort to address the limited availability of Langmuir Isotherm parameters for crucial organic solvents used in the pharmaceutical industry. Specifically, experimental results from single component adsorption of acetone, dichloromethane, chloroform, toluene, hexane, and methyl-isobutyl ketone on activated carbon are compiled from the literature and fitted to the Langmuir Isotherm, thus forming an extensive database of parameters for future simulation needs. Langmuir Isotherm parameter accuracy is essential to the successful application of adsorption dynamic modelling and process optimisation. Therefore, the herein established database, spanning activated carbons with different source materials, activation protocols and by association BET surfaces areas and pore volumes, ensures that a wide array of parameter options is available when volatile organic compound adsorption experiments are not possible.

12.2 Development of a multicomponent adsorption dynamic model.

After the extensive study of dynamic adsorption models with varying degrees of complexity available in the literature, this PhD thesis develops a first-principles based multiscale adsorption model to combine both macroscopic and microscopic levels for successful multicomponent adsorption breakthrough modelling. The dynamic adsorption model is one-dimensional in space (z-axis) and accounts for solid phase mass transport with the Linear Driving Force model on a microscopic level. Heat transfer is modelled with a detailed heat balance that can account for adiabatic heat transfer conditions too. Pressure drop is simulated with Ergun's Equation, while multicomponent equilibrium is modelled with the extended Langmuir Isotherm. This model is successfully validated against published experimental data for trace concentration, binary systems of dichloromethane-acetone, heptane-decane, acetone-toluene and benzene-toluene with air or nitrogen as the carrier gas. The model is successful in accurately predicting breakthrough behaviour, temperature profiles and pressure drop across several conditions and input mixtures, either with our own estimated Langmuir Isotherm parameters, or from literature-sourced parameter values, thus proving its versatility and flexibility of use.

12.3 Determination of multicomponent VOC adsorption breakthrough order.

In this PhD thesis multicomponent mixtures of pharmaceutically relevant VOCs are examined for the first time. The adsorption of trace concentration binary mixtures of dichloromethane-acetone, dichloromethane-chloroform, dichloromethane-toluene is simulated with our validated gPROMS® adsorption model and their breakthrough order strength is revealed as dichloromethane being the weakest held component, followed by acetone, followed by toluene and finally chloroform. Moreover, the adsorption of trace binary mixtures of acetone-toluene, and benzene-toluene is used for validation against published experimental data which demonstrates the success of our modelling framework even under lack of crucial parameter values from the original publication. Finally, the successful simulation of binary mixtures of hexane-toluene, hexane-acetone and hexane-dichloromethane reveal the breakthrough order strength among these VOCs to be, from weakest to strongest held: dichloromethane, hexane, acetone, and toluene. Based on the above it is deducted that for solvents belonging in the same family (e.g., heptane-decane, dichloromethane-trichloromethane) the molecular weight proves to be the deciding factor for strength of retention from the activated carbon, while for solvents belonging in different chemical families the situation is case specific and dependent on the specific properties of the activated carbon. The significance of these results regarding breakthrough order becomes paramount in industrial settings, as they can inform strategic waste stream management protocols with selective stream routing and hold periods to delay breakthrough onset of tightly regulated solvents. In tandem with environmental regulation limits and best available practices, operational interventions such as isolating the dichloromethane streams, or pairing streams of higher emission limit VOCs with lower emission limit VOCs would significantly extend breakthrough onset times, which in turn would imply more time on-line of each adsorption column.

12.4 Sensitivity analyses of multicomponent VOC adsorption.

This thesis, apart from examining the breakthrough order in multicomponent VOC mixture adsorption, further investigated the effect on several key operating parameters. First, the temperature sensitivity analysis conducted via dynamic simulation revealed that higher operating temperatures lead to shorter breakthrough onset times, which is attributed to the exothermic nature of the process. The effect of porosity was also investigated on Chapter 5, revealing case and mixture specific behaviour, thus allowing the conclusion that for different bed porosities detailed simulations are necessary. Examination of the effect of adiabatic heat transfer conditions further revealed heat build-up within the adsorption column, due to adsorption exothermicity. Such temperature rises increase with heavier solvent loads on the emission streams and could pose a significant risk for bed fires if not monitored properly, as well as, could overall impede adsorption efficiency due to the elevated temperature conditions. Decreasing flowrate is associated with later onset and longer duration of breakthrough and reduction of pressure drop in all cases examined. Finally, in view of industrial applications, larger bed length investigations resulted in later onset and longer duration of breakthrough.

12.5 Hodograph Theory applications for multicomponent VOCs

This PhD thesis further demonstrates the application of the, often overlooked, Hodograph Theory on multicomponent mixtures for volatile organic compounds in the pharmaceutical industry for the first time. Specifically, the Hodograph Theory corroborates simulation results from Chapters 5 and 7 based on Langmuir Isotherm parameters. On a qualitative level, simulation results agree with the theory in that dichloromethane is displaced by acetone, chloroform, and toluene, as well as, in Chapter 7, acetone is displaced by toluene and benzene by toluene. Moreover, theoretical breakthrough metrics such as the mean residence time and breakthrough shock time are for the first time tested on pharmaceutical VOC multicomponent mixtures, albeit originally derived for single component streams. It is herein shown that detailed simulations are essential to optimising VOC adsorption processes, as the accuracy of these metrics is limited when applied to multicomponent mixtures. Finally, the application of Hodograph Theory maximum concentration predictions for binary VOC mixtures for pharmaceutical applications (acetone-toluene and benzene-toluene) is for the first time compared vis-à-vis with both experimental and simulation results and it is shown that it can be a useful and quick indicator, although simulations offer greater accuracy. These results can help guide industrial operational decisions regarding stream pairings that allow later breakthrough onset. This PhD thesis succeeds in showing that Hodograph Theory, even though derived for single components and isothermal conditions, can provide initial insights, albeit somewhat crude (in the range of one order of magnitude), on breakthrough order, duration, and maximum outlet concentration predictions. Hence, Hodograph Theory constitutes a valuable diagnostic tool before the engagement of further resources such as the deployment of more analytical methods, i.e., detailed simulation campaigns and potentially pilot plant experiments.

12.6 Transient feed multicomponent VOCs simulations

This thesis addresses transient feed adsorption scenarios for multicomponent volatile organic compound solvents used in the pharmaceutical industry for the first time. The modus operandi of VOC abatement systems in industrial settings is characterised by transient feeds and periods of inactivity. The detailed examination of six transient feed patterns is informed by industrial emission readings and applied to key solvent mixtures. First, the binary mixture of hexane-toluene is used to test the conditions under which hexane breakthrough onset is later under a transient feed regime and it is found that a constant high concentration of toluene (250 ppm) results in a later breakthrough onset compared to the low constant concentration of toluene (100 ppm). Next four patterns of transient feeds are examined for the binary mixtures of dichloromethane-acetone, dichloromethane-chloroform, and dichloromethane-toluene. There it is concluded that the breakthrough onset of DCM, even if present in a high load, is prolonged by components at a low concentration (acetone/toluene/chloroform). The effect of changing inlet mixtures on breakthrough, and even more so on industrial length columns, proves a valuable tool to the understanding of emissions control operations, not only in the field of adsorption, but also for integrated biofiltration systems where adsorption columns act as a pre-processing step. Optimal stream routing based on these results could be the combination of streams with gradual increase of dichloromethane feed concentration in combination with a low, constant inlet concentration of the strongly adsorbing component (acetone, toluene, chloroform), while if the emission limit for hexane were lower, it's stream would have a later breakthrough onset with a higher constant concentration of toluene (250 ppm). Development of stream routing protocols based on transient feed simulations is one step closer to technoeconomic optimisation on several emission capture vistas.

12.7 Multicomponent VOC mixture column operation

In this PhD thesis, for the first time, the effect of superficial velocity across laboratory to industrial column lengths for multicomponent VOC mixtures is explored. Specifically, three binary mixtures (hexane-acetone, hexane-dichloromethane, hexane-toluene) are simulated for four different bed lengths (0.25, 0.50, 0.75, 1 m) and six different superficial velocities (0.1, 0.2, 0.3, 0.5, 0.7, 0.9 m s^{-1}). Key breakthrough metrics reveal preferential adsorption of acetone and toluene over hexane, and hexane over dichloromethane. Temperature peaks are moderate while pressure drops increase at longer column lengths and higher flow rates. The new breakthrough onset metric introduced, breakthrough onset over column length, reveals that breakthrough onset rate does not follow a linear profile with increasing bed length for low superficial velocities. This suggests improved column utilisation operating regimes based on multicomponent mixture composition, flow rate and column length, by assessing the tradeoff between constructing and operating a very long column with limited benefits to its useful time on stream before breakthrough onset, which could potentially be handled by a shorter column. Undoubtedly, future column design specifications should be adjusted to optimise the intended operation with respect to solvent flowrates and operating expenses.

12.8 Mixed Integer Linear Programming scheduling model

In this PhD thesis a MILP model is formulated and applied in a pharmaceutical manufacturing context, not only to meet demand but also to include gas waste capture via adsorption for the first time. Specifically, a 35-state, 16-task State-Task-Network (STN) is constructed based on a batch API manufacturing recipe, which includes the gas abatement tasks associated with production emissions treatment. This model is called to find the optimal production schedule for a minimal makespan objective. The input parameters are not only based on the recipe, but also on VOC adsorption simulations. To this end, five binary VOC (chloroform-toluene) emission mixtures (ranging from 50 to 250 ppm) simulation results regarding breakthrough onset were used as the duration of the adsorption tasks with respect to the most up-to-date emission limits. The optimal schedules for all five cases have a similar form, with sequential execution of tasks, and emission abatement tasks taking place as soon as the emission producing tasks are completed. The overall makespan result is 125 h. This PhD thesis highlights the importance of tying production optimisation with waste treatment, and although not observed in these case studies, it is likely that parallel stage plant operation would result in more complex adsorption task patterns and, depending on the VOC mixture, duration which could impact product makespan.

12.9 Operational expenditure evaluation and comparison for industrial operation

For the first time, based on the MILP schedules and industrial data, VOC abatement system annual Operating Expenditure projections are estimated. Comparisons are made for two VOC emission mixture compositions (DCM-TOL at 250 ppm with TCM-TOL at concentrations ranging between 50-250 ppm), two solvent mass loads (2% vs 5% of total solvent mass), three adsorbent changeover scenarios (18, 20, 22 per year), three makespans (120, 125, 130 h) and two solvent price cases (original and 50% off). It is determined that the makespan duration does not affect operating expenditure, as the VOC abatement column is operated continuously even though the production is batch. This comprehensive evaluation demonstrates that the VOC mixture composition and load, as well as, number of adsorbent changeovers per year are the root causes of OpEx fluctuations.

Specifically, it is remarkable that a 3% difference in the VOC emissions fraction of the total solvent load (2% vs 5%) leads to cost savings of up to over 10%, while the decreasing the need for adsorbent changeovers in a year by four, leads again to cost savings of up to over 10%. The combined 50% reduction of the above scenarios leads to remarkable (35%) OpEx savings. This in turn implies, that strategic stream routing protocols, based on the detailed dynamic simulations are essential to optimal economic efficiency. It could be the case that isolating waste streams with easily displaceable components (e.g. DCM) and pairing of DCM containing streams with low concentration strongly adsorbing solvents (e.g. TCM) would prolong breakthrough onset, and over the course of the year, decrease the number of adsorbent changeovers necessary. Moreover, in-vessel VOC emission capture could be improved with the presence of condensers, which would decrease the load of solvents sent to the activated carbon beds. Thus, later breakthrough onset of tightly regulated VOCs due to well informed stream pairing protocols, as well as interventions in process vessels can contribute significantly to cost minimisation of emissions abatement via adsorption. This PhD thesis concretely proves the need for detailed multicomponent mixture adsorption dynamic simulations for process optimisation.

Chapter 13

Thesis Conclusions

This thesis presents a comprehensive framework for dynamic modelling, simulation, and operational optimisation of Volatile Organic Compounds emissions abatement in the pharmaceutical industry. This PhD thesis focuses on the development and implementation of a dynamic, non-isothermal adsorption model used for studying binary VOC trace mixture adsorption on industrial activated carbon beds for a wide variety of structural properties and operating conditions. A scenario-based investigation of binary mixture behaviour examines (via multiple dynamic simulations, experimental corroboration, and predictive formulas) the effect of key parameter changes on bed performance such as temperature, mixture composition, flowrate, heat transfer boundary conditions, column length, bed porosity.

Theoretical bed performance analysis (employing Glueckauf hodographs) has been employed to provide valuable insight into nonisothermal VOC capture bed operation breakthrough metrics, for both clean and used beds, for the mixtures of dichloromethane-acetone, dichloromethane-chloroform, and dichloromethane-toluene, as well as, maximum outlet concentration for clean beds for the binary mixtures of acetone-toluene, benzene-toluene.

Furthermore, this PhD thesis introduced transient feed concentration simulations for VOC binary mixtures for the first time, thus enabling investigations under realistic operating conditions in a concentrated effort to highlight the effect and potential value of waste stream feed sequencing towards activated carbon bed utilisation optimisation. Finally, a new metric of breakthrough onset time over column length is introduced to assess the rate of change of breakthrough onset for different mixtures and columns lengths spanning from the laboratory to the industrial length under a broad range of superficial velocities to inform column design and operation decisions.

Mixed Integer Linear Programming is then employed to formulate a production scheduling model which not only meets production demands, but also includes and places VOC emissions abatement tasks under consideration in the wider production schedule. For the first time, breakthrough onset times calculated from the dynamic gPROMS® simulations are used to inform task duration for the API manufacturing schedule, thus linking individual process characteristics with the overall plant operation, and providing realistic batch schedules for five scenarios of VOC emission concentrations. Finally, a scenario-based investigation of industrial VOC abatement systems operating expenditure is performed. The effects of solvent load, mixture composition, makespan duration, number of adsorbent changeovers and solvent prices are examined and it is determined that solvent load, VOC mixture composition and number of adsorbent changeovers play a leading role on the process operating cost. Thus, strategic stream routing protocols based on breakthrough order results and operating conditions can effectively impact the breakthrough onset time. This conclusively underscores the necessity of detailed VOC mixture adsorption investigation for process operation optimisation, so as to not only positively contribute to sustainability goals but also, ensure advanced process efficiency at lower operational expenditure.

The results presented in this thesis are subject to various assumptions and limitations which could be addressed by future research.

- All simulations are based on the premise that no moisture is present in the streams. However, in many cases, moisture plays a significant role in adsorption efficiency, as it could interfere with the other adsorbates' retention by the adsorbent. Accounting for water presence in VOC adsorption could be a promising field for future research.
- Production scheduling on an industrial level consists of multiple stages operating concurrently at the plant. In this PhD thesis the case study presented involves one stage of API production. More realistic scenarios would involve multiple stages running concurrently, which could be a topic of future dedicated MILP research.
- All case studies presented in this PhD thesis assume an operational starting point of a "clean", i.e. free of adsorbents, activated carbon bed. Future research could expand on used bed scenarios and their effect on multicomponent VOC mixture adsorption.
- The cases investigated herein highlight the significant role of systematic and rigorous model-based simulation and optimisation campaigns for VOC abatement systems, and the applicability of the methodologies outlined in this PhD thesis in industrial operations. The frameworks presented here can be extended across industries with similar processes and solvent usage and demonstrate the immense value of academic and industrial collaboration for environmental protection at high production efficiency.

PART VII

AUXILIARY CHAPTERS

Appendix A

Nomenclature and Acronyms

A.1 Acronyms

DRK	Dubinin-Radushkevitch-Kaganer
BET	Brunauer-Emmett-Teller
FH-VSM	Flory-Huggins Vacancy Solution Model
CProS	Chemical Production Scheduler
VOC(s)	Volatile Organic Compound(s)
MILP	Mixed Integer Linear Programming
MiBK	Methyl isobutyl ketone
UN	United Nations
PDE(s)	Partial Differential Equation(s)
STN	State Task Network
GAMS	General Algebraic Modelling Software
API(s)	Active Pharmaceutical Ingredient(s)
UK	United Kingdom
SDG(s)	Sustainable Development Goals
MINLP	Mixed Integer Non Linear Programming
Lannual	Annual labour costs
Mannual	Annual maintenance costs
MATannual	Annual material costs
ACannual	Annual adsorbent changeover costs
OpExannual	Annual operating expenditure
Uannual	Annual utilities costs
AC	Activated Carbon
IAST	Ideal Adsorbed Solution Theory
MS	Makespan
SA	Surface Area
PAN	Polyacrilonitrile
LDF	Linear Driving Force

CS	Case Study
NIST	National Institute for Standards and Technology
DAEBDF	Differential-Algebraic Equation Backward Difference Formulae
SEPA	Scottish Environmental Protection Agency
BC	Boundary Conditions
DASolver	Differential-Algebraic Solver

A.2 Molecules

ACT	Acetone
DCM	Dichloromethane
HEX	Hexane
TCM	Trichloromethane (Chloroform)
TOL	Toluene
N_2	Nitrogen
O_2	Oxygen

A.3 Symbols

A.3.1 Latin Letters and Symbols

% R.E.	Percentage of relative error
I_k^+/I_k^-	tasks producing/consuming material *k*
J_i	units that can process task *i*
α_{ij}	cost of processing task *i* in unit *j*
$\beta_j^{MIN}/\beta_j^{MAX}$	minimum /maximum capacity of unit *j*
γ_k^{MAX}	storage vessel capacity for material *k*

ξ_{kn}	amount of raw material *k* delivered at time *n* (>0) / demand for material *k* at time *n* (<0)
π_k	revenue from selling unit quantity of material *k*
ρ_{ik}	fraction of material *k* produced (>0) or consumed (<0) in task *i*
τ_{ij}	processing time for task *i* in unit *j*
$\Delta t_{5\%}^{102.5\%}$	breakthrough duration from 5% to 102.5% of final concentration of component i (s)
$\Delta t_{5\%}^{105\%}$	breakthrough duration from 5% to 105% of final concentration of component i (s)
$\Delta t_{5\%}^{95\%}$	breakthrough duration from 5% to 95% of final concentration of component i (s)
b_i	Langmuir affinity coefficient (m^3 mol^{-1})
$b_{o,i}$	pre-exponential Langmuir constant (m^3 mol^{-1})
$C_{,i}$	component gas phase VOC concentration (mol m^{-3})
$C_{0,i}$	inlet concentration of i (mol m^{-3})
$C_{max,E}$	maximum concentration at column outlet obtained by publ. experiment (mol m^{-3})
$C_{max,H}$	maximum concentration at column outlet predicted by hodograph theory (mol m^{-3})
$C_{max,S}$	maximum concentration at column outlet predicted by simulation (mol m^{-3})
Cp_g	specific heat capacity of gas (J kg^{-1} K^{-1})
Cp_p	specific heat capacity of particle (J kg^{-1} K^{-1})
$C_{s0,i}$	adsorbed phase concentration at equilibrium with $C_{0,i}$ (mol m^{-3})
C_t	total gas phase VOC concentration (mol m^{-3})
D	bed inner diameter (m)
$D_{AB,i}$	molecular diffusivity (m^2 s^{-1})
$D_{eff,i}$	effective diffusivity of i (m^2 s^{-1})
$D_{k,i}$	Knudsen diffusivity (m^2 s^{-1})
d_{lm}	mean logarithmic column diameter (-)
d_p	particle diameter (m)

$D_{z,i}$	axial dispersion coefficient (m^2 s^{-1})
H-E	Hodograph-Experiment
h_{int}	internal heat transfer coefficient (W m^{-2} K^{-1})
h_o	overall heat transfer coefficient (W m^{-2} K^{-1})
i	Mixture component / tasks in MILP Chapter
j	units
k	materials
k_{eff}	effective thermal conductivity (W m^{-1} K^{-1})
k_{ew}	effective wall thermal conductivity (W m^{-1} K^{-1})
k_{ez}	effective axial thermal conductivity (W m^{-1} K^{-1})
$k_{f,i}$	effective mass transfer coefficient of component i (m s^{-1})
k_g	gas thermal conductivity (W m^{-1} K^{-1})
$k_{LDF,i}$	LDF mass transfer coefficient (s^{-1})
k_p	particle thermal conductivity (W m^{-1} K^{-1})
k_w	wall thermal conductivity (W m^{-1} K^{-1})
L	bed length (m)
M	positive root of coherence equation (-)
m_{AC}	mass of activated carbon (kg)
M_r	molecular weight (g mol^{-1})
N	negative root of coherence equation (-)
P	pressure (atm only in Eq.(10)) / (Pa)
$q_{e,i}$	equilibrium adsorption capacity of i (mol kg^{-1})
q_i	adsorbed phase VOC concentration (mol m^{-3})
$q_{m,i}$	maximum adsorption capacity of material for component i (mol kg^{-1})

$q_{pe,i}$	equilibrium adsorption capacity of i (mol m^{-3})
R	column inner radius (m)
Re_p	Reynolds number (adsorbent particle)
r_p	average pore radius ($1.1\cdot10^{-9}$ m)
R_p	particle radius (m)
SA	Surface area of adsorbent material (m^2 g^{-1})
Sc_i	Schmidt number of i
$S\text{-}E$	Simulation-Experiment
Sh	Sherwood number (-)
$S\text{-}H$	Simulation-Hodograph
T	temperature (K)
$t_{105\%,i}$	breakthrough time of outlet concentration at 105% of final concentration of component i (s)
$t_{5\%,i}$	breakthrough onset time of component i (s)
$t_{95\%,i}$	breakthrough time of outlet concentration at 95% of final concentration of component i (s)
t_{CPU}	Cloud server CPU run time (s)
$t_{drt,i}$	breakthrough duration of component i (s)
T_{in}	inlet temperature (K)
T_{max}	maximum temperature (K)
$t_{shock,i}$	shock breakthrough time of component i (s)
T_w	wall temperature (K)
u	interstitial velocity (m s^{-1})
V_{pore}	adsorbent pore volume ($6.1\cdot10^{-4}$ m^3 kg^{-1})
V_s	superficial velocity (m s^{-1})
x	wall thickness (m)

$\Delta H_{ad,i}$	heat of adsorption (J mol^{-1})
$\Delta t_{9\_ppm,i}$	breakthrough duration until 9 ppm concentration at column exit of component i (s)
$\Delta t_{CProS,TASK}$	adsorption task duration in CProS (h)

A.3.2 Greek Letters and Symbols

α_0	empirical mass diffusion correction factor (20)
ε_b	bulk bed porosity (-)
ε_p	particle porosity (-)
μ	gas viscosity (Pa s)
$\mu_{RT,i}$	mean residence time of component i (s)
ρ_b	bed density (kg m^{-3})
ρ_g	gas density (kg m^{-3})
ρ_p	particle density (kg m^{-3})
Σv	atomic diffusion volume (A: VOC, B: carrier)
τ_p	particle tortuosity (-)

Appendix B

Peer-Reviewed Publications

The work in this PhD thesis has been published in various peer-reviewed publications.

B.1 Journal Articles

Tzanakopoulou, V. E., Pollitt, M., Castro-Rodriguez, D., & Gerogiorgis, D. I. (2024). MILP scheduling and economic evaluation for Volatile Organic Compound (VOC) emissions abatement in the pharma industry. *Chemical Engineering Research and Design*, (submitted/under review).

Tzanakopoulou, V. E., Pollitt, M., Castro-Rodriguez, D., & Gerogiorgis, D. I. (2024). Adsorption column performance analysis for Volatile Organic Compound (VOC) emissions abatement in the pharma industry. *Processes*, (revision under review).

Tzanakopoulou, V. E., Narasinghe, K, Pollitt, M., Castro-Rodriguez, D., & Gerogiorgis, D. I. (2024). Dynamic simulation and analysis of dichloromethane-acetone, dichloromethane-trichloromethane and dichloromethane-toluene VOC mixture abatement systems under transient feed conditions. *Computers & Chemical Engineering*, (accepted/in press).

Tzanakopoulou, V.E., Pollitt, M., Castro-Rodriguez, D., & Gerogiorgis, D. I. (2024). Dynamic modelling and simulation of multicomponent Volatile Organic Compound (VOC) abatement systems. *Industrial & Engineering Chemistry Research*, 63, **16**, 7281-7299.

Tzanakopoulou, V. E., Pollitt, M., Castro-Rodriguez, D., Costa, A., & Gerogiorgis, D. I. (2023). Dynamic modelling, simulation and theoretical performance analysis of volatile organic compound (VOC) abatement systems in the pharma industry. *Computers & Chemical Engineering*, **174**, 108248.

B.2 Book Chapter Contributions

Tzanakopoulou, V.E., Pollitt, M., Castro-Rodriguez, D., & Gerogiorgis, D. I. (2024). An industrial case study of dynamic adsorption simulation for Volatile Organic Compound (VOC) pharmaceutical emission abatement. In *Computer Aided Chemical Engineering*, Manenti, F., Reclaitis, G.V., (Eds.), Elsevier, **53**, (in press).

Tzanakopoulou, V.E., Costa, A., Castro-Rodriguez, D., & Gerogiorgis, D. I. (2022). Multicomponent, nonisothermal VOC adsorption modelling for pharmaceutical effluent purification: effect of operating conditions on bed performance. In *Computer Aided Chemical Engineering*, Montastruc, L., Negny, S., (Eds.), Elsevier, **51**, 331-336.

Tzanakopoulou, V.E., Castro-Rodriguez, D., & Gerogiorgis, D. I. (2021). Process modelling and simulation of Volatile Organic Compound (VOC) recovery from pharmaceutical gas emission streams. In *Computer Aided Chemical Engineering*, Turkay, M., Gani, R., (Eds.), Elsevier, **50**, 717-723.

B.3 Conference Proceedings

Tzanakopoulou, V.E., Pollitt, M., Castro-Rodriguez, D., & Gerogiorgis, D. I. An industrial case study of dynamic adsorption simulation for Volatile Organic Compound (VOC) pharmaceutical emission abatement. *In 34th European Symposium on Computer Aided Process Engineering*, Manenti, F., Reclaitis, G.V., *Computer Aided Chemical Engineering*, Elsevier, 2024, **53**, (in press).

Tzanakopoulou, V.E., Costa, A., Castro-Rodriguez, D., & Gerogiorgis, D. I. Multicomponent, nonisothermal VOC adsorption modelling for pharmaceutical effluent purification: effect of operating conditions on bed performance. *In 32nd European Symposium on Computer Aided Process Engineering*, Montastruc, L., Negny, S., *Computer Aided Chemical Engineering,* Elsevier, *Computer Aided Chemical Engineering*, Elsevier, 2022, **51**, 331-336.

Tzanakopoulou, V.E., Castro-Rodriguez, D., & Gerogiorgis, D. I. Process modelling and simulation of Volatile Organic Compound (VOC) recovery from pharmaceutical gas emission streams. *In 31st European Symposium on Computer Aided Process Engineering*, Turkay, M., Gani, R., *Computer Aided Chemical Engineering,* Elsevier, 2021, **50**, 717-723.

B.4 Presentations & Symposia

Presenting author in bold.

Tzanakopoulou, V.E., & **Gerogiorgis, D. I.** (2024). Process Modeling, Simulation and Technoeconomic Evaluation of Batch Vs. Continuous Pharmaceutical Manufacturing (CPM) of Cephalexin. Proceedings of the 2024 AIChE Annual Meeting, San Diego (CA), USA, Oct. 27– Nov. 03, 2024.

Tzanakopoulou, V.E., Pollitt, M., Castro-Rodriguez, D., & Gerogiorgis, D. I. An industrial case study of dynamic adsorption simulation for Volatile Organic Compound (VOC) pharmaceutical emission abatement. Proceedings of the 34th European Symposium on Computer Aided Process Engineering, (ESCAPE-34), Florence, Italy, June 2-6, 2024.

Tzanakopoulou, V.E., Castro-Rodriguez, D., & Gerogiorgis, D. I. In Scottish Research Partnership in Engineering Annual Conference, November 21 2022, Edinburgh, Scotland, UK.

Blair, M., Tzanakopoulou, V.E., Jones, W., & **Gerogiorgis, D. I.** (2023). Process Modeling, Simulation and Technoeconomic Evaluation of Batch Vs. Continuous Pharmaceutical Manufacturing (CPM) of Cephalexin. Proceedings of the 2023 AIChE Annual Meeting, Orlando (FL), USA, Nov 05–10, 2023.

Tzanakopoulou, V.E., Narasinghe, K., & Gerogiorgis, D. I. Multicomponent, nonisothermal VOC adsorption modelling for pharmaceutical emission abatement. In Scottish Research Partnership in Engineering Annual Conference, October 31 2023, Glasgow, Scotland, UK.

Gerogiorgis, D. I., Blair, M., Jones, W., & Tzanakopoulou, V.E. (2023). Process Design and Optimisation: The Critical Role of Property Prediction in Advanced (Bio)Pharmaceutical Manufacturing. Proceedings of the 14th European Congress of Chemical Engineering, (EFCE), Berlin, Germany, September 12-15, 2022.

Tzanakopoulou, V.E., Castro-Rodriguez, D., & Gerogiorgis, D. I. Process modelling and simulation of Volatile Organic Compound (VOC) recovery from pharmaceutical gas emission streams. Proceedings of the 31st European Symposium on Computer Aided Process Engineering, (ESCAPE-31), Istanbul, Turkiye, June 6-9, 2021.

Tzanakopoulou, V.E., & Gerogiorgis, D. I. In Scottish Research Partnership in Engineering Annual Conference, November 21 2022, Edinburgh, Scotland, UK.

Appendix C

Literature References

1. Akbar, M., & Irohara, T. (2018). Scheduling for sustainable manufacturing: A review. *Journal of Cleaner Production*, *205*, 866-883.

2. Atkinson, R. (2000). Atmospheric chemistry of vocs and nox. *Atmospheric Environment*, *34*(12), 2063-2101.

3. Balasubramanian, P., Philip, L., & Murty Bhallamudi, S. (2012). Biotrickling filtration of complex pharmaceutical voc emissions along with chloroform. *Bioresour Technol*, *114*, 149-159.

4. Borkar, C. T., D.; Gumma, S. (2010). Adsorption of dichloromethane on activated carbon. *Journal of Chemical & Engineering Data*, *55*, 1640-1644.

5. Cai, Z. L., & Sorial, G. A. (2009). Treatment of dynamic voc mixture in a trickling-bed air biofilter integrated with cyclic adsorption/desorption beds. *Chemical Engineering Journal*, *151*(1-3), 105-112.

6. Castro, P. M., Grossmann, I. E., & Zhang, Q. (2018). Expanding scope and computational challenges in process scheduling. *Computers & Chemical Engineering*, *114*, 14-42.

7. Castro, P. M., Novais, A. Q., & Carvalho, A. (2008). Optimal equipment allocation for high plant flexibility: An industrial case study. *Industrial & Engineering Chemistry Research*, *47*(8), 2742-2761.

8. Chen, Y., Mockus, L., Orcun, S., & Reklaitis, G. V. (2012). Simulation-optimization approach to clinical trial supply chain management with demand scenario forecast. *Computers & Chemical Engineering*, *40*, 82-96.

9. Chiang, Y.-C. C., P.-C.; Huang, C.-P. (2001). Effects of pore structure and temperature on voc adsorption on ativated carbon. *Carbon*, *39*, 523-534.

10. Chuang, C. L., Chiang, P. C., & Chang, E. E. (2003). Modeling vocs adsorption onto activated carbon. *Chemosphere*, *53*(1), 17-27.

11. Chung, W.-C., Mei, D.-H., Tu, X., & Chang, M.-B. (2018). Removal of vocs from gas streams via plasma and catalysis. *Catalysis Reviews*, *61*(2), 270-331.

12. Coker, A. K. (2007). Physical properties of liquids and gases. In A. K. Coker (Ed.), *Ludwig's applied process design for chemical and petrochemical plants* (4th ed., pp.

103-132). Guld Professional Publishing. https://doi.org/10.1016/B978-0-7506-7766-0.50028-2

13. Constable, D. J. C., Jimenez-Gonzalez, C., & Henderson, R. K. (2007). Perspective on solvent use in the pharmaceutical industry. *Organic Process Research & Development*, *11*(1), 133-137.

14. Couper, J. R. (2003). *Process engineering economics*. Marcel Dekker.

15. Darracq, G., Couvert, A., Couriol, C., Amrane, A., & Le Cloirec, P. (2010). Kinetics of toluene and sulfur compounds removal by means of an integrated process involving the coupling of absorption and biodegradation. *Journal of Chemical Technology and Biotechnology*, *85*(8), 1156-1161.

16. Das, D., Gaur, V., & Verma, N. (2004). Removal of volatile organic compound by activated carbon fiber. *Carbon*, *42*(14), 2949-2962.

17. David, E., & Niculescu, V. C. (2021). Volatile organic compounds (vocs) as environmental pollutants: Occurrence and mitigation using nanomaterials. *Int J Environ Res Public Health*, *18*(24).

18. Debono, O., Gaudion, V., Redon, N., Locoge, N., & Thevenet, F. (2018). Photocatalytic treatment of voc industrial emissions: Ipa removal using a sensor-instrumented reactor. *Chemical Engineering Journal*, *353*, 394-409.

19. Delage, F., Pré, P., & Le Cloirec, P. (2000). Mass transfer and warming during adsorption of high concentrations of vocs on an activated carbon bed:: Experimental and theoretical analysis. *Environmental Science & Technology*, *34*(22), 4816-4821.

20. Delage, F. P., P.; Le Cloirec, P. (2000). Mass transfer and warming during adsorption of high concentrations of vocs on an activated carbon bed: Experimental and theoretical analysis. *Environmental Science & Technology*, *34*, 4816-4821.

21. Department of Environment, F. a. R. A., UK Government. (2023). *Emissions of air pollutants in the uk – non-methane volatile organic compounds (nmvocs) - gov.Uk*. Retrieved 11 September 2023 from https://www.gov.uk/government/statistics/emissions-of-air-pollutants/emissions-of-air-pollutants-in-the-uk-non-methane-volatile-organic-compounds-nmvocs

22. Elekidis, A. P., & Georgiadis, M. C. (2022). Optimal contract selection for contract manufacturing organizations in the secondary pharmaceutical industry. *Computers & Chemical Engineering*, *165*.

23. EPA, U. (2024). *What are volatile organic compounds (vocs)?* Retrieved 08 April from https://www.epa.gov/indoor-air-quality-iaq/what-are-volatile-organic-compounds-vocs

24. Floudas, C. A., & Lin, X. (2004). Continuous-time versus discrete-time approaches for scheduling of chemical processes: A review. *Computers & Chemical Engineering*, *28*(11), 2109-2129.

25. Fournel, L., Mocho, P., Brown, R., & le Cloirec, P. (2010). Modeling breakthrough curves of volatile organic compounds on activated carbon fibers. *Adsorption*, *16*(3), 147-153.

26. Gabelman, A. P. E. (2017, Jul 2017). Adsorption basics: Part 1. *Chemical Engineering Progress*, *113*(7), 48-53.

27. Gales, L., Mendes, A., & Costa, C. (2003). Recovery of acetone, ethyl acetate and ethanol by thermal pressure swing adsorption. *Chemical Engineering Science*, *58*(23-24), 5279-5289.

28. Gales, L. M., A.; Costa, C. (2000). Hysteresis in the cyclic adsorption of acetone ethanol and ethyl acetate on activated carbon. *Carbon*, *38*, 1083-1088.

29. Ge, C. Q., & Yuan, Z. H. (2021). Production scheduling for the reconfigurable modular pharmaceutical manufacturing processes. *Computers & Chemical Engineering*, *151*.

30. Giraudet, S. P., R.; Le Cloirec, P. (2009). Modelling the heat and mass transfers in temperature-swing adsorption of volatile organic compounds onto activated carbons. *Environmental Science & Technology*, *43*, 1173-1179.

31. Griffiths, G. W. (2016). Dissipation and dispersion. In G. W. Griffiths (Ed.), *Numerical analysis using r: Solutions to odes and pdes* (pp. 264-284). Cambridge University Press. https://doi.org/DOI: 10.1017/CBO9781316336069.006

32. Grodowska, K., & Parczewski, A. (2010). Organic solvents in the pharmaceutical industry. *Acta Poloniae Pharmaceutica*, *67*(1), 3-12.

33. Grunow, M., Günther, H. O., & Yang, G. (2003). Plant co-ordination in pharmaceutics supply networks. *Or Spectrum*, *25*(1), 109-141.

34. Gu, Z. K., Zhu, C. Y., Huang, Z. Q., Xu, M. H., & Gong, L. (2021). Numerical simulations on the adsorption characteristics of aromatics on activated carbon by the gcmc method. *Case Studies in Thermal Engineering*, *26*.

35. Han, Z. W., Wang, D., Jiang, P., Sui, H., He, L., & Li, X. G. (2020). Enhanced removal and recovery of binary mixture of <i>n</i>-butyl acetate and <i>p</i>-xylene by

temperature swing-vacuum pressure swing hybrid adsorption process. *Process Safety and Environmental Protection*, *135*, 273-281.

36. Harjunkoski, I., Maravelias, C. T., Bongers, P., Castro, P. M., Engell, S., Grossmann, I. E., Hooker, J., Méndez, C., Sand, G., & Wassick, J. (2014). Scope for industrial applications of production scheduling models and solution methods. *Computers & Chemical Engineering*, *62*, 161-193.

37. Hassan, A. A., & Sorial, G. A. (2011). Treatment of dynamic mixture of hexane and benzene vapors in a trickle bed air biofilter integrated with cyclic adsorption/desorption beds. *Chemosphere*, *82*(4), 521-528.

38. Henderson, R. K., Jiménez-González, C., Constable, D. J. C., Alston, S. R., Inglis, G. G. A., Fisher, G., Sherwood, J., Binks, S. P., & Curzons, A. D. (2011). Expanding gsk's solvent selection guide - embedding sustainability into solvent selection starting at medicinal chemistry. *Green Chemistry*, *13*(4), 854-862.

39. Ikaunieks, J., Mezmale, L., Zandeckis, A., Pubule, J., Blumberga, A., & Veidenbergs, I. (2011). Non-thermal plasma for voc treatment in flue gases. *Scientific Journal of Riga Technical University. Environmental and Climate Technologies*, *6*(-1).

40. Izquierdo, M. T., Martínez de Yuso, A., Rubio, B., & Pino, M. R. (2011). Conversion of almond shell to activated carbons: Methodical study of the chemical activation based on an experimental design and relationship with their characteristics. *Biomass and Bioenergy*, *35*(3), 1235-1244.

41. Jecha, D., Brummer, V., Lestinsky, P., Martinec, J., & Stehlik, P. (2014). Effective abatement of voc and co from acrylic acid and related production waste gas by catalytic oxidation. *Clean Technologies and Environmental Policy*, *16*(7), 1329-1338.

42. Jiun-Horng, T., Hsiu-Mei, C., Guan-Yinag, H., & Hung-Lung, C. (2008). Adsorption characteristics of acetone, chloroform and acetonitrile on sludge-derived adsorbent, commercial granular activated carbon and activated carbon fibers. *Journal of Hazardous Materials*, *154*(1-3), 1183-1191.

43. Jose, J., & Philip, L. (2021). Continuous flow pulsed power plasma reactor for the treatment of aqueous solution containing volatile organic compounds and real pharmaceutical wastewater. *Journal of Environmental Management*, *286*.

44. Kabra, S., Shaik, M. A., & Rathore, A. S. (2013). Multi-period scheduling of a multi-stage multi-product bio-pharmaceutical process. *Computers & Chemical Engineering*, *57*, 95-103.

45. Kagawa, S., Takeda, T., & Le, M. Y. (2009). Feed gas concentration and column diameter effect in vacuum pressure swing adsorption without purge gas. *Kagaku Kogaku Ronbunshu*, *35*(6), 608-612.

46. Kalender, M. A., C. (2015). Removal of chlorinated volatile organic compounds by fixed bed adsorption technique: Dsorption equilibrium and breakthrough analyses. *Romanian Biotechnological Ltters*, *20*(2), 10245.

47. Karatum, O., & Deshusses, M. A. (2016). A comparative study of dilute vocs treatment in a non-thermal plasma reactor. *Chemical Engineering Journal*, *294*, 308-315.

48. Kim, D., Cai, Z., & Sorial, G. A. (2006). Determination of gas phase adsorption isotherms--a simple constant volume method. *Chemosphere*, *64*(8), 1362-1368.

49. Kim, D., Cai, Z. L., Sorial, G. A., Shin, H., & Knaebel, K. (2007). Integrated treatment scheme of a biofilter preceded by a two-bed cyclic adsorption unit treating dynamic toluene loading. *Chemical Engineering Journal*, *130*(1), 45-52.

50. Kim, S. J. C., S.Y.; Kim, T.Y. (2002). Adsorption of chlorinated volatile organic compounds in a fixed bed of activated carbon. *Korean Journal of Chemical Engineering*, *19*(1), 61-67.

51. Knox, J. C., Ebner, A. D., LeVan, M. D., Coker, R. F., & Ritter, J. A. (2016). Limitations of breakthrough curve analysis in fixed-bed adsorption. *Ind Eng Chem Res*, *55*(16), 4734-4748.

52. Kondili, E., Pantelides, C. C., & Sargent, R. W. H. (1993). A general algorithm for short-term scheduling of batch-operations .1. Milp formulation. *Computers & Chemical Engineering*, *17*(2), 211-227.

53. Koppmann, R. (2007). *Volatile organic compounds in the atmosphere* (R. Koppmann, Ed.). Blackwell Publishing Ltd.

54. Krishna, R., & van Baten, J. M. (2012). Investigating the validity of the bosanquet formula for estimation of diffusivities in mesopores. *Chemical Engineering Science*, *69*(1), 684-688.

55. Lafita, C., Penya-Roja, J. M., Gabaldón, C., & Martínez-Soria, V. (2012). Full-scale biotrickling filtration of volatile organic compounds from air emission in wood-coating activities. *Journal of Chemical Technology and Biotechnology*, *87*(6), 732-738.

56. Lashaki, M. J., Kamravaei, S., Hashisho, Z., Phillips, J. H., Crompton, D., Anderson, J. E., & Nichols, M. (2023). Adsorption and desorption of a mixture of volatile organic compounds: Impact of activated carbon porosity. *Separation and Purification Technology*, *314*.

57. Lee, S. W., Cheon, J. K., Park, H. J., & Lee, M. G. (2008). Adsorption characteristics of binary vapors among acetone, mek, benzene, and toluene. *Korean Journal of Chemical Engineering*, *25*(5), 1154-1159.

58. Lemus, J., Martin-Martinez, M., Palomar, J., Gomez-Sainero, L., Gilarranz, M. A., & Rodriguez, J. J. (2012). Removal of chlorinated organic volatile compounds by gas phase adsorption with activated carbon. *Chemical Engineering Journal*, *211-212*, 246-254.

59. Lhuissier, M., Couvert, A., Dabert, P., Amrane, A., Kane, A., Audic, J. L., & Dumont, E. (2022). Removal of a mixture of seven volatile organic compounds (vocs) using an industrial pilot-scale process combining absorption in silicone oil and biological regeneration in a two-phase partitioning bioreactor (tppb). *Energies*, *15*(13), Article 4576.

60. Li, Y., Chang, H., Yan, H., Tian, S., & Jessop, P. G. (2021). Reversible absorption of volatile organic compounds by switchable-hydrophilicity solvents: A case study of toluene with n,n-dimethylcyclohexylamine. *ACS Omega*, *6*(1), 253-264.

61. Li, Z., Li, Y., & Zhu, J. (2021). Straw-based activated carbon: Optimization of the preparation procedure and performance of volatile organic compounds adsorption. *Materials (Basel)*, *14*(12).

62. Lillo-Ródenas, M. A., Fletcher, A. J., Thomas, K. M., Cazorla-Amorós, D., & Linares-Solano, A. (2006). Competitive adsorption of a benzene–toluene mixture on activated carbons at low concentration. *Carbon*, *44*(8), 1455-1463.

63. Liu, T., Miao, H. C., He, J., Shi, T. Z., & Chen, S. M. (2022). The migration and diffusion of unsteady-state vocs flow on activated carbon adsorption beds. *Environmental Technology*, *43*(8), 1103-1117.

64. Liu, Y. J., Holland, C. E., & Ritter, J. A. (1998). Solvent vapor recovery by pressure swing adsorption. Ii. Experimental periodic performance of the butane-activated carbon system. *Separation Science and Technology*, *33*(16), 2431-2463.

65. Ma, J. W., & Li, L. (2024). Voc emitted by biopharmaceutical industries: Source profiles, health risks, and secondary pollution. *Journal of Environmental Sciences*, *135*, 570-584.

66. Ma, L., He, M., Fu, P., Jiang, X., Lv, W., Huang, Y., Liu, Y., & Wang, H. (2020). Adsorption of volatile organic compounds on modified spherical activated carbon in a new cyclonic fluidized bed. *Separation and Purification Technology*, *235*.

67. Manjare, S. D. G., A.L. (2006). Studies on adsorption of ethyl acetate vapor on activated carbon. *Industrial & Engineering Chemistry Research*, *45*, 6563-6569.

68. Méndez, C. A., Cerdá, J., Grossmann, I. E., Harjunkoski, I., & Fahl, M. (2006). State-of-the-art review of optimization methods for short-term scheduling of batch processes. *Computers & Chemical Engineering*, *30*(6-7), 913-946.

69. Meng, F. Y., Song, M., Wei, Y. X., & Wang, Y. L. (2019). The contribution of oxygen-containing functional groups to the gas-phase adsorption of volatile organic compounds with different polarities onto lignin-derived activated carbon fibers. *Environmental Science and Pollution Research*, *26*(7), 7195-7204.

70. Misra, S., Buttazoni, L. R., Avadiappan, V., Lee, H. J., Yang, M., & Maravelias, C. T. (2022). Cpros: A web-based application for chemical production scheduling. *Computers & Chemical Engineering*, *164*.

71. Moe, W. M., Collins, K. L., & Rhodes, J. D. (2007). Activated carbon load equalization of gas-phase toluene: Effect of cycle length and fraction of time in loading. *Environmental Science & Technology*, *41*(15), 5478-5484.

72. Moniz, S., Barbosa-Póvoa, A. P., & de Sousa, J. P. (2014). Simultaneous regular and non-regular production scheduling of multipurpose batch plants: A real chemical-pharmaceutical case study. *Computers & Chemical Engineering*, *67*, 83-102.

73. Moufawad, T., Gomes, M. C., & Fourmentin, S. (2022). Deep eutectic solvents as absorbents for voc and voc mixtures in static and dynamic processes. *Chemical Engineering Journal*, *448*, Article 137619.

74. Nabatilan, M. M., Harhad, A., Wolenski, P. R., & Moe, W. M. (2009). Activated carbon load equalization of transient concentration spikes of gas-phase toluene. *Chemical Engineering Journal*, *152*(2-3), 449-457.

75. Nabatilan, M. M., & Moe, W. M. (2010). Effects of water vapor on activated carbon load equalization of gas phase toluene. *Water Research*, *44*(13), 3924-3934.

76. National Institute of Standards and Technology (NIST). (2023). *Thermophysical properties of fluid systems*. https://webbook.nist.gov/chemistry/fluid/

77. Navarri, P., Marchal, D., & Ginestet, A. (2001). Activated carbon fibre materials for voc removal. *Filtration + Separation*, *38*(1), 34-40.

78. Ouzzine, M., Romero-Anaya, A. J., Lillo-Ródenas, M. A., & Linares-Solano, A. (2019). Spherical activated carbons for the adsorption of a real multicomponent voc mixture. *Carbon*, *148*, 214-223.

79. Pak, S. H., & Jeon, Y. W. (2017). Effect of vacuum regeneration of activated carbon on volatile organic compound adsorption. *Environmental Engineering Research*, *22*(2), 169-174.

80. Palau, J., Izquierdo, M., Marzal, P., & Martínez-Soria, V. (2015). Coupling adsorption and biological technologies for multicomponent and fluctuating volatile organic compounds emissions abatement: Laboratory-scale evaluation and full-scale implementation. *Industrial & Engineering Chemistry Research*, *54*(6), 1713-1722.

81. Palmiotto, M., Fattore, E., Paiano, V., Celeste, G., Colombo, A., & Davoli, E. (2014). Influence of a municipal solid waste landfill in the surrounding environment: Toxicological risk and odor nuisance effects. *Environment International*, *68*, 16-24.

82. Pantelides, C. C. (1993). Unified frameworks for optimal process planning and scheduling. Proceedings of the Second International Conference on Foundations of Computer-Aided Process Operations, Crested Butte, Colorado, USA.

83. Papageorgiou, L. G., Rotstein, G. E., & Shah, N. (2001). Strategic supply chain optimization for the pharmaceutical industries. *Industrial & Engineering Chemistry Research*, *40*(1), 275-286.

84. Pre, P., Delage, F., & Le Cloirec, P. (2002). A model to predict the adsorber thermal behavior, during treatment of volatile organic compounds onto wet activated carbon. *Environmental Science & Technology*, *36*(21), 4681-4688.

85. Pui, W. K., Yusoff, R., & Aroua, M. K. (2019). A review on activated carbon adsorption for volatile organic compounds (vocs). *Reviews in Chemical Engineering*, *35*(5), 649-668.

86. Ramirez, D., Qi, S. Y., & Rood, M. J. (2005). Equilibrium and heat of adsorption for organic vapors and activated carbons. *Environmental Science & Technology*, *39*(15), 5864-5871.

87. Ruthven, D. M. (1984). *Principles of adsorption and adsorption processes*. John Wiley & Sons Inc.

88. Saleh, T. A., Alhooshani, K. R., & Abdelbassit, M. S. A. (2015). Evaluation of ac/zno composite for sorption of dichloromethane, trichloromethane and carbon tetrachloride: Kinetics and isotherms. *Journal of the Taiwan Institute of Chemical Engineers*, *55*, 159-169.

89. Samaddar, P., Kim, K. H., Yip, A. C. K., Zhang, M., Szulejko, J. E., & Khan, A. (2019). The unique features of non-competitive vs. Competitive sorption: Tests against single volatile aromatic hydrocarbons and their quaternary mixtures. *Environmental Research*, *173*, 508-516.

90. Sampat, A. M., Kumar, R., Pushpangatha Kurup, R., Chiu, K., Saucedo, V. M., & Zavala, V. M. (2021). Multisite supply planning for drug products under uncertainty. *AIChE Journal*, *67*(1), e17069.

91. San-Valero, P., Gabaldón, C., Alvarez-Hornos, F. J., Izquierdo, M., & Martínez-Soria, V. (2019). Removal of acetone from air emissions by biotrickling filters: Providing solutions from laboratory to full-scale. *Journal of Environmental Science and Health Part a-Toxic/Hazardous Substances & Environmental Engineering*, *54*(1), 1-8.

92. Sempere, F., Gabaldón, C., Martínez-Soria, V., Penya-Roja, J. M., & Alvarez-Hornos, F. J. (2009). Evaluation of a combined activated carbon prefilter and biotrickling filter system treating variable ethanol and ethyl acetate gaseous emissions. *Engineering in Life Sciences*, *9*(4), 317-323.

93. Sempere, F., Martínez-Soria, V., Penya-roja, J. M., Izquierdo, M., Palau, J., & Gabaldón, C. (2010). Comparison between laboratory and pilot biotrickling filtration of air emissions from painting and wood finishing. *Journal of Chemical Technology and Biotechnology*, *85*(3), 364-370.

94. Servapure. (2023). *Calgon olc 12x30 mesh coconut shell activated carbon.* Retrieved November from https://www.servapure.com/Calgon-OLC-12-x-30-Mesh-Coconut-Shell-Activated-Carbon-1-Cu-Ft-Box_p_6949.html

95. Shah, N. (2004). Pharmaceutical supply chains: Key issues and strategies for optimisation. *Computers & Chemical Engineering*, *28*(6-7), 929-941.

96. Shah, N., Pantelides, C. C., & Sargent, R. W. H. (1993). A general algorithm for short-term scheduling of batch-operations .2. Computational issues. *Computers & Chemical Engineering*, *17*(2), 229-244.

97. Shaik, M. A., & Floudas, C. A. (2007). Improved unit-specific event-based continuous-time model for short-term scheduling of continuous processes: Rigorous treatment of storage requirements. *Industrial & Engineering Chemistry Research*, *46*(6), 1764-1779.

98. Sheldon, R. A. (2007). The e factor: Fifteen years on. *Green Chemistry*, *9*(12), 1273-1283.

99. Shi, T. Z., Liu, T., Qiang, N., He, J., Li, Z. H., Cao, Y. Q., & Shi, X. B. (2023). Diffusion, separation, and buffering of non-steady-state vocs flow on activated carbon. *Separations*, *10*(11), Article 571.

100. Shim, W. G., Lee, J. W., & Moon, H. (2003). Equilibrium and fixed-bed adsorption of n-hexane on activated carbon. *Separation Science and Technology*, *38*(16), 3905-3926.

101. Siddhaye, S., Camarda, K., Southard, M., & Topp, E. (2004). Pharmaceutical product design using combinatorial optimization. *Computers & Chemical Engineering*, *28*(3), 425-434.

102. Simayi, M., Shi, Y. Q., Xi, Z. Y., Ren, J., Hini, G., & Xie, S. D. (2022). Emission trends of industrial vocs in china since the clean air action and future reduction perspectives. *Science of the Total Environment*, *826*.

103. Sircar, S., & Hufton, J. R. (2000). Why does the linear driving force model for adsorption kinetics work ? *Adsorption-Journal of the International Adsorption Society*, *6*(2), 137-147.

104. Siu, B., Chowdhury, A. R., Yan, Z. W., Humphrey, S. M., & Hutter, T. (2023). Selective adsorption of volatile organic compounds in metal-organic frameworks (mofs). *Coordination Chemistry Reviews*, *485*, Article 215119.

105. Sorrels, J. L., Baynham, A., Randall, D.D., Schaffner, K.S. . (2018). *Carbon adsorbers*. Retrieved from https://www.epa.gov/sites/default/files/2018-10/documents/final_carbonadsorberschapter_7thedition.pdf

106. Spectrum Chemical Manufacturing Mfg Corp. (2024). *Dichloromethane*. Retrieved 03 April 2024 from https://www.spectrumchemical.com/chemical/organic-chemicals/monofunctional-alpha-omega-bifunctional-alkanes/alpha-omega-bifunctional-alkanes/methylene-chloride-technical-m1252

107. Suzuki, K., Takeda, T., Le, M., Shinkai, M., & Kagawa, S. (2007). Operation of vacuum pressure swing adsorption without purge gas and proposal of a valuation method. *Journal of Chemical Engineering of Japan*, *40*(9), 736-740.

108. Suzuki, M. (1990). *Adsorption engineering*. Kodansha Ltd and Elsevier Science Publishers.

109. Talmoudi, R., AbdelJaoued, A., & Chahbani, M. H. (2018). Dynamic study of vsa and tsa processes for vocs removal from air. *International Journal of Chemical Engineering*, *2018*.

110. Tefera, D. T., Hashisho, Z., Philips, J. H., Anderson, J. E., & Nichols, M. (2014). Modeling competitive adsorption of mixtures of volatile organic compounds in a fixed-bed of beaded activated carbon. *Environmental Science & Technology*, *48*(9), 5108-5117.

111. Tefera, D. T., Lashaki, M. J., Fayaz, M., Hashisho, Z., Philips, J. H., Anderson, J. E., & Nichols, M. (2013). Two-dimensional modeling of volatile organic compounds adsorption onto beaded activated carbon. *Environmental Science & Technology*, *47*(20), 11700-11710.

112. Tzanakopoulou, V. C., A.; Castro-Rodriguez, D.; Gerogiorgis, D.I. (2022). Multicomponent, nonisothermal voc adsorption modelling for pharmaceutical effluent purification: Effect of operating conditions on bed performance. *Computer Aided Chemical Engineering*, *51*, 331-336.

113. Tzanakopoulou, V. E., Pollitt, M., Castro-Rodriguez, D., Costa, A., & Gerogiorgis, D. I. (2023). Dynamic modelling, simulation and theoretical performance analysis of volatile organic compound (voc) abatement systems in the pharma industry. *Computers & Chemical Engineering*, *174*.

114. UK Department Energy Security and Net Zero. (2024). *Prices of fuels purchased by manufacturing industry*. Retrieved 06 April from https://www.gov.uk/government/statistical-data-sets/prices-of-fuels-purchased-by-manufacturing-industry

115. UK Office for National Statistics (ONS). (2023). *Low and high pay uk: 2023*. Retrieved 06 April 2024 from https://www.ons.gov.uk/employmentandlabourmarket/peopleinwork/earningsandworkinghours/bulletins/lowandhighpayuk/2023

116. United Nations. (2023). *The 17 goals*. Retrieved 27 September 2023 from https://sdgs.un.org/goals

117. Vieira, M., Pinto-Varela, T., & Barbosa-Póvoa, A. P. (2017). Production and maintenance planning optimisation in biopharmaceutical processes under performance decay using a continuous-time formulation: A multi-objective approach. *Computers & Chemical Engineering*, *107*, 111-139.

118. Vuong, F., Chauveau, R., Grevillot, G., Marsteau, S., Silvente, E., & Vallieres, C. (2016). Predicting the lifetime of organic vapor cartridges exposed to volatile organic compound mixtures using a partial differential equations model. *J Occup Environ Hyg*, *13*(9), 675-689.

119. Wantz, E., Kane, A., Lhuissier, M., Amrane, A., Audic, J. L., & Couvert, A. (2021). A mathematical model for vocs removal in a treatment process coupling absorption and biodegradation. *Chemical Engineering Journal*, *423*, Article 130106.

120. Yang, X., Yi, H. H., Tang, X. L., Zhao, S. Z., Yang, Z. Y., Ma, Y. Q., Feng, T. C., & Cui, X. X. (2018). Behaviors and kinetics of toluene adsorption-desorption on activated carbons with varying pore structure. *Journal of Environmental Sciences*, *67*, 104-114.

121. Yao, X. L., Liu, Y., Li, T., Zhang, T. T., Li, H. L., Wang, W., Shen, X. B., Qian, F., & Yao, Z. L. (2020). Adsorption behavior of multicomponent volatile organic compounds on a citric acid residue waste-based activated carbon: Experiment and molecular simulation. *Journal of Hazardous Materials*, *392*.

122. Yun, J. H., Choi, D. K., & Kim, S. H. (1999). Equilibria and dynamics for mixed vapors of btx in an activated carbon bed. *AIChE Journal*, *45*(4), 751-760.

123. Zehraoui, A., & Sorial, G. A. (2015). Treatment of dynamic mixture of <i>n</i>-hexane, benzene, and methanol and fungi community characterization in an integrated scheme of cyclic adsorption/desorption beds and trickle bed air biofilter. *Air Soil and Water Research*, *8*.

124. Zhang, X. Y., Gao, B., Creamer, A. E., Cao, C. C., & Li, Y. C. (2017). Adsorption of vocs onto engineered carbon materials: A review. *Journal of Hazardous Materials*, *338*, 102-123.

125. Zhou, X. H., Zhou, X. A., Wang, C. M., & Zhou, H. D. (2023). Environmental and human health impacts of volatile organic compounds: A perspective review. *Chemosphere*, *313*.

126. Zhu, J., Zhan, H. L., Zhao, K., Miao, X. Y., Zhou, Q., & Yue, W. Z. (2019). Competitive and synergistic adsorption of binary volatile organic compound mixtures on activated carbon. *Chinese Physics B*, *28*(2).